

POLITECNICO DI MILANO

Facoltà di Ingegneria Industriale

Corso di Laurea in
Ingegneria energetica



**THERMAL CHARACTERIZATION OF LITHIUM-ION
BATTERY CELL**

Relatore: Prof. Angelo Onorati

Co-relatore: Dr. Marcello Canova

Tesi di Laurea di:

Matteo Muratori

Matr. 720824

Anno Accademico 2008 - 2009

Dedicatio

I would first like to thank Professor Giorgio Rizzoni and my advisor, Professor Angelo Onorati, for giving me the opportunity to participate to this research experience. I would also like to thank Dr. Marcello Canova for his supervision, his help and all his suggestions during these months. A special thank to Prof. Yann Guezennec, Ning Ma and John Neal for their support and precious suggestions.

Finally, I would like to thanks all my friends and, above all, my family.

Table of contents

List of symbols	I
Abstract	III
Sommario	V
1. Introduction	1
1.1 Motivation and objectives of the thesis	4
1.2 Structure of the thesis	5
2. Review of the state of art for Li-Ion battery modeling	7
2.1 Electrical characterization	8
2.2.1 Fundamental models	11
2.2.2 Phenomenological models	17
2.2 Thermal characterization	23
2.3.1 Single cell thermal models	24
2.3.2 Battery pack thermal models	29
2.3.3 Thermal management systems	47
2.3 Summary	52
3. Modeling the thermal dynamics of Li-Ion batteries	53
3.1 Thermal modeling approach and mathematical formulation	54
3.1.1 Basic equation for energy conservation	54
3.1.2 Basic equation for fluid flow	55
3.1.3 Basic equations for heat transfer	59
3.2 Assumptions for battery thermal modeling	67
3.2.1 Mathematical formulation of the simplified system	68
3.3 Summary	69
4. Development of the thermal modeling approach	71
4.1 Introduction and scope of the work	71
4.2 Development of thermal model structure	74
4.2.1 General mathematical formulation of 1-D temperature distribution in a prismatic finite medium	74
4.2.2 Formulation of model with convective boundary conditions	81

4.2.3 Formulation of 1+1D pack model with air cooling	88
4.2.4 Formulation of model with imposed temperature boundary conditions.....	94
4.2.5 Formulation of 1+1D pack model with cooling bar system	99
4.3 Summary.....	104
5. Calibration and validation of the models	105
5.1 Technical specification of modeled Li-Ion battery cell.....	105
5.1.1 Description of the battery module	106
5.2 Calculation of the battery thermal parameters.....	108
5.2.1 Calculation of cell density, thermal capacity and thermal conductivity	108
5.2.2 Convective heat transfer coefficient	113
5.3 Definition of the model inputs: current profile and heat generation rate	116
5.4 Model calibration and validation	118
5.4.1 Experimental set-up	118
5.4.2 Thermal conductivity experiment.....	122
5.4.3 FEM comparison.....	126
5.5 Summary.....	132
6. Conclusions.....	133
6.1 Future work.....	134
Bibliography	135
Appendix A: Product specification ePLBc020B	141
Appendix B: A reduced order model for the thermal dynamics of Li-Ion battery cells.....	151
Appendix C: A model order reduction method for the temperature estimation in a cylindrical Li-Ion battery cell	157
Appendix D: A 1+1D thermal dynamic model of a Li-Ion battery cell	165

Acronyms

BC	Boundary Condition
BEV	Battery Electric Vehicle
BMS	Battery Management System
BVP	Boundary Value Problem
CAR	Center for Automotive Research
COM	Control Oriented Model
EMS	Energy Management System
EV	Electric Vehicle
FEM	Finite Elements Method
HEV	Hybrid Electric Vehicle
IC	Initial Condition
Li-Ion	Lithium ion
Ni-Cd	Nickel-Cadmium battery
Ni-MH	Nickel-metal hydride battery
NREL	National Renewable Energy Laboratory
ODE	Ordinary Differential Equation
PDE	Partial Differential Equation
PHEV	Plug-in Hybrid Electric Vehicle
RC	Randle Circuit
SoC	State of Charge
SoH	State of Health

Abstract

The electro-thermal characterization of Li-Ion batteries is today a forefront topic, due to the recent interest in Electric Vehicles (EVs), Plug-in Electric Vehicles (PHEVs) and Hybrid Electric Vehicles (HEVs).

In order to control and manage these devices, suitable models are needed. For control-oriented applications, the electro-thermal behavior of a battery is typically modeled using an equivalent circuit analogy approach. This leads to phenomenological models that capture the essential steady-state and dynamic behavior of the system (typically voltage as a function of a current input), relying on a set of calibration parameters. The model parameters, such as the open-circuit voltage, battery capacity and internal resistance, are typically scheduled with respect to the temperature, which is regarded as static input to the model.

The assumption commonly made in this case is to consider the temperature uniform throughout the whole system. However, in a real case a battery cell presents an internal temperature distribution, due to its thermal resistance and the internal heat generation. Although these phenomena are often overlooked in these simplified models, they may be quite relevant for safety and aging related issues. Therefore, for applications related to battery management systems design and optimization, or for the thermal management of such components, it is necessary to provide information on the battery internal temperature.

In this thesis, a general modeling methodology that accounts for the internal temperature dynamics is proposed to predict the temperature distribution within a prismatic battery cell, accounting for different operating conditions. Unlike most control-oriented models, based on identification techniques, the proposed modeling approach is physically based, relying on the fundamental equations for heat diffusion and convection. This ensures consistency with the system behavior, and relies on a set of physical parameters that can be easily obtained from the open literature or from experimental tests. Various models have been developed, considering different cooling solutions commonly available for battery packs for motive applications. First, a general model is developed starting from the formulation of 1D unsteady heat diffusion problem that accounts for different boundary conditions. Then, the 1D model structure developed is extended to a 1+1D scheme in order to account for the variability of the boundary conditions. A spatial discretization is operated along the second direction to account for the evolution of the boundary conditions. Within each cell lump, the internal temperature profile is determined by solving the unsteady heat diffusion equation with internal heat generation and the proper boundary conditions. The proposed modeling approach allows for a

complete mapping of a Li-Ion battery cell temperature with respect to both time and space. At the same time, the solution scheme adopted leads to an algorithm that is sufficiently simple and computationally efficient. The 1+1D modeling approach developed allow for an easy and rapid comparison of different cooling systems.

The modeling methodology developed is applied to a pouch-style Li-Ion battery cell and an experimental setup is developed ad hoc to characterize the thermal behavior of a Li-Ion battery cell. The experimental results are used to calibrate the model. A 1+1D model of a cooling air system is developed and then validated though a comparison with an advanced finite element simulator.

The model developed is general and characterized by a flexible structure, which allows one easily select cooling parameters, such as cooling air velocity, air temperature, air duct geometry, etc., and compare the effects of different cooling systems. The consistency with the FEM solution, the simple structure, and the computational efficiency make the model an ideal candidate for simulation of battery packs, performance estimation, design of cooling systems, and optimization of thermal management systems.

Key words: *Energy storage systems, Li-Ion battery, Thermal characterization, Battery modeling.*

Sommario

I temi del risparmio energetico e dell'eco-sostenibilità sono al giorno d'oggi in primo piano per lo sviluppo della società.

Nel settore dei trasporti su ruota, i veicoli ibridi (HEV/PHEV) sono la soluzione seguita dai grandi costruttori per far fronte al problema. A tutt'oggi, il maggior ostacolo alla diffusione di questi veicoli resta lo stoccaggio dell'energia. Le batterie agli ioni di litio (Li-Ion), data la loro grande potenza ed energia specifica, sono la prima scelta come sistema di stoccaggio dell'energia a bordo di tali veicoli. Tali dispositivi, d'altro canto richiedono un sistema di gestione e controllo dedicato.

In questo lavoro di tesi viene affrontato il tema della modellazione termica di batterie agli ioni di litio. I modelli volti al controllo e alla gestione delle batterie approssimano normalmente il funzionamento di tali dispositivi attraverso l'uso di circuiti elettrici equivalenti. I parametri di tali circuiti, quali tensione a circuito aperto, resistenza interna e capacità della batteria, vengono tabulati in funzione dello stato di carica (SoC) e della temperatura.

La maggior parte dei modelli volti al controllo delle batterie ipotizzano che il sistema sia a temperature uniforme. Tuttavia la resistenza termica della batteria e il calore generato internamente fanno sì che si generi una distribuzione instazionaria tridimensionale di temperatura all'interno della batteria stessa.

Da questo l'esigenza di sviluppare modelli termici più dettagliati, che siano in grado di predire la distribuzione di temperatura all'interno di una batteria senza d'altro canto diventare eccessivamente inefficienti dal punto di vista del tempo di calcolo e della memoria richiesti. In questa tesi viene sviluppata una metodologia di modellazione per predire la distribuzione di temperatura in una batteria agli ioni di litio, in presenza di generazione interna di calore e considerando diverse condizioni di funzionamento. L'approccio seguito si basa solo su principi fisici e non su tecniche d'identificazione sperimentale normalmente usate per caratterizzare tali modelli.

In primo luogo è presentata una revisione dell'attuale stato dell'arte. Partendo dalla caratterizzazione elettrica sono definiti e descritti modelli "fondamentali" e "fenomenologici". Particolare rilievo è dato ai modelli volti al controllo e alla gestione delle batterie agli ioni di litio (control-oriented models). Un ampio esame delle tecniche e degli approcci di modellazione della parte termica è fornito nella seconda parte del Capitolo 2. Questa parte è divisa in tre sottosezioni, rispettivamente caratterizzazione termica di una singola cella, caratterizzazione termica di un pacco di batterie e sistemi di gestione termica delle batterie.

Il Capitolo 3 presenta l'approccio seguito in questa tesi per modellare la dinamica termica di una batteria agli ioni di litio. Dato che tale approccio

fonda su principi fisici, è proposta una revisione dei concetti di bilancio energetico e delle equazioni di base di trasmissione del calore.

Nel Capitolo 4 viene sviluppata la metodologia di modellazione. In primo luogo è stato risolto un problema monodimensionale. L'equazione della diffusione del calore è risolta applicando il metodo delle trasformate integrali, ottenendo una soluzione in grado di predire la distribuzione interna di temperatura con qualsiasi condizione al contorno. In particolare sono presentati due casi di particolare interesse: condizioni al contorno di convezione e condizioni di temperatura di parete imposta.

Il primo modello simula il comportamento della batteria quando raffreddata con un flusso d'aria mentre il secondo riproduce le condizioni a cui è sottoposta la batteria durante i test di identificazione dei parametri interni. In questi test la batteria viene posta in mezzo a due celle di Peltier che impongono una temperatura di parete al sistema. I due modelli 1D sono poi estesi seguendo un approccio 1+1D in modo da tenere in considerazione la variabilità delle condizioni al contorno nella seconda direzione spaziale.

Il sistema viene discretizzato in questa direzione ed in ogni blocco il modello 1D è utilizzato per predire la distribuzione di temperatura. Questo consente di ottenere una distribuzione bi-dimensionale della temperatura, mantenendo una struttura semplice e un'elevata efficienza computazionale. Il modello 1+1D con temperatura imposta simula il comportamento di un "cooling bar system". I modelli sviluppati consentono una rapida comparazione tra i due sistemi di raffreddamento e la metodologia può trovare applicazioni nel settore del design e dell'ottimizzazione di sistemi di raffreddamento e gestione termica di pacchi di batterie.

Nel Capitolo 5 la metodologia sviluppata viene applicata per modellare un modulo agli ioni di litio prodotto da EiG. Come primo approccio i parametri termici della batteria richiesti dal modello sono calcolati a partire da dati disponibili in letteratura.

Un setup sperimentale ad hoc ed un laboratorio sono stati allestiti per effettuare la caratterizzazione termica di batterie. La conduttività termica della cella prima calcolata, è stata misurata sperimentalmente in modo da calibrare il modello sviluppato.

I risultati del modello sono stati comparati con simulazioni effettuate con un noto software basato sul metodo delle differenze finite. Alla fine del lavoro, il modello 1+1D è stato calibrato e validato tramite tale comparazione. I risultati ottenuti sono sufficientemente accurati da poter affermare che la metodologia sviluppata è adeguata allo scopo per il quale è stata implementata. La sua semplice struttura e l'efficienza computazionale rendono il modello proposto un candidato ideale per la simulazione del comportamento termico di pacchi di batterie, per il design di sistemi di raffreddamento o sistemi di gestione termica. Possibili applicazioni dell'approccio presentato possono

essere trovati nel settore dell'analisi e comparazione di diverse tecnologie di raffreddamento delle batterie.

CHAPTER 1

1. Introduction

The modern society relies completely on the fossil fuels - natural gas, coal and oil - for its energetic needs. Their reserves are however limited and the environmental concern is nowadays haunting the society.

The utilization of energy in a sustainable way is the only pursuable solution to cope with these problems. On a short-medium time frame the energy systems are experiencing an increasing of their electrification, in order to reduce fuel consumption and emissions.

Thus, the conversion and storage of energy is becoming a necessary step for the global efficiency of the energy generation and utilization process. The most used devices to store energy are, nowadays, electro-chemical batteries. They interconvert chemical and electrical energy and are widely used in all sectors of industry (automotive, aerospace, medical, military, etc.) and in consumer oriented applications (e.g., appliances, laptop computers or any electronic device).

In order to maintain competitiveness, automakers have to improve powertrain performance and reduce pollutant emissions. In particular, stricter emission standards are spurring new interest in batteries for electric-vehicle applications.

Lithium-based batteries are attractive as energy storage systems in hybrid and electric vehicles due to their high theoretical energy densities. Furthermore, they are less toxic than nickel cadmium or lead acid cells, and their disposal poses fewer environmental problems.

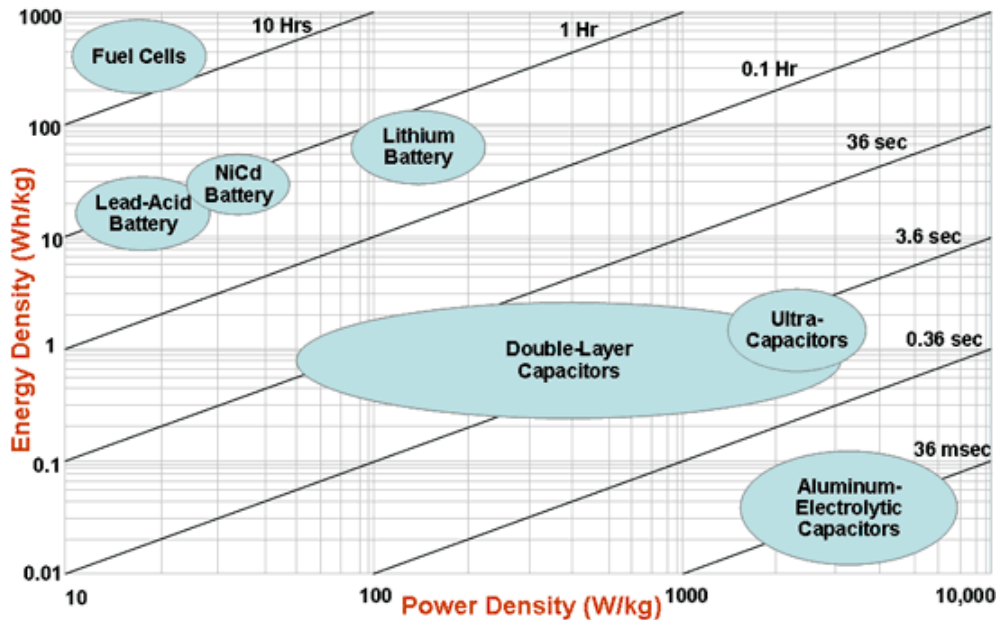
Figure 1.1 shows a Ragone¹ plot for various electro-chemical systems, which reveals that, at one extreme, energy can be stored into, or extracted from, capacitors in milliseconds, making them ideal devices for example to exploit regenerative braking energy in Electric Vehicles (EVs) applications.

At the other end, fuel cells have a very poor dynamic performance requiring more time to convert and deliver energy. This limits their application in automotive applications where they are often used in conjunction with batteries

¹ A Ragone plot, like the ones depicted in Figure 1.1 and 3, is a double chart used for performance comparison of various energy storing devices. On such a chart the values of energy density [Wh/kg] are plotted versus power density [W/kg]. Both axes are logarithmic, which allows comparing performance of very different devices (for example extremely high, and extremely low power).

Conceptually, the vertical axis describes how much energy is available, while the horizontal axis shows how quickly that energy can be delivered. The sloping lines on the Ragone plots indicate the relative time to get the charge in or out of the device.

or capacitors to overcome this problem. Lithium based batteries are somewhere in between and provide a reasonable compromise between the two.



Source US Defence Logistics Agency

Figure 1.1. Ragone plot of various electro-chemical conversion systems [1].

A lithium ion (Li-Ion) battery is a type of rechargeable battery where lithium ions move from the anode (negative pole) to cathode (positive pole) during discharge and from the cathode to the anode during the charge process. Figure 1.2 reports a sketch of the chemistry of a Li-Ion cell.

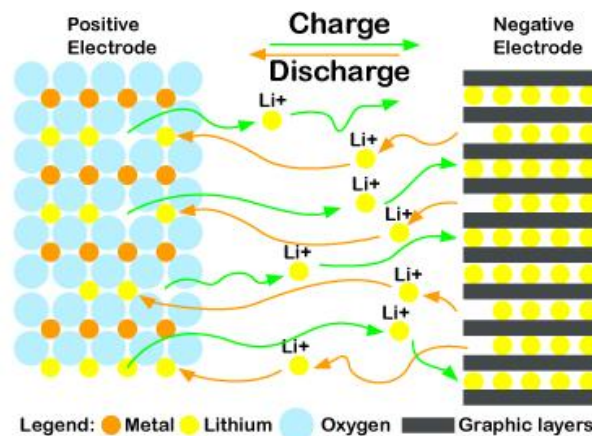


Figure 1.2. Li-Ion electro-chemical or elementary cell, [1].

Different types of Li-Ion batteries use different chemistries and present different performance, cost, and safety characteristics.

These electric storage devices, first proposed by M.S. Whittingham in the 70's, now represent a substantial part of the fast growing battery market [2]. They achieved this predominant role because Li-Ion storage systems present the best specific energy and power densities among the chemical storage systems, as shown in Figure 1.3.

Li-Ion batteries are rapidly becoming the technology of choice for the next generation of Electric Vehicles, Battery Electric Vehicles, Plug-In Hybrid and Hybrid Electric Vehicles (EVs/BEVs/PHEVs/HEVs). The automotive industry is increasingly committed to electrified vehicles to providing sustainable mobility in the next decade. Li-Ion battery, so far, is the technology that best fits for the need of these vehicles, due to their large specific energy density and specific power, making these cells ideally suited for high rate-of-discharge applications such as acceleration of electric vehicles (see Figure 1.3).

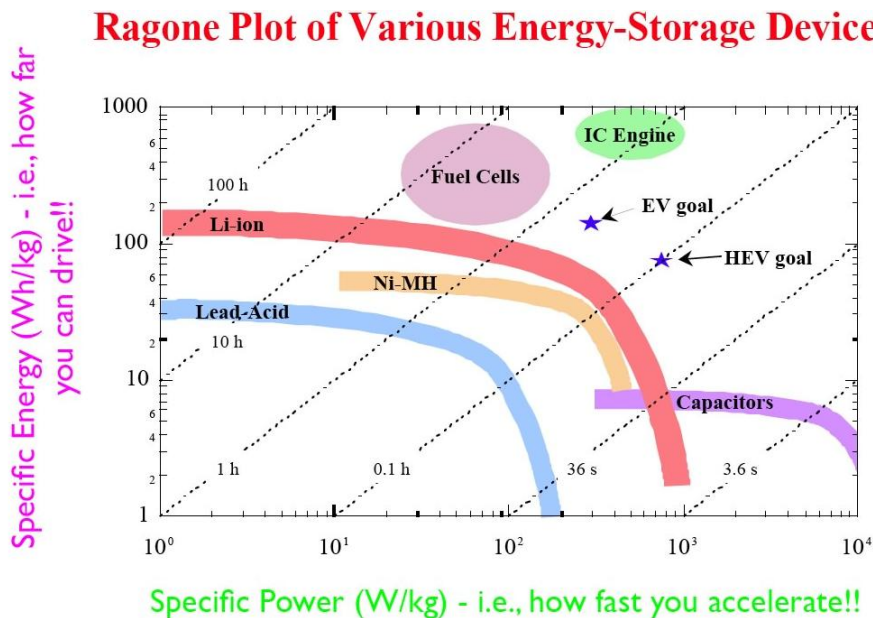


Figure 1.3. Ragone plot of energy-storage devices for automotive applications, [3].

Right now, the major obstacle to an increased market share of HEVs and mass-produced commercialization of PHEVs is the battery, and in particular its cost, reliability and safety. To this end, great effort is being devoted to address the safety, performance and aging² issues of Li-Ion batteries [4].

To achieve the required reduction in fossil fuel consumption, a significant percentage of the world automobile fleet of 1 billion vehicles will be electrified in the coming decade [5]. Ultimately all production, currently 52 Million vehicles per year (according to the International Organization of Motor Vehicle

² A Li-Ion battery is subjected to two different kinds of aging. One is driven by thermal effects the other is by current loads and cycling.

Manufacturers), will be replaced with highly electrified vehicles: PHEVs and BEVs [6]. To this extend, great interest is devoted to improve the performance of such vehicles and their components. In particular, a lot of emphasis and efforts been dedicated to the development of new battery technologies over the last decade.

1.1 Motivation and objectives of the thesis

Since the performance, life and reliability of Li-Ion batteries are quite dependent on the operating temperature, great interest has been devoted to study cooling solutions and control algorithms for thermal management.

Detailed studies of the temperature distribution within Li-Ion battery cells during charging and discharging conditions have been proposed by several authors (see [7], [8], [9], [10]). Most of these studies are conducted utilizing FEM (Finite Element Method) thermal simulators, often coupled with detailed models that characterize the electrochemical reactions and transport phenomena that take place inside a battery.

Such simulators are extremely useful to gain understanding on how the temperature distribution affects the performance of a battery cell. Moreover, they also provide important information for cell modeling and design; for instance they can help identifying hot spots. On the other hands, such tools are too complex to be applied to studies oriented to the characterization of the electro-thermal performance of modules and packs, or to the design of battery cooling systems and control algorithms.

This thesis presents a computationally efficient modeling approach to characterize the internal temperature distribution within a Li-Ion battery cell. This would serve as a tool to design models characterizing the thermal behavior of Li-Ion battery cells to be used in the area of performance and thermal management studies for battery pack cooling systems.

To meet these objectives, the model must be both sufficiently simple to be executed almost in real-time, and accurate enough to provide a reasonably estimation of thermal dynamics inside the cell.

Computationally efficient models that can provide a reasonable estimate of the cell thermal field, with limited calibration effort, can be useful tools for battery pack designers and integrators.

The modeling methodology presented in this thesis is based on the unsteady heat diffusion equation, for which an analytical solution is obtained through the integral transform method proposed by Ozisik, [11].

First of all, a general one-dimensional thermal model is developed to predict the temperature distribution inside a prismatic Li-Ion battery cell under different boundary and initial conditions.

Second, a specific case with convective boundary conditions is studied with the objective of characterizing a cell cooled by a forced air flow.

To characterize the effects of the cooling system on the temperature distribution within the cell, the one-dimensional solution is then extended to a 1+1D³ model that accounts for the variability of the boundary conditions in the flow direction. Then a 1D model with imposed boundary conditions is developed to predict the temperature distribution within a Li-Ion battery cell during the typical electrical characterization experiment, where two Peltier junctions are used to keep the temperature of the cell walls at imposed values. Finally, the latter case study is extended to a 1+1D model in order to characterize the behavior of a cooling bar system.

The inputs needed by the model, namely the heat generation rate and the thermal parameters, will be presented. Finally, an ad hoc experimental set-up to measure the thermal parameters of the studied Li-Ion battery cell will be developed.

The calibration and validation of the model will be presented, adopting a detailed 2D FEM simulator as a benchmark.

1.2 Structure of the thesis

The thesis is organized as follows. In the second chapter a literature review of the state of art of Li-Ion battery modeling is presented, with particular focus on the thermal characterization aspects.

Chapter 3 presents the approach to model the thermal dynamics of a Li-Ion battery and the basic physical principles needed to implement a thermal model.

In Chapter 4 the modeling methodology to predict the internal temperature distribution in a prismatic Li-Ion battery cell is developed. First, a general 1D modeling approach is described and then it is extended to a 1+1D approach.

In Chapter 5 the modeling technique developed is first experimentally calibrated, and then validated through a comparison with a finite element (FEM) software.

³ A 1+1D approach is an approximated method to model a 2D problem. It consists in solving the mono-dimensional (x -direction) associated problem, which presents an easier mathematical solution. Then, by performing a spatial discretization in the second direction (y -direction), it is possible to capture the trend along this direction. In this case, a battery cell is discretized along the y direction into a certain number N of lumps. The 1D solution in x -direction is applied in each lump along the y -direction, thus obtaining a solution varying with respect to both x and y . The solution results in a simple mathematical formulation and is much more computationally efficient than the 2D solution.

CHAPTER 2

2. Review of the state of art for Li-Ion battery modeling

Li-Ion batteries are becoming the dominant battery technology, in particular for high power systems. However, they must be used properly to prevent accelerated aging, decreasing of performance or damages.

Therefore, there is a fundamental need for a battery management system (BMS) capable of assessing and controlling the state of charge (SoC⁴) and state of health (SoH⁵) of a battery pack (see [12] or [13] for a discussion on BMS).

These two parameters (SoC and SoH) allow the vehicle energy management system (EMS) and the battery management system (BMS) to determine the optimal operating strategy so that fuel consumption is minimized and battery pack longevity maximized.

SoC and SoH are difficult quantities to estimate because direct measurements are either unreliable or impossible [14]. For example, SoC can be measured via current integration, but noise in the electrical current measurement can cause the estimate to deviate from the true value. SoH is often assessed in terms of capacity or power fading, both of which are measurable in a laboratory environment, but are almost impossible to estimate during vehicle operations.

Many algorithms have been proposed in the literature to face this problem [15], [16]. They range from data correlation methods such as artificial neural networks [17] and fuzzy logic systems [18] to model based approaches such as Kalman filtering [19] and sliding mode observers [20]. Model-based approaches

⁴ The SoC is defined as the capacity still available in a battery cell. It is normally expressed as a percentage of the rated capacity of a new cell and a 0% SoC means empty battery while a 100% SoC means fully charged battery.

Knowing the amount of energy left in a battery compared with the energy it had when it was fully charged gives the user an indication of how much longer a battery will be able to supply a load before it needs recharging. Several methods of estimating the SoC of a battery are used: SoC from specific gravity measurement, voltage based estimation methods, internal impedance or current based estimations.

⁵ The SoH is an indication of the point which has been reached in the life cycle of the battery. SoH is an estimation rather than a measurement. It reflects the general condition of a battery and its ability to deliver the specified performance compared with a new battery, taking into account such factors as charge acceptance, internal resistance, voltage, and self-discharge [1]. Knowledge of the SoH can be used to make prognosis or diagnosis and plan replacements [4]. This is essentially a monitoring function tracking the long term changes in the battery.

are attractive since they provide good result requiring a small effort for the calibration [21].

However, in order to take advantage of model-based approaches, it is necessary to define models of the behavior of the battery. In doing so, it is critical to balance the accuracy with the complexity and computational time

This chapter presents a literature review on different approaches to Li-Ion battery modeling. First, a review of the electrical characterization techniques will be presented. Then fundamental and phenomenological models will be defined and explained. Finally, an extensive review of the thermal characterization modeling and thermal management systems will be presented. The open literature consists of many papers providing analysis of lithium-based batteries. Perhaps the most comprehensive reference books on the subject are [1] and [22].

With the increase of computational power and the need to analyze the problems in a more detailed way, modeling approaches are becoming more and more important. Many ways to model electrochemical energy storage systems exist: normally they are classified as fundamental or phenomenological.

The former can be defined as *First Principles Models*, as they attempt at representing a system starting from its physical foundations. Alternatively, phenomenological models refer to models that provide a representation of the input/output relationships of a system without investigating the fundamental physics.

In particular, this study focuses on control oriented models which are low-order dynamic models (linear or quasi-linear) used to design control algorithms. Such models, because of the need for simple structure and low computation effort, are mostly phenomenological.

2.1 Electrical characterization

The first step in the development of a battery model is to perform an electrical characterization of the system.

The typical lithium elementary cell is made up of a metal negative electrode (anode), an electrolyte which serves as an ionic path between electrodes, a positive electrode (cathode), such as Mn_2O_4 , and a polymeric separator.

Figure 2.1 shows a typical Li-Ion elementary cell under the discharge process. Note that during the charge the lithium ions and the electrons move in the opposite direction, namely from cathode (positive pole) to anode (negative pole).

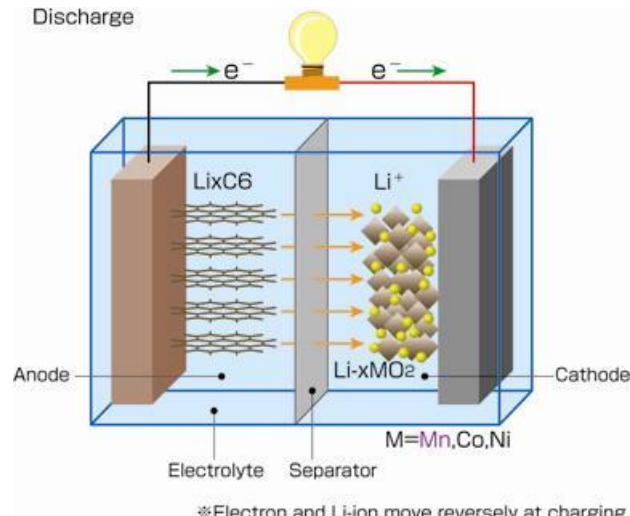


Figure 2.1. Electrons and Li-ion movement during discharge, [1].

In this thesis the term elementary or electro-chemical cell will be used to denote the sandwich anode-electrolyte-cathode shown in Figure 2.1. A battery cell is composed by a number of elementary cells in series and is a device which is able to supply an electrical load, like the one in Figure 2.2.

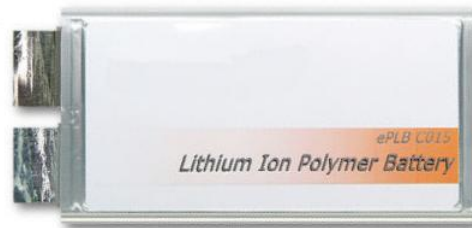


Figure 2.2. Li-Ion battery cell, [23].

A battery module consists of the union of two or more cells electrically connected, while, as shown in Figure 2.3, a battery pack is the union of two or more battery modules.



Figure 2.3. Example of battery pack composed by four modules, [24].

Regarding an elementary cell, a highly reactive material is desired for the negative electrode to give a higher cell potential, and hence a higher theoretical energy density. Unfortunately, the more reactive the electrode material the more likely it reacts irreversibly with the electrolyte. The high reactivity of lithium metal is a significant problem for lithium based batteries. To avoid this problem, lithium battery systems feature a protective film that forms on the electrode surface.

Alternatively, the lithium metal negative electrode can be replaced with a lithium alloy or compound. These materials stabilize the lithium, but also reduce the energy density of the cell since the added material is not used in the operation of the system.

Rechargeable batteries for electric-vehicle applications require long cycle life; 500 to 1000 cycles are desired before the capacity falls below 80% of its initial value. For this to be possible, the electrochemical reactions must be highly reversible. Some of the most reversible electrodes operate through insertion reactions.

The lithium ion dual insertion systems exhibit the largest theoretical specific energy densities for lithium-based systems, although the energy necessarily is reduced from corresponding systems utilizing solid lithium anodes, as shown in Figure 2.4, proposed by [25].

The latter systems, however, present instability problems and they are not commercially available.

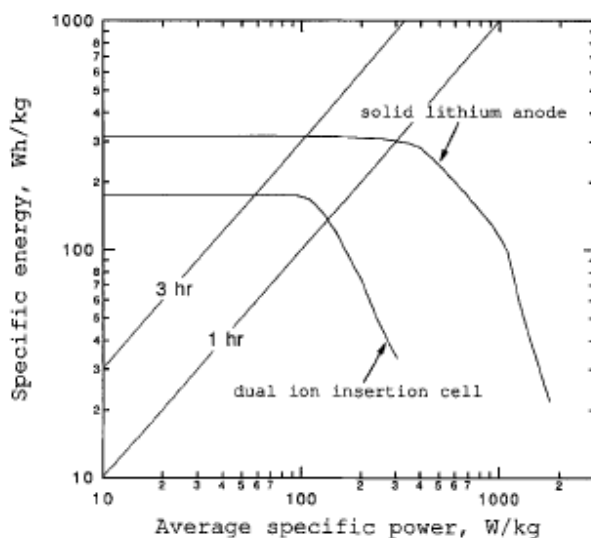


Figure 2.4. Comparison of Ragone plots for the dual ion insertion and solid lithium electrode systems. The systems are identical except for the negative electrode. The solid lithium at full charge has four times the capacity required according to the stoichiometry, [25].

The attainable power is also large, making dual insertion cells ideally suited for high rate-of-discharge applications such as acceleration of electric vehicles.

To model the electro-chemical behavior of a battery cell, essentially two different approaches have been proposed in literature:

- **Fundamental, or particle-based distributed, models:**
These models account for particle movement and chemical reactions using PDEs. They are rather accurate but on the other hand numerically intensive to solve and computationally consuming.
- **Phenomenological models:**
These models, instead of investigating the fundamental physics, provide a representation of the input/output relationship of the system, often adopting a lumped-parameters framework. This is a way of simplifying the behavior of spatially distributed systems into a topology consisting of discrete entities that approximate the behavior of the distributed system under certain assumptions. These models present less complexity and mathematically they are cast into ordinary differential equations (ODEs), simple to solve and suitable for real-time simulation. On the other hand, these models are not able to achieve comparable accuracy to fundamental models.

In this section, a review of the electro-chemical modeling techniques for Li-Ion battery cells is presented.

2.2.1 Fundamental models

The word “fundamental” refers to models that describe the behavior of a battery cell starting from its physical foundations principles.

The literature on fundamental models is quite extensive, see [26] for a review of the work proposed in the last 20 years. The first approach to model Li-Ion with two composite electrodes and a separator was developed by Fuller, Doyle and Newman at the University of California, Berkeley in the first half of the 90’s. [25], [27]. A literature review of this topic revealed that most modern models are derived from that original work which is considered a milestone for the argument.

In their original works, [25] and [27], Fuller et al. modeled the galvanostatic charge and discharge of a dual lithium ion insertion cell, shown in Figure 2.5.

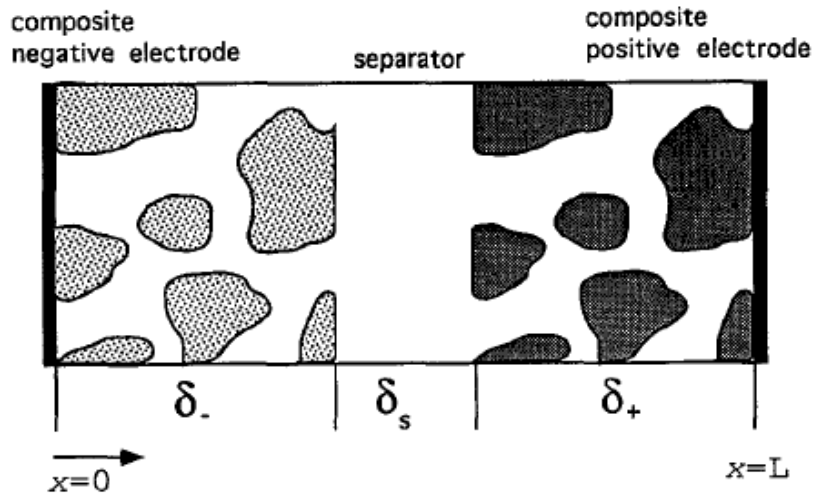


Figure 2.5. Dual-insertion cell sandwich consisting of composite negative and positive electrodes and separator, [25].

Transport in the electrolyte is described with concentrated solution theory and the insertion of lithium into and out of the active electrode material has been simulated using a superposition approach, greatly simplifying the numerical calculations. Given its importance, a specific review of this model will be presented below.

The model is general and can be used to simulate any cell utilizing two composite electrodes composed of a mixture of active insertion material, electrolyte, and inert conducting material. In particular, the diffusion in the solid material will be assessed since it is considered to be a strong limitation in some cells. The concentrated solution theory with variable physical properties allows one to deal rigorously with the transport phenomena. Following this approach, the driving force for mass transfer is the gradient in electrochemical potential given by:

$$c_i \nabla \mu_i = \sum_{j \neq i} K_{ij} (v_j - v_i) \quad (2.1)$$

where c is the concentration of species [mol/l], μ is the electrochemical potential of species [J/mol], v is the velocity of the species [m/s] and K is the frictional coefficient describing the interaction between species i and j [Js/m⁵].

The total current flux I is uniform and flows through either the insertion material phase (i_1) or the electrolyte phase (i_2). Since the current in the two phases is conserved, it can be stated that:

$$I = i_1 + i_2 \quad (2.2)$$

The current flowing in the matrix is governed by Ohm's law:

$$i_1 = -\sigma \nabla \Phi_1 \quad (2.3)$$

where σ is the conductivity of the solid matrix [S/cm²] and Φ represents the electric potential [V].

On the other hand, the variation of potential in the electrolyte can be written as:

$$i_2 = -k\nabla\Phi_2 + \frac{kRT}{F} \left(1 + \frac{\partial \ln f_A}{\partial \ln c}\right) (1 - t_+^0) \nabla \ln c \quad (2.4)$$

where k is the reaction rate constant, c is the concentration of electrolyte, [mol/dm³], f_A is the activity coefficient of salt, T is the temperature, F and R are the Faraday's and universal gas constants, respectively, and Φ_2 has been measured with a lithium reference electrode in solution.

According to the authors, a material balance on the electrolyte gives:

$$\epsilon \frac{\partial c}{\partial t} = \nabla(\epsilon D \nabla c) - \frac{i_2 \nabla t_+^0}{z_+ v_+ F} + \frac{a j_n (1 - t_+^0)}{v_+} \quad (2.5)$$

where ϵ is the volume fraction of the electrolyte, D is the diffusion coefficient [cm/s], z is the capacity ratio between positive to negative electrode and j_n is the pore-wall flux across interface [mol/m² s].

$$j_n = -D_s \frac{\partial c_s}{\partial r} \text{ at } r = R_s \quad (2.6)$$

The boundary conditions for such equations can be derived from the condition that the flux density of each ionic species must be zero at the ends of the cell. In that point it is possible to infer also that the current flows only in the solid matrix ($i_2 = 0$).

As the diffusion coefficient of the inserted lithium ions has been here assumed to be constant, this is a linear problem and it can be solved by the method of superposition. In brief, the flux at the surface of the insertion particles can be calculated from the prior surface concentrations and a series of coefficients which are calculated separately.

The open-circuit potential of insertion materials varies with the amount of lithium inserted and is expressed by a general function of concentration in the particle:

$$U = U^\theta - U_{ref}^\theta + F(c_s) \quad (2.7)$$

where U is the open circuit potential, c_s represents the concentration of lithium in the solid particle phase and the function $F(c_s)$ can vary widely depending on the insertion chemistry of the material.

When developing this model, one must consider that universally accepted values of the lithium ion transference number and salt diffusion coefficient do not exist in the literature. In their works (see [25], [27]) the

authors proposed some results that allow for a better comprehension of the problem.

According to [28], there is a strict connection between the reversible open circuit voltage of a cell and its maximum efficiency. The operating voltage of a battery cell can also be very easily related to its efficiency.

Figure 2.6 shows the cell potential as a function of utilization of positive electrode material for galvanostatic charge and discharge for the carbon/manganese dioxide cell.

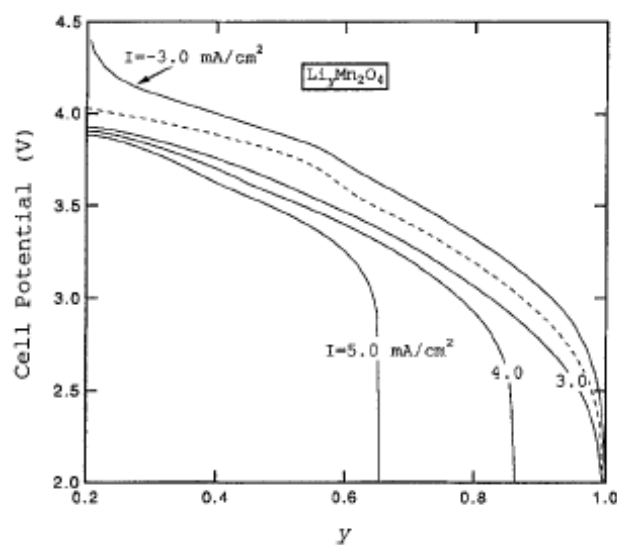


Figure 2.6. Cell potential vs. state of discharge for the manganese dioxide/carbon system analyzed in [25] at various discharge rates. The dashed line is the open-circuit potential of the cell..

The term y represents the stoichiometry of the positive electrode and it has been here used to measure the state of charge (SoC).

The voltage drops result from three major irreversibilities, [28]:

1. *Activation losses*. These are caused by the slowness of the reactions taking place on the surface of the electrodes. A proportion of the voltage generated is lost in driving the chemical reaction that transfers the electrons to or from the electrode. This voltage drop results to be highly non-linear.
2. *Ohmic losses*. This voltage drop is the straightforward resistance to the flow of electrons through the material of the electrodes and the various interconnections, as well as the resistance to the flow of ions through the electrolyte. This voltage drop is essentially proportional to current density, and so linear.

3. *Mass transport or concentration losses.* These result from the change in concentration of the reactants at the surface of the electrodes. Because the reduction in concentration is the result of a failure to transport sufficient reactant to the electrode surface, this type of loss is also often called mass transport loss.

For Li-Ion batteries, the abrupt drop in cell potential at the higher discharge rates is caused by concentration polarization. At high current densities, the cell potential is lower irrespective of concentration polarization and, thus, it is apparent that the material utilization is limited at higher discharge rates.

An important factor in optimizing the performance of the cell is full utilization of the active material. For a specified battery performance the cell potential should fall below its cutoff value only after nearly all the active material is consumed.

This result requires an understanding of the transport limitations in each phase of the composite electrodes, as these lead to non-uniform reaction distributions. The importance of diffusion in the solid electrode material can be assessed using the dimensionless parameter S_s :

$$S_s = \frac{R_s^2 I}{D_s n F (1 - \epsilon - \epsilon_{f,+}) (c_t - c_s^0) \delta_+} \quad (2.8)$$

which is the ratio of the diffusion time in either electrode to the discharge time for the positive electrode. For $S_s \ll 1$, diffusion in the solid phase can be neglected. According to the authors, it is possible to use S_s to predict the radius of the particles for which severe diffusion limitations exist in the solid phase for this system.

An analogous parameter relates the time constant for transport of the electrolyte to the time of the discharge:

$$S_e = \frac{L^2 I}{D n F (1 - \epsilon - \epsilon_{f,+}) (c_t - c_s^0) \delta_+} \quad (2.9)$$

The time for transport in the electrolyte may be small in comparison to the discharge time which results in a quasi-steady-state concentration profile. Transport limitations in the electrolyte phase are the main factor limiting the performance of this cell at high discharge rates.

The mechanism of failure is the depletion of the electrolyte in the solution phase, which leads to a large concentration over-potential. This result is less of a problem with larger values of the salt diffusion coefficient, the initial salt concentration, or the lithium ion transference number.

At higher discharge rates, the concentration in the solution phase can be driven to zero well before 100% utilization has been attained, leading therefore to

incomplete utilization of the active material. As this is the major cause of the end of discharge, it suggests that increasing the electrolyte concentration would improve the performance of the system at high rates of discharge.

The advantages in terms of the increased concentration in the depth of the porous electrode generally outweigh the increase in ohmic drop.

The maximum concentration attained by the system can be checked using the current model to ensure that a solubility limit is not surpassed. It should be mentioned that this model does not account for salt precipitation, but this is an undesirable situation that should be avoided in practice.

An analysis of the current distribution in these systems shows the importance of the rate of change of the open-circuit potential of the insertion material with the state of charge.

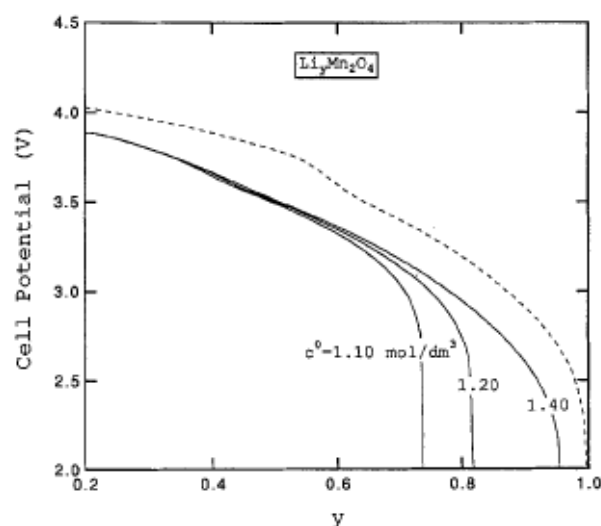


Figure 2.7. Cell potential vs. state of discharge for the manganese dioxide/carbon system with the initial electrolyte concentration as a parameter. The dashed line is the open-circuit potential of the cell. The discharge rate is $I = 5.0 \text{ mA/cm}^2$ [25].

The great emphasis given to the model presented in [25] and [27] is due to the fact that this work is very useful to understand the main limitations that have to be faced to improve the performance of Li-Ion batteries.

The work of Fuller, Doyle and Newman was extended by Ramadass et al. [29] to account for the decay in capacity of the cell with cycle number. Further extensions to this model were made by Sikha et al. [30] to include the change in the porosity of the electrode material as a function of time.

In all these models, the concentration of lithium within the solid phase was either calculated using the superposition principle [11] or solved for rigorously, using a pseudo second dimension along the radius of the particle. Since the concentration of lithium at the particle surface is the only variable of interest, this methodology is cumbersome and time consuming.

A very good approximation of the concentration profile within the solid phase was presented independently by Wang et al. [31] and Subramanian et al. [32] based on the integral approach outlined by Ozisik [11]. In this second approach, the concentration profile within the solid particle is approximated by a second degree polynomial whose coefficients are expressed in terms of the average concentration of lithium inside the particle and the concentration at the surface. Thus, the need to solve for the concentration profile within the solid phase is eliminated.

Fundamental models allow understanding completely the physics beyond a Li-Ion battery cell and they can be used to compare or calibrate other models that neglect the physical diffusion problems.

2.2.2 Phenomenological models

The word “phenomenological” refers to models that provide a representation of the input/output relationship of a system without investigating the fundamental physics. These models are in contrast with the fundamental models analyzed before, which describe the behavior of a battery cell starting from its physical foundations principles.

Among phenomenological models, control oriented models (COM) are low-order dynamic models (linear or quasi-linear) that are used to design control algorithms.

Examples of phenomenological models are the equivalent circuit models. Quoting [16], the equivalent circuit model has a simple structure but can capture sufficient dynamics under both temperature and SoC variation, thus making it applicable for use with real-time model-based estimation algorithms in automotive applications.

Equivalent circuits are often used to model the electrical part of batteries. They consist of a series of Randle⁶ circuits, as shown in Figure 2.8. By piecing together multiple RC circuits, one is essentially providing a piecewise constant approximation of the frequency response amplitude.

⁶ In electrochemical studies Randle circuits are often used. They consist of an active electrolyte resistance R in series with the parallel combination of the double-layer capacitance and an impedance of a Faradaic reaction.

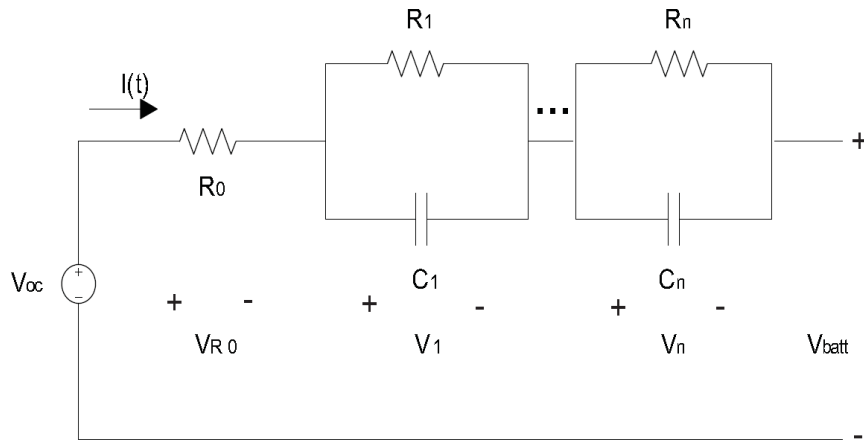


Figure 2.8. Sketch of an n^{th} order equivalent circuit to model the electrical dynamic of a battery, [16].

In [33] a first-order equivalent circuit model with parameters scheduled on SoC and temperature is presented. The first order model captures the dominant transient processes that are neglected by a zero-order model, while avoiding the computational and calibration complexity of higher-order circuits. Figure 2.9 depicts the electrical equivalent circuit. The simple first-order model is able to adequately compute the voltage-current relationship of the battery over a wide range of operating conditions due to the SoC and temperature scheduling of the open circuit voltage E_0 , internal resistances R and R_0 , and capacitance C_0

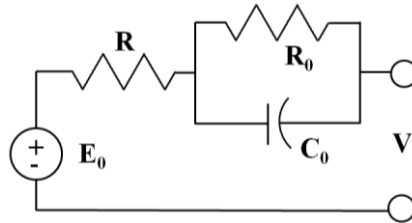


Figure 2.9. First-order equivalent circuit model of battery electrical dynamics, from [33].

The electrical model equations, obtained using Kirchoff's current law, are reported in equations (2.10) and (2.11).

$$\dot{V}_c = -\frac{1}{R_0 C_0} V_c + \frac{1}{C_0} I \quad (2.10)$$

$$V = E_0 - IR - V_c \quad (2.11)$$

The input to the electrical modeling circuit is the current, I , and the output is the battery terminal voltage V . Note that, in this model, the total pack voltage is obtained by scaling a single cell voltage by the number of cells.

The SoC dynamics are determined through Equation (2.12).

$$\frac{dSoC}{dt} = -\frac{I(t)}{C_n} \quad (2.12)$$

where I is assumed to be positive during the discharge and C_n is the nominal capacity⁷ of the pack.

Realistically, the internal resistance, open circuit voltage, and capacity of batteries are influenced by a number of factors, including SoC, temperature, and current direction. The parameters of the equivalent circuit model describing the electrical dynamics must approximate this dependency. This has been accomplished successfully throughout the open literature. For example, Figure 2.10, from [16] shows the temperature-SoC-resistance relationship for cells similar to those modeled in this work.

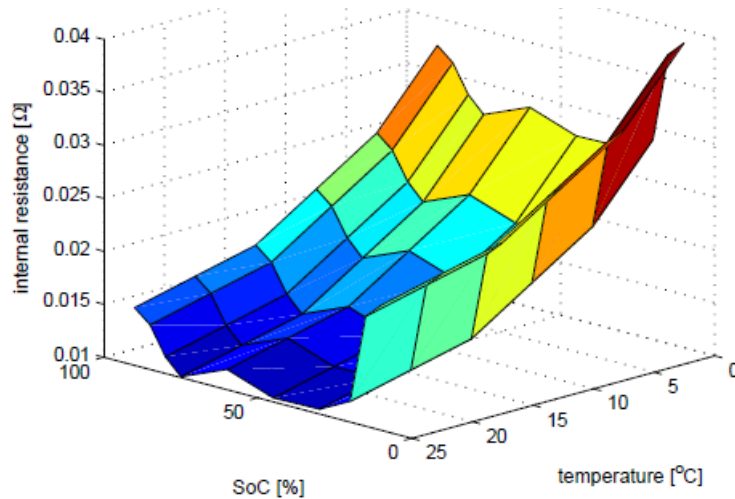


Figure 2.10. Internal resistance as function of temperature and SoC, [16].

If a battery is excited and then allowed to relax for long periods of time, the rested terminal voltage at the same SoC varies depending on the type, duration, and strength of the previous excitation. This phenomenon is typically characterized by a very slow dynamics, which is not captured by the Randle circuits. Because a simple equivalent circuit cannot capture such effects directly, a hysteresis voltage element is appended (V_h).

In [16], a second order equivalent circuit is used and an additional hysteresis term is considered. The dynamic equation that describes the voltage across the i^{th} RC circuit is given by:

⁷ The nominal capacity of a battery is defined as the amount of Ah that can be drawn from the battery at 1C-rate discharge at room temperature.

$$\frac{dV_i}{dt} = \frac{1}{R_i C_i} V_i + \frac{1}{C} I \quad (2.13)$$

where $i=1,2$.

The total voltage can then be expressed as the sum of all the voltage components:

$$V_{batt} = V_{OC} - R_O I - \sum_{i=1}^2 V_i + V_h \quad (2.14)$$

The model structure presented in [16], and extended to battery packs in [34], is intuitive and the identification procedure provided is systematic; providing thus a method for generating accurate yet simple equivalent circuit models for batteries under conditions of varying temperatures.

The dynamic pack behavior can be approximated by a scaled-up model of a single cell, hence implying that all cells are the same. This approximation is well depicted in [34] even though its assumption fails on multiple grounds due to small manufacturing differences, unavoidable thermal gradients and different degradation due to aging in each cell.

In [34] a lumped parameter, distributed battery pack dynamic model was introduced. It allows for the simulation of the electrical dynamics of all the cells in an arbitrarily configured series-parallel pack similar to those used in automotive applications.

A low-order equivalent circuit has been chosen to model the electrical part of the battery, as:

$$V_C(t) = e^{-\beta T} V_C(t_0) + \frac{\gamma i(t)}{\beta} (1 - e^{-\beta T}) \quad (2.15)$$

$$\text{where } \beta = \frac{1}{RC} \text{ and } \gamma = \frac{1}{C}$$

To simulate the pack model, two assumptions are necessary: the current input is constant over the simulation time interval and the SoC does not change during the simulation time itself.

In order to obtain meaningful data from simulation of the battery pack, it is necessary to enforce variability between cells. This variability may be caused by manufacturing differences, aging, or other conditions.

A simulation tool has been developed to perform Monte Carlo simulations on typical automotive current profiles.

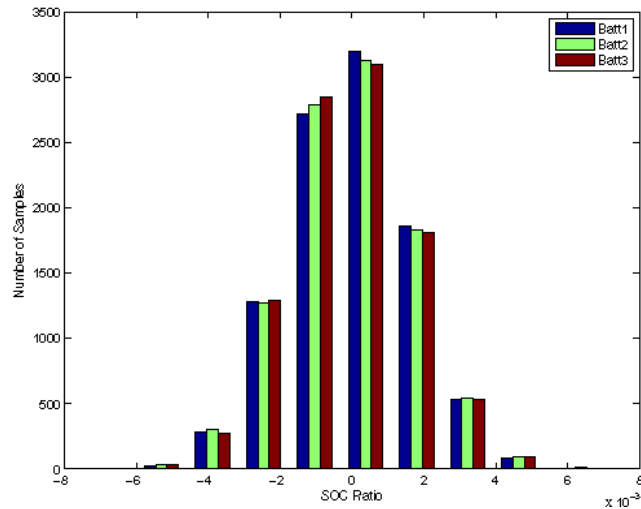


Figure 2.11. Average SoC ratio divergence. [34].

Figure 2.11 shows the distribution of the different SoC ratios of each of the different batteries in the battery pack over 100 simulations where each R_0 parameter of each cell is perturbed per simulation run. As expected, the distribution appears to be normal and the SoC ratio scale is small, since the value represents the amount of SoC deviation per second.

Equivalent circuit models are inherently simple and fit for real time implementation. On the other hand they are phenomenological models and thus require some simplifications. This leads to an accuracy which is lower than fundamental models.

In automotive applications, control-oriented models are used by the management system to optimize the performance of the vehicle and of its components. Control-oriented models of batteries are composed, as shown in Figure 2.12, by two sub-systems:

- The electrical model
- The thermal model

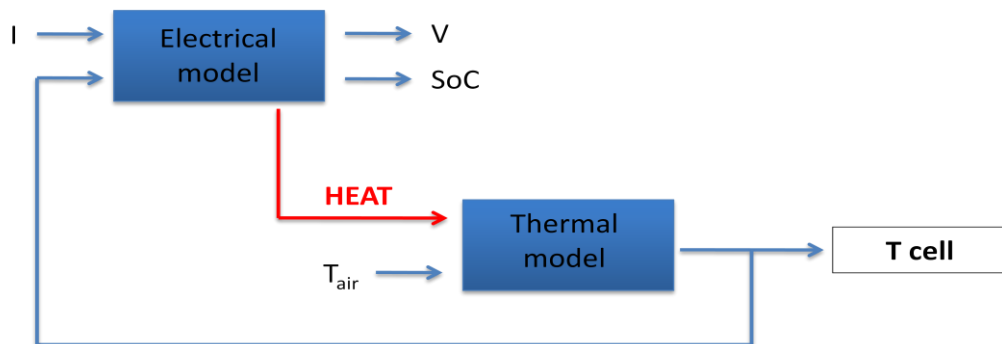


Figure 2.12. Example of control-oriented model for batteries.

The electrical part of the battery is normally modeled through an equivalent circuit with parameters (as the internal resistance and the open circuit voltage) scheduled with respect to SoC and temperature.

The SoC is computed with a current based estimation, according to:

$$\text{SoC}(t) = \text{SoC}_0 - \int_{t=0}^t \frac{\eta I(t)}{C_n} dt \quad (2.16)$$

where C_n is the nominal capacity of the cell, SoC_0 is the initial state of charge and η is the Coulombic efficiency of the cell, here supposed to be equal to 1 (according to [35]).

The performance of batteries strictly depends on the internal temperature field [12], thus the electrical model is coupled with a lumped⁸ thermal model. In this model the battery is assumed to be a lumped body (see Section 3.1.3 for a review of the topic) cooled by convection with a known heat transfer coefficient h . The model predicts the uniform temperature of the battery starting from the ambient temperature T_∞ and solving the general heat balance.

$$\frac{dT}{dt} = \frac{\dot{Q} - Ah(T - T_\infty)}{m c} \quad (2.17)$$

where $\dot{Q} = RI^2 + \sum_{n=1}^N R_i I_i^2$ is the heat generated inside the battery, in [W]. The battery dynamic is modeled through an equivalent circuit of order N and the subscript i , referred to the current and the resistance, indicates that those quantities are referred to the i^{th} Randle circuit. m is the mass, and c is the specific thermal capacity of the entire system [J/kg K].

Once the temperature and SoC have been calculated, the model computes the open circuit voltage, the internal resistance and the capacity and resistance of the Randle circuits. These parameters are normally scheduled as function of temperature and SoC using different algebraic functions for charge and discharge processes.

The model is simple and suitable for control-oriented and on-board implementation. From an electric point of view the accuracy is sufficiently high, as reported in [21]. From a thermal point of view, however, the model is fairly inaccurate since the temperature distribution within the battery cell has been completely disregarded.

Since the performance, SoH, and optimization of battery module and cells are mainly affected by the operating temperature it is a crucial point to improve this aspect of these simplified models.

⁸ In a lumped system the temperature distribution is spatially uniform at any instant during the transient heat transfer process, [44].

Very accurate models of both electro-chemistry and heat diffusion inside a battery are performed with finite element software, like ANSYS[®] or COMSOL[®]. However, these software applications are so memory and time consuming that there is no possibility for any on-board or real-time application. In this thesis a modeling approach to account for the temperature dynamic inside a Li-Ion battery cell, suitable with a control-oriented approach, will be developed.

2.2 Thermal characterization

The topic of thermal characterization and modeling of Li-Ion batteries is a fairly new research area which has attracted the attention of both industry and academia in the last decade. In 1995 John Newman and Caroline Pals published two fundamental journal papers on the topic: the first is related to the thermal modeling of a single Li-Ion battery cell, [8], and the second represents an extension to a cell stack, [9]. Later on a refining of the single cell modeling has been proposed by the same authors in [36].

In their work, [37], Bernardi et al. presented a general energy balance for battery systems on which most subsequent model relies. A few years later, Pesaran et al. presented a work on the thermal performance of EVs and HEVs battery cells and packs [24], developed at NREL⁹. The same authors proposed some extension to that original work from the battery management system point of view [7], [38],[12].

In 2004 Chen et al. proposed a remarkable work on the optimal approach to simplify the thermal model of a Li-Ion battery [10].

As regard the thermal behavior of battery packs, important results were obtained by Lee et al. [39] and Innui et al [40]. The latter, in 2006, proposed an interesting comparison between prismatic and cylindrical battery cells.

From the thermal management point of view, a complete work was proposed in 2009 by Kuper et al. [41].

The papers reviewed are organized into three categories:

- Single cell thermal model;
- Whole pack thermal models;
- Battery thermal management systems.

⁹ National Renewable Energy Laboratory, Golden (CO), U.S.A.

2.3.1 Single cell thermal models

In their first work [8], Newman and Pals presented an extension of the work proposed in 1993 by Fuller and Doyle, [27], to introduce an energy balance for a battery cell. In the previous models, a uniform temperature was assumed throughout the cell, although the temperature was allowed to vary with time. In this work a 1D thermal model has been introduced.

Thermal modeling is particularly important for Li-Ion batteries because the heat produced during charge and discharge may cause either irreversible side reactions or damage and even melting of the solid lithium. This is a primary safety concern for the battery manufacturer.

The energy balance used in [8], and first introduced by [37], is given by:

$$\dot{Q} = I \left(V_{oc} - V - T \frac{\partial V_{oc}}{\partial T} \right) = h_{conv} (T - T_{\infty}) + m_c c_p \frac{dT}{dt} \quad (2.18)$$

where m_c is the cell mass per unit area [g/cm^2]. The term $I(V_{oc} - V)$ is the heat produced due to cell polarization, and the term $-IT(\partial V_{oc}/\partial T)$ is due to the reversible entropy change in the cell.

Isothermal modeling is important because it helps one understanding the operation of the battery at different temperatures.

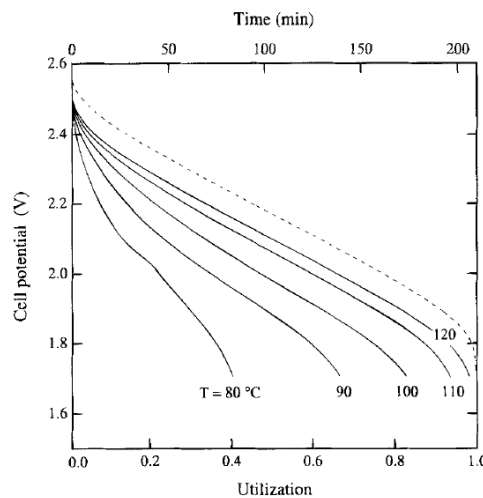


Figure 2.13. Cell potential as a function of utilization and time for isothermal discharge of the cell at $I = 1.1 \text{ mA}/\text{cm}^2$ for several temperatures, from [8].

In the isothermal calculations it is assumed that all the heat generated in the cell is transferred out of the system without considering the details of how it is done. Figure 2.13 shows the cell potential as a function of utilization and time for isothermal discharge. The dashed line is the open-circuit potential of the cell. The figure shows also how the cell performance is affected by the temperature of operation. At higher temperatures, the cell potential is higher for a given

value of active material utilization. The cell also utilizes more of the active material at higher temperatures.

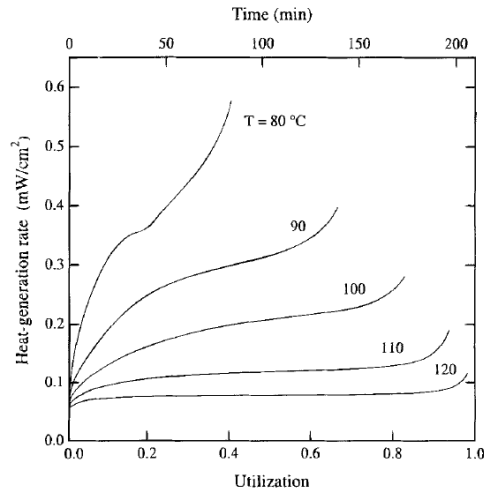


Figure 2.14. Heat-generation rate as a function of utilization and time for isothermal discharge of the cell at $I = 1.1 \text{ mA/cm}^2$. [8].

The heat-generation rate as a function of time and utilization is given in Figure 2.14 for the same simulations. This figure demonstrates that the heat generation rate is much larger for lower temperatures than it is for higher temperatures.

This result may also be seen by examining the cell-potential behavior: The heat generation rate is equal to the product of the current density and the difference between the open-circuit potential and the cell potential. At lower temperatures, the conductivity is lower, and the larger Ohmic drop leads to larger heat generation rates.

For design purposes, it is useful to examine the temperature dependence of the energy and average power densities that the system can provide.

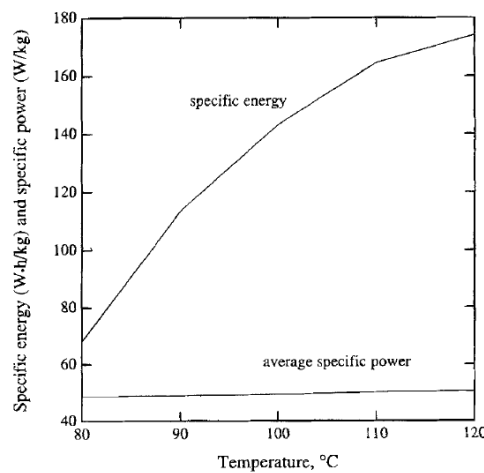


Figure 2.15. Specific energy and average specific power of the cell as functions of temperature for isothermal, galvanostatic discharge at $I = 1.1 \text{ mA/cm}^2$, [8].

At lower temperatures, from 80° to 100 °C, the specific energy increases steadily as the cell attains a higher utilization with increasing temperature.

Then, at temperatures from 100 °C to 120°C, the energy density continues to rise, but at a slower pace, as the cell is reaching nearly 100% utilization. Above 120°C the specific energy begins to level off to its theoretical value.

In this paper, adiabatic discharge behaviors are also presented: adiabatic modeling is important because it simulates the consequences of no heat removal, for example, if the temperature control system fails.

In [8] it is also anticipated that the one-cell model can be used to analyze the behavior of a cell stack under heat-transfer conditions by defining an appropriate per-cell heat-transfer coefficient for each cell in the cell stack.

The authors consider 1D heat transport in the direction perpendicular to cell layers. This assumption is valid when transport in the direction parallel to cell layers can be neglected, such as when the cell stacks are very thin, or when the ends of the stack perpendicular to cell layers are insulated.

To use the one-cell model for cell-stack calculations, the per-cell heat transfer coefficient h_s must be related to the convective heat transfer coefficient.

$$\frac{1}{h_s} = \frac{1}{2k_{cell} l_{cell}} \left[\left(\frac{L}{2} \right)^2 - x^2 \right] + \frac{L}{2h_{conv} l_{cell}} \quad (2.19)$$

Now that the per-cell heat transfer coefficient has been related to the convective heat-transfer coefficient, the temperature and discharge behavior for each cell in the cell stack can be calculated from known values of the convective heat-transfer coefficient and from cell properties.

The one-cell model proposed by Newman and Pals could be used to estimate the temperature and discharge behavior of the battery when the cell-stack temperature gradient can be neglected.

The results presented show that an increasing of the per-cell heat transfer coefficient causes the cell potential and temperature to decrease. This behavior is expected because as the heat transfer coefficient increases, more heat is transferred out of the cell stack to the surroundings causing the cell temperature to decrease. This lower temperature causes the cell potential to decrease, as was seen in isothermal discharges.

The per-cell heat generation rate increases as the temperature of the cell decreases, due to the increase in over potentials in the cell.

Concluding, the simulations showed that the cell potential, along with the active-material utilization at the cutoff potential, increases with increasing temperature. Following the cell-potential behavior, it was seen that the heat-generation rate of the cell decreases with increasing temperature.

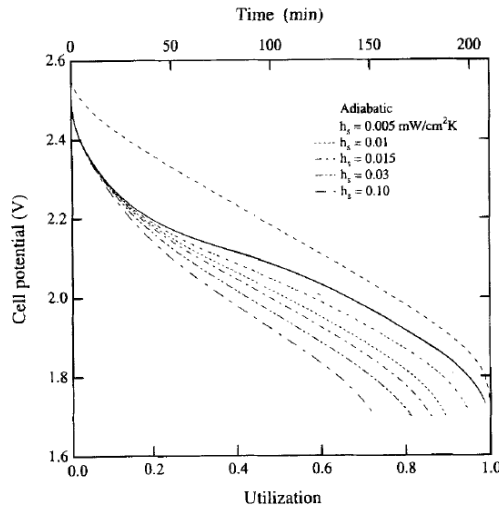


Figure 2.16. Cell potential as a function of time and utilization for galvanostatic discharges at $I = 1.1 \text{ mA/cm}^2$, from [8].

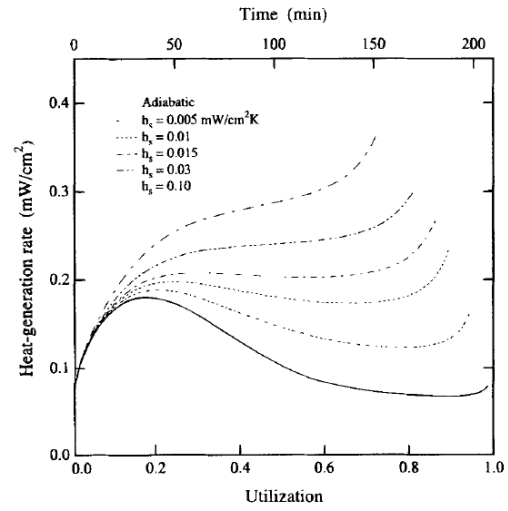


Figure 2.17. Heat-generation rate as a function of utilization and time for galvanostatic discharges at $I = 1.1 \text{ mA/cm}^2$, from [8].

In the paper the per-cell heat-transfer coefficient was defined for each cell in the cell stack. Simulations were presented for discharge behavior for various values of the per-cell heat transfer coefficient. The simulations presented for the per-cell heat transfer coefficient can also be used if the temperature gradient in the cell stack is negligible according to the accuracy requirements of the calculations.

Later on, in [36], Newman et al. presented a general review of the several key aspects that must be considered in modeling the behavior of Li-ion batteries. The electrodes are generally porous, and therefore the distribution of the reaction through the depth of the electrode must be considered. The active material is an insertion compound, in which the chemical potential and other thermodynamic properties may vary continuously with inserted lithium concentration, and solid-state diffusion of lithium through the active material must be considered.

Finally, in most batteries, the electrolyte is a concentrated, non-ideal solution, and mass transport across the electrolyte has a significant effect on battery performance. The basic modeling framework consists of porous electrode theory, concentrated solution theory, Ohm's law, kinetic relationships, and charge and material balances.

Porous electrode theory treats the porous electrode as a superposition of active material, electrolyte, and filler, with each phase having its own volume fraction. Concentrated solution theory provides the relationship between driving forces and mass flux.

A charge balance is also needed to keep track of how much current has passed from the electrode into the electrolyte. Ohm's law describes the potential drop across the electrode and also in the electrolyte.

Finally, the Butler–Volmer equation generally is used to relate the rate of electrochemical reaction to the difference in potential between the electrode and solution.

A big deal in modeling batteries is that the dependent variables of concentration, potential, reaction rate and current density each appear in more than one governing equation, and therefore the coupled governing equations must be solved simultaneously.

In addition, material properties often vary considerably with concentration. Thus, battery simulation requires a numerical technique, such as the finite-difference technique BAND suggested by the authors, that can solve multiple coupled, nonlinear differential equations.

The flux of one species is inherently coupled to the fluxes of all other species present, as set forth in the Stefan–Maxwell equations:

$$c_i \nabla \mu_i - \sum_j \frac{c_i c_j}{c_T D_{ij}} (v_j - v_i) \quad (2.20)$$

where c_i is concentrations, D_{ij} the diffusion coefficients, v the velocity, i and j the species indices, and C_T is the total molar concentration. With the Onsager reciprocal relations, these principles yield $n(n-1)/2$ transport properties, where n is the number of species in solution.

In the second part of the paper, the authors present three analyses of mass-transport-related effects in Li-ion batteries.

The first section demonstrates how a continuous side reaction could cause error in measurements of the transference number. The second section discusses the heat effect associated with the formation and relaxation of concentration gradients. The third section presents the results of molecular dynamics simulations which give insight into the decrease in conductivity with increasing salt concentration in liquid carbonate electrolytes.

Measurement of the transference number in polymer electrolytes is difficult because the polymer electrolytes are opaque and poorly conductive. The galvanostatic polarization technique has been previously developed by the authors to provide a simple yet rigorous method of obtaining transference numbers in non-ideal polymeric electrolytes.

The concentration gradients formed during the passage of current are also associated with heat effects. The heat is released (or possibly even absorbed) during relaxation after the current is turned off. An equal and opposite amount of heat is absorbed (or possibly released) during formation of the concentration gradients while current is flowing.

This heat of relaxation is termed heat of mixing; an energy balance which includes the heat effects of heat of mixing looks like:

$$\dot{Q} = I \left(V - U^{avg} + T \frac{\partial U^{avg}}{\partial T} \right) + c_p \frac{dT}{dt} + \int \sum_i (\bar{H}_i - \bar{H}_i^{avg}) \frac{\partial c_i}{\partial t} dv \quad (2.21)$$

where \dot{Q} is the rate of heat exchange with the surroundings [W], I the current (assumed positive on discharge), V the cell potential, U the open-circuit potential, the superscript ‘avg’ means evaluated at the volume-average concentration (e.g. U^{avg} is the potential to which the cell would relax if the current were interrupted), T the temperature, C_p the heat capacity, \bar{H}_i the partial molar enthalpy of species i , and c is concentration

It is important to notice that if the partial molar enthalpies are constant with composition, then the heat of mixing term is zero. In addition, heat of mixing can be endothermic or exothermic, depending on how \bar{H}_i varies with composition.

This work states that the heat released during relaxation is much smaller than the resistive and entropic heat. For cells properly designed to mitigate concentration over-potential, heat of mixing will be negligible.

2.3.2 Battery pack thermal models

The thermal characterization of a whole battery pack is even more important because, when small batteries are scaled up, the internal heat generation becomes large, leading to the temperature rise and the occurrence of an uneven temperature distribution in the battery.

According to [24], battery pack performance in an automotive application directly affects the all-electric (zero-emission) range, power for acceleration, fuel economy, and charge acceptance during energy recovery from regenerative braking. Thus any parameter that affects the battery pack must be optimized.

The battery operating temperature range changes depending on the electrochemical couple used. Generally, higher temperatures improve the battery's performance because of increased electrochemical reaction rates. However, the battery's lifetime decreases because elevated temperatures increase corrosion promoting the aging of the battery.

Predicting temperature profiles is important to design a thermal management system for the battery, as well as predict how the temperature variation in the battery affects its performance.

In [24], an overview of heat generation in battery modules is presented. As stated before, heat is generated within a cell by two effects: entropy change from electrochemical reactions and Joule's effect caused by current flux.

At practical EV and HEV rates, the first term (reversible entropy change) is usually small compared to the second one (Ohmic and other irreversible effects). Thus, the heat is generated and released from the cell during both charge and discharge.

As heat is generated in a module, it is either removed/rejected to the surrounding area, accumulated in the module, or both. It is also possible that if the surrounding area is at a higher temperature than the module, heat will be transferred into it. An overall energy balance on a battery module leads to:

$$\dot{Q} - h_b A_{bs} (T_{bs} - T_f) - \sigma \varepsilon F_{bs} A_{bs} (T_{bs}^4 - T_f^4) = m_b c_b \left(\frac{dT_{batt}}{dt} \right) \quad (2.22)$$

where:

h_b = Convective heat transfer coefficient between battery surface and its surrounding fluid [W/m^2K];

A_{bs} = Battery surface area exposed to the surrounding;

T_{bs} = Temperature of the battery surface;

σ = Stefan-Boltzman constant ($5.67 \cdot 10^{-8}$ [W/m^2K^4]);

ε = Battery surface emissivity;

F_{bs} = Shape factor between the battery and its surroundings ;

c_b = Weighted-average module heat capacity [J/kgK].

The radiative term (the third one) is usually small compared to the convective term (second one) if temperatures are below 100 °C, so it is disregarded for common battery applications.

In Equation (2.22), an average battery temperature has been considered. However, in reality, a three-dimensional temperature distribution exists in the module. A commercial finite element analysis software has been used by the authors to solve for temperature distribution in HEV modules.

The overall energy balance can be used to obtain the temperature distribution in a pack of modules. For example, if a certain amount of a fluid is passed around a module, the fluid temperature change can be obtained from overall energy balance for the module:

$$h_b A_{bs} (T_{bs} - T_f) = \dot{m}_f c_f (T_{out} - T_{in})_{fluid} \quad (2.23)$$

The overall temperature change in the fluid can be obtained from the overall energy balance:

$$N \left(\dot{Q} - m_b c_b \frac{dT_{batt}}{dt} \right) = \left[\dot{m}_f c_f (T_{out} - T_{in}) - \dot{m}_f c_f \left(\frac{dT_f}{dt} \right) \right]_{pack} \quad (2.24)$$

where N is the number of modules in the path of \dot{m}_f .

The second terms on each side of the equation are thermal inertia of the module and the fluid, respectively, and could be ignored for short-term transient and steady state cases.

To obtain thermal performance in modules and packs, the author proposes to use finite element analysis, to solve the two-dimensional or three-dimensional

transient or steady state heat conduction equation for a set of modules at the beginning of the pack.

If the interest is limited to the average battery temperature, conduction can be ignored, assuming a single temperature for the modules. It is possible taking advantage of symmetry to solve for the minimum number of modules or even sections of a module to reduce computational efforts.

Using an iterative process, the energy balance between the module surface temperature and its surroundings has been used to find the overall temperature change in the fluid. Temperature distribution in any module in the pack could be obtained by using the superposition principle and overall energy balance.

For the analysis, the authors used a prismatic, valve-regulated, lead-acid battery module.

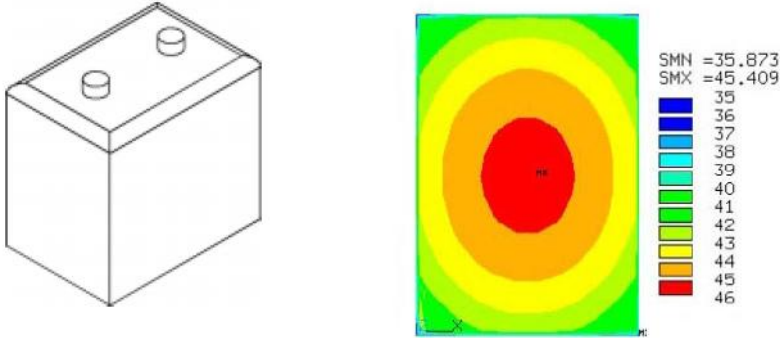


Figure 2.18. Sketch of the battery module analyzed in [24] and 2D temperature distribution.

In this analysis, an air flow cools a series of 10 battery modules, as depicted in Figure 2.19. The air temperature rises by 1.3 °C as it passes by each module, resulting in a variation of 13 °C between the inlet and the outlet.

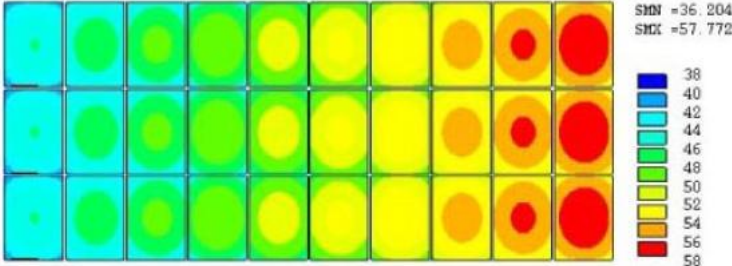


Figure 2.19. Steady-state 2-D temperature distribution in battery pack cooled by an air flow, [24].

There is also a variation of about 4.5 °C within each battery module. Although this cooling arrangement is not ideal, it is much better than placing the pack in a closed box, as shown in Figure 2.20.

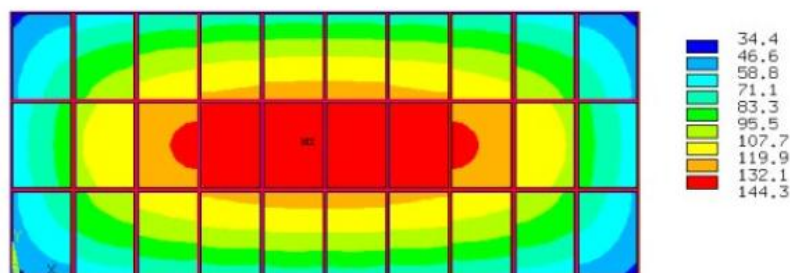


Figure 2.20. Steady-state 2-D temperature distribution in an enclosed battery pack, [24]

Obtaining thermal images of a battery module or a pack is a useful way to obtain information on temperature variation and compare that with analytical results. It is more productive and less intrusive than installing many temperature sensors on the walls of the battery.

At the NREL both IR photography and liquid crystal thermography are used. The battery pack performance, and thus the performance of an EV or HEV, is affected by its operating temperature and the degree of temperature gradient in the pack. Thermal issues are of more concern in an HEV pack because of higher power and more aggressive charge/discharge profile.

Using finite element analysis software, temperature distributions in a hypothetical module and pack is obtained. Even with reasonable air flow rates, the temperature in the pack can vary significantly; a pack with no air flow can reach unacceptably high temperature levels.

NREL analysis indicated that adding ventilation holes improved the thermal performance of an HEV battery module. IR and LC thermography were used to obtain thermal images of an HEV module and a simulated HEV pack.

Newman et al., in the second part of their work, [9], proposed a model that uses heat generation rates calculated from isothermal discharges of the one-cell model presented in Part I to calculate temperature profiles in cell stacks.

This allow taking into account that cells on the outside of the stack operate at a lower temperature than cells on the inside of the stack, due to conductive heat-transfer limitations of the system.

In this model, again, the heat is assumed to be transferred only in the direction perpendicular to cell layers. Due to geometric consideration the temperature behavior of the full cell stacks is assumed to be symmetric.

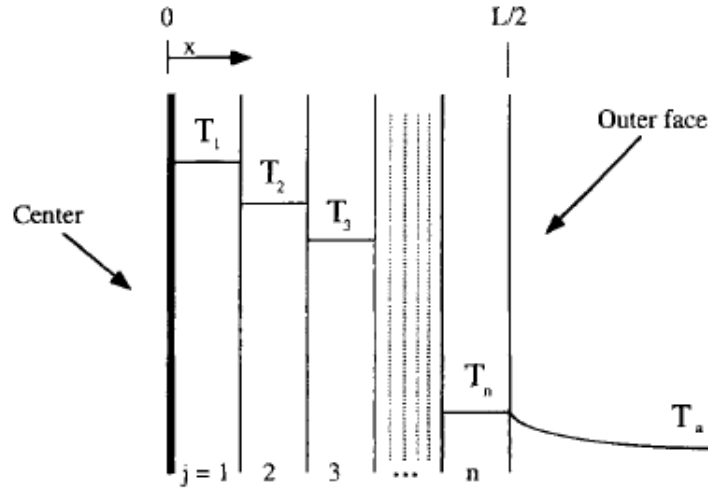


Figure 2.21. Schematic diagram of one-half of a cell stack studied in [9].

The energy generation in cell j , \dot{Q}_j , may be calculated from the one-cell model given previously, but this requires running the previous one-cell program for each cell, which means a large amount of computer time required. To reduce the computer time needed to solve the temperature profiles, the authors introduced a simplified heat generation rate calculation:

- For cell 1:

$$\frac{mc_p}{\Delta t}(T_1^{new} - T_1^{old}) = \frac{k}{l}(T_1^{new} - T_2^{new}) + \dot{Q}_1 \quad (2.25)$$

- For cells 2 to n-1:

$$\frac{mc_p}{\Delta t}(T_j^{new} - T_j^{old}) = \frac{k}{l}(T_{j+1}^{new} - 2T_j^{new} + T_{j-1}^{new}) + \dot{Q}_j \quad (2.26)$$

- For cell n (the last one):

$$\frac{mc_p}{\Delta t}(T_n^{new} - T_n^{old}) = \frac{k}{l}(T_{n-1}^{new} - T_n^{new}) + \dot{Q}_n - h(T_n - T_\infty) \quad (2.27)$$

To simplify the calculations, the heat-generation rate as a function of time and temperature for isothermal discharge as calculated by the previous one-cell model are considered to give an accurate approximation to the heat-generation rate as a function of time and position for non-isothermal discharge (\dot{Q}_j).

This means that a cell that discharges non-isothermally to a particular temperature and state of charge presents the same heat generation rate (as well as other discharge characteristics) as a cell discharged isothermally at that temperature to the same state of charge.

Various experiments showed that the estimated heat generation rates and corresponding temperatures are most accurate for higher heat transfer coefficients where the cell temperature remains nearly constant.

In this work, the temperature behavior of the battery is considered as a function of the stack thickness, heat transfer coefficient, and discharge rate. All simulations were made for a nominal 3 h discharge rate, 1.1 mA/cm^2 , using 90°C for the initial cell temperature and 89°C for the ambient air temperature.

The figure below shows that as the cell stack thickness increases, its overall temperature increases, and the cell temperature profile gets steeper. The temperature profiles are considered at the end of discharge.

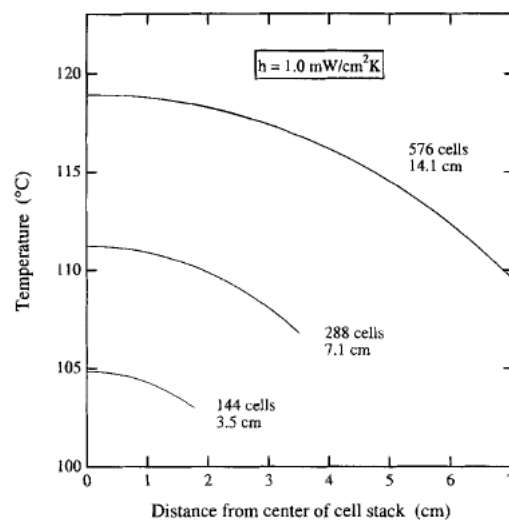


Figure 2.22. Temperature profiles at the end of discharge for cell stacks of several widths for galvanostatic discharge at 1.1 mA/cm^2 , [9].

For early times, the temperature has not risen much, and there is little temperature variation in the cell stack. As the discharge proceeds, however, the temperature variation increases.

For the 576 cells stack, at the end of discharge, the temperature at the center reaches 117°C while the temperature at the outer face reaches only 104°C .

As it can be noticed in Figure 2.23, the heat-generation-rate profile is relatively flat at the beginning of discharge. As the discharge proceeds, the heat-generation rate decreases through most of the cell stack, but a gradient develops. At the end of discharge, the cells at the outer face of the stack are generating heat at over twice the rate of the cells at the center of the stack.

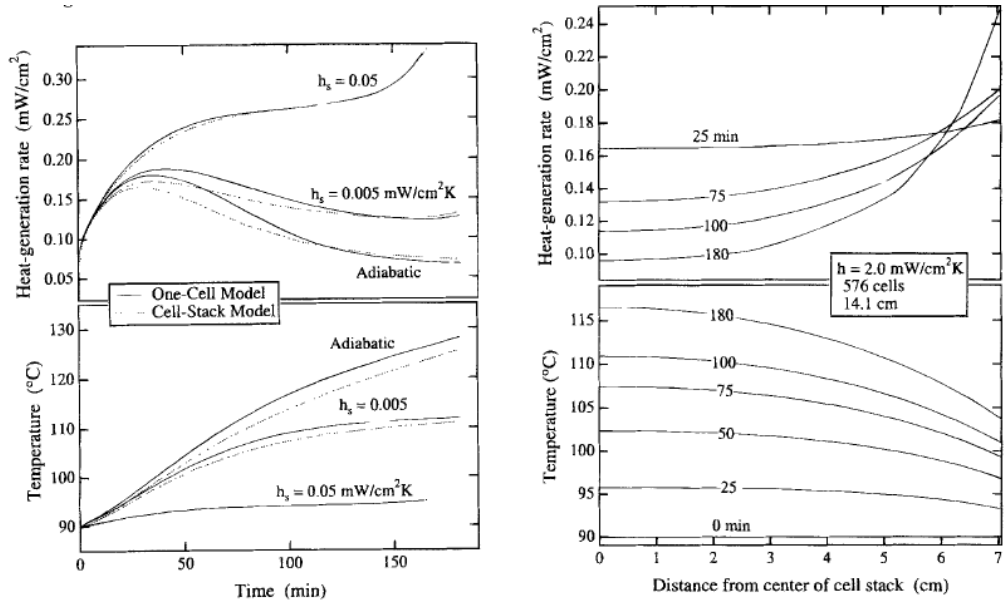


Figure 2.23. Temperature and heat-generation rate, of a single cell and for a 576 cells stack, as functions of time for various heat-transfer conditions, [9].

For automotive purpose a 144 cells stack has been chosen. There is a cooling channel every two cells stacks and the battery pack consists of 16 stacks.

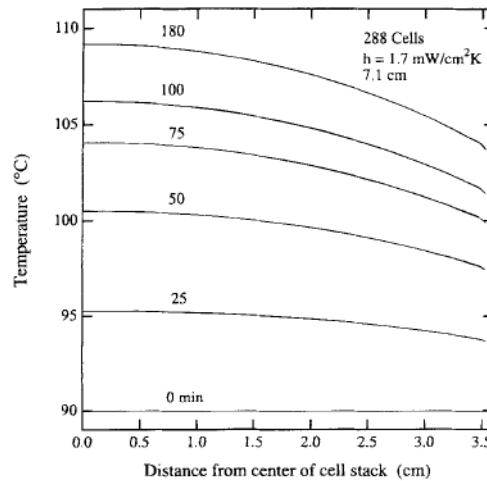


Figure 2.24. Temperature profiles as a function of time for the proposed electric vehicle battery design, [9].

For the cells in the middle of the cell stack, the models show good agreement for both heat generation rate and temperature. The models predict a center temperature of 108 °C at the end of discharge, with a variation between models of less than 0.5 °C.

The models disagree more strongly on both temperature and heat generation rate for the outer face of the cell stack (102.5 °C versus 105 °C).

The difference between the cell-stack and the one-cell calculations for the temperature of the cell at the outer face of the stack can be explained by examining differences in the development and use of the models.

The cells in the cell-stack model vary in both temperature and heat generation rate from their neighboring cells, and therefore a temperature gradient is established in the stack. The one-cell model, considers one cell with a uniform temperature and heat generation rate with heat transfer from the cell calculated using an averaged value of the per-cell heat transfer coefficient based on the position of the cell in the cell stack.

For the one-cell model, the time constant for heat transfer to the surroundings is a relatively large number, while for the cell-stack model it's a relatively small number.

This means that in the cell-stack model, the cell at $x = L/2$ transports more heat to the surroundings earlier in discharge and does not appreciably heat up until the temperature profile in the cell stack is developed and the outer cell can receive heat from the internal cells. Thus the outer cell temperature calculated by the cell-stack model rises more slowly and reaches a lower value than its corresponding temperature calculated by the one-cell model.

For a single cell, or for a cell stack with a negligible temperature gradient, differences between calculated heat generation rates and temperatures from the one-cell model and the cell-stack model are due to the heat-generation rate approximation.

From examination of a heat generation rate profile, it was concluded in [9], that heat was generated at lower rates in higher temperature areas of the stack, and at higher rates in lower temperature areas of the stack. This type of non-uniform heat generation rate tends to flatten the temperature profile of the cell stack.

Because of the methods in which the models were developed, the one-cell model is more accurate than the cell-stack model for calculating temperatures in cell stacks with negligible temperature gradients, and the cell-stack model is more accurate for calculating temperature profiles in stacks with appreciable temperature gradients.

Y. Inui et al. presented, in [40], a comparison analysis: two-dimensional simulation for cylindrical battery and three-dimensional simulation for prismatic battery. The former is done because the cylindrical shape is most popular for the commercially available small size batteries while the latter choice is due to the fact that prismatic battery cells have an advantage in comparison with cylindrical ones when combining them in modules.

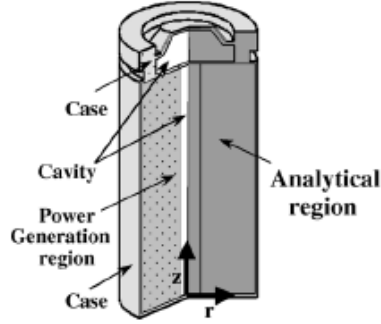


Figure 2.25. Schematic diagram of cylindrical Li-Ion secondary battery and analytical region, [40].

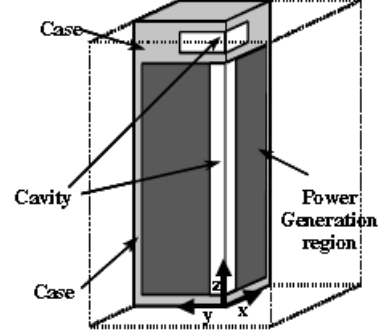


Figure 2.26. Schematic diagram of prismatic Li-Ion secondary battery and analytical region, [40].

The following equations can be used to calculate the transient response of the temperature distribution in the **cylindrical** battery:

- Power generation region:

$$\rho c_p \frac{\partial T}{\partial t} = \frac{1}{r} \frac{\partial}{\partial r} \left(\lambda_r r \frac{\partial T}{\partial r} \right) + \frac{\partial}{\partial z} \left(\lambda_z \frac{\partial T}{\partial z} \right) + \bar{q} \quad (2.28)$$

$$\frac{ds}{dt} = -\frac{i}{c_i} \quad (2.29)$$

$$i = \frac{E_0 - E}{r_i} \quad (2.30)$$

$$I = \iint_S 2\pi r i dr dz \quad (2.31)$$

- Case and cavity:

$$\rho c_p \frac{\partial T}{\partial t} = \frac{1}{r} \frac{\partial}{\partial r} \left(\lambda_r r \frac{\partial T}{\partial r} \right) + \frac{\partial}{\partial z} \left(\lambda_z \frac{\partial T}{\partial z} \right) \quad (2.32)$$

Where s is the local state of charge, E is the terminal voltage, I is the discharge current, ρ is the mass density, c is the specific heat, λ is the thermal conductivity, c_i is the capacity per unit volume of the power generation region, S is the power generation region on the r - z plane and the subscripts r and z denote the values along the radial and axial-directions, respectively.

In this model the battery is assumed to be cooled by natural convection. This heat flux is employed as the boundary condition on the battery surface required for calculation of the temperature distribution.

Numerical simulations of the transient responses of the temperature distribution in the battery are performed for 0.9 A (0.5 C) and 1.8 A (1.0 C) constant current

discharges. The authors confirmed that the simulation results of the transient temperature and voltage variations coincide very well with the experimental results for both the 0.9 A and 1.8 A constant current discharge, as shown in Figure 2.27

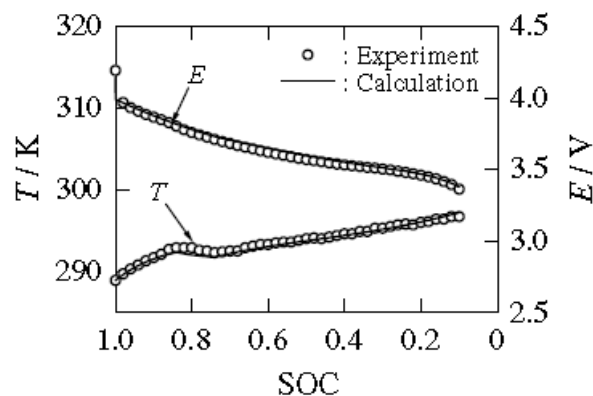


Figure 2.27. Experimentally and numerically obtained transient temperature and voltage variations of cylindrical battery for 0.9 A constant current discharge, [40].

Figure 2.28 shows the temperature distribution in a cylindrical battery at the end of a 1.8A (1 C) constant current discharge.

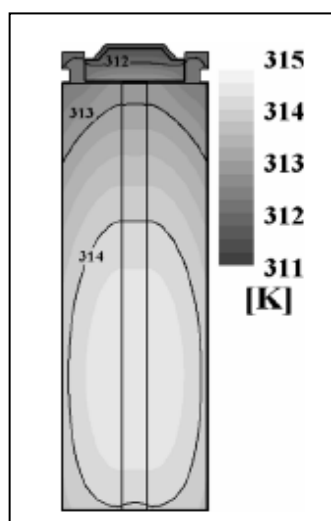


Figure 2.28. Numerically obtained temperature distribution in cylindrical battery at end of 1.8 A constant current discharge, [40].

In the case of prismatic batteries a 3D simulation code is needed to compute the temperature distribution. To calculate the transient response of the temperature distribution in the prismatic battery, Equation (2.28) must be replaced with:

$$\rho c_p \frac{\partial T}{\partial t} = \frac{\partial}{\partial x} \left(\lambda_x \frac{\partial T}{\partial x} \right) + \frac{\partial}{\partial y} \left(\lambda_y \frac{\partial T}{\partial y} \right) + \frac{\partial}{\partial z} \left(\lambda_z \frac{\partial T}{\partial z} \right) + \bar{q} \quad (2.33)$$

Similar to the two-dimensional code, the three-dimensional code calculates the transient response of the temperature distribution in the battery along with the transient responses of the current distribution, state of charge distribution and terminal voltage for given discharge current by solving the above equations simultaneously.

The temperature rise during the discharge becomes different depending upon the cross sectional shape even under the condition of the same battery volume and capacity. Selecting a prismatic battery with laminated cross section (pouch-style battery, i.e. 137.6 mm x 8.6 mm x 68.8 mm), has a remarkable effect on suppression of the temperature rise in comparison with a battery with the square cross section, (i.e. 68.8 mm x 17.2 mm x 68.8 mm).

This result is considered to be caused by the difference in the surface area. The cooling effect by the ambient air is proportional to the surface area, and batteries with laminated cross section have the largest surface area.

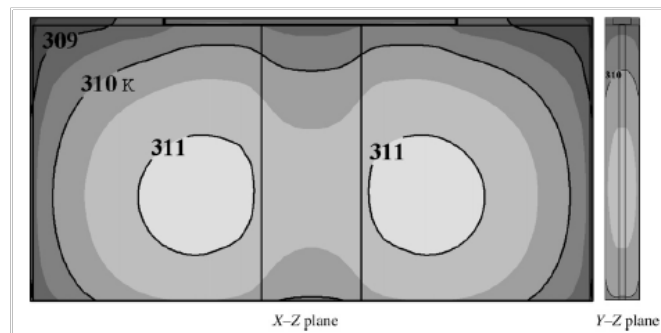


Figure 2.29. Numerically obtained temperature distribution for laminated prismatic battery at end of 9.0 A constant current discharge, [40].

According to the authors, the effect of the lamination on the suppression of the temperature unevenness is, however, unexpectedly small, and some other measure is considered to be needed to suppress this unevenness. These results are very informative to determine the cross sectional shape of large size batteries.

At Argonne National Laboratory, J. Lee et al. developed a three-dimensional thermal modeling of electric vehicles batteries, [39]. Once the cell design specification, the thermal properties, and the electrical performance characteristics of a battery system are given, the battery temperature distribution can be predicted by the model for different operating and ambient conditions.

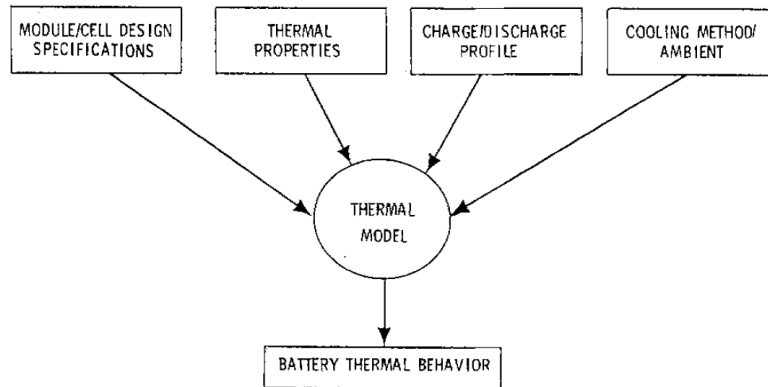


Figure 2.30. Inputs to battery thermal model, according to [39].

Generally, the temperature rise will be higher, and the temperature gradients will be larger, for a collection of cells in comparison with a single cell. The thermal behavior of individual cells and modules in the battery pack is also affected by the asymmetrical boundary conditions imposed by the packaging requirements of the vehicle.

In this work, each cell is divided into two regions, namely the core region and the boundary region. The equation describing the temperature distribution in the **core region** is:

$$\rho c_p \frac{\partial T}{\partial t} = \frac{\partial}{\partial x} \left(\lambda_x \frac{\partial T}{\partial x} \right) + \frac{\partial}{\partial y} \left(\lambda_y \frac{\partial T}{\partial y} \right) + \frac{\partial}{\partial z} \left(\lambda_z \frac{\partial T}{\partial z} \right) + \bar{q} - \rho c_p U_x \frac{dT}{dx} \quad (2.34)$$

where the convective velocity U is assumed to exist only in the x -direction and represents the average motion of a composite mass, which is equivalent to the actual movement of the electrolyte. In most cases, such a movement is caused by the change of electrode porosity as electrochemical reactions occur.

Here, for simplicity, \bar{q} is written as: $\bar{q} = \frac{I}{W_e} \left[V + \frac{\Delta H^0}{nF} + \frac{\Delta c_p}{nF} (T - T_{ref}) \right]$

where T is the temperature at the surface of the core region, W_e is the thickness of a composite element. ΔH^0 is considered to be negative for exothermic reactions and $I < 0$ for discharge.

However, the requirement of knowing I and V *a priori* imposes a limitation on the predictive power of the model. The heat generation rate cannot be calculated without knowledge of the variations of I and V during cell operation. Theoretically, I , V , and T are dependent upon one another, therefore, determining I and V without knowing T results difficult.

The **boundary region** denotes the cell case and the electrolyte surrounding the core region. In terms of heat transfer, the boundary region separates the core region from the outside environment and thus imposes an additional barrier to heat dissipation. However, the electrolyte in this region absorbs heat generated in the core region and thus serves as a heat sink.

$$-k_n \frac{\partial T(n)}{\partial n} = h(T_s - T_\infty) + \varepsilon\sigma(T_s^4 - T_\infty^4) + \rho_b c_{p,b} H_b \frac{\partial T_b}{\partial t} - \rho c_p T U_x \quad (2.35)$$

where T_s is the temperature at the external cell surface, H_b is the thickness of the boundary region and the fourth right-hand side term accounts for the variation of mass in the boundary region. Equation (2.35) can be used for all three directions ($n = x, y, \text{ or } z$). Here T_s is considered to be:

$$T_s = c_b T + (1 - c_b) T_\infty \quad \text{where } c_b = \left(1 + \frac{hH_l}{\lambda_l} + \frac{hH_c}{\lambda_c}\right)^{-1} \quad (2.36)$$

where H_l , and k_l are the thickness and thermal conductivity of liquid electrolyte, and H_c and k_c are the same for the cell case material.

One needs to use different coefficients for boundaries in different spatial directions when the heat transfer coefficient (h) and the amount of electrolyte in the boundary region are not identical in each direction.

In the paper a dimensionless analysis is proposed in order to obtain generalized characteristics of thermal behavior and reduce the number of parameters.

At high rates of discharge, the thermal resistance and capacitance imposed by the cell case and the surrounding electrolyte become relevant. However, their effects diminish as the size of the cell increases, due to the reduction of external surface area per unit volume.

In addition, the internal thermal conductivity becomes more important in larger cells. In most cases, the effects of radiation on total heat loss are small (~10% of convection), except at low discharge rates ($C/3$ or less) under natural convection. Results for a lead-acid battery are presented in the paper and are shown in Figure 2.31.

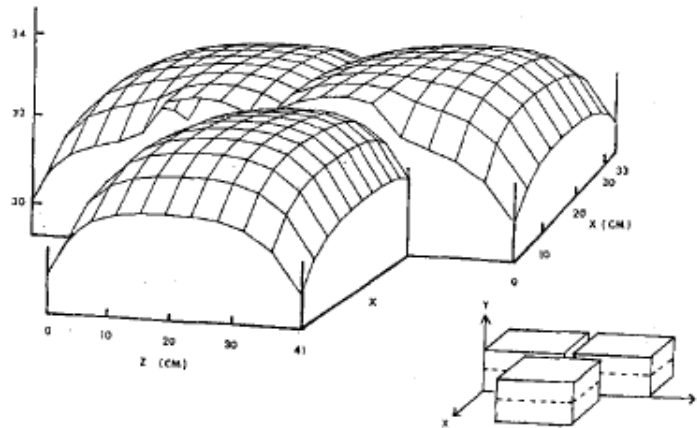


Figure 2.31. Calculated temperature distribution at mid-height cross section of three-module lead-acid battery after 2h of charge at 3h rate under natural convection cooling, [39].

Figure 2.31 shows that the average temperature of the battery increased from 25 °C to approximately 33°C after 2 hours of charging at a 3C rate. The flat temperature profile at the center of each module indicates that the internal thermal resistance is relatively small compared with that at the boundaries.

The result also shows that a higher temperature exists near the surface area where modules face one another.

Application of the thermal model to various batteries indicated that excessive temperature rise will occur in a closely packed 330 Ah module of five cells. Forced air convection is not effective for cooling the module.

To provide sufficient capacity, a large-scale Li-Ion battery generally consists of many individual cells that are connected in parallel. Given the results shown in [39], it is evident that this configuration inherently increases the thermal resistance of a battery, so thermal management becomes critical for operation.

Generally, when modeling battery modules and packs some simplified strategies are adopted to avoid computing an unacceptable amount of calculations. It is possible to neglect the radiative heat transfer on the boundaries, take the layered-structure of the cells as the homogeneous materials, transfer the container to be a part of the boundary equations, or degrading a three-dimensional system to a 2D or 1D model.

In [10], Chen et al. developed a detailed thermal model to verify the correctness of the assumptions and to determine the optimal approach to simplify the thermal model of a battery.

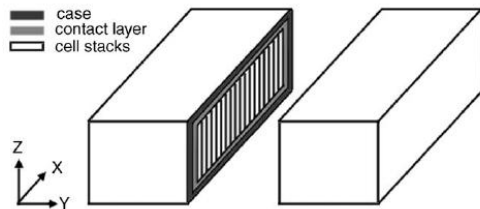


Figure 2.32. Schematic representation of a typical lithium-ion battery, [10].

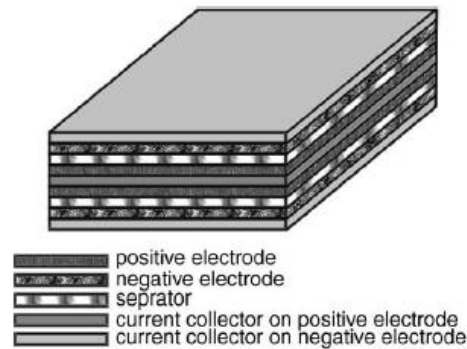


Figure 2.33. Schematic diagram of a typical lithium-ion unit cell, [10].

Inside the battery conduction is the main heat transfer mechanism and the transient heat conduction equation is:

$$\rho c_p \frac{\partial T}{\partial t} = \frac{\partial}{\partial x} \left(k_x \frac{\partial T}{\partial x} \right) + \frac{\partial}{\partial y} \left(k_y \frac{\partial T}{\partial y} \right) + \frac{\partial}{\partial z} \left(k_z \frac{\partial T}{\partial z} \right) + \bar{q} \quad (2.37)$$

where ρ , Cp , k and \bar{q} are the density, heat capacity, thermal conductivity and heat-generation rate per unit volume, respectively.

At the boundary, both convection and radiation must be considered and they expressed as:

$$Q_r = \varepsilon\sigma(T_s^4 - T_\infty^4) \quad (2.38)$$

$$Q_c = h_c(T_s - T_\infty)$$

Note that $T_{surface}$ may vary with location and h_c may be a function of both location and temperature. In case of forced convection the convective heat transfer coefficient can be determined as $h_c = f_2 \sqrt{\frac{V}{L}}$ where f_2 , V and L are a temperature-dependent coefficient, the velocity of the airflow, and the characteristic length of the surface, respectively.

In addition, the heat-generation rate of a lithium-ion battery during operation needs to be determined. The authors adopted the equation derived by Bernardi [37]:

$$\bar{q} = \frac{I}{Vol} (E_{OC} - E - T \frac{dE_{OC}}{dT}) \quad \left[\frac{W}{m^3} \right] \quad (2.39)$$

where I , Vol , E_{oc} and E denote respectively the total current of the battery, the total volume of the core region, the open-circuit potential and the working voltage, respectively.

This equation is efficient enough but it is important to notice that the potential terms should be obtained, and the effect of temperature on electrochemical behaviors cannot be evaluated.

Finally, it is necessary to determine several physical parameters at the interfaces between the different components inside a lithium-ion battery. The product value of density and heat capacity is calculated based on the volume of each component while the thermal conductivity at the interface should be determined based on connection between components and the contact resistance of the interface. Fortunately, the effect of contact resistance on effective thermal conductivity is insignificant in this case, because most of the pores and gaps are filled with liquid electrolyte, and the thermal conductivity of the liquid electrolyte is comparable with that of the materials.

The 3D detailed thermal model presented is not the best candidate to perform the practical simulations due to its inefficient calculation. However, such detailed model could be useful for validate with a comparison more simple models.

Table 2.1. Detailed information of simplified thermal models examined in [10].

Number	Dimension	Core region	Case and contact layer	Radiation
1	1D (X)	X : considering the layered-structure, Y, Z : ignored	X : considered, Y, Z : ignored	Considered
2	1D (Y)	Y : taking the average property, X, Z : ignored	Y : considered, X, Z : ignored	Considered
3	1D (Z)	Z : taking the average property, X, Y : ignored	Z : considered, X, Y : ignored	Considered
4	2D (X, Y)	X and Y : considering the layered-structure, Z : ignored	X, Y : considered, Z : ignored	Considered
5	2D (X, Z)	X and Z : considering the layered-structure, Y : ignored	X, Z : considered, Y : ignored	Considered
6	2D (Y, Z)	Y and Z : taking the average property, X : ignored	Y, Z : considered, X : ignored	Considered
7	3D (X, Y, Z)	Considering the layered-structure	Ignored	Considered
8	3D (X, Y, Z)	Considering the layered-structure	Transferred to boundary conditions	Considered
9	3D (X, Y, Z)	Considering the layered-structure	Considered	Ignored
10	3D (X, Y, Z)	Taking the average property	Considered	Considered
11	3D (X, Y, Z)	Considering the layered-structure	Considered	Considered

Number 11 is a detailed thermal model, which is taken as a reference for the simulation.

The accuracy for each thermal model is evaluated quantitatively by four representative indexes:

- Absolute deviation of maximum temperature (important for secure design);
- The minimum temperature (easy to measure from surface);
- The average temperature (indicates the total heat left in the system);
- Standard deviation of temperature distribution at the end of discharge (degree of consistency of the temperature profile).

Then compact indexes, shown in Figure 2.34, have been computed.

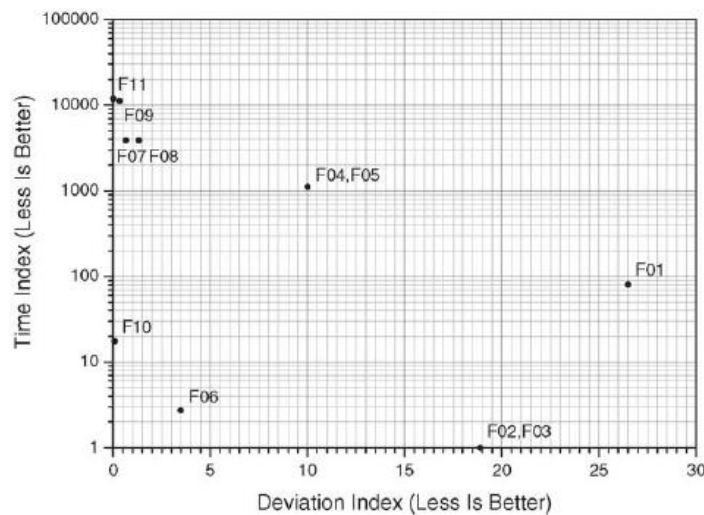


Figure 2.34. Deviation index and time index of simplified thermal models developed in [10], under forced convection ($h = 100\text{W/m}^2\text{K}^1$).

According to the results, it is found that, for the system considered in the study, a 1D model is insufficient to represent the thermal behavior, especially for the battery under forced convection. 2D models provide better accuracy but consume more time than 1D models. 3D thermal models provide the best accuracy, although the calculation time is expanded to 3000–11,000 times that of the one-dimensional models. The only exception is model number 10 (3D model that considers average properties instead of a layered structure), which is the optimum simplification proposed in this work (660 times faster than the detailed model).

It is important to notice also that the resistance in the x -direction is significantly larger than in y and z directions, which means that conduction in x -direction is the less important.

The temperature on the surface is lower than at the centerline, but the excellent thermal conductivity of the case offers a shortcut for heat to flow from the high temperature region to the low temperature region, so that small temperature gradients are maintained on the surface. By contrast, the high thermal resistance in the x -direction of the core region decreases the heat flow, whereby a steep temperature gradient is formed inside the battery.

Therefore, according to this model, the temperature in the central region of the surface $X=0$ is lower than the surrounding temperature.

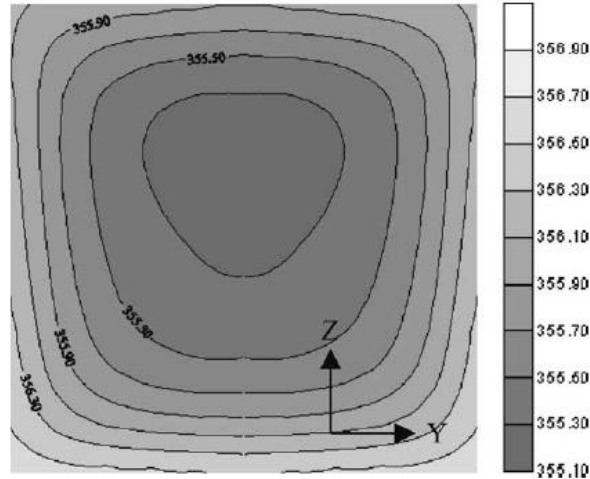


Figure 2.35. Temperature distribution on the surface $X = 0$ at the end of 3C discharge procedure, [10].

The data discussed above clearly indicates that both the contact layer and the case strongly affect the temperature distribution in a Li-Ion battery, and that the temperature distribution inside the battery may be different from that on the surface.

Forced convection is employed whenever possible since it generally offers much better heat transfer than natural convection. Obviously, enhancing the forced convection greatly depresses both the maximum temperature and the minimum temperature in the system, as shown in Figure 2.36

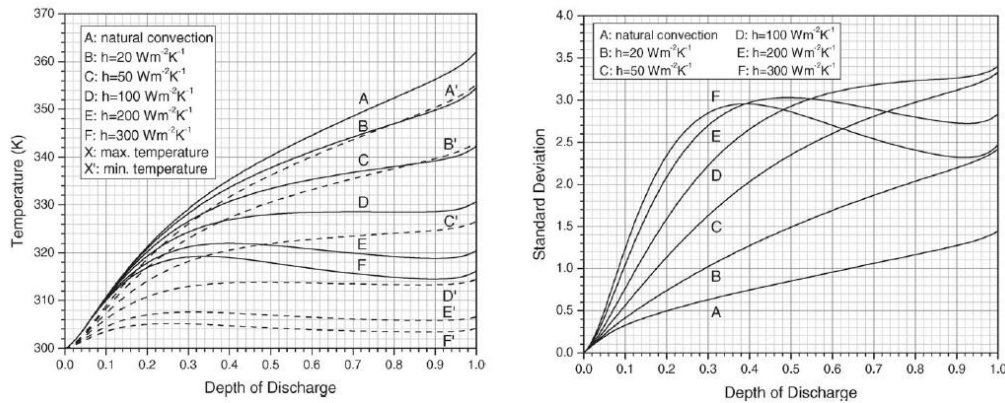


Figure 2.36. Temperature variation and standard deviation of temperature under different convection conditions at 3C discharge rate, [10].

However note that there exists an optimum condition for forced convection to control effectively the system in a suitable temperature range without waste of energy.

Temperature uniformity, which is a very important issue, can be evaluated quantitatively by examining the standard deviation of the temperature distribution.

Figure 2.36 shows that the standard deviation increases with enhancing the extent of convection under low to moderate convection. On the other hand increasing the forced convection does not induce further increase in the standard deviation under strong forced convection.

According to the authors this study revealed that the battery case and the contact layer (a barrier to the heat conduction but an extra capacity that mitigates the temperature rise) are important components, and the complicated core region can be further simplified by adopting the average properties.

The simulation results from the detailed thermal model show that the temperature distribution inside the battery is asymmetric. Analyzing the temperature distribution it comes out that the heat transfer is greater in y and z directions, and the metal case effectively spreads heat on the surface. Furthermore, radiation is found to be an important process for heat dissipation, especially in situations under natural convection and high temperatures.

In summary, the research papers surveyed evidence that the temperature distribution in a Li-Ion battery module strongly depends on the cooling conditions adopted.

A thermal management system becomes critical to properly operate a battery module or pack to avoid premature aging or decreased performance.

2.3.3 Thermal management systems

The heat generated within a battery must be dissipated to improve reliability and prevent failure. A thermal management system is the framework of processes and procedures used to control and regulate the battery operating parameters that influence the battery temperature.

To optimize the performance of a battery pack, the thermal management system should deliver:

- Optimum operating temperature range for all battery modules;
- Small temperature variations within a module;
- Small temperature variations among various modules.

Uneven temperature distribution in a pack could lead to electrically unbalanced modules and thus to lower performance for the pack and vehicle.

If temperature uniformity can be obtained within and between modules, then, the pack can operate closer to its desired optimum operating temperature range, thus improving his performance.

Battery pack thermal management and control could be achieved by air or liquid systems, insulation, thermal storage (phase-change material), active or passive approaches, or a combination of the above techniques.

According to [7], the location of each module in a battery pack, the external conditions and the type of heating and cooling could create uneven temperature distributions.

To quantify the impact of the temperature on the performance of a battery, temperature-dependent battery performance models are needed (see previous section).

In order to evaluate the thermal performance of battery models and packs and to improve designs, NREL has been using computer aided engineering tools. The author have used finite element analysis software for performing two and three-dimensional thermal analysis. ANSYS, a widely accepted commercial software package, was used.

The model treats the battery core and battery case as two separate isothermal nodes. All the components inside the case, such as active material, cathode and anode, current collectors, separator, etc. are assumed to be a single homogenous material with averaged properties. Thus, the core can be approximated as a homogeneous material with different thermal conductivities in different directions. Since its thermal mass is quite small the temperature of the case is very close to the core one.

Currently the ADVISOR¹⁰ battery model, developed at NREL, uses the parallel airflow approach which is also used in the Toyota Prius. In this approach, the cooling air is distributed (usually) under the pack and flows up along each module, then is collected in a space above the pack and exhausted. This has the potential advantage of allowing every module to experience the same amount of air and inlet air temperature, leading to a more uniform pack temperature. Consequently, from a modeling standpoint, it means that the pack thermal behavior can be reasonably represented by modeling a single module.

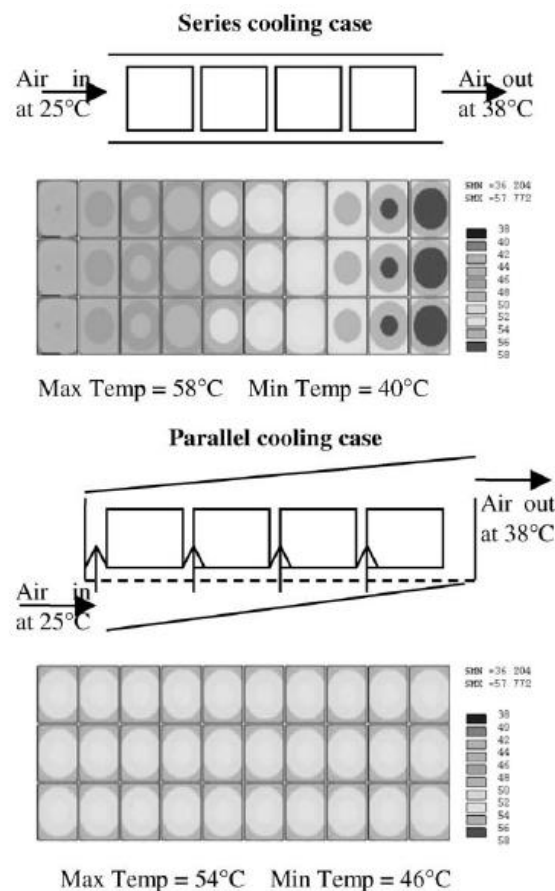


Figure 2.37. 2D analysis of a 30-module battery pack with two types of air cooling, [7].

Heat is generated in the core region due to electrochemical reactions and Joule effect and then conducted through the case and finally convected to the surrounding. In the paper, the rate of heat rejection is defined as:

¹⁰ ADVISOR is an advanced vehicle simulator, implemented in MATLAB/SIMULINK environment at NREL.

$$\dot{Q} = \frac{T_s - T_\infty}{\frac{1}{hA} + \frac{w}{kA}} \quad (2.40)$$

where the heat transfer coefficient h is estimated from correlation taken from heat transfer textbooks and they include a minimum value to account for natural convection.

The temperature rise in the battery is calculated based on the energy balance between battery heat generation, amount of heat lost from the battery, thermal mass of the battery and duration of battery use:

$$T_s = \int_0^t \frac{Q_{gen} - \dot{Q}}{m_{bat} c_{p,batt}} dt \quad (2.41)$$

Different thermal modeling approaches are then proposed in [7] to predict thermal performances. The lumped capacitance thermal model is integrated with ADVISOR battery performance models thus allowing one to predict the temperature changes in a vehicle's battery according to the drive cycle, air cooling flow rate and battery type.

Since the battery performance model is temperature dependent, the impact of varying temperature on battery performance automatically affects the vehicle performance.

In 2009, Kuper et al. proposed an extensive analysis of thermal management for hybrid vehicle battery systems, [41]. The thermal management system is used to optimize the performance of the battery pack during vehicle operations.

During the operation of the vehicle the battery system is subjected to a wide range of thermal and electrical load conditions. Since batteries are electro-chemical systems, lower temperatures lead to decreasing power capability and elevated temperatures can lead to premature aging of the device [1].

Moreover, in [41], the temperature influence on the aging of the battery is studied. It is shown that an Arrhenius type law of this kind:

$$K_{aging} = e^{-\frac{E_a}{RT}} \quad (2.42)$$

is suitable to account for the temperature effects on the aging of the battery. The higher the temperature, the higher value of K (note that K ranges between 0, at $T=0$ K, and 1, as $T \rightarrow \infty$).

A battery cooling system is needed to avoid reaching temperature that would lead to premature aging of the battery.

Depending on the operational profile, the size of the battery system and the vehicle environment, a suitable cooling system can be chosen from the available

alternatives. The authors identified essentially three types of cooling system, distinguished by the cooling medium:

- Air;
- Water/glycol mixtures;
- Refrigerant.

The essential idea of an air cooled battery system is to utilize the conditioned air from the passenger compartment to maintain the battery in desired temperature range in warm ambient temperatures.

As stated earlier, the cooling system must be able to keep the cell temperatures as uniform as possible. Air flow simulations are executed in the course of the battery development to ensure this goal will be met. Simulations as well as measurements on real battery systems show that up to four cells in series can be cooled sufficiently in most applications.

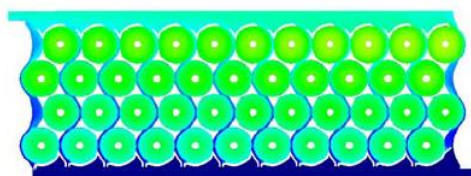


Figure 2.38. CFD simulation of the air flow and cell temperature uniformity for a 44 cell stack of cross flow type, [41].

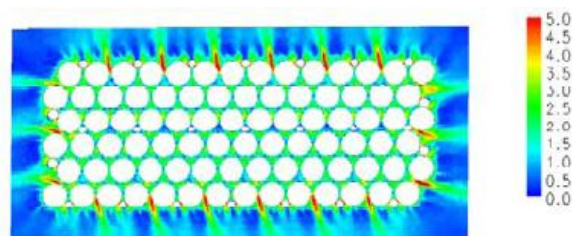


Figure 2.39. CFD simulation of the air flow for a 96 cell stack of axial cooling type, [41].

Figure 2.40 shows a scheme of the climatic system of a vehicle with refrigerant cooled battery parallel to the AC loop for passengers' cabin cooling.

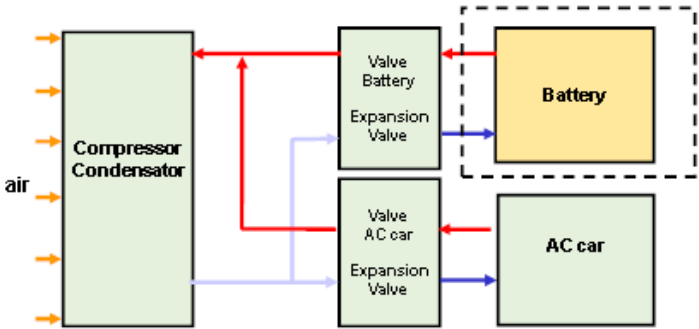


Figure 2.40. Schematic of the climatic system of a vehicle with refrigerant cooled battery parallel to the AC loop for passenger cabin cooling, [41].

As regard liquid cooling systems, Figure 2.41 shows a typical heat transfer system of a liquid cooled battery.

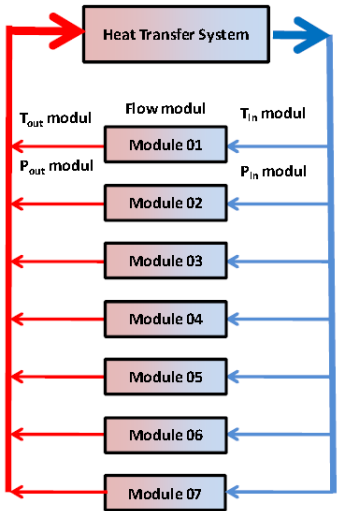


Figure 2.41. Schematic of the heat transfer system of a liquid cooled battery, [41].

The choice of battery cooling system depends on the constraints and requirements of the vehicle application. The total cost impact to the vehicle must also be considered. Heat exchanger possibilities, available space for fans and air ducts, as well as safety constraints must be taken into account.

Where the operating environment is particular harsh or the duty cycle is extreme, closed loop systems like water/glycol or refrigerant may provide better cooling efficiency.

Since active cooling requires energy – to operate fans or coolant pumps, to control valves or to put additional load onto the drive train for more AC power – the cooling intensity should be controlled to maintain the temperature level of the battery cells but also minimize the total energy usage of the system.

This can be achieved by design, including the right choice and size of the battery cooling system, and by implementation of appropriate thermal and electrical management strategies.

An active thermal management strategy keeps the cell temperatures in the appropriate range, to provide sufficient power capability as well as to avoid aging rates higher than anticipated.

2.3 Summary

In this chapter an extensive literature review on the modeling of both electrical and thermal aspects of a Li-Ion battery cell has been presented.

The electrical characterization has been proposed from both, fundamental and phenomenological points of view. In particular, control-oriented models of Li-Ion batteries for automotive application have been presented and discussed in detail.

The review of the thermal characterization of Li-Ion battery have been divided in two parts, namely single cell thermal models and pack thermal models. At the end a review of the state of art of thermal management system of Li-Ion battery has been presented.

Analyzing the state of the art, it can be concluded that a more detailed thermal model, able to capture the temperature dynamic of a Li-Ion battery cell, is needed to improve the accuracy of models developed for control and optimization.

In Chapter 3 the modeling approach to implement a model of the thermal dynamics of a Li-Ion battery cell will be presented

CHAPTER 3

3. Modeling the thermal dynamics of Li-Ion batteries

As stated in Chapter 1, Li-Ion batteries are becoming the dominant battery technology, in particular for high power systems. Their greater specific power and energy content allow overcoming limitations in meeting the power demands of HEVs and PHEVs typical of Ni-MH batteries. Moreover they are able to withstand a wider range of temperatures.

However, Li-Ion batteries must be controlled during their operation, in order to prevent accelerated aging, decreasing of performance or damages.

Models based on first principles (referred to as fundamental models) are often very accurate, but they are generally not suitable for real-time implementation, due to their inherent complexity in describing the chemical behavior of the battery (i.e. [36]). The type of model that is often used as a compromise between accuracy and complexity is the equivalent circuit model. This class of models is inherently phenomenological and is intended to approximate the dynamic behavior of the battery.

Equivalent circuit models for batteries are generally of low order and are relatively simple to work with, in the context of on-board implementation and real-time algorithms. The terminology “control-oriented” means that the model must be simple in structure and yet still able to provide enough accurate results to suit the application.

Most of the works on control-oriented modeling and identification available in the open literature focus on isothermal (constant temperature) models, which are electro-thermal models whose parameters are scheduled assuming isothermal condition within a battery cell.

Notwithstanding, it is well known ([8]) that the dynamic behavior of batteries depends on temperature as well as on SoC. The isothermal assumption thus inevitably leads to errors and hence more accurate models are needed.

One way of compensating for SoC and temperature influence is to incorporate their dependency into the equivalent circuit model parameters (see i.e. [34] and [42]). Following this approach, however, requires high laboratory capability and a considerable amount of time. Many experiments have to be carried out at various temperatures and moreover the results are applicable only for the particular battery cell tested.

Besides, due to limitations in the experimental capabilities, the model the parameters are identified based on the surface temperature of the cell, since

these tests are performed imposing a constant wall temperature (see Figure 4.21 for a typical experimental setup).

This assumption is evidently in contrast with the experimental and numerical results published to date, which state that inside a cell, the thermal conductivity and the heat generated by electro-chemical reactions and irreversibilities, lead to a three-dimensional temperature distribution. This causes the temperature inside a cell to be considerably different respect to the surface temperature.

Hence, accounting for the temperature distribution becomes necessary in order to properly model the battery behavior. A detailed thermal model would allow accounting for the spatial distribution of the temperature within a battery cell.

Developing a modeling approach able to characterize the spatial temperature distribution within a Li-Ion battery cells is the main objective of this thesis.

3.1 Thermal modeling approach and mathematical formulation

In order to design a thermal model of a prismatic Li-Ion battery cell two different heat transfer problems have to be solved. First of all a conduction problem within the battery cell must be formulated as an unsteady problem with non-homogeneous boundary conditions varying with respect to both time and space. Then an energy conservation problem at the boundaries needs to be introduced to describe the behavior of the medium used to cool the battery. In this section, a review of the basic concept of heat transfer problems will be presented, in relation to the specific problem here considered.

3.1.1 Basic equation for energy conservation

The problem of heat transfer can be approached in several ways. Many textbooks (for instance [43] or [44]) tend to introduce the basic equation for heat transfer starting from the fundamental laws of thermodynamics.

The subjects of thermodynamics and heat transfer are highly complementary. In some aspects, because it treats the rate at which the heat is transferred, heat transfer theory may be viewed as an extension of thermodynamics.

The **first law of thermodynamics**, according to [43], may be expressed as follows: *The net change (increase or decrease) in the total energy of the system during a process is equal to the difference between the total energy entering and the total energy leaving the system during that process.*

Energy can be transferred to or from a system by heat or work, and it can enter or leave the system by exchanging mass flows directly through the boundaries. The total energy of a simple compressible system consists of internal, kinetic, and potential energies.

Normally, in heat transfer analysis, the only form of energy of interest is the one that can be transferred as a result of a temperature difference, that is, heat or thermal energy. Therefore it is possible to write a heat balance equation:

$$\dot{Q}_{in} - \dot{Q}_{out} + \dot{E}_{gen} = dE_{thermal\ system} \quad [\text{W}] \quad (3.1)$$

In a closed system, where there are no mass flows, and when system involves heat transfer only and no work interactions across its boundary, the power balance relation further reduces to:

$$\dot{Q} = mc_v \Delta T \quad [\text{W}] \quad (3.2)$$

3.1.2 Basic equation for fluid flow

In systems where fluid flows are present, the energy exchanged through the boundaries associated to transfer of mass, has to be considered, other than the energy fluxes. These problems can be modeled following the control volumes approach.

According to [44], the inflow and outflow terms are surface phenomena. That is, they are associated exclusively with processes occurring at the control surface and are generally proportional to the surface area. These flow terms include heat transfer (which can be by conduction, convection or radiation) and work interaction occurring at the system boundaries as well as energy advected by mass entering and leaving the control volume.

The flow of a fluid through a pipe or duct can normally be approximated to be one-dimensional. As a result, all properties are assumed to be uniform at any cross section normal to the flow direction, and the properties are assumed to have bulk average values over the entire cross section.

Under the one-dimensional flow approximation, the mass flow rate of a fluid flowing in a pipe or duct is defined as:

$$\dot{m} = \rho v A \quad \left[\frac{\text{kg}}{\text{s}} \right] \quad (3.3)$$

where v is the mean velocity and A the cross-section area.

The general energy conservation law, written in its differential form, can be cast as follows:

$$\frac{dE}{dt} = mc_v \frac{dT}{dt} = \dot{m} \left(h + \frac{1}{2} v^2 + gz \right)_{in} - \dot{m} \left(h + \frac{1}{2} v^2 + gz \right)_{out} + \dot{Q} - \dot{W} \quad (3.4)$$

where \dot{W} represents the work term (not including the flow work) and h^{11} is the enthalpy per unit mass, in $\left[\frac{\text{J}}{\text{kg}} \right]$.

¹¹ $h = u + pv$ where u is the specific internal energy and the term pv represents the flow work per unit mass.

Figure 3.1 gives a representation of an energy balance for an open system.

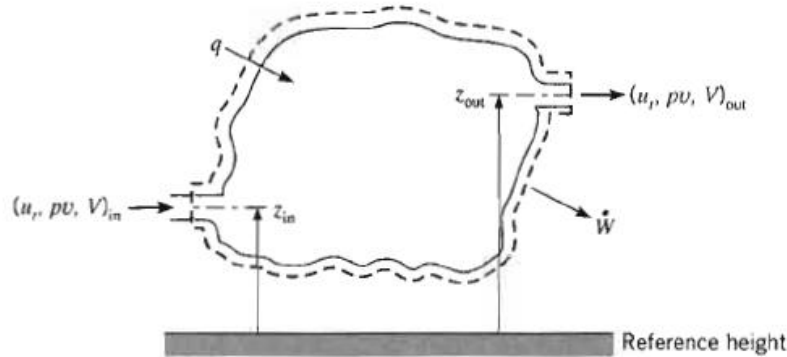


Figure 3.1. Open system energy balance representation.

For a steady-flow system with one inlet and one outlet, the rate of mass flow into the control volume must be equal to the rate of mass flow out of it. That is, $\dot{m}_{in} = \dot{m}_{out} = \dot{m}$. When the changes in kinetic and potential energies are negligible, which is usually the case, and there is no work interaction, the energy balance for such a steady-flow system reduces to:

$$mc_v \Delta T = \dot{Q} - \dot{m} \Delta h = \dot{Q} - \dot{m} c_p \Delta T \quad (3.5)$$

By solving this balance it is possible to find how the mean temperature varies in the system considered.

Fluid flow is streamlined and thus laminar at low velocities, but turns turbulent as the velocity is increased beyond a critical value. Transition from laminar to turbulent flow does not occur suddenly; rather, it occurs over some range of velocity where the flow fluctuates between laminar and turbulent flows before it becomes fully turbulent.

The Reynolds number is a dimensionless parameter that accounts for fluid properties and flow condition and allow one to discriminate between the two kinds of flow [44].

$$Re = \frac{\rho v_m L_c}{\mu} \quad (3.6)$$

$Re < 2300$	<i>Laminar flow</i>
$2300 < Re < 10,000$	<i>Transitional flow</i>
$Re > 10,000$	<i>Turbulent flow</i>

Flowing through a tube, the fluid particles in the layer in contact with the surface of the tube will come to a complete stop. This layer will also cause the fluid particles in the adjacent layers to slow down gradually as a result of friction.

To make up for this velocity reduction, the velocity of the fluid at the midsection of the tube will have to increase to keep the mass flow rate through the tube constant. As a result, a *velocity boundary layer* develops along the tube. The thickness of this boundary layer increases in the flow direction until the boundary layer reaches the tube center and thus fills the entire tube, as shown in Figure 3.2.

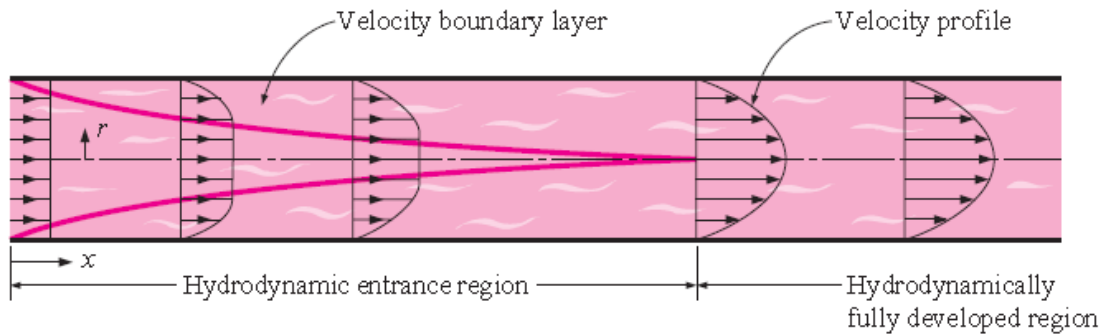


Figure 3.2. The development of the velocity boundary layer in a tube, [43].

Similarly, along the fluid flow direction, a thermal boundary layer develops as shown in Figure 3.3.

The region in which the flow is both hydro-dynamically and thermally developed and thus both the velocity and dimensionless temperature profiles remain unchanged is called fully developed region.

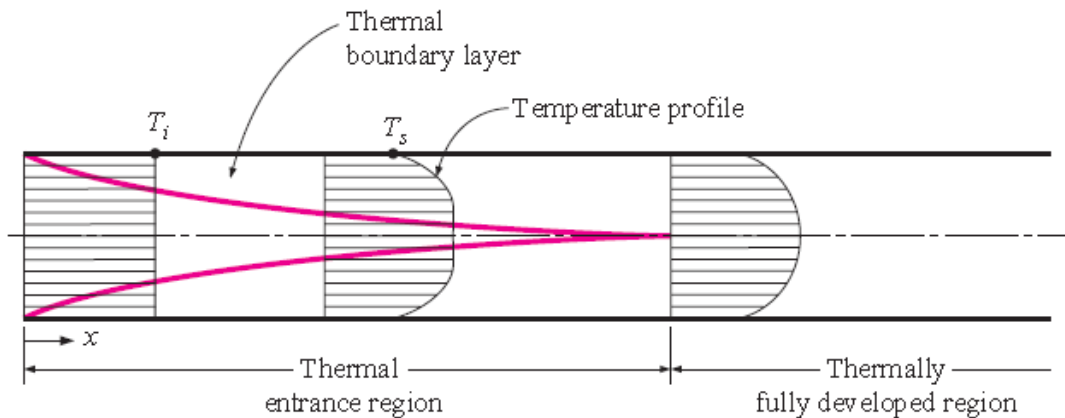


Figure 3.3. The development of the thermal boundary layer in a tube, [43].
(in this case the fluid is being cooled).

Fluid flow problems are normally solved using experimental correlations that are available for both laminar and turbulent flows and for entry region as well as for fully developed region.

Since an in depth discussion on this topic is out of the scope of this work, more references can be found in [44], [45] or [46].

Nonetheless, a quantity of great interest in the analysis of tube flow is the *pressure drop* ΔP since this value is directly related to the power requirements of the fan or pump to maintain the flow. It is convenient to express this quantity as:

$$\Delta P = f \frac{L}{D} \frac{\rho v_m^2}{2} \quad (3.7)$$

where L is the tube length, D the diameter, v_m the mean velocity, ρ the density and f the friction factor, which is a function of the Reynolds number.

The friction factor and the heat transfer coefficient are highest at the tube inlet where the thickness of the boundary layers is zero, and decrease gradually to the fully developed values, as shown in Figure 3.4.

Therefore, the pressure drop and heat flux are higher in the entrance regions of a tube. The effect of the entrance region is always to enhance the average friction and heat transfer coefficients for the entire tube. This enhancement can be significant for short tubes but negligible for long ones.

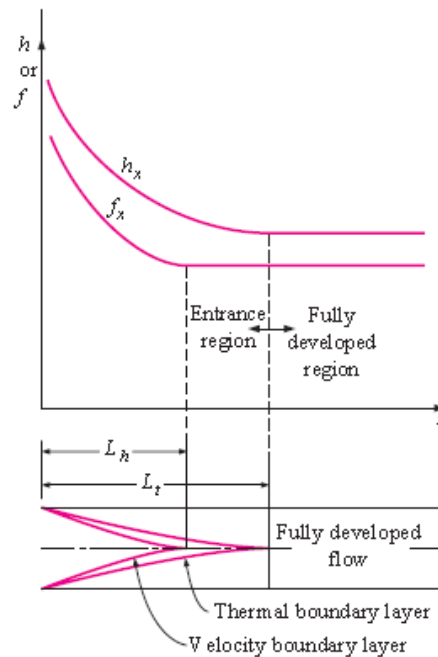


Figure 3.4. Variation of the friction factor and of the convection heat transfer coefficient in the flow direction for flow in a tube ($Pr > 1$), [43].

Typically, engineering problems involve a consideration of both the heat transfer rates between the fluids and the mechanical pumping power expended to overcome the friction and move the fluids. The so called friction-power

expenditure, as the ratio between the power needed to move the fluid and the heat exchanged is defined in [45], is a parameter of great importance in the development of heat exchangers or in the analysis of fluid flow that involve heat transfer.

The friction between the fluid layers in a tube may cause a slight rise in fluid temperature as a result of mechanical energy being converted to thermal energy. However, this frictional heating is too small to warrant any consideration in calculations, and thus is generally disregarded.

Remember that, although the theory of fluid flow is reasonably well understood, theoretical solutions are obtained only for a few simple cases such as the fully developed laminar flow in a circular pipe. Therefore, one must rely on the experimental results and the empirical relations obtained for most fluid flow problems rather than closed form analytical solutions. Errors of approximately 10-15 % are considered normal in this kind of applications.

3.1.3 Basic equations for heat transfer

A major objective in a heat transfer analysis is to determine the temperature field in a medium resulting from conditions imposed on its boundaries.

Heat is a form of energy in transit due to a temperature difference. There are three ways this transfer can occur:

- *Conduction* of heat throughout a medium due to transfer of energy from the more energetic particles of a substance to the adjacent less energetic ones, as a result of interactions between the particles;
- *Convection*, which is defined as heat transfer between a surface and a moving fluid;
- *Radiation* of energy emitted by matter in the form of electromagnetic waves (or photons) as a result of the changes in the electronic configurations of the atoms or molecules.

Unlike conduction and convection, the transfer of energy by **radiation** does not require the presence of an intervening medium.

This form of transfer relies on the Stefan-Boltzmann law, which for a grey surface is written as:

$$\dot{q}_{rad} = \varepsilon\sigma(T_{surface}^4 - T_{surroundings}^4) \left[\frac{W}{m^2} \right] \quad (3.8)$$

where σ is the Stefan-Boltzmann constant = $5.67 * 10^{-8} \frac{W}{m^2K^4}$ and ε is the surface emissivity.

According to [44], radiation is usually significant relative to conduction or natural convection, but negligible relative to forced convection. Thus radiation in forced convection applications, when temperatures are below large values (on the order of 10^2 degree Celsius), is disregarded. Sometimes this way of heat transfer is accounted for in the computation of the convective heat transfer coefficient obtaining thus an overall coefficient for both way of heat diffusion. In this work radiation will always be neglected.

The **convection** heat transfer mode is comprised of two mechanisms: energy transfer due to random molecular motion (diffusion) and macroscopic motion of the fluid (advection).

Regardless of the particular nature of the convection heat transfer process the appropriate rate equation is given by the *Newton's law of cooling*:

$$\dot{q}_{conv} = h (T_{surface} - T_{\infty}) \left[\frac{W}{m^2} \right] \quad (3.9)$$

where h is the convective heat transfer coefficient [W/m^2K] and T_{∞} is the average bulk temperature of the fluid. Any study of convection ultimately reduces to a study of means by which h may be determined.

The convection heat transfer coefficient is not a property of the fluid. It is an experimentally determined parameter whose value depends on all the variables influencing convection such as the surface geometry, the nature of fluid motion, the properties of the fluid, and the bulk fluid velocity.

Convection is called forced convection if the fluid is forced to flow over the surface by external agents such as a fan, pump, or the wind. In contrast, convection is called natural (or free) if the fluid motion is caused by buoyancy forces that are induced by density differences due to the variation of temperature in the fluid. Plenty of empirical correlations have been derived for external flows, internal flows, natural convection and boiling or condensation phenomena.

For most **conduction** problems the first law of thermodynamic, the energy conservation law, represents the essential tool that provides the solution to the problem. To determine the temperature distribution in a body, a precise methodology has to be followed and thus it is necessary to, respectively, define a differential control volume, identify the relevant energy transfer processes and introduce appropriate rate equations.

The conduction heat transfer fundamentally relies on the **heat diffusion equation** which provides the basic tool for heat conduction analysis. Its general form in Cartesian coordinates is:

$$\frac{\partial}{\partial x} \left(k_x \frac{\partial T}{\partial x} \right) + \frac{\partial}{\partial y} \left(k_y \frac{\partial T}{\partial y} \right) + \frac{\partial}{\partial z} \left(k_z \frac{\partial T}{\partial z} \right) + \bar{q} = \rho c_p \frac{\partial T}{\partial t} \quad (3.10)$$

where k_i ($i=x,y,z$), is the thermal conductivity in different spatial directions [W/mK], ρ the density [kg/m³], c_p thermal capacity [J/kgK] and \bar{q} the heat generation rate per unit volume, [W/m³].

In the case of isotropic material, which is a common assumption in heat transfer problems, the thermal conductivity does not vary with respect to the direction chosen and so the equation above can be written as:

$$\left(\frac{\partial^2 T}{\partial x^2} + \frac{\partial^2 T}{\partial y^2} + \frac{\partial^2 T}{\partial z^2}\right) + \frac{\bar{q}(x,t)}{k} = \frac{1}{\alpha} \frac{\partial T}{\partial t} \quad (3.11)$$

where $\alpha = \frac{\text{Heat conducted}}{\text{Heat stored}} = \frac{k}{\rho c_p}$ is the thermal diffusivity [$\frac{m^2}{s}$], and represents how fast heat diffuses through a material.

In the technical literature, i.e. [43] or [44], many simplified problems are considered and solved. Particularly relevant to this study is the solution of Equation (3.11) for one-dimensional case, specifically when $\frac{\partial T}{\partial y} = \frac{\partial T}{\partial z} \triangleq 0$, the heat diffusion equation reduces to:

$$\frac{\partial^2 T}{\partial x^2} + \frac{\bar{q}(x,t)}{k} = \frac{1}{\alpha} \frac{\partial T}{\partial t} \quad (3.12)$$

First of all the body will be considered to be in a **steady-state** situation which means that the temperature does not vary with respect the time but only along the spatial direction. In absence of internal heat generation the problem can be stated with the well known *Laplace* equation:

$$\frac{\partial^2 T}{\partial x^2} = 0 \quad (3.13)$$

Solution of Equation (3.13) leads one to find that the temperature distribution varies linearly with respect to the space coordinate x and performing a double integration the analytical solution obtained is: $T(x) = C_1 x + C_2$ where the two variables are obtained imposing the boundary conditions.

Considering now the case with presence of heat generation at a rate \bar{q} , the problem becomes:

$$\frac{\partial^2 T}{\partial x^2} + \frac{\bar{q}}{k} = 0 \quad (3.14)$$

And the corresponding analytical solution is: $T(x) = -\frac{\bar{q}}{2k} C_1 x + C_2$

Just as an example, the cartesian solution of a steady-state conduction problem within a plane wall of thickness L in presence of heat generation and with symmetrical convective boundary conditions results to be:

$$T(x) = T_{surface} + \frac{\bar{q} L^2}{2k} \left(1 - \frac{x^2}{L^2}\right) \quad \text{where } T_{surface} = T_{\infty} + \frac{\bar{q} L}{h} \quad (3.15)$$

The **transient** cases are more complex, since now the temperature varies with respect to both space and time. A fairly representative problem of one-dimensional transient heat conduction, without heat generation, has the form:

$$\frac{\partial^2 T}{\partial x^2} = \frac{1}{\alpha} \frac{\partial T}{\partial t} \quad (3.16)$$

These kinds of problems can be solved by the separation of variables method or applying advanced mathematical or numerical methods. However they are often treated using the lumped parameters method.

This simplified approach assumes that the temperature of a solid varies with time but remains uniform throughout the system at any time. As suggested in [43], this assumption provides great simplification in certain classes of heat transfer problems without much sacrifice in terms of accuracy.

The temperature distribution with respect to the time can be find performing an energy balance of the solid for the time interval dt . Consider a body of arbitrary shape of mass m , volume V , surface area A_s , density ρ , and specific heat c_p initially at a uniform temperature T_i . At time $t = 0$, the body is placed into a medium at temperature T_{∞} , and heat transfer takes place between the body and the medium with a heat transfer coefficient h , as shown in Figure 3.5.

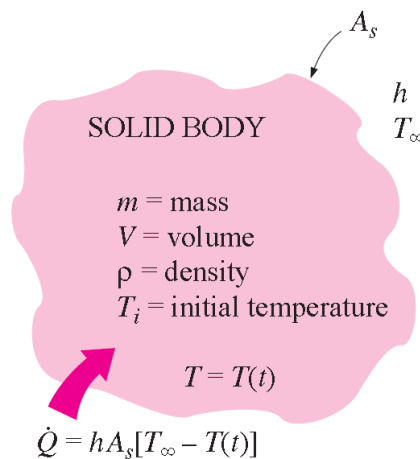


Figure 3.5. Geometry and parameters involved in the lumped parameters analysis, from [43].

The heat transferred to the body during dt equals the increasing in the energy of the body during the same time step.

$$hA(T_{\infty} - T)dt = mc_p dT \quad (3.17)$$

Considering $dT=d(T-T_{\infty})$ since $T_{\infty} = \text{constant}$, Equation (3.17) can be expressed as:

$$\frac{d(T-T_{\infty})}{T-T_{\infty}} = -\frac{hA}{\rho V c_p} dt \quad (3.18)$$

Equation (3.18) can be easily integrated to obtain the solution to the problem:

$$\frac{T(t)-T_{\infty}}{T(t=0)-T_{\infty}} = e^{-bt} \quad \text{where } b = \frac{hA}{\rho V c_p} \quad (3.19)$$

The lumped system analysis certainly provides great convenience in heat transfer analysis, but one must wonder when it is appropriate to use it.

The criterion used to establish whether the lumped parameters approach is applicable or not consists on the relative comparison of the conduction resistance within the body and the convection resistance at the surface of the body.

$$Bi = \frac{\text{Conduction resistance within the body}}{\text{Convection resistance at the surface}} = \frac{L_c/k}{1/h} = \frac{h L_c}{k} \quad (3.20)$$

The dimensionless **Biot** number is the ratio of the internal resistance of a body to heat conduction to its external resistance to heat convection [44].

Therefore, a small Biot number represents small resistance to heat conduction, and thus small temperature gradients within the body.

Lumped system analysis assumes a uniform temperature distribution throughout the body, which will be the case only when the thermal resistance of the body to heat conduction is zero. Thus, lumped system analysis would be exact in the limit case of $Bi = 0$ and approximate or fairly inaccurate when $Bi > 0$.

It is generally accepted that lumped system analysis is applicable when $Bi < 0.1$ [44].

In a typical case of a Li-Ion battery, nevertheless, the Biot number results to be much larger than 0.1 (typical values are between 0.2 and 1.0) and thus the lumped parameters approach is definitely inaccurate.

To complete the review of the basic equations, the heat transfer from **extended surfaces** has to be analyzed. Consider the case of a solid that experiences energy transfer by conduction within its boundaries, as well as convection (or radiation) between its boundaries and the surroundings.

The convective removal of heat from a surface can be substantially improved putting some extensions on that surface, in order to increase its area. Such an extended surface is termed a *fin*.

These extensions can take a variety of forms and configurations, as shown in Figure 3.6 and Figure 3.7.

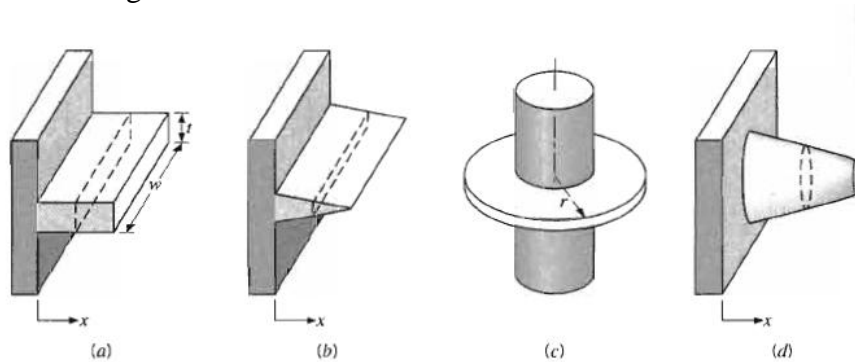


Figure 3.6. Fin configurations. (a) Straight fin of uniform cross section. (b) Straight fin of non-uniform cross section. (c) Annular fin. (d) Pin fin, [44].

A straight fin is any extended surface that is attached to a plane wall. It may be of uniform sectional area or its cross-sectional area may vary with the distance x from the wall. An annular fin is circumferentially attached to a cylinder, and its cross section varies with radius from the centerline of the cylinder.

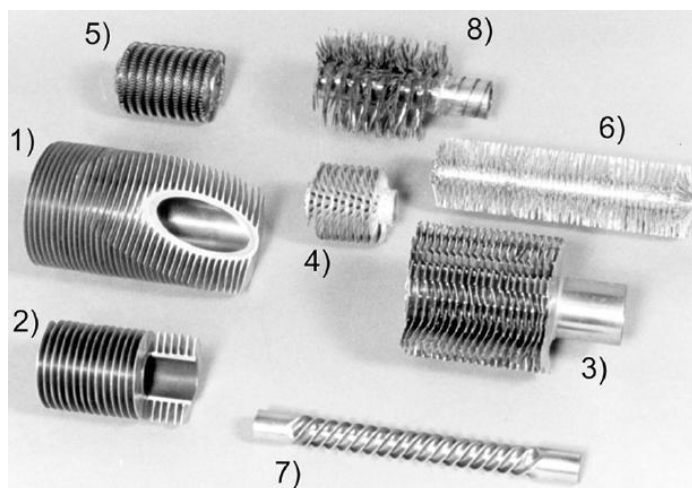


Figure 3.7. Examples of externally finned tubing, [47]: 1) and 2) are typical commercial circular fins of constant thickness; 3) and 4) serrated circular fins and dimpled spirally-wound circular fins, both intended to improve convection; 5) spirally-wound copper coils outside and inside; 6) and 8) bristle fins, spirally-wound and machined from base metal; 7) a spirally indented tube to improve convection and increase surface area

In the analysis of fins, steady-state operation with no heat generation in the fin is considered, and the thermal conductivity k of the material is assumed to remain constant. The convection heat transfer coefficient h is also considered to be constant and uniform over the entire surface of the fin for convenience in the analysis.

Considering a volume element of a fin, at location x , having a length of Δx , cross-sectional area of A_c , and perimeter p , as shown in Figure 3.8, it is possible to write an energy balance:

$$\dot{Q}_{cond,x} = \dot{Q}_{cond,x+\Delta x} + \dot{Q}_{conv} \quad [\text{W}] \quad (3.21)$$

where

$$\dot{Q}_{conv} = h(p \Delta x)(T - T_\infty) \quad [\text{W}] \quad (3.22)$$

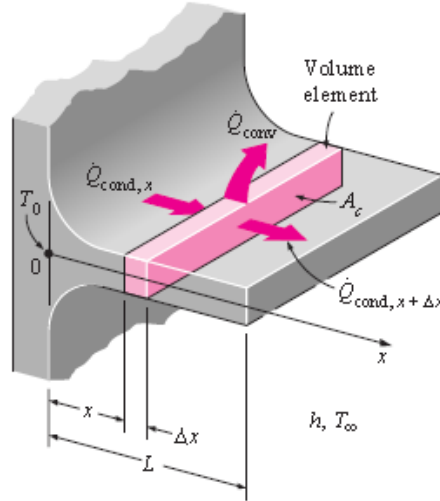


Figure 3.8. Volume element of a fin, [43].

Substituting Equation (3.22) into (3.21), dividing by Δx and taking the limit as $\Delta x \rightarrow 0$:

$$\frac{d\dot{Q}_{cond}}{dx} + h dA_c (T - T_\infty) = 0 \quad (3.23)$$

Fourier's law of heat conduction states that:

$$\dot{Q}_{cond} = -k A_c \frac{dT}{dx} \quad (3.24)$$

It is possible to express the differential equation governing heat transfer in fins as:

$$\frac{d^2 T}{dx^2} + \left(\frac{1}{A_c} \frac{dA_c}{dx} \right) - \left(\frac{1}{A_c} \frac{h dA_c}{k dx} \right) (T - T_\infty) = 0 \quad (3.25)$$

In the case of constant cross-sectional area, constant thermal conductivity and defining the excess temperature θ to be: $\theta(x) = T(x) - T_\infty$ the solution of Equation (3.25) is:

$$\frac{d^2\theta}{dx^2} - m^2\theta = 0 \quad \text{where} \quad m^2 \equiv \frac{hp}{kA_c} \quad (3.26)$$

Equation (3.26) is a linear, homogeneous, second-order differential equation with constant coefficients. The fundamental theory of differential equations states that such an equation has two linearly independent solution functions, and its general solution is the linear combination of those two solution functions.

$$\theta(x) = C_1 e^{mx} + C_2 e^{-mx} \quad (3.27)$$

where C_1 and C_2 are arbitrary constants whose values are to be determined from the boundary conditions at the base and at the tip of the fin.

The temperature of the plate to which the fins are attached is normally known in advance and considered to be kept constant. Therefore, at the fin base a specified temperature boundary condition is considered, expressed as:

$$\theta(0) = \theta_b = T_b - T_\infty$$

As regard the fin tip various boundary conditions are possible, including specified temperature, negligible heat loss (idealized as an insulated tip), convection, and combined convection and radiation, as shown in Table 3.1.

Table 3.1. Summary of temperature distribution and heat loss for fins of uniform cross section, [44].

Case	Tip Condition ($x = L$)	Temperature Distribution θ/θ_b	Fin Heat Transfer Rate q_f
A	Convection heat transfer: $h\theta(L) = -kd\theta/dx _{x=L}$	$\frac{\cosh m(L-x) + (h/mk) \sinh m(L-x)}{\cosh mL + (h/mk) \sinh mL}$	$M \frac{\sinh mL + (h/mk) \cosh mL}{\cosh mL + (h/mk) \sinh mL}$
B	Adiabatic $d\theta/dx _{x=L} = 0$	$\frac{\cosh m(L-x)}{\cosh mL}$	$M \tanh mL$
C	Prescribed temperature: $\theta(L) = \theta_L$	$\frac{(\theta_L/\theta_b) \sinh mx + \sinh m(L-x)}{\sinh mL}$	$M \frac{(\cosh mL - \theta_L/\theta_b)}{\sinh mL}$
D	Infinite fin ($L \rightarrow \infty$): $\theta(L) = 0$	e^{-mx}	M

$\theta \equiv T - T_\infty$ $m^2 \equiv hp/kA_c$
 $\theta_b = \theta(0) = T_b - T_\infty$ $M \equiv \sqrt{hPkA_c} \theta_b$

Although the heat diffusion problem (Equation (3.12)) can be solved in a large number of practical cases by means of suitable approximation, a general

solution for the transient one-dimensional boundary-value problem of heat conduction in a finite region with heat generation within the solid and with non-homogeneous boundary conditions is hard to obtain.

For this kind of problem, it is not possible to find a simple solution and so a more complex mathematical analysis has to be performed.

To solve non-homogeneous boundaries problems it is common to use a Laplace transform to remove time variable from the partial differential equation.

However, in many problems it is more convenient to apply an integral transformation that removes the space variable from the partial differential equation.

According to [11], the integral transform technique is especially attractive for transient and steady-state heat conduction problems in which it treats all space variables in the same manner and has no inversion difficulties as in the case of Laplace transformation. This is due to the fact that both the integral transform and the inversion formula are defined at the onset of the problem.

For a given problem, however, the type of integral transform and the corresponding inversion formula depend on the range of the space variables (finite, semi-infinite or infinite extend) and on the type of the boundary conditions.

The integral transform technique is used in this work to solve the conduction problem. The complete solution will be shown in a few pages when the development of the detailed thermal model will be presented (Section 4.2.1).

3.2 Assumptions for battery thermal modeling

In this section, the mathematical assumptions and simplification adopted to write the equations of the battery cell models developed in Chapter 4 will be discussed, starting from the basic, general, equations presented above.

First of all, as in major heat transfer problem, common assumptions about the different materials that compose the battery are made:

- The cell materials are considered to be homogeneous and without bulk motion;
- The cells are considered to be isotropic, so that all the properties don't depend on the direction;
- The thermal conductivity, k , and the other thermo-physical properties are assumed to be constant.

Moreover some simplifying assumptions are used when approaching the heat transfer problem:

- The radiation heat transfer is neglected, since the temperatures and their differences are not in this kind of heat transmission interest;
- Perfect contact at the interface of two surface and thus no concentrated temperature drop (negligible contact resistance);
- The heat generated within the battery to be homogeneously distributed within the cell volume;
- All the flows are considered to present uniform velocity distribution;
- The pressure drop across the channels is negligible.

3.2.1 Mathematical formulation of the simplified system

From a mathematical standpoint, the problem can be cast into a non-homogeneous boundary-value problem (BVP). For the case of one-dimensional, unsteady heat conduction it is represented by the heat diffusion equation mentioned above (Equation (3.12)):

$$\frac{\partial^2 T}{\partial x^2} + \frac{\bar{q}(x, t)}{k} = \frac{1}{\alpha} \frac{\partial T}{\partial t}$$

To solve this equation two boundary conditions and one initial condition must be chosen. In general, there are three kinds of different boundary conditions:

- Specified temperature of an exposed surface (e.g. $T(x=x_0, t)=const$);
- Specified heat flux from or to an exposed surface (e.g. $\dot{q} = -k \frac{\partial T(x=x_0, t)}{\partial x} = const$).
Note that insulation and symmetry are particular cases of this kind of boundary condition ($\dot{q} = -k \frac{\partial T(x=x_0, t)}{\partial x} = 0$);
- Convection or radiation (e.g. $-k \frac{\partial T(x=x_0, t)}{\partial x} = h_{conv} (T(x = x_0, t) - T_\infty)$
or $-k \frac{\partial T(x=x_0, t)}{\partial x} = \varepsilon \sigma (T^4(x = x_0, t) - T_{surr}^4)$).

The initial condition is relative to the temperature at which the medium is at a specific instant of time, $t=0$ when the analysis of the problem starts.

3.3 Summary

In this chapter the approach to model the thermal dynamics of a Li-Ion battery has been presented and an overview of the basic physical principles needed to implement such a model has been given.

The basic principles and physical laws of the energy conservation analysis, fluid flows and heat transfer have been discussed in detail. The principles described here will be instrumental to solve the problem under study. For any further detail, it is possible to consult the wide literature available for such topics (for example [43]-[48]).

In Chapter 4 this approach will be used to implement a Li-Ion thermal modeling methodology.

CHAPTER 4

4. Development of the thermal modeling approach

In this chapter, the development of a general modeling methodology to characterize the thermal behavior of a Li-Ion battery cell will be described. The purpose of this work is to obtain a family of models that can predict the temperature distribution within a battery cell under varying operating conditions.

The models must be sufficiently simple to be implemented nearly in real-time, yet accurate enough to provide a reasonable estimate of the dynamic of the temperature distribution inside the cell. Possible applications can be in the design and simulation of thermal management systems for battery packs.

In the previous chapter, a review of the mathematical equations on which the solution relies has been presented, and then assumptions made to simplify the mathematical formulation have been shown.

This chapter presents the approach followed to implement a general thermal model, together with a detailed description of the model assumptions and the mathematical framework. Then different models will be developed to represent different cooling systems, in particular first an air cooled battery cell will be described and then a cooling bar system will be modeled.

4.1 Introduction and scope of the work

The purpose of this work is to implement a family of simplified thermal models of a prismatic Li-Ion battery cell that approximate the temperature distribution in presence of uniform internal heat generation and under different boundary and initial conditions.

These models predict the temperature distribution inside the battery cell with respect to both time and space, thus providing a real-time thermal characterization of a Li-Ion cell.

The intent of these models is to serve applications in the areas of performance and thermal management studies for battery pack cooling systems.

Due to their high specific energy and power, Li-Ion batteries have recently been considered the technology of choice for application in the automotive field, such as energy storage system for BEV/PHEV/HEV.

In particular, prismatic Li-Ion batteries with a pouch-style shape are today largely used due to advantages in packaging and cooling. Figure 4.1 shows an example of prismatic pouch-style battery cell.



Figure 4.1. Examples of pouch-style battery cells available on the market.

Figure 4.2 shows the reference geometry for a typical pouch-style prismatic battery cell. Note that, for this system, the dimensions in the length and width directions (y and z) are much larger than in the thickness direction (x).

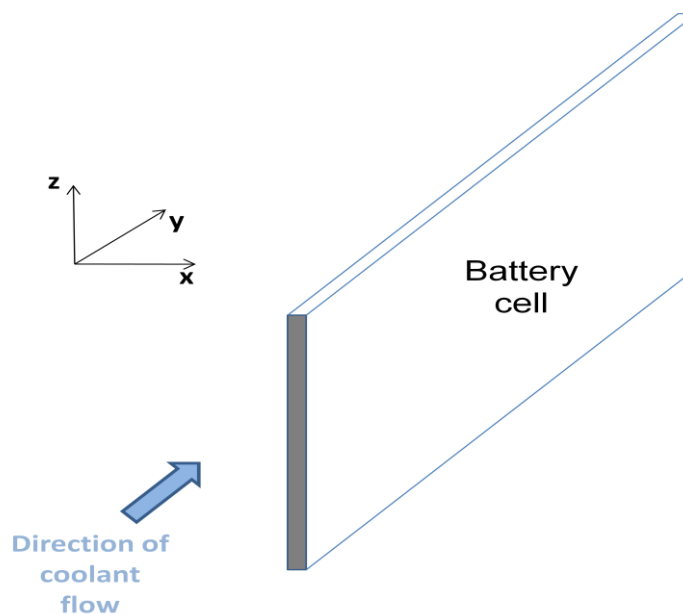


Figure 4.2. Pouch-style battery cell sketch and coordinate system.

For the system shown in Figure 4.2, the heat diffusion equation can be applied in Cartesian coordinates:

$$\frac{\partial}{\partial x} \left(k_x \frac{\partial T}{\partial x} \right) + \frac{\partial}{\partial y} \left(k_y \frac{\partial T}{\partial y} \right) + \frac{\partial}{\partial z} \left(k_z \frac{\partial T}{\partial z} \right) + \bar{q} = \rho c_p \frac{\partial T}{\partial t} \quad (4.1)$$

Such three dimensional equation is generally complex to solve, unless numerical approximations are introduced. In case of pouch-style cell, such as the system shown in Figure 4.2, it is possible to operate a simplification of Equation (4.4.1) into a 1-D problem. This assumption can be verified by a simple order of magnitude analysis. As suggested in [46], Equation (4.4.1) can be non-dimensionalized by defining the following variables:

$$\begin{aligned} x^* &= \frac{x}{L_c}; & y^* &= \frac{y}{L_c}; & z^* &= \frac{z}{L_c} \\ \tau &= \frac{t}{T}; & T^* &= \frac{T - T_\infty}{T_0 - T_\infty} \end{aligned} \quad (4.2)$$

Equation (4.4.1) becomes then:

$$\frac{\partial}{\partial x^*} \left(k_x \frac{\partial T^*}{\partial x^*} \right) + \frac{\partial}{\partial y^*} \left(k_y \frac{\partial T^*}{\partial y^*} \right) + \frac{\partial}{\partial z^*} \left(k_z \frac{\partial T^*}{\partial z^*} \right) + \bar{q} = \rho c_p \frac{\partial T^*}{\partial \tau} \quad (4.3)$$

For a pouch-style battery cell, the order of magnitude of the length in x direction is typically 10^{-1} mm. Instead, the dimensions in y and z directions are two orders of magnitude larger than that (as in Figure 4.2).

$$x^* \ll y^* \quad \text{and} \quad x^* \ll z^* \quad (4.4)$$

On the other hand, Li-Ion battery cells present anisotropic thermal conductivity. It can be inferred from literature data (see i.e. [39] or [49]) that $k_y = k_z \sim 100 k_x$. Therefore, the second and third term of Equation (4.3) are of the same order of magnitude but the temperature gradient with respect to x -direction results to be larger, considering that x^* appears in the denominator elevated to the second power.

$$\frac{\partial}{\partial x^*} \left(k_x \frac{\partial T^*}{\partial x^*} \right) \gg \frac{\partial}{\partial y^*} \left(k_y \frac{\partial T^*}{\partial y^*} \right) \quad \text{and} \quad \frac{\partial}{\partial x^*} \left(k_x \frac{\partial T^*}{\partial x^*} \right) \gg \frac{\partial}{\partial z^*} \left(k_z \frac{\partial T^*}{\partial z^*} \right) \quad (4.5)$$

Hence, for a pouch-style Li-Ion battery cell, the heat diffusion can be approximated as a one-dimensional problem in the x -direction, and the heat flux along y and z can be neglected for engineering purpose.

By consequence, a 1D approach has been chosen in this work to solve the heat transfer problem and determine the dynamic temperature distribution inside a Li-Ion battery cell.

In order to characterize the effects of different cooling systems on the temperature distribution within the cell, the one-dimensional solution is then extended to a 1+1D model that accounts for the variability of the boundary

conditions. This allows one to characterize the temperature dynamics when the cell is cooled by an external source, as explained in Section 4.2.3.

4.2 Development of thermal model structure

Starting from the basic principles outlined in Section 3.1, a modeling approach to characterize the temperature dynamics of a prismatic Li-Ion battery cell is here developed.

First a general one-dimensional model is presented to predict the temperature field in a prismatic medium in presence of uniform internal heat generation and under different conditions (various initial and boundary conditions).

Then, a model with convective boundary conditions will be presented. This 1D model is able to characterize the temperature distribution in the x direction, assuming uniform coolant temperature. However, as the air flows in the channel, its temperature increases, hence decreasing its ability to extract heat from the cell.

The one-dimensional model is then extended to a 1+1D model that accounts for the variability of the boundary conditions in the air flow direction (y).

Finally, a model with imposed temperature boundary conditions will be presented and then extended to a 1+1D model to simulate the behavior of a battery pack including cooling bars.

The extension to the 1+1D approach allows for comparing the effects of different cooling systems. The simple structure and the computational efficiency make the model an ideal candidate for design of thermal management systems and real-time simulations.

4.2.1 General mathematical formulation of 1-D temperature distribution in a prismatic finite medium

This sub-section describes the development of a general modeling approach that, relying on the transformation method, predicts the temperature distribution within a battery cell under different conditions.

As stated above, the starting point is the unsteady heat diffusion equation for 1D conduction problem in x direction:

$$\frac{\partial^2 T}{\partial x^2} + \frac{\bar{q}(x,t)}{k} = \frac{1}{\alpha} \frac{\partial T}{\partial t} \quad (4.6)$$

Figure 4.3 shows a sketch of a prismatic battery cell in presence of internal heat generation and subjected to general boundary conditions.

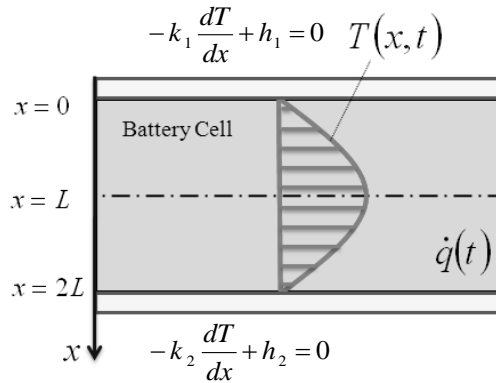


Figure 4.3. Sketch of a battery cell subjected to general boundary conditions,[50].

To solve the problem two boundary conditions and an initial condition have to be imposed.

$$\begin{cases} T = T_0 & \text{at } 0 \leq x \leq 2L, t = 0 \\ -k_x \frac{\partial T}{\partial x} + h_2 = 0 & \text{at } x = 2L, t > 0 \\ -k_x \frac{\partial T}{\partial x} + h_1 = 0 & \text{at } x = 0, t > 0 \end{cases} \quad (4.7)$$

Although analytical solutions have been developed for particularly simple cases (see 3.1.3), to solve the most general case (transient boundary-value problem in a finite region in presence of heat generation and with non-homogeneous boundary conditions), numerical techniques are normally used.

However, it is possible to find an analytical solution for the general problem that does not require iterations/discretizations by applying the integral transformation method, as proposed i.e. in [11] or [51].

The integral transforms for use in the Cartesian coordinate system are usually called Fourier transforms because they are derived from Fourier series expansion of an arbitrary function in a given interval. This solution method was largely used in the 60's -70's when the numerical methods and the computational power were not as developed as nowadays.

The method is essentially a projection technique where the problem is solved using a functional space. In this auxiliary space, the space variable is removed from the partial differential equation (PDE). To understand the concept beyond this method, one should think about the Laplace transform.

The Laplace transform is commonly used in engineering for solving differential and integral equations. Many examples of application can be found, for example solution of electrical circuits or mechanical systems. In these analyses, the Laplace transform is often interpreted as a transformation from the *time-domain*, in which inputs and outputs are functions of time, to the *frequency-domain*, where the same inputs and outputs are functions of complex angular frequency,

in radians per unit time. Given a simple mathematical or functional description of an input or output to a system, the Laplace transform provides an alternative functional description that often simplifies the process of analyzing the behavior of the system.

In solving the transient heat-conduction problem, it is common to use a Laplace transform to remove time variable from the partial differential equation, as show for example in [52] or [53].

However, in some heat transfer problems, it is more convenient to apply an integral transformation that removes the space variable from the equation. Using such methodology it is possible to avoid the inversion difficulties that the Laplace transform presents in cases where complex geometries or boundary conditions are present.

The Fourier integral transform method allows solving the PDE applying the following procedure:

- Transform the problem, projecting it to the functional space;
- Solve the equation in the functional space;
- Inverse-transform to obtain the dimensional solution to the problem.

The general formulation of the Fourier transform, and the corresponding inversion formula, for a function $F(x)$ in the finite interval $0 \leq x \leq 2L$ look like:

$$(Integral\ transform): \bar{F}(\beta_m) = \int_{x=0}^{2L} K(\beta_m, x) \cdot F(x) dx \quad (4.8)$$

$$(Inversion\ formula): F(x) = \sum_{m=1}^{\infty} K(\beta_m, x) \cdot \bar{F}(\beta_m) \quad (4.9)$$

where the transform operator K depends on the boundary conditions.

With reference to the heat transfer problem shown in Figure 4.3, the terms that must be transformed are the initial temperature T_0 and the heat generation rate per unit volume \bar{q} :

$$\bar{F}(\beta_m) = \bar{T}_0(\beta_m) = \int_{x'=0}^L K(\beta_m, x') \cdot T_0(x') dx' \quad (4.10)$$

$$\tilde{q} = \int_{x'=0}^L K(\beta_m, x') \cdot \bar{q}(x', t) dx' \quad (4.11)$$

The terms K that compare in the transform functions are called *Kernel* and are the transformation operators that allow for passing from the dimensional space into the functional space.

The inversion formulas are obtained from the expansion of the homogeneous associated system in an infinite series of the normalized eigenfunctions of the eigenvalue problem:

$$\begin{cases} \frac{d^2X}{dx^2} + \beta X = 0 & \text{in } 0 \leq x \leq 2L \\ \frac{dX}{dx} = 0 & \text{at } x = 0 \\ X = 0 & \text{at } X = 2L \end{cases} \quad (4.12)$$

As mentioned above, these terms depend on the boundary conditions other than on the range of the space variables. In the Table 4.1, it is possible to find analytical expressions of the Kernel for different boundary conditions in the case of a finite solid, [11].

In this formulation the boundary conditions are expressed by the term $H = \frac{h_{conv}}{k_{cond}}$, where H_1 refers to the boundary condition at $x=0$ and H_2 to the one at the other surface of the solid.

Table 4.1. Kernel for different boundary conditions, [11].

Boundary condition at $x=0$	Boundary condition at $x=2L$	KERNEL(β_m, x)
3 rd kind $H_1 = \text{finite}$	3 rd kind $H_2 = \text{finite}$	$\sqrt{2} \frac{\beta_m \cos(\beta_m x) + H_1 \sin(\beta_m x)}{\left[(\beta_m^2 + H_1^2) \left(2L + \frac{H_2}{\beta_m^2 + H_1^2} + H_1 \right) \right]^{1/2}}$
3 rd kind $H_1 = \text{finite}$	2 nd kind $H_2 = 0 (h_2=0)$	$\sqrt{2} \left[\frac{\beta_m^2 + H_1^2}{2L(\beta_m^2 + H_1^2) + H_1} \right]^{1/2} \cos(\beta_m (2L - x))$
3 rd kind $H_1 = \text{finite}$	1 st kind $H_2 = \infty (k_2=0)$	$\sqrt{2} \left[\frac{\beta_m^2 + H_1^2}{2L(\beta_m^2 + H_1^2) + H_1} \right]^{1/2} \sin(\beta_m (2L - x))$
2 nd kind $H_1 = 0 (h_1=0)$	3 rd kind $H_2 = \text{finite}$	$\sqrt{2} \left[\frac{\beta_m^2 + H_2^2}{2L(\beta_m^2 + H_2^2) + H_2} \right]^{1/2} \cos(\beta_m x)$
2 nd kind $H_1 = 0 (h_1=0)$	2 nd kind $H_2 = 0 (h_2=0)$	$\sqrt{\frac{2}{2L}} \cos(\beta_m x)$
2 nd kind $H_1 = 0 (h_1=0)$	1 st kind $H_2 = \infty (k_2=0)$	$\sqrt{\frac{2}{2L}} \cos(\beta_m x)$

1 st kind $H_1 = \infty (k_1=0)$	3 rd kind $H_2 = \text{finite}$	$\sqrt{2} \left[\frac{\beta_m^2 + H_2^2}{2L(\beta_m^2 + H_2^2) + H_2} \right]^{1/2} \sin(\beta_m x)$
1 st kind $H_1 = \infty (k_1=0)$	2 nd kind $H_2 = 0 (h_2=0)$	$\sqrt{\frac{2}{2L}} \sin(\beta_m x)$
1 st kind $H_1 = \infty (k_1=0)$	1 st kind $H_2 = \infty (k_2=0)$	$\sqrt{\frac{2}{2L}} \sin(\beta_m x)$

The terms β are the positive roots of a transcendental function that varies for different boundary conditions, as shown in Table 4.2:

Table 4.2. Transcendental functions for the terms β , [11].

Boundary condition at $x=0$	Boundary condition at $x=2L$	Eigenvalues β_m (positive roots of):
3 rd kind $H_1 = \text{finite}$	3 rd kind $H_2 = \text{finite}$	$\tan(\beta 2L) = \frac{\beta(H_1 + H_2)}{\beta^2 - H_1 H_2}$
3 rd kind $H_1 = \text{finite}$	2 nd kind $H_2 = 0 (h_2=0)$	$\beta \tan(\beta 2L) = H_1$
3 rd kind $H_1 = \text{finite}$	1 st kind $H_2 = \infty (k_2=0)$	$\beta \cot(\beta 2L) = -H_1$
2 nd kind $H_1 = 0 (h_1=0)$	3 rd kind $H_2 = \text{finite}$	$\beta \tan(\beta 2L) = H_2$
2 nd kind $H_1 = 0 (h_1=0)$	2 nd kind $H_2 = 0 (h_2=0)$	$\sin(\beta 2L) = 0$
2 nd kind $H_1 = 0 (h_1=0)$	1 st kind $H_2 = \infty (k_2=0)$	$\cos(\beta 2L) = 0$
1 st kind $H_1 = \infty (k_1=0)$	3 rd kind $H_2 = \text{finite}$	$\beta \cot(\beta 2L) = -H_2$
1 st kind $H_1 = \infty (k_1=0)$	2 nd kind $H_2 = 0 (h_2=0)$	$\cos(\beta 2L) = 0$
1 st kind $H_1 = \infty (k_1=0)$	1 st kind $H_2 = \infty (k_2=0)$	$\sin(\beta 2L) = 0$

Applying the transform method, Equation (4.4.8) and Equation (4.4.9), to the heat diffusion equation (Equation (4.6)), the analytical solution results:

$$T(x, t) = \sum_{m=1}^{\infty} e^{-\alpha\beta^2 t} K(\beta_m, x) \cdot \left[\bar{F}(\beta_m) + \int_{t=0}^t e^{\alpha\beta^2 t} A(\beta_m, t) dt \right] \quad (4.13)$$

$$A(\beta_m, t) = \frac{\alpha}{k} \tilde{q}(\beta_m, x) + \alpha \left(\frac{K(\beta_m, x=0)}{k} f_1(t) + \frac{K(\beta_m, x=L)}{k} f_2(t) \right)$$

where $\bar{F}(\beta_m)$ is the transformed initial condition, $\tilde{q}(\beta_m, x)$ the transformed heat generation rate and f_1 and f_2 represent the boundary condition of the problem:

$$f_1(t) = -k_1 \frac{\partial T}{\partial x} + h_1 T = h_1 T_{\infty} \quad (4.14)$$

$$f_2(t) = -k_2 \frac{\partial T}{\partial x} + h_2 T = h_2 T_{\infty} \quad (4.15)$$

Due to the symmetry of the problem considered:

$$H_1 = H_2 = \frac{k}{h} \left[\frac{1}{l_m} \right] \quad (4.16)$$

Equation (4.4.13) can be expanded and divided into two parts:

Part 1: (4.17)

$$T(x, t) = \sum_{m=1}^{\infty} e^{-\alpha\beta^2 t} K(\beta_m, x) \bar{F}(\beta_m)$$

Part 2: (4.18)

$$T(x, t) = \sum_{m=1}^{\infty} e^{-\alpha\beta^2 t} \left[\int_{t=0}^t e^{\alpha\beta^2 t} \left(\frac{\alpha}{k} \tilde{q}(\beta_m, x) + \alpha \left(\frac{K(\beta_m, x=0)}{k} f_1 + \frac{K(\beta_m, x=L)}{k} f_2 \right) dt \right) \right]$$

The total solution will result by summing the two parts.

It is possible to note the presence of exponential terms whose argument depending on t and β^2 in both Equation (4.4.17) and Equation (4.4.18). Depending on the algorithm used for solving such equations, the above terms might lead to indetermination.

For part 1, it is clear that, being K and \bar{F} bounded, $\lim_{t \rightarrow \infty} T(x, t)$ converges. As for part 2, it can be noticed the presence of the term: $\sum_{m=1}^{\infty} e^{-\alpha\beta^2 t} \int_{t=0}^t e^{\alpha\beta^2 t}$ which leads to indetermination for large values of t , and thus there is the need to further elaborate as follows. Noting that at any instant t_i :

$$e^{-\alpha\beta^2 t} \left(\int_0^t e^{\alpha\beta^2 t} F(t) dt \right) = e^{-\alpha\beta^2 t} \left(\int_0^{t_{i-1}} e^{\alpha\beta^2 t} F(t) dt \right) + e^{-\alpha\beta^2 t} \left(\int_{t_{i-1}}^{t_i} e^{\alpha\beta^2 t} F(t) dt \right) \quad (4.19)$$

Considering the trapezoidal rule to approximate the integral calculation:

$$\int_a^b F(t) dt \cong \frac{\Delta t}{2} [F(a) + F(b)] \quad (4.20)$$

It is possible to write the second term of the right-hand side of Equation (4.4.19) as:

$$e^{-\alpha\beta^2 t} \left(\int_{t_{i-1}}^{t_i} e^{\alpha\beta^2 t} F(t) dt \right) \cong \frac{\Delta t}{2} e^{-\alpha\beta^2 t_i} [e^{\alpha\beta^2 t_{i-1}} F(t_{i-1}) + e^{\alpha\beta^2 t_i} F(t_i)] = \frac{\Delta t}{2} [e^{\alpha\beta^2 \Delta t} F(t_{i-1}) + F(t_i)] \quad (4.21)$$

This procedure allows one to avoid the indetermination issue and, ultimately, any computational problem. The model can be then implemented as a Matlab[®] function, whose input/output block diagram is shown in Figure 4.4.

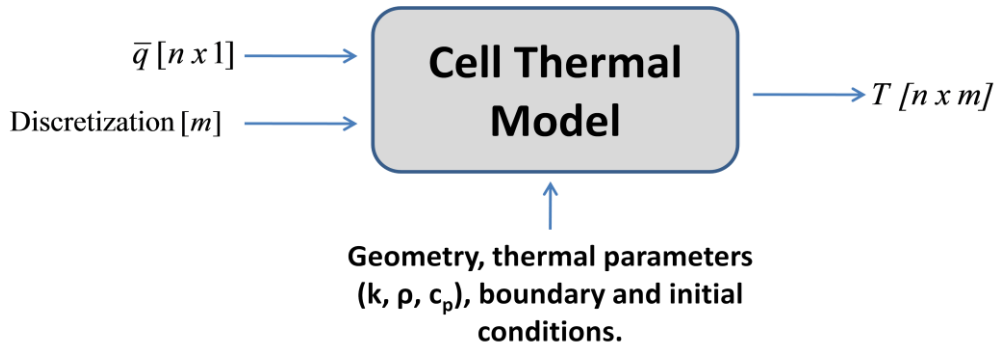


Figure 4.4. General thermal model input / output diagram.

The output of the model, T , is the temperature distribution in the space (x -direction) and time (a matrix which dimensions are the length of the heat generation profile and the discretization grid in which the x direction has been divided). The thermal parameters needed to solve the problem are the overall thermal conductivity k of the cell, the average cell heat capacity c_p , and the average cell density ρ . In case of convective boundary conditions the value of the convective heat transfer coefficient h must be provided as input to the model.

The model parameters can be determined from experimental studies or from results published in the open literature (i.e., [8], [10] and [39]). Table 4.3 reports the values initially adopted for this study.

Table 4.3. Typical values of thermal parameters for Li-Ion batteries.

Thermal parameter	Typical Range	Value
k [W/mK]	0.40 – 0.85	0.66
c_p [J/kgK]	650 - 950	795
ρ [kg/m ³]	1700 - 2500	2100

4.2.2 Formulation of model with convective boundary conditions

Since most battery modules are cooled by forced convection, it is useful to apply the modeling methodology developed to characterize this problem. The geometry shown in Figure 4.5 is representative of a portion of a battery module. Such system will be described in detail in Section 5.1.1. The air flow is supposed to approach the battery cell at ambient temperature (25°C) and cool it with a certain heat transfer coefficient h .

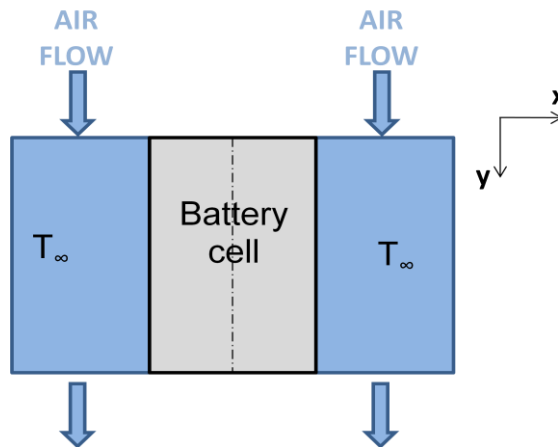


Figure 4.5. Simplified sketch of a battery cell cooled by a forced air flow.

The convective heat transfer coefficient can be computed from empirical correlations available in the open literature (i.e. [43],[44] or more specifically for laminar flows [54]). In general, the convection coefficient is expressed as a function of the Nusselt number, which represents the dimensionless temperature gradient at the surface:

$$h = \frac{Nu k_{fluid}}{L_c} \quad (4.22)$$

From experimental and numerical studies on convective heat transfer, it is possible to assume a standard representation for the Nusselt number, in the form of a power law:

$$Nu = C Re^m Pr^n \quad (4.23)$$

Mathematically, for this model the boundary and initial conditions are:

$$\begin{cases} -k \frac{\partial T}{\partial x} = h(T - T_\infty) & \text{for } x = 0, t > 0 \\ -k \frac{\partial T}{\partial x} = h(T - T_\infty) & \text{for } x = 2L, t > 0 \\ T = T_0 & \text{for } 0 \leq x \leq 2L, t = 0 \end{cases} \quad (4.24)$$

In this case, boundary conditions of the 3rd kind are applied to both the two boundaries.

As regard the air flows, analyzing the study reported in [7], it is possible to consider the two flow rates cooling the surfaces of the cell to be equivalent, using a parallel cooling case system, as shown in Figure 2.37 (see Section 2.3.3). This means that the air has the same velocity profile in the two channels. In such a case the problem becomes symmetrical and the mathematical formulation can be simplified. Since h is a function of the velocity of the air flows, the two H terms can be considered to have the same value.

The transcendental function that have to be solved to compute the terms β can be found in Table 4.2:

$$\tan(2\beta L) = \frac{\beta(H_1 + H_2)}{\beta^2 - H_1 H_2} \quad (4.25)$$

Equation (4.4.25) is plotted in Figure 4.6. It is interesting to notice that this transcendental function has a periodicity of $\frac{\pi + 2k\pi}{2L}$, where $2L$ is the battery cell thickness. This is true in the entire real positive axis except for one additional asymptote due to the rational term. Thereby there is a root of the equation that is between zero and the second root that does not present the same periodicity. It is important to remind this, when implementing the code, in order to correctly account for all of the function zeros.

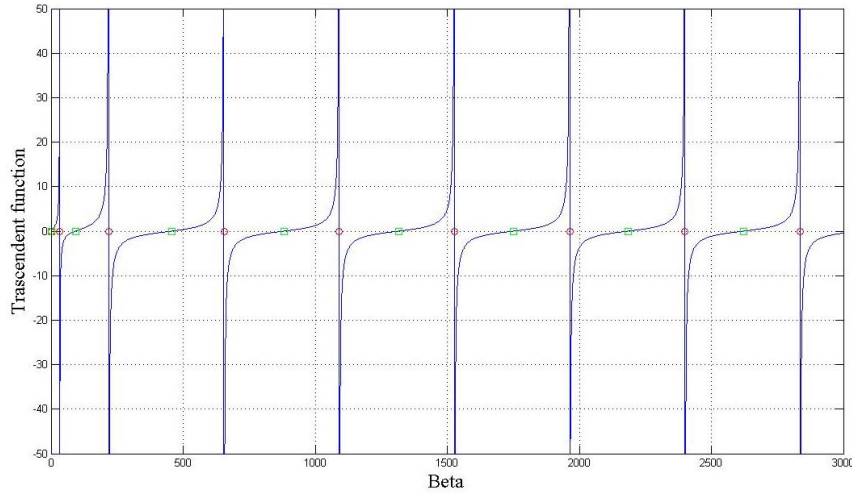


Figure 4.6. Calculation of the terms β for convective boundary condition assuming $L=0.0036$ m, $k=0.66$ W/mK and $h=20$ W/m²K.

The transcendent function written above (Equation (4.4.25)) depends on H and hence on the thermal parameters of the problem, namely the conductivity of the cell and the convective heat transfer coefficient.

As regard the convective heat transfer coefficient, it has been here supposed to be $h= 20$ [W/m²K] which is a reasonable value for forced laminar convection, e.g. [44], [45] or [54].

In Table 4.4 the value of the terms β for this case are shown.

Table 4.4. Numerical values of the eigenvalues β for convective boundary conditions, assuming $L=0.0036$ m, $k=0.66$ W/mK and $h=20$ W/m²K.

Terms	1 st	2 nd	3 rd	4 th	5 th	6 th	7 th	8 th	9 th	10 th
Beta	0	93	456	883	1315	1750	2185	2621	3057	3493

The Kernel function, as stated in Table 4.1, is:

$$K = \sqrt{2} \frac{\beta_m \cos(\beta_m x) + H_1 \sin(\beta_m x)}{\left[(\beta_m^2 + H_1^2) \left(2L + \frac{H_2}{\beta_m^2 + H_1^2} + H_1 \right) \right]^{1/2}} \quad (4.26)$$

There are an infinite numbers of kernel terms and therefore the accuracy of the solution increases if more terms are considered. However it is possible to notice that the terms after the fifth do not improve the accuracy for this specific problem, and thus they are negligible. Figure 4.7 shows the first relevant Kernel terms.

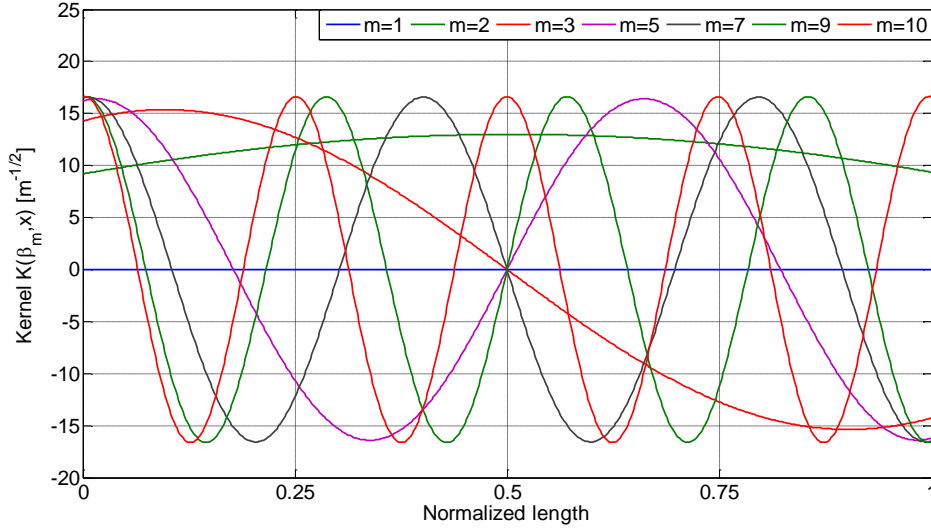


Figure 4.7. Kernel function for convective boundary conditions, computed assuming $L=0.0036$ m, $k=0.66$ W/mK and $h=20$ W/m²K.

As stated above, and depicted by the diagram in Figure 4.4, the thermal model requires a heat generation rate as an input. The heat generation rate can be computed starting from the electrical data (current, voltage and open circuit voltage) of a typical discharge cycle for electro-thermal characterization (see i.e. [16]). The internal heat generation is computed as:

$$\dot{Q} = I \left(E_0 - V - \frac{\partial E_0}{\partial T} T \right) \quad [\text{W}] \quad (4.27)$$

where, in case of Li-Ion batteries, the latter term can be neglected. This is due to the fact that the open circuit voltage, which is measured in a non-operating condition, depends only on the ions concentration. This quantity does not depend on the temperature, unless considering very high or low values that are not in the normal operating temperature range [21].

The heat generation rate used as input to the model is shown in Figure 4.8, it has been taken from a 3000 s discharge cycle used for identification of electro-thermal models (see [16]). It consists of a series of steps and short pulses that simulate the conditions to which a battery is subjected during a common driving cycle.

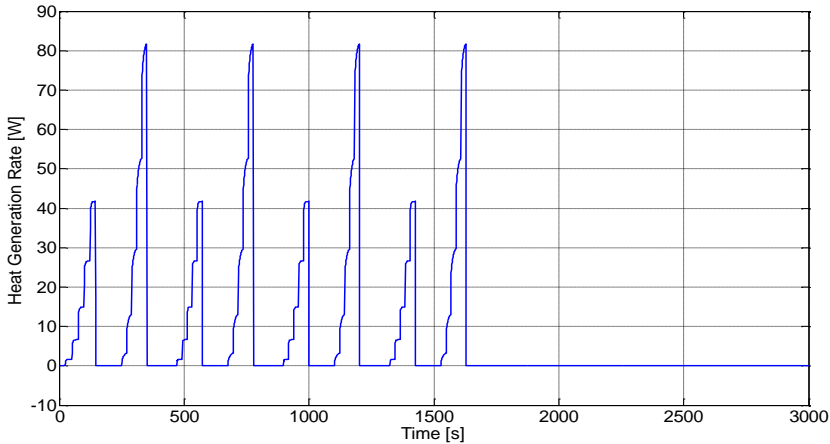


Figure 4.8. Heat generation rate profile.

In Figure 4.9 the temperature distribution inside a battery cell under these conditions is shown:

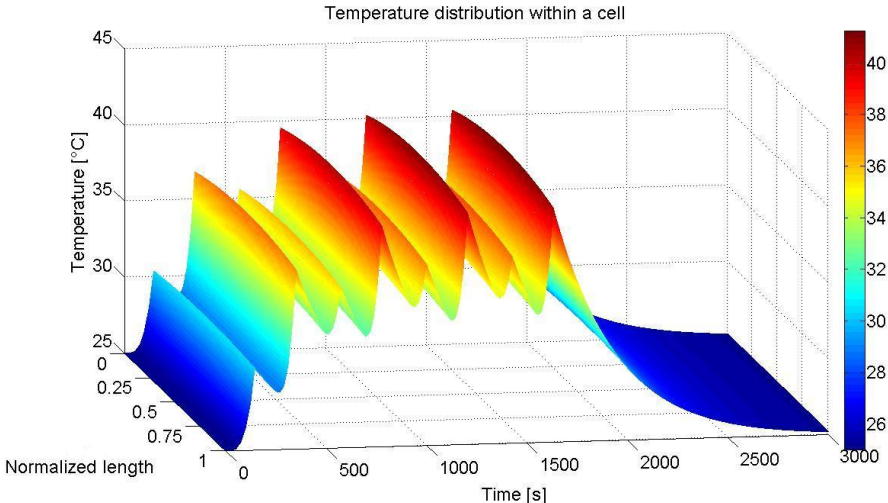


Figure 4.9. Temperature distribution within a battery cell assuming $L=0.0036$ m, $k=0.66$ W/mK and $h=20$ W/m²K.

Figure 4.10 presents the specific heat generation rate per unit volume and the comparison of the temperature at the surfaces and at the center of the cell.

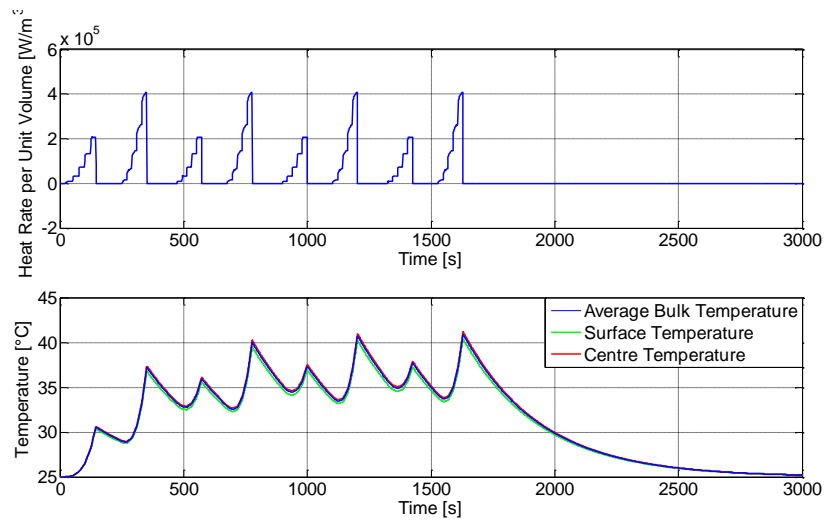


Figure 4.10. Center and surface temperature trends, assuming $L=0.0036$ m, $k=0.66$ W/mK and $h=20$ W/m²K.

From Figure 4.10 it is possible to note that the temperature distribution is pretty flat across the cell thickness (x -direction) and there are no appreciable differences between the center and the surfaces temperature. This is due to the geometry of the cell, the low heat conductivity and the low heat removal capability at the boundaries.

The previous results considered h to be 20 [W/m²K]. In the case of a typical turbulent flow, the heat transfer coefficient results to be significantly increased: $h=150$ [W/m²K]

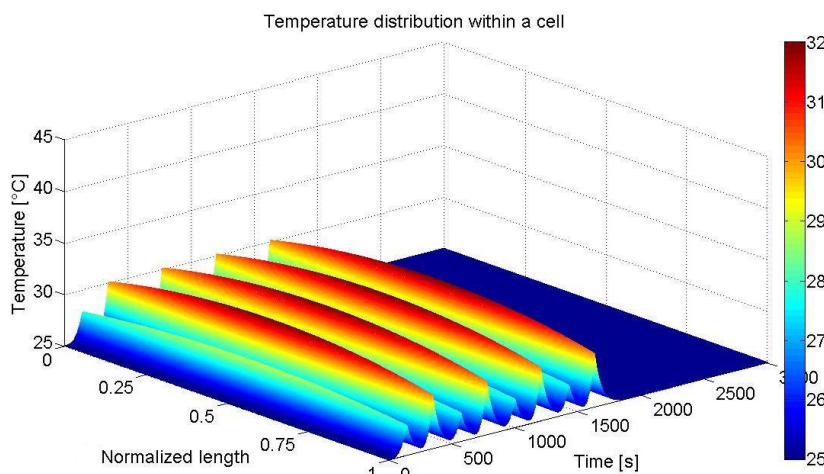


Figure 4.11. Temperature distribution within a battery cell assuming $L=0.0036$ m, $k=0.66$ W/mK and $h=150$ W/m²K.

Although the terms β and the Kernels present slight variation, the temperature profile results completely changed respect to the previous, laminar case. As expected, increasing the heat removal capability, the temperature reaches much lower values (almost 10°C less than the previous case), but the curvature of the temperature distribution results greatly increased (see Figure 4.11). The difference between the center and the surface temperature is more than three times respect to the previous case, as results comparing Figure 4.12 with Figure 4.10.

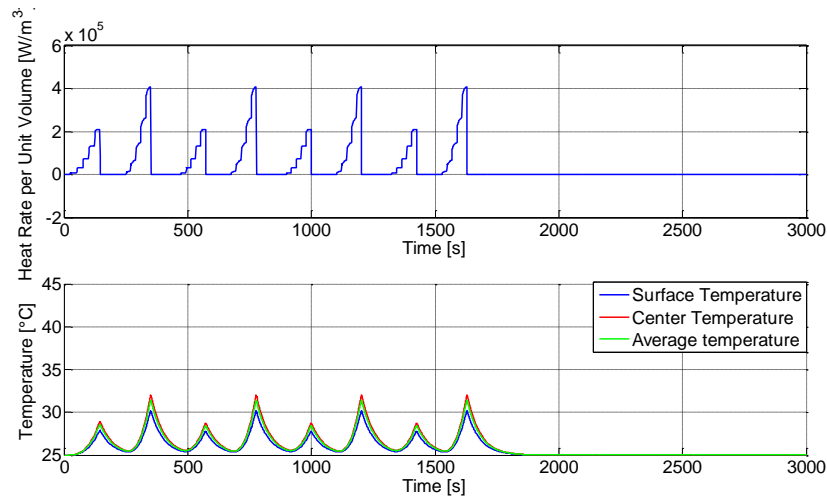


Figure 4.12. Center and surface temperature trends, assuming $L=0.0036$ m, $k=0.66$ W/mK and $h=150$ W/m²K.

Other than geometry, thermal parameters and boundary conditions, the model needs as input the initial temperature distribution.

In order to evaluate the sensitivity of the model to the initial condition, Figure 4.13 shows the result for a battery cell initially at 5°C. The ambient air temperature is still 25 °C and the cell is subjected to the heat generation rate showed in Figure 4.8.

Analyzing Figure 4.13, compared to Figure 4.9, it is possible to notice that the difference in the initial value of the cell temperature does not influence the final temperature distribution. The only difference is in the first part of the simulation, where the air warm up the battery due the temperature difference between the two media even if there is no heat generation in that time period.

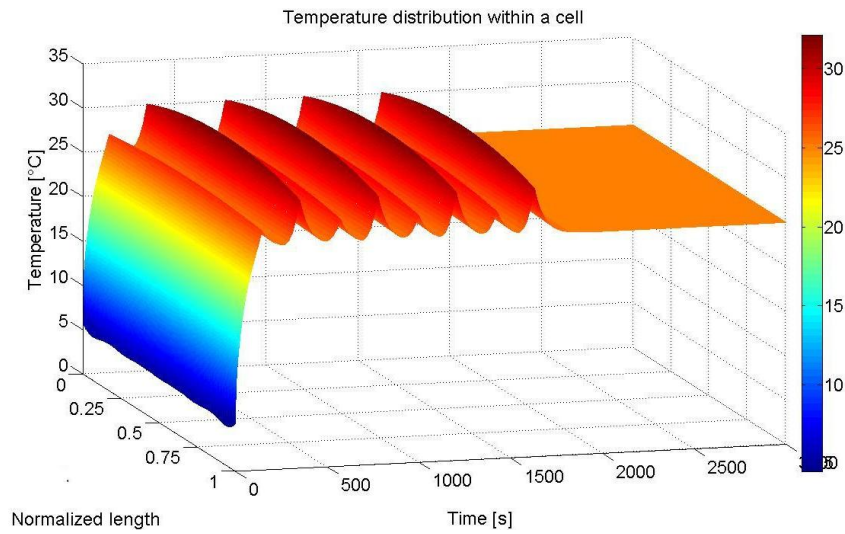


Figure 4.13. Temperature distribution within a battery cell, assuming $L=0.0036$ m, $k=0.66$ W/mK, $h=20$ W/m²K, considering an initial temperature of 5 °C.

With its characteristics, the model allows for a complete prediction of the 1D internal temperature distribution of a prismatic Li-Ion battery cell cooled by an air flow, under all the possible practical condition that the device could face during its operations.

4.2.3 Formulation of 1+1D pack model with air cooling

The 1D model developed in Section 4.2.2 is able to characterize the temperature distribution within a battery cell in the x direction, assuming uniform coolant temperature. However, as the cooling air flows through a battery pack, its temperature start rising, due to the convective heat flux from the cell walls. In order to characterize the air temperature variation along the air flow direction (here denoted with y), the 1D model has been extended to 1+1D model, where the cell is discretized into a finite number N of lumps along the y -direction, as shown in Figure 4.14.

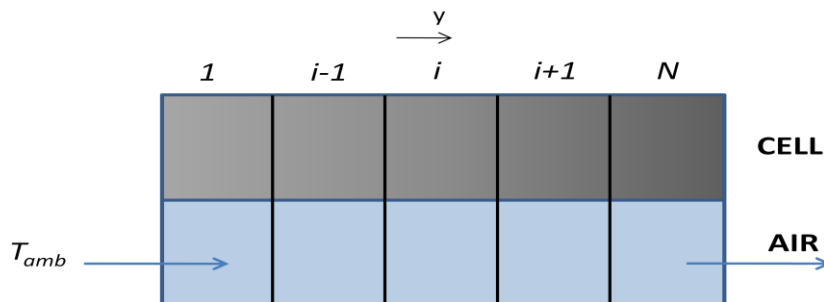


Figure 4.14. 1+1D model approach.

As the air moves along the channel, its temperature increases, hence decreasing the ability of the air to extract heat from the cell. Each cell lump is cooled by an air flow at a different temperature, as the air is gradually heated flowing along the cooling channel.

In each cell lump, the 1D model described before (Section 4.2.1) can be used to compute the temperature distribution in the x -direction. To model the temperature distribution in both x and y directions the model needs as input the air temperature at each lump, namely the boundary condition of each 1D problem.

As shown in Figure 4.15, the temperature of the air in the lump $i-1$ ($T_{air, i-1}$) is used, as boundary condition, in the 1D model of the lump i .

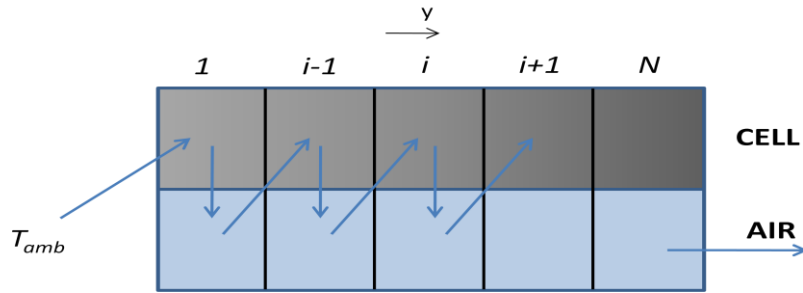


Figure 4.15. Marching approach to compute the boundary conditions in the 1+1D model.

Just for clarification, the notation $T_{air,i}$ refers to the temperature of the air in the lump i ; $T_{wall,i}$ indicates the cell surface temperature of the battery cell at the position corresponding to the i^{th} lump.

The wall temperature of the cell i is then used to solve the energy balance shown in Equation (4.4.28), allowing to determine the temperature of the air in the lump i . Thus, marching in the air flow direction, it is possible to capture the 1D temperature distribution of each battery cell lump. This assumption is justified by the fact that the air is moving in the positive y direction during the analysis.

Following this approach, the temperature distribution in i^{th} battery cell lump results to be a function only of the air temperature and air properties in the lump $i-1$ ($T_{air, i-1}$ and $c_{p air, i-1}$).

The resulting model is called 1+1D, since it is able to predict the temperature distribution in both in x and y directions. The air temperature evolution along the y direction needs thus to be explicitly computed.

The air is assumed to be at constant temperature within each single lump. Under this assumption, Figure 4.16 shows an energy balance for the generic i^{th} lump: The energy balance for the air flow is:

$$m c_v \frac{dT_{air,i}}{dt} = \dot{m} c_p T_{air,i-1} - \dot{m} c_p T_{air,i} + Ah(T_{wall,i} - T_{air,i}) \quad (4.28)$$

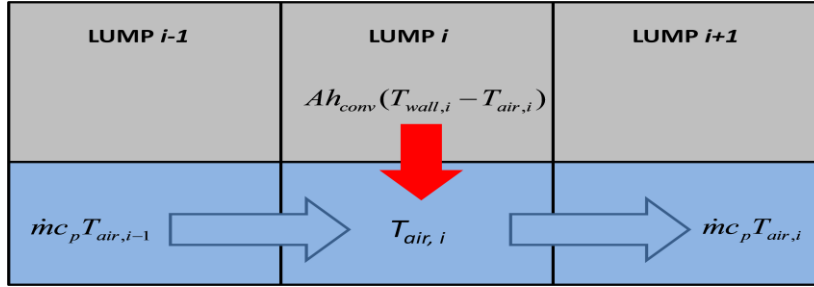


Figure 4.16. Air energy balance representation.

By solving Equation (4.4.28), the air temperature evolution can be obtained. Equation (4.4.28) can be re-written as:

$$mc_v \frac{dT_{air,i}}{dt} + (\dot{m}c_p + Ah)T_{air,i} = C \quad (4.29)$$

where $C = \dot{m}c_p T_{air,i-1} + AhT_{wall,i}$ is a constant. The linear equation can be solved, with respect to $T_{air,i}$, using the Laplace method. The initial condition is $T = T_0$.

$$\mathcal{L}(4.29) \rightarrow mc_v(sT_{air,i}(s) - T_0) + (\dot{m}c_p + Ah)T_{air,i}(s) = \frac{C}{s} \quad (4.30)$$

$$T_{air,i}(s) = \frac{C}{s} \frac{1}{mc_v s + \dot{m}c_p + Ah} + \frac{mc_v T_0}{mc_v s + \dot{m}c_p + Ah} \quad (4.31)$$

$$T_{air,i}(s) = \frac{C}{s} \frac{1}{mc_v s + \dot{m}c_p + Ah} + \frac{T_0}{s + \frac{\dot{m}c_p + Ah}{mc_v}} \quad (4.32)$$

Equation (4.4.32) is the sum of two terms. The solution of the problem, due to the superposition principle, will result in the sum of the solutions of each part separately. The first term in the right hand side of Equation (4.4.32) can be written as:

$$\text{part 1: } T_{air,i}(s) = \frac{C}{s} \frac{1}{mc_v s + \dot{m}c_p + Ah} = \frac{C}{s} \frac{1/mc_v}{s+p} \quad (4.33)$$

where $p = \frac{\dot{m}c_p + Ah}{mc_v}$. The anti-transform of Equation (4.4.33) is found by computing the residuals of the equation, as:

$$\begin{cases} F(s) = \frac{\alpha}{s} + \frac{\beta}{s+p} = \frac{C}{s} \frac{1/mc_v}{s+p} \\ \alpha = F(s) \cdot s \quad \text{for } s = 0 \\ \beta = F(s) \cdot (s+p) \quad \text{for } s = -p \end{cases} \quad (4.34)$$

where $\alpha = \frac{C/mc_v}{s+p}$ and $\beta = -\frac{C/mc_v}{p}$.

Thus, the solution the first part of Equation (4.4.32) is:

$$\mathcal{L}^{-1}\left(\frac{C/mc_v}{p/s} - \frac{C/mc_v}{p} \frac{1}{s+p}\right) \rightarrow T_{air,i}(t) = \frac{C/mc_v}{p} - \frac{C/mc_v}{p} e^{-pt} \quad (4.35)$$

The anti-transform of the second part of Equation (4.4.32) can be easily obtained from the Laplace transform table [55], and turns out to be:

$$\mathcal{L}^{-1}\left(\frac{T_0}{s + \frac{\dot{m}c_p + Ah}{mc_v}}\right) \rightarrow T_{air,i}(t) = T_0 e^{-\frac{\dot{m}c_p + Ah}{mc_v}t} \quad (4.36)$$

Summing equations (4.4.35) and (4.4.36) the overall solution of Equation (4.4.32) results to be:

$$T_{air,i}(t) = \frac{C/mc_v}{p} - \frac{C/mc_v}{p} e^{-pt} + T_0 e^{-pt} \quad (4.37)$$

$$= \frac{\dot{m}c_p T_{air,i-1} + AhT_{wall,i}}{\dot{m}c_p + Ah} + \left(T_0 - \frac{\dot{m}c_p T_{air,i-1} + AhT_{wall,i}}{\dot{m}c_p + Ah}\right) e^{-\frac{\dot{m}c_p + Ah}{mc_v}t}$$

The explicit solution of the air energy balance, shown in Equation (4.4.37), allows capturing the temperature distribution of the air along the flow direction (y direction).

Figure 4.17 shows the air temperature evolution with respect to time for different lumps of the battery cell. For these simulations the heat generation rate is imposed as in Figure 4.8.

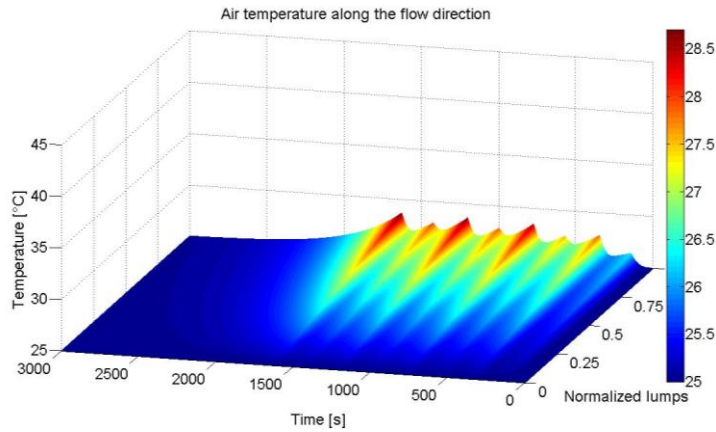


Figure 4.17. Air temperature distribution along the flow direction, assuming $k=0.66$ W/mK, $h=20$ W/m²K and $v=3$ m/s.

As expected, in the first lump (inlet of the cooling channels) the air is at the ambient temperature. As moving along the channels (normalized lumps in y direction), the air is warmed up by the heat received from the battery cell. The last lump results to be the hottest. Along the time, the air temperature profile follows the heat generation rate profile used as input to the model, with just a minor delay respect to the battery cell.

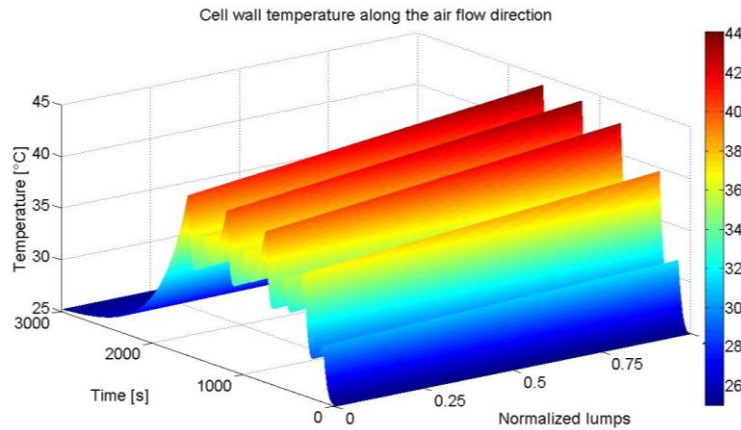


Figure 4.18. Battery cell lumps temperature distribution at the surface, assuming $k=0.66$ W/mK, $h=20$ W/m²K and $v=3$ m/s.

Since the air temperature changes in the y direction, each lump is subjected to a different boundary condition, and thus the cell temperature evolves in this direction, other than in x direction.

Figure 4.18 shows the temperature distribution of the battery cell walls. It changes with respect to time, due to heat generation rate profile, and in the y -direction (different lumps), due to the change of the boundary conditions. The temperature distribution in the x -direction has been shown in Figure 4.11, and it is not depicted here.

It is interesting to analyze the temperature distribution in the first and last lumps. Figure 4.19 shows the temperature distribution at the inlet of the air channel (first lump, $y=0$). In this lump, the air temperature is constant and equal to the ambient temperature. The cell temperature is the same as the one shown in Figure 4.10 for the 1D model, since this lump is subjected to the same boundary conditions.

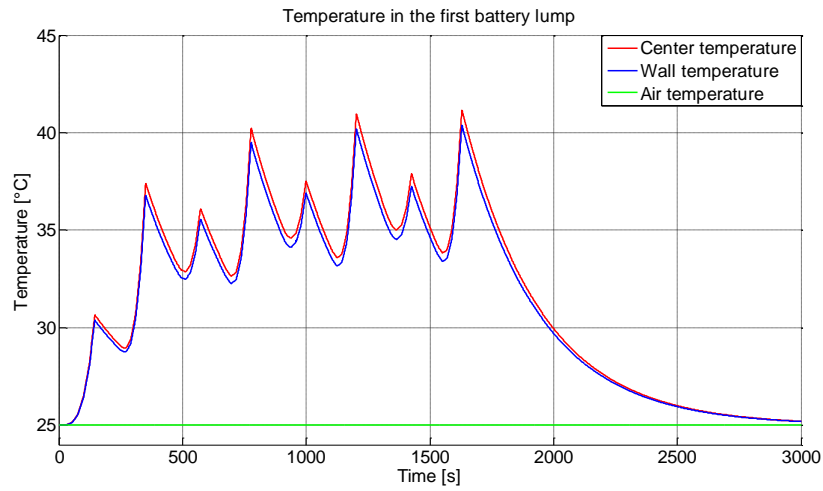


Figure 4.19. Center and surface temperature trend in the first battery lump, assuming $h=20 \text{ W/m}^2\text{K}$ and $v=3 \text{ m/s}$.

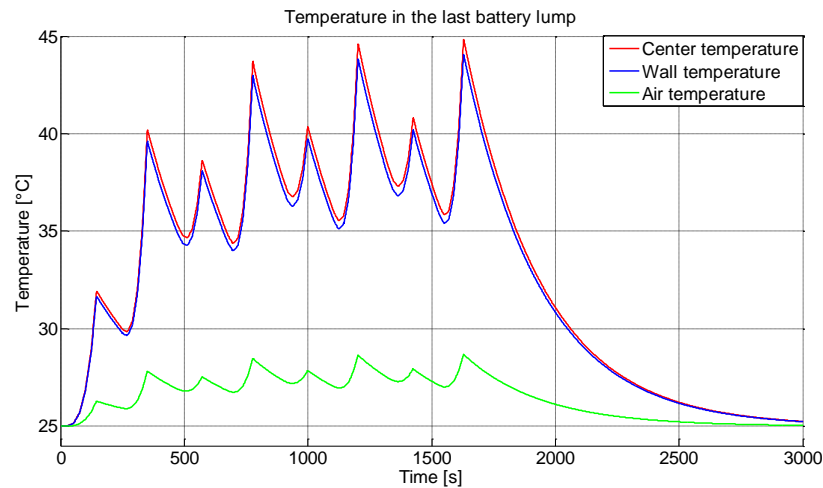


Figure 4.20. Center and surface temperature trend in the last battery lump, assuming $h=20 \text{ W/m}^2\text{K}$ and $v=3 \text{ m/s}$.

The last lump presents a different air temperature profile, as shown in Figure 4.20. The air temperature now evolves also with respect to the time, following the heat generation rate profile. It reaches almost $28 \text{ }^\circ\text{C}$ during the peaks, starting from an initial temperature of $25 \text{ }^\circ\text{C}$.

In this lump, due to the different boundary conditions, higher temperature are reached inside the battery cell and the peak temperature results almost 5°C higher respect to the first lump.

Nonetheless, it should be considered that, in this model, a 1D approach has been followed, which means neglecting the conduction along the y direction. In reality, it is expected that some heat is conducted within the battery in the y

direction, from the last, hotter lump toward the first. This will result in a temperature profile more flat than the one predicted by this model.

Its intrinsic simplicity and computational efficiency make the 1+1D model proposed an ideal candidate for design and simulation of thermal management systems for battery packs.

4.2.4 Formulation of model with imposed temperature boundary conditions

In applications related to control and diagnostics of batteries, the parameters identification is typically done with experimental data, using a set-up consisting of a programmable load that imposes a determined current profile to reproduce various battery usage conditions. Two Peltier junctions maintain the surfaces temperature of the battery cell at a prescribed value.

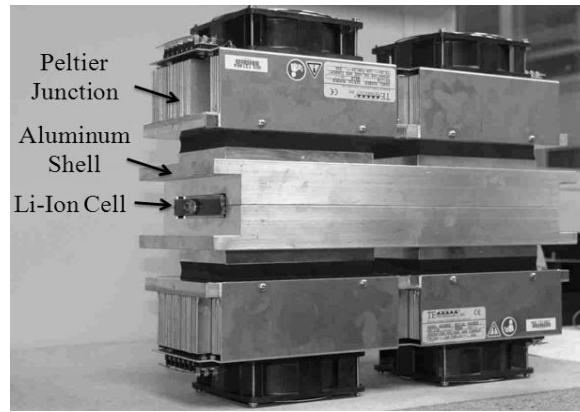


Figure 4.21. Imposed surface temperature experimental set-up, from [50].

This third model considers boundary conditions of the 1st kind, in order to impose a constant temperature at the surfaces of the cell. This allows obtaining a 1D temperature map of the core region of the battery while performing such tests. Mathematically the problem is cast in the form:

$$\frac{\partial^2 T}{\partial x^2} + \frac{\bar{q}(x,t)}{k} = \frac{1}{\alpha} \frac{\partial T}{\partial t} \quad (4.38)$$

Also:

$$\begin{cases} T(x = 0, t > 0) = T_{amb} \\ T(x = 2L, t > 0) = T_{amb} \\ T(0 \leq x \leq 2L, t = 0) = T_0 \end{cases} \quad (4.39)$$

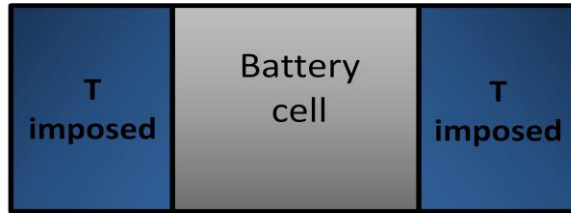


Figure 4.22. Sketch of the imposed surface temperatures model.

Figure 4.22 shows a visual representation of the problem. Imposing these boundary conditions, the Kernel and the transcendental functions are shown in Figure 4.23 and Figure 4.24:

$$\sin(\beta 2L) = 0 \tag{4.40}$$

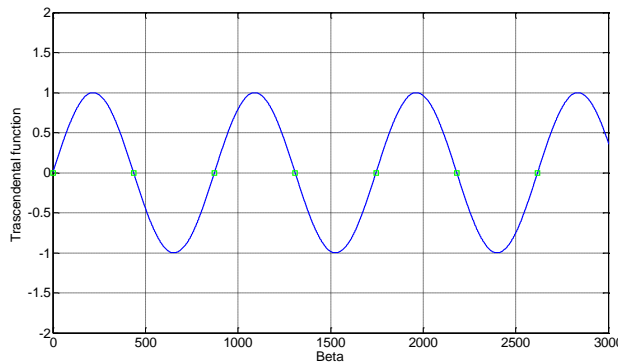


Figure 4.23. Calculation of the terms β for imposed boundary conditions, assuming $L=0.0036$ m.

Table 4.5 shows the numerical values of the first 10 eigenvalues β .

Table 4.5. Numerical values of the eigenvalues β for imposed temperature boundary conditions, assuming $L=0.0036$ m.

Terms	1 st	2 nd	3 rd	4 th	5 th	6 th	7 th	8 th	9 th	10 th
Beta	0	436	873	1309	1745	2181	2618	3054	3491	3927

$$K = \sqrt{\frac{2}{2L}} \sin(\beta_m x) \tag{4.41}$$

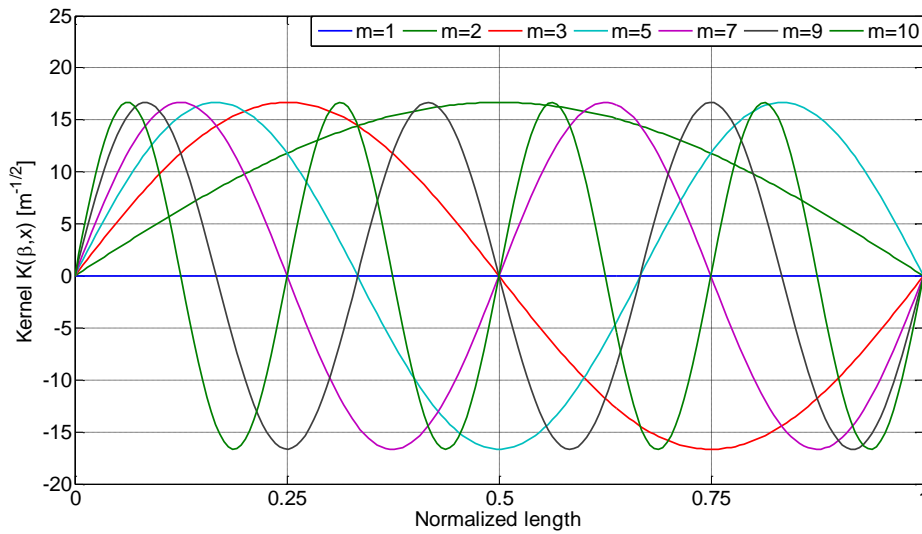


Figure 4.24. Kernel function for imposed temperature boundary conditions, assuming $L=0.0036$ m.

Using as input to the model the heat generation rate represented in Figure 4.8, and using the thermal parameters shown in Table 4.3, it is possible to obtain the temperature distribution for this case study.

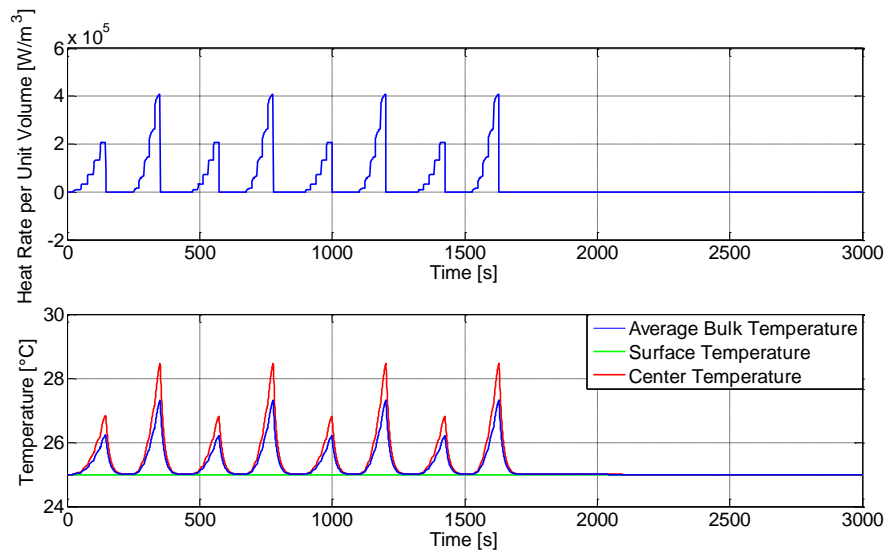


Figure 4.25. Temperature evolution for imposed temperature boundary conditions, assuming $L=0.0036$ m, $k=0.66$ W/mK.

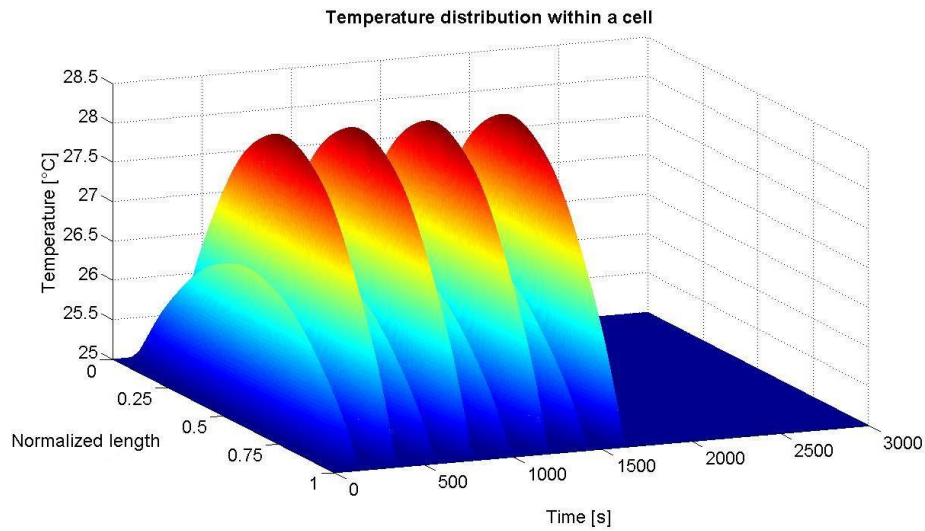


Figure 4.26. Temperature distribution within a battery cell under imposed temperature boundary conditions, assuming $L=0.0036$ m, $k=0.66$ W/mK

The results using imposed temperature boundary conditions, shown in the last two figures, have been calculated with the same thermal parameters used in the Section 4.2.2 for the convective boundary conditions (see Figure 4.9 and Figure 4.10). It is interesting to notice that, in this case, the cell reaches much lower values of temperature. However, the temperature profile looks definitely more curved in the x direction and the difference between the center and surface temperature is definitely relevant.

This is due to the fact that the boundary conditions of the first kind (imposed temperature) do not limit in any way the heat removal capability of the system. The curvature of the profile, now, depends only on the thermal conductivity of the battery cell itself, and not anymore on the convective heat transfer coefficient h .

Assuming a higher thermal conductivity for the cell, i.e. $k = 2$ [W/mK], Figure 4.27 and Figure 4.28 show that the temperature reaches lower values and the profile looks more flat.

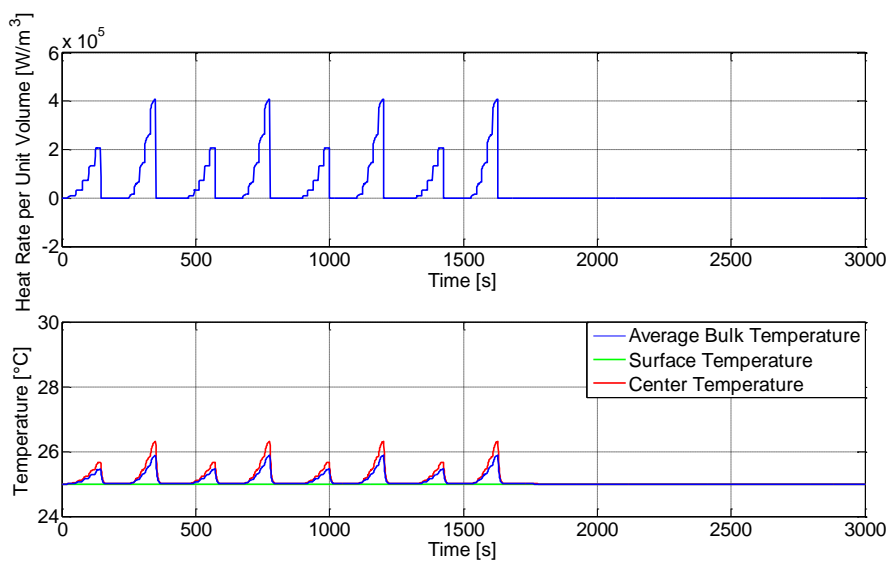


Figure 4.27. Temperature evolution assuming $L=0.0036$ m, $k=2$ W/mK.

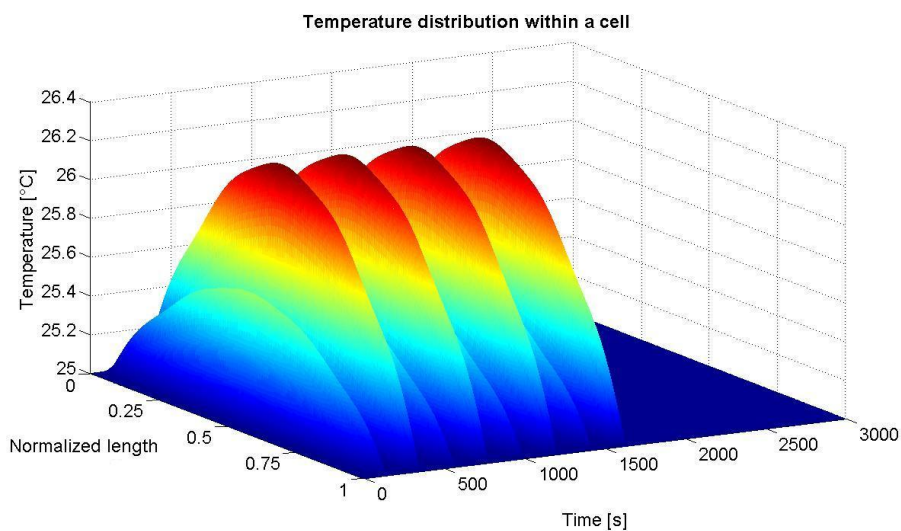


Figure 4.28. Temperature distribution within a battery cell under imposed temperature boundary conditions, assuming $L=0.0036$ m, $k=2$ W/mK.

This 1D model allows for a prediction of the temperature distribution inside a Li-Ion battery cell subject to the conditions normally used during electro-thermal characterization tests of such devices. This tool can be used to calibrate low-order or reduced models or to better characterize a Li-Ion cell thermal behavior.

4.2.5 Formulation of 1+1D pack model with cooling bar system

As analogously treated in paragraph 4.2.3 to model an air cooling system, the 1D model with imposed boundary conditions can be extended to a 1+1D model in order to simulate the behavior of a cooling bar system (see Figure 4.29).

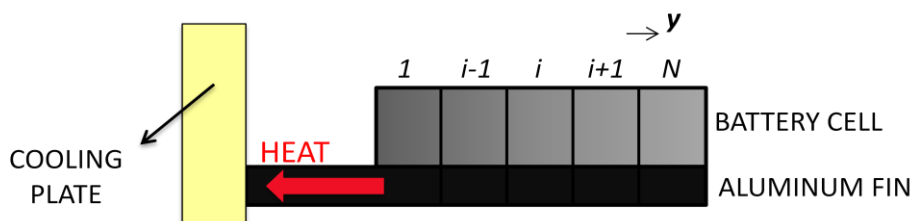


Figure 4.29, General sketch of a cooling bar system.

This system consists of a cooling plate, maintained at a constant imposed temperature by an external cooling system, to which several aluminum fins are attached.

The cooling plate presents:

- High thermal mass;
- High thermal conductivity;
- Constant temperature.

Given its characteristics, the cooling plate system can be viewed as an infinite heat sink.

Each battery cell is positioned in between two fins and the heat generated within the cell is removed by conduction from the cell to the fins, and ultimately to the cooling plate. In the automotive field, this system can be interfaced with the pre-existing cooling system, often in parallel with the air conditioning circuit, without adding any significant complication to the cooling system.

The idea beyond this approach is to substitute the air channels with a more effective heat removal system. The limit of the air cooling system is given, essentially, by the convection resistance; here the cells are directly in contact with a high conductivity material, such as aluminum, which is able to rapidly spread the heat. Hence the battery results cooled only by conduction. The thermal conductivity of the aluminum is two orders of magnitude higher than the conductivity of the Li-Ion cell and thus the heat transfer is limited only by the contact resistance between the two domains and the conductivity of the Li-Ion cell itself.

With reference to the geometry shown in Figure 4.30, the aluminum fins are characterized by very small thickness, compared to their length. Combined with their high thermal conductivity, it can be safely assumed that it is possible to neglect the temperature distribution along the x direction. Therefore, in order

to model the system, only the heat fluxes in the y direction will be here considered.

Note that the assumptions introduced are aligned with the results obtained for fins, [44]. See Section 3.1.3 for a discussion of heat transfer from extended surfaces.

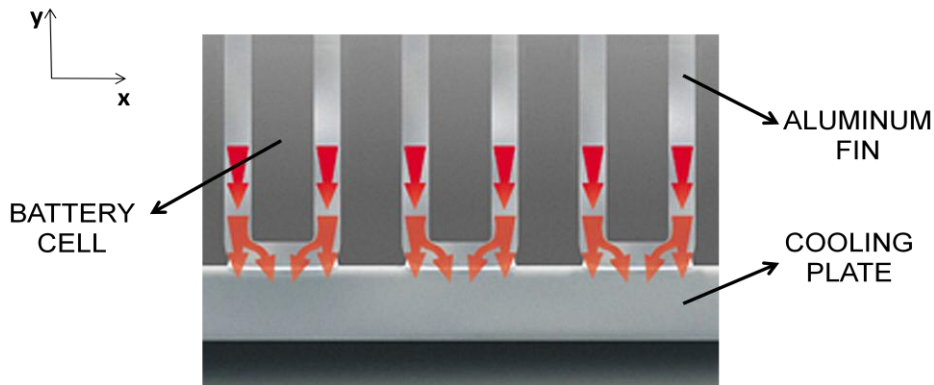


Figure 4.30. Heat fluxes in a cooling bar system.

In this case, instead of solving an energy balance for an air flow (as proposed in paragraph 4.2.3), the fin temperature distribution in y direction has to be calculated.

The cell walls are directly in contact with the fins. Discretizing the system, as shown in Figure 4.29, it is possible to use the fin temperature in each lump as imposed boundary condition for the corresponding battery cell lump. In each cell lump is thus possible to apply the model with imposed temperature boundary conditions presented in Section 4.2.4.

The 1D model allows for finding the temperature distribution in x direction, while the variability of the boundary conditions allows for capturing the temperature distribution in y direction.

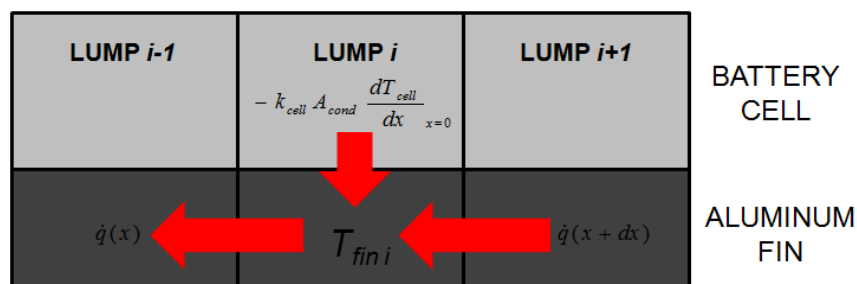


Figure 4.31. Energy balance for a cooling bar system.

To solve the conduction problem along a fin an Euler energy balance can be performed, as shown in Figure 4.31. Each fin lump has been assumed to be in steady-state due to its high conductivity and small thickness:

$$\dot{q}(x) = \dot{q}(x + dx) + \dot{q}_{batt} \quad (4.42)$$

where $\dot{q}(x) = -k_{Al} A_F \frac{dT_{fin}}{dy}$, $\dot{q}(x + dx) = -k_{Al} A_F \frac{dT_{fin}}{dy} - k_{Al} \frac{d}{dy} \left(A_F \frac{dT_{fin}}{dy} \right)$.

A_F is the front sectional area of the fin and \dot{q}_{batt} is the heat flux, [W/m²], conducted from the battery cell to the fin in the x direction.

Due to the energy conservation principle the heat flux at the surface of the battery cell enters the fin and thus \dot{q}_{batt} is computed as:

$$\dot{q}_{batt} = -k_{cell} A_{cond} \left. \frac{dT_{cell}}{dx} \right|_{x=0} \quad (4.43)$$

where A_{cond} is the area of contact between each cell and fin lump.

Substituting Equation (4.43) into the balance shown in Equation (4.42) it is possible to find the analytical expression for the fin temperature along its length (y direction).

$$-k_{Al} A_F \frac{dT_{fin}}{dy} = -k_{Al} A_F \frac{dT_{fin}}{dy} - k_{Al} \frac{d}{dy} \left(A_F \frac{dT_{fin}}{dy} \right) - k_{cell} A_{cond} \left. \frac{dT_{cell}}{dx} \right|_{x=0} \quad (4.44)$$

$$\frac{d^2 T_{fin}}{dy^2} = - \frac{K_{cell} A_{cond}}{k_{Al} A_F} \left. \frac{dT_{cell}}{dx} \right|_{x=0} \quad (4.45)$$

To integrate Equation (4.45), two boundary conditions are needed. In this case an imposed temperature at the root of the fin ($x=0$) is chosen while the fin tip ($x=L$) is supposed to be insulated.

$$\begin{cases} T_{fin}(y = 0) = T_0 \\ \left. \frac{dT_{fin}}{dy} \right|_{x=L} = 0 \end{cases} \quad (4.46)$$

The solution of Equation (4.45) results to be:

$$T_{fin}(y) = \frac{1}{2} A y^2 - A L y + T_0 \quad (4.47)$$

where L is the fin length and $A = - \frac{K_{cell} A_{cond}}{k_{Al} A_F} \left. \frac{dT_{cell}}{dx} \right|_{x=0}$

Imposing the heat generation rate shown in Figure 4.8 as input to the system, and using the typical thermal parameters for Li-Ion batteries (Table 4.3), it is possible to solve the 1+1D cooling bar model. Figure 4.32 shows the temperature along a 0.5 mm thick aluminum fin.

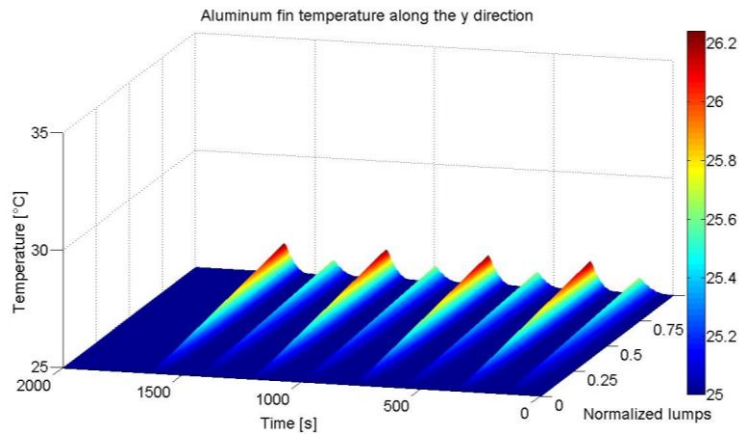


Figure 4.32. Fin temperature distribution along the flow direction, assuming $k=0.66$ W/mK, $h=20$ W/m²K.

Increasing the thickness of the fins results in a decreased thermal resistance, allowing to reach even lower values of temperature. However, a thickness of 0.5 mm is a reasonable compromise between weight-cost and efficiency for a fin used to cool a pouch-style Li-Ion battery cell. Figure 4.33 shows the Li-Ion cell temperature distribution in the y direction along the centerline of the cell (again, the temperature distribution in x direction is not shown in this picture).

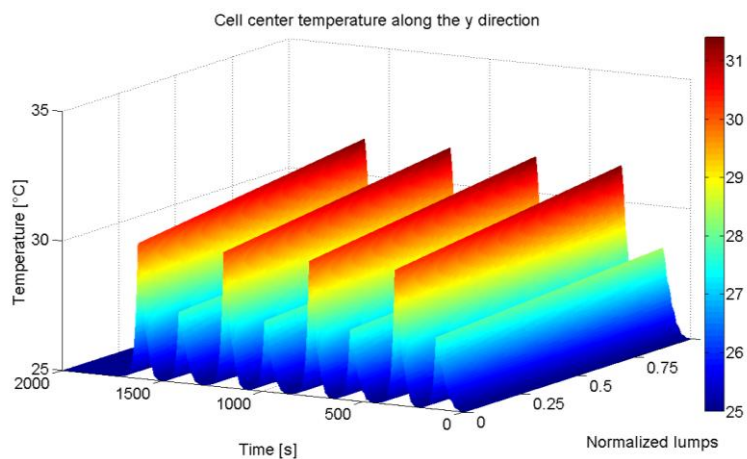


Figure 4.33. Battery cell temperature distribution along the centerline, assuming $k=0.66$ W/mK and $y=0.5$ mm

Figure 4.33 shows that the battery cell cooled with a cooling bar system reaches much lower temperature ($\sim 30^{\circ}\text{C}$) than the one cooled by an air flow ($\sim 40^{\circ}\text{C}$),

showed in Figure 4.18. Moreover, it is interesting to notice that the cooling bar system presents a really fast dynamic behavior.

The heat generation rate profile used as input the models (Figure 4.8) lasts for 1600 s. Using the cooling bar system, after only 400 s from the moment the current is zero all the effects of the heat generated inside the battery have been removed by the cooling system and the temperature of the whole system is equal to the ambient one. To obtain the same result with the air cooling system almost 1000 s more are needed.

Figure 4.34 shows the temperature of the center of the cell and of the aluminum fin in the first lump. As expected, the fin temperature is constant and equal to the temperature of the cooling bar to which it is attached, the center of the cell, instead, reaches temperatures that are at maximum 5°C over this value.

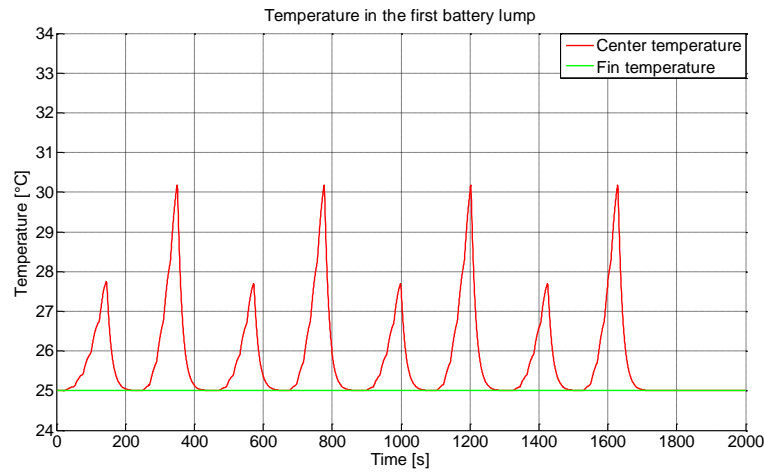


Figure 4.34. Center and fin temperature trend in the first battery lump, assuming $k=0.66$ W/mK and $y=0.5$ mm.

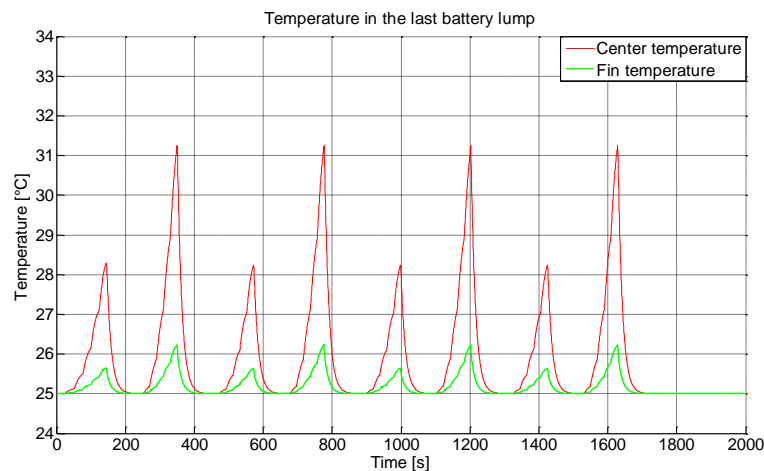


Figure 4.35. Center cell and fin temperature trend in the first battery lump, assuming $k=0.66$ W/mK and $y=0.5$ mm.

In the last lump also the fin presents a time-varying temperature profile. Here the temperature of the Li-Ion cell reaches values a bit higher than in the first lump, but still very low (~ 31 °C).

4.3 Summary

In this chapter the development of a general modeling methodology to characterize the thermal behavior of a Li-Ion battery cell has been described.

First, a general 1D model has been developed to predict the temperature distribution in a Li-Ion battery cell under any kind of boundary conditions. Then the model methodology has been applied to model two particular cases: imposed temperature boundary conditions and convective boundary conditions.

The 1D models have been extended to 1+1D models in order to simulate complete cooling systems, namely a air cooling system and a cooling bar system. Concluding, the models predict that a cooling bar system is able to cool definitely better a Li-Ion battery module respect to a normal air cooling system. On the other hand, the former system requires much more energy to keep the cooling plate at the constant temperature of 25 °C and its weight is definitely higher than the weight of the fans used to cool the battery using an air cooling system.

The 1+1D modeling approach developed allow for an easy and rapid comparison of different cooling systems and can be used for simulation of battery packs and as a tool for design and optimization of different cooling systems.

In the next chapter the modeling methodology developed will be applied to a pouch-style Li-Ion battery cell and experimental results will be used to calibrate the model. A 1+1D model of a cooling air system will be then validated through a comparison with an advanced finite element simulator.

CHAPTER 5

5. Calibration and validation of the models

The modeling methodology developed in Chapter 4 is absolutely general and it can be applied to various systems under different conditions. In order to calibrate and validate the models, although, the 1+1D convection model described in section 4.2.3 is here applied to characterize the temperature distribution in a real Li-Ion prismatic battery produced by EiG.

First of all, the Li-Ion battery cell and module will be described in detail. Then the thermal parameters used in the model will be computed and the current profile, and the heat generation rate used to perform the calibration, will be presented.

The thermal parameters of the cell are then experimentally measured in order to calibrate the model.

Finally, to provide a validation framework for the 1D and the 1+1D model, a FEM model was developed in COMSOL® and the results of the simulation are used to calibrate the modeling technique.

5.1 Technical specification of modeled Li-Ion battery cell

The models developed were applied to a rechargeable Li-Ion polymer battery. In particular, a prismatic pouch-style LiFePO₄ battery, produced by EiG (model *ePLB C020B*) is considered in this study.



Figure 5.1, EiG ePLB C020B battery cell.

The Li-Ion cell analyzed has been developed in 2009 for motive power applications (small electric vehicles, up to hybrid vehicles). Figure 5.2 shows a sketch of a cell with the coordinate system here adopted.

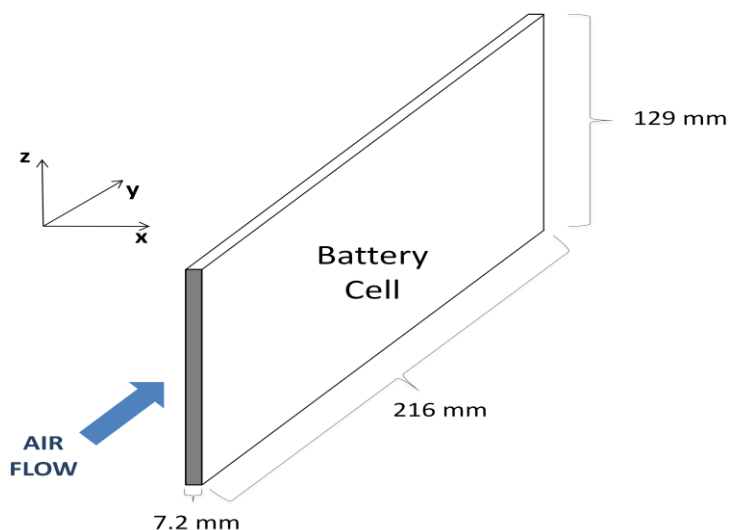


Figure 5.2. Battery cell sketch and coordinates system.

The nominal specifications of the battery are listed in Table 5.1:

Table 5.1. Battery cell technical specifications.

ITEMS	SPECIFICATIONS
Nominal Capacity	20 Ah
Nominal Voltage	3.65 V
Cell Dimensions	Thickness: 7.2 ± 0.2 mm (fully charged) Width: 129 ± 0.5 mm 216 ± 1.0 mm
Operation Temperature	Charge: 0 °C to 40 °C Discharge: -30 °C to 55 °C
Weight	425 ± 3 g.
Energy Density	Volume: 360 Wh/l Mass: 175 Wh/kg

Where unless otherwise specified all tests have been performed at 25 °C. For any further specification on tests methods used see the attached appendix A

5.1.1 Description of the battery module

The battery cell described above is part of a 20-cell high-power, high-capacity module. This product has been developed for application such electric

scooters, golf carts, and wheelchairs as an interest in non-polluting transportation method increases.

The general specifications of the module are shown in Table 5.2.

Table 5.2. Battery module specifications.

ITEMS	SPECIFICATIONS
Length	291.0 ± 5 mm
Width	150.0 ± 5 mm
Height	273.0 ± 5 mm (without terminals)
Weight	Approx. 13.6 kg
Nominal Voltage	72.0 V
Nominal Capacity	20.0 Ah
Energy Density	Volume: 120 Wh/l Mass: 105 Wh/kg
Maximum Charge Voltage	83.0 V (4.15 V per cell)
Recommended Charge Current	10 A (0.5 C)
Maximum Charge Current (<1hr by 90 %)	20 A (fast charge)
Recommended Voltage Limit for Discharge	60.0 V
Lower Voltage Limit for Discharge	55.0 V
Maximum Discharge Current (Continuous)	60.0 A (2 C)
Maximum Discharge Current (Peak, < 10 sec)	100.0 A (5 C)

The battery module presents a prismatic shape and it is cooled by a forced air flow. A conceptual representation of the cross-section of the module, showing the position of cells and cooling channels, is presented in Figure 5.3.

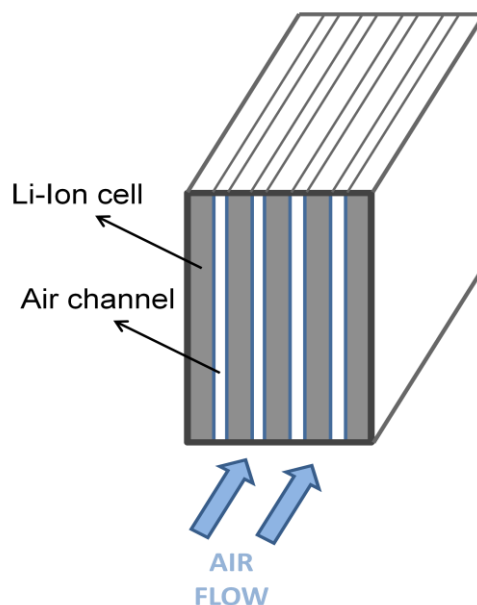


Figure 5.3, Cross-sectional view of a typical battery module.

The battery cells are separated by flow channels wherein air is forced through by a fan. The air is the cooling medium of the battery and removes the heat generated inside the cells due to irreversibilities and electrochemical reactions. Each of the 19 cooling channels is 5 mm (a battery cell has a thickness of 7.2 mm) and has the same y and z dimensions of the battery cell (129 x 216 mm).

5.2 Calculation of the battery thermal parameters

As can be noticed from the equations shown in Chapter 3 and 4, the thermal parameters required for the model are the thermal diffusivity (α) of the cell and, the convective heat transfer coefficient h .

$$\alpha = \frac{\text{ability to conduct thermal energy}}{\text{ability to store thermal energy}} = \frac{k}{\rho c_p} \left[\frac{\text{m}^2}{\text{s}} \right] \quad (5.1)$$

First of all these three intrinsic parameters of the cell (k , ρ , c_p) will be computed, and then the convective heat transfer coefficient will be calculated.

5.2.1 Calculation of cell density, thermal capacity and thermal conductivity

The density of the cell can be calculated starting from the data shown in Table 5.1, resulting 2118 [kg/m³]. However, among the data given by the manufacturer, the thermal capacity and the thermal conductivity of the cell are missing.

The latter data has been computed in the open literature (i.e. [8] or [10]) applying the Meredith and Tobias theory to calculate the conductivity of a system of uniform spheres arranged in a cubic lattice (see Table 4.3 for typical values).

Here, a simple calculation has been performed to compute the thermal conductivity of a single cell. Analyzing the literature, e.g. [49], the cell has been assumed to be a series of elementary cells coupled together. The elementary cells are often referred as jelly roll and an example is shown in Figure 5.4.

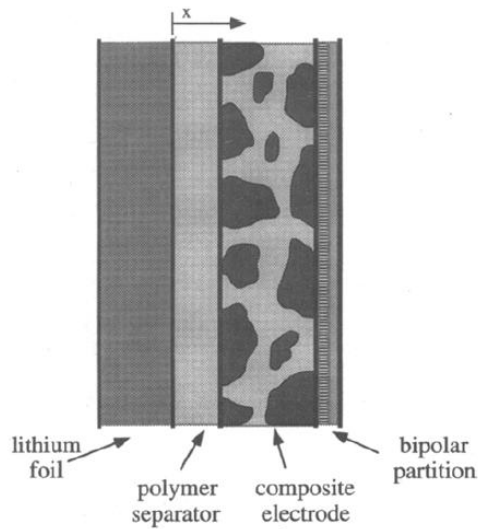


Figure 5.4. Schematic diagram of the Lithium negative electrode \ solid polymer separator \ insertion positive electrode elementary cell, from [8].

The dimensions of the cell layers depicted in Figure 5.4 are shown in Table 5.3.

Table 5.3. Dimensions of the elementary cell layers (jelly roll).

Layers in x-direction	Thickness [μm]
Graphite (anode)	60
Separator	40
Composite electrode (LiFePO_4)	125
Bipolar partition	10
Total elementary cell	235

The thickness of the cell constituents have been taken from digital optical microscope imaging for Li-Ion battery cell available on the market for automotive applications [49].

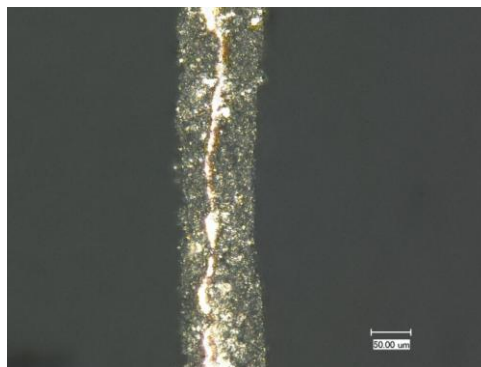


Figure 5.5. Electronic microscope imaging of the anode, [49].

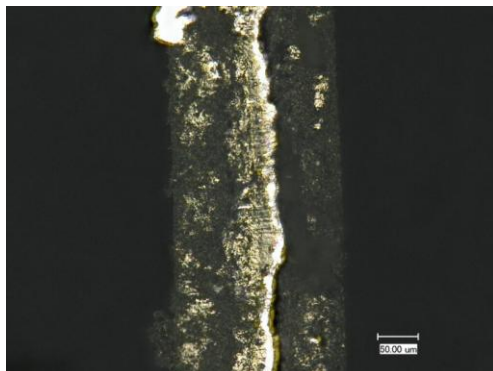


Figure 5.6. Electronic microscope imaging of the cathode, [49].

A battery cell is then composed by putting together various layers of the jelly roll, as qualitatively shown in Figure 5.7

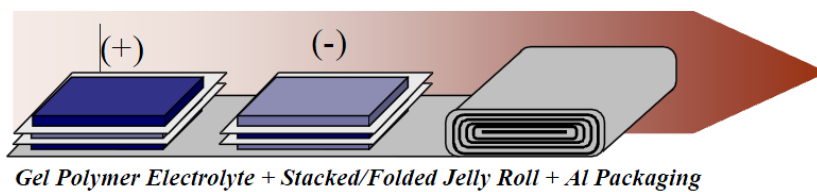


Figure 5.7. Example of jelly roll manufacturing process [22].

A battery cell is then composed by putting together various layers of the jelly roll, as qualitatively shown in Figure 5.7. The anode is considered to be made of Graphite with 95% of purity. This assumption is necessary since the conductivity of the graphite (k_{graphite}) strongly depends on its purity. From the open literature, various values of the graphite conductivity at different percentage of purity are available. By performing an analytical interpolation, an approximate correlation between the graphite purity and its own conductivity has been obtained, resulting 65.82 [W/m K].

In the x direction, the layers shown in Figure 5.4 are in series. The overall thermal conductivity in this direction can be computed, using the electrical analogy (see i.e. [44]), as shown in Figure 5.8.

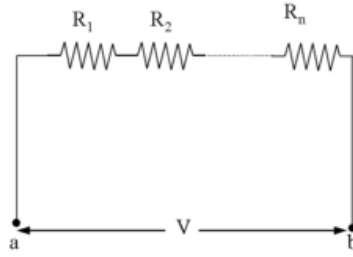


Figure 5.8. Series thermal-electric analogy.

$$k_x = \frac{R_{tot}}{L_{tot}} = \frac{R_1+R_2+R_3+R_4}{L_1+L_2+L_3+L_4} \quad (5.2)$$

where L_n is the length of each layer in the x direction and R_n is the thermal resistance on each layer, defined as:

$$R_n = \frac{k_n}{L_n} \left[\frac{m^2 K}{W} \right] \quad (5.3)$$

From the open literature (i.e.[8],[10]) and technical datasheets of the conductivity of pure materials, the overall thermal conductivity of the cell is calculated, as shown in Table 5.4.

Table 5.4. Elementary cell thermal conductivity in x direction.

x-direction	Length [m]	k [W/m K]	Thermal resistance [m² K/W]
Graphite (anode)	6.00E-05	65.82	9.59E-07
Separator	4.00E-05	0.16	2.5E-04
Composite electrode (LiFePO4)	1.25E-04	1.47	8.5034E-05
Bipolar partition	1.00E-05	6.53	1.53139E-06
Total	2.35E-04	0.6963	3.37525E-04

In the y and z directions, the layers are in parallel and then the overall thermal conductivity has to be computed according to:

$$k_{y,z} = \frac{R_{tot}}{L_{tot}} \text{ where } \frac{1}{R_{tot}} = \frac{1}{R_1} + \frac{1}{R_2} + \frac{1}{R_3} + \frac{1}{R_4} \quad (5.4)$$

The parallel resistance analogy is depicted in Figure 5.9.

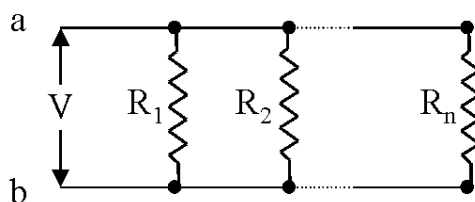


Figure 5.9, Parallel thermal-electric analogy.

Table 5.5. Elementary cell thermal conductivity in y direction.

y-direction	Length [m]	k [W/m K]	Thermal resistance [m ² K/W]
Graphite (anode)	2.16E-01	65.82	3.51E-03
Separator	2.16E-01	0.16	1.35
Composite electrode (LiFePO ₄)	2.16E-01	1.47	0.146938776
Bipolar partition	2.16E-01	6.53	3.3078101E-02
Total	2.16E-01	73.980	3.10E-03

Table 5.6. Elementary cell thermal conductivity in z direction.

z-direction	Thickness [m]	k [W/m K]	Thermal resistance [m ² K/W]
Graphite (anode)	1.29E-01	65.82	2.10E-03
Separator	1.29E-01	0.16	0.80625
Composite electrode (LiFePO ₄)	1.29E-01	1.47	8.7755102E-02
Bipolar partition	1.29E-01	6.53	1.9754977E-02
Total	1.29E-01	73.980	1.85E-03

As expected, the thermal resistance varies in y and z directions due to different geometry. However, the conductivity, which is an intrinsic property of the materials, does not change in these two directions.

The overall cell conductivity results 0.696 [W/mK] along the thickness direction and 73.980 [W/mK] along the other two directions. The values found are consistent with the range that can be found in the open literature, summarized in Table 4.3.

As regard the thermal capacity, determining its numerical value is a complex task, due to the need of dedicated experimental equipment to measure the thermal diffusivity (such as Flash Diffusivity Systems or Differential Scanner Calorimeters).

For this reason, in this study, values proposed in the literature, [10], will be used (in particular $c_p = 795 \text{ [J/kg K]}$).

5.2.2 Convective heat transfer coefficient

It is well known that the convective heat transfer solutions rely on empirical correlations that are based on the use of dimensionless numbers. In this work a forced flow in a rectangular duct has to be analyzed.

The Reynolds number for internal flows in non-circular tubes can be expressed as:

$$Re = \frac{\rho u_m D_h}{\mu} \quad (5.5)$$

where u_m is the mean velocity of the fluid, which has been here chosen to be equal to 3 m/s, and D_h is the hydraulic diameter:


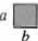

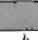
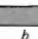
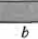
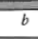
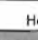
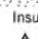

$$D_h = \frac{4A_c}{p} \quad (5.6)$$

where p is the wet perimeter of the channel and A_c is the flow cross-sectional area. For the battery channels described in 5.1.1 the hydraulic diameter results to be equal to 9.6 mm.

The Reynolds number results to be 1854, indicating laminar flow conditions.

Table 5.7, taken from [44], shows the values of the Nusselt number and friction factor for fully developed laminar flow in rectangular ducts.

Table 5.7. Nusselt numbers and friction factors for fully developed laminar flow in tubes of different cross section, [44].

Cross Section	$\frac{b}{a}$	$Nu_D \equiv \frac{hD_h}{k}$		$f Re_{D_h}$
		(Uniform q''_s)	(Uniform T_s)	
	—	4.36	3.66	64
	1.0	3.61	2.98	57
	1.43	3.73	3.08	59
	2.0	4.12	3.39	62
	3.0	4.79	3.96	69
	4.0	5.33	4.44	73
	8.0	6.49	5.60	82
	∞	8.23	7.54	96
	∞	5.39	4.86	96
	—	3.11	2.49	53

According to the nomenclature used in Table 5.7, the aspect ratio $\frac{b}{a} = \frac{216}{5} = 43.2, \rightarrow \infty$ and thus the suitable Nusselt number for this problem results to be 8.23.

The heat flux rate is assumed to be uniform along the section, while the temperature should vary.

Obtained the Nu number from the literature, it is simple to compute the convective heat transfer coefficient:

$$h = \frac{Nu k_{air}}{D_h} \quad (5.7)$$

which, for fully developed flow, is constant along the flow direction.

For the EiG module modeled in this work the fully developed convective heat transfer coefficient h results to be equal to 22.27 [W/m²K].

However, the hydrodynamic entry length, for laminar flows [44], is an expression of the form:

$$\left(\frac{x_{fd,h}}{D_h}\right) \approx 0.05 Re \quad (5.8)$$

For the EiG battery module analyzed, the entry region length results to be 0.89 m and thus appropriate correlations must be considered. A complete treatment of forced laminar flow in ducts can be found in [54]. Note that here the aspect ratio is considered as: $\frac{a}{b} = \frac{5}{216} = 0.023$.

Table 5.8. Nusselt number for rectangular ducts as function of normalized position x^* and aspect ratio α , considering $Pr=0.72$, [54].

$\frac{1}{x^*}$	$Nu_{m,T}$				
	Aspect Ratio, α^*				
	1.0	0.5	1/3	0.25	1/6
10	3.75	4.20	4.67	5.11	5.72
20	4.39	4.79	5.17	5.56	6.13
30	4.88	5.23	5.60	5.93	6.47
40	5.27	5.61	5.96	6.27	6.78
50	5.63	5.95	6.28	6.61	7.07
60	5.95	6.27	6.60	6.90	7.35
80	6.57	6.88	7.17	7.47	7.90
100	7.10	7.42	7.70	7.98	8.38
120	7.61	7.91	8.18	8.48	8.85
140	8.06	8.37	8.66	8.93	9.28
160	8.50	8.80	9.10	9.36	9.72
180	8.91	9.20	9.50	9.77	10.12
200	9.30	9.60	9.91	10.18	10.51
220	9.70	10.00	10.30	10.58	10.90

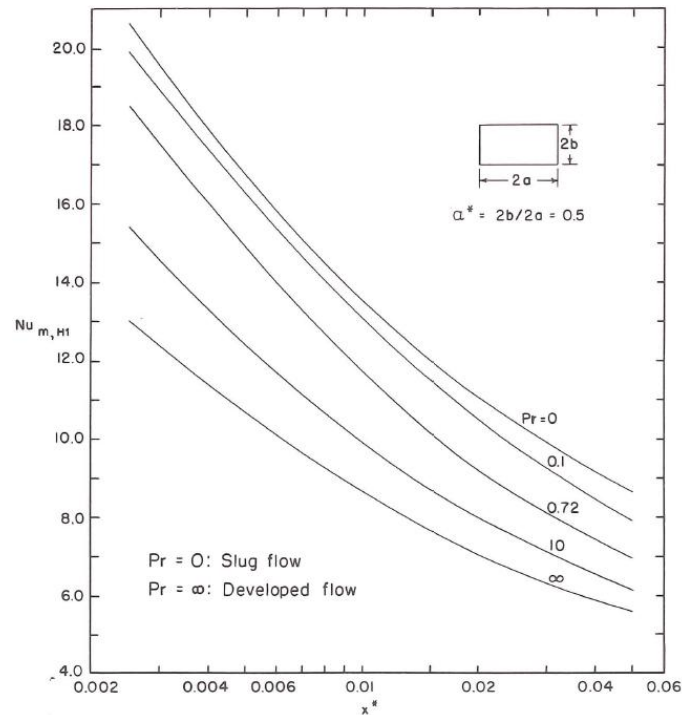


Figure 5.10. Nusselt number for laminar flow in a rectangular duct as function of Pr and normalized position x^* for $\alpha = 0.5$. [54].

As can be noticed in Figure 5.10, the heat transfer coefficient tends to really high values near the entry edge and then it settles to a value similar to the one obtained for the fully developed region.

The large value of the heat transfer coefficient in the entry region leads to a great heat removal capability. This condition is obtained with a laminar flow in small hydraulic diameter passage and allow for a compact design of the battery module [56]. This confirms that laminar flow is the preferred choice for this kind of systems and the channels dimensions are appropriate to the purpose of optimizing the cooling system.

Since a closed correlation to calculate the heat transfer coefficient with respect to the position along the duct is not available it has been decided to run the model with a constant h , assuming fully developed conditions.

Then, in 5.4.3, the model will be compared with a FEM 3D simulation and the heat transfer coefficient will be calibrated in order to account for the developing region.

As a final remark, it is possible to verify the modeling assumptions proposed in 3.2. Using the values calculated for the considered battery module the Biot number results to be 0.23, indicating that a lumped analysis would be a fairly inaccurate solution method for this problem.

5.3 Definition of the model inputs: current profile and heat generation rate

Since the transient temperature rise of the Li-Ion battery originates in its internal heat generation during its operation, a precise estimation of the heat generation rate is indispensable to calculate the temperature distribution with high accuracy. This term depends on the current, voltage and open-circuit voltage of the battery cell, as stated in 4.2.1.

For this kind of model, combinations of pulses and steps, shown in Figure 5.11 and Figure 5.12, can provide the necessary excitation for the dynamics modeled.

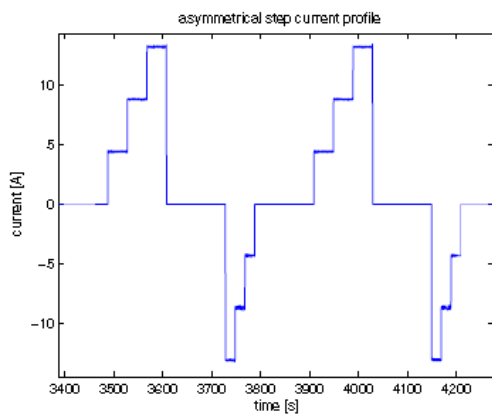


Figure 5.11. Asymmetric step current profile, [34].

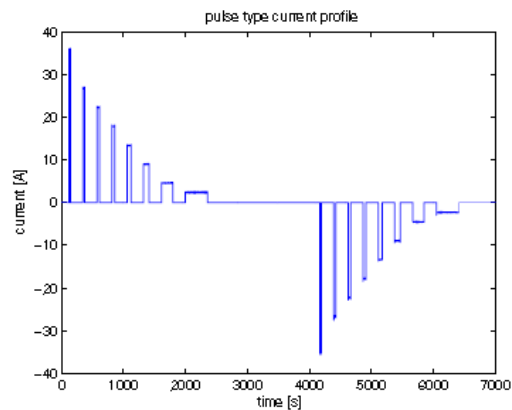


Figure 5.12. Pulse current profile, [34].

The step profile provides more of a PHEV type current request where the C-rate is moderate but the duration of power request is longer. The pulse profile provides more of a HEV type power request.

The values of the current and voltage used in this section were taken from a 24000 seconds cycle implemented *ad hoc* for electrical characterization of Li-Ion battery. This cycle, shown in Figure 5.13, alternating symmetric steps and impulses, allows for a complete mapping of the possible operating conditions.

The open-circuit voltage, E_0 , has been obtained performing an electrical characterization of the battery [42].

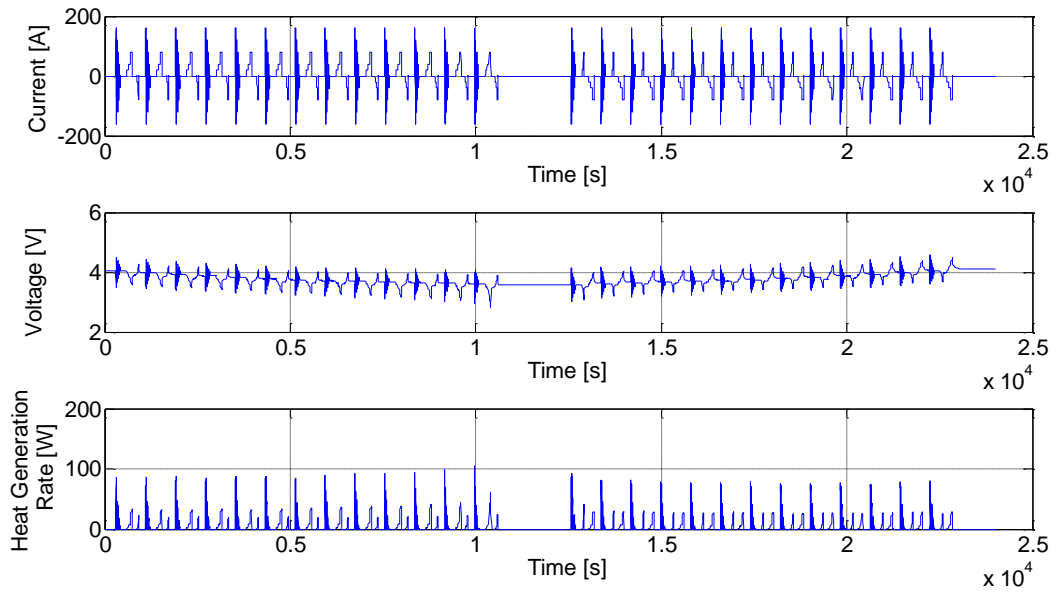


Figure 5.13. Current, voltage and heat generation rate profile.

For the purpose of showing model results, the 800 s cycle between $t = 200$ s and $t = 1000$ s, shown in Figure 5.14 has been chosen.

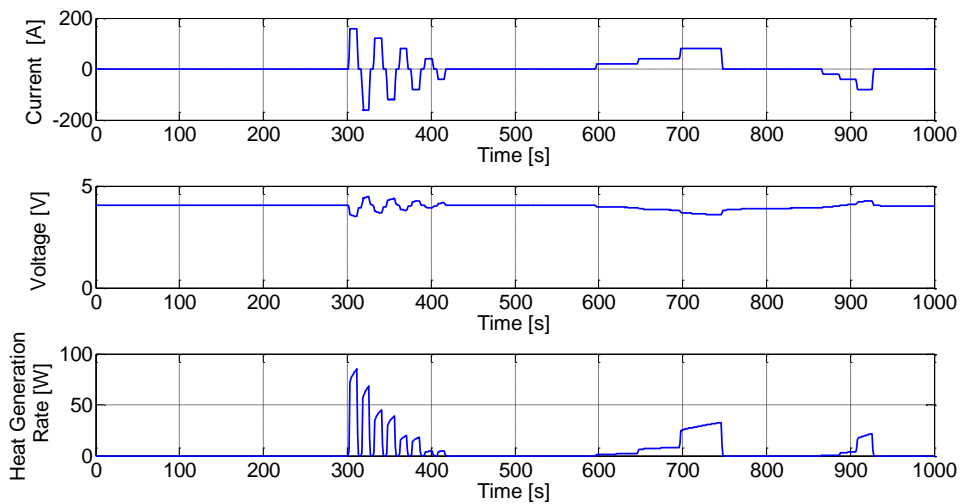


Figure 5.14. Current voltage and heat generation rate profile used to perform the simulations.

Figure 5.15 shows the heat generation rate per unit volume generated within each Li-Ion battery cell.

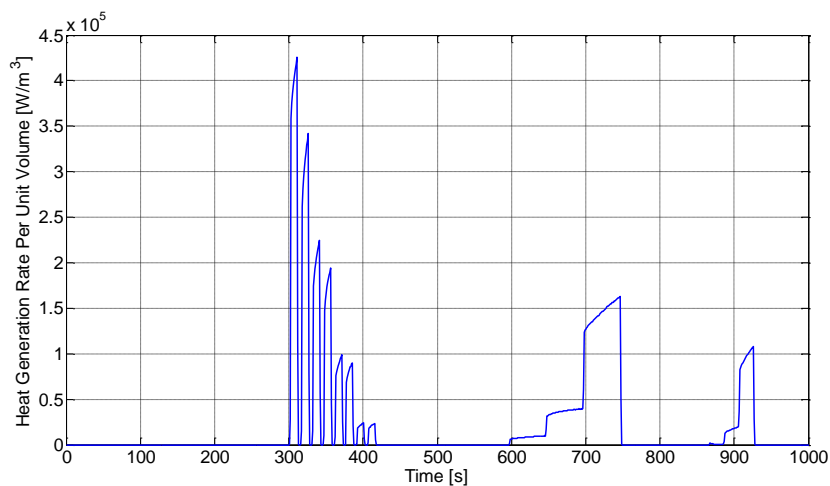


Figure 5.15. Heat generation rate per unit volume used to perform the simulations.

5.4 Model calibration and validation

In order to calibrate and validate the modeling approach described in the previous chapter, an experimental set-up has been developed and a comparison with advanced finite element simulation software (FEM) has been performed.

5.4.1 Experimental set-up

At CAR¹², extensive research and experimental studies are conducted to test various kinds of batteries.

Electrical characterizations are performed to compute the open circuit voltage and electrical parameters of battery cells and modules. Current profiles have been generated *ad hoc* for various applications and studies about battery aging are performed.

These laboratories contains multiple stations capable of running tests of arbitrary lengths and can accommodate 24/7 unattended operation if needed. Each station testing a single cell or module consists of:

- Power supply;
- Programmable electronic load;
- Data acquisition and control computer;
- Peltier junctions (and/or environmental chamber) and associated controllers;
- Electrochemical impedance spectroscopy equipment EIS (mounted externally).

¹² Center for Automotive Research, The Ohio State University, Columbus (OH), U.S.A.



Figure 5.16. Battery test bench.

Each experimental station shown in Figure 5.16, consists of an 800W programmable electronic load and a 1.2 kW programmable power supply.

The testing stations are calibrated on a regular basis to ensure the best possible sensor measurements. Three measurements are collected during each test: current (inductive), voltage, and temperature. All measurements are sampled at 10 Hz.

The instrumentation allows for running test for temperatures ranging between -25°C to +60 °C. For large battery packs, environmental chambers are used to keep the temperature constant, while for smaller cells the use of the Peltier junction is preferable.

Environmental chambers are devices that are used to simulate an environment of a different temperature humidity or climate, etc. They are also used to simulate and test for various effects, such as altitude, radiation, wind, bacteria, dust, chemical exposure and vacuums. These chambers are used in many different industries and especially useful for the testing of electronic and telecommunication components to see how they perform in various types of conditions. The chambers are ideal for performing quality control tests along with other types of experiments.

Battery aging tests are actually conducted at different temperatures to test the influence of the temperature on the battery parameters. The environmental chamber, controlling temperature and humidity, is used to simulate the climate that is desired for the aging process.



Figure 5.17. Environmental chamber.

Small battery cells are kept at constant imposed temperature using a Peltier junction. This device is based on the thermo-electric effect known as the Peltier effect: when a voltage is applied across a semiconductor thermocouple, any surplus charge carriers present in the semiconductor will be attracted towards the terminal with the opposite polarity, as shown in Figure 5.18. Thus electrons in the N type material migrate towards the positive terminal causing a surplus to accumulate in the region of the semiconductor next to the terminal leaving a deficit at the negative side of the device. Similarly holes in the P type material migrate towards the negative terminal. In other words the charge carriers are swept through the material accelerating as they do so, due to the electric field created by the voltage between the terminals of the device, and their increased kinetic energy is manifest as heat.

The temperature within the device depends on the number and the kinetic energy of the charge carriers. The temperature will therefore be higher in the region where the charge carriers are concentrated and lower in the region they have just vacated where charge density is consequently lower. Thus a temperature gradient, proportional to the magnitude of the applied current, builds up across the device. This temperature gradient can only be maintained, however, if heat can be removed from the hot junction. Otherwise the temperature will tend to equalize across the device and continued current flow will cause the device to overheat. This results in a cooling effect on the colder side of the junction itself (thermo-electric cooling).

The heat absorbed or created at the junctions is proportional to the electrical current flow and the proportionality constant is known as the Peltier coefficient.

Contrary to Joule heating (I^2R), the Peltier effect is reversible depending on the direction of the current

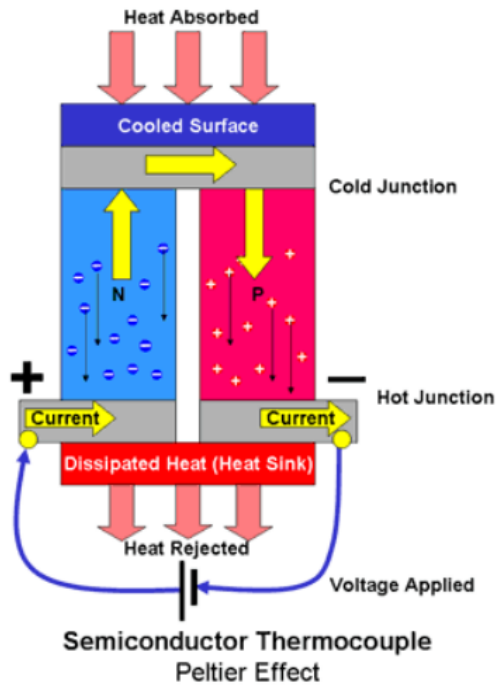


Figure 5.18. Operation scheme of a Peltier junction, [57].

To ensure tight tolerance on the battery temperature under any current profile, each test specimen is fixtured in a specially machined aluminum or stainless steel plate with a large thermal mass.

Figure 5.19 shows one machined stainless steel plate with channels for the thermocouples wires and fixing holes.

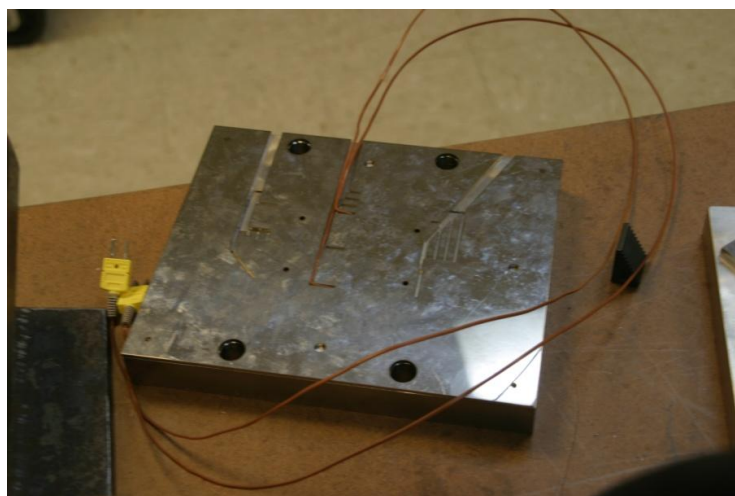


Figure 5.19. Machined stainless steel plate with inserted thermocouples.

The thermal acquisition system consists of a National Instrument signal conditioning with 32 thermocouples channels, as shown in Figure 5.20. Each input channel includes an instrumentation amplifier, a cold-junction compensation and a 2 Hz low-pass filter.

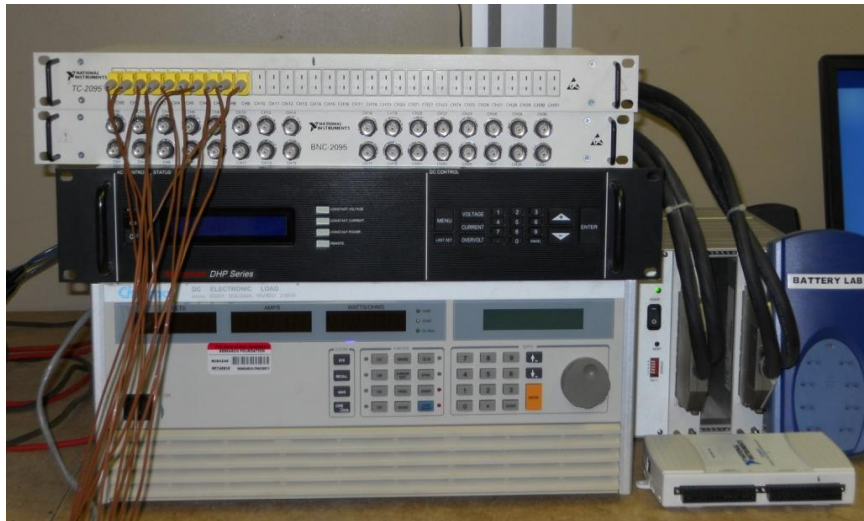


Figure 5.20. Thermal signal conditioning system.

Thermal imaging cameras are also available in the laboratory. Figure 5.21 shows a thermal image of a battery during a characterization test.

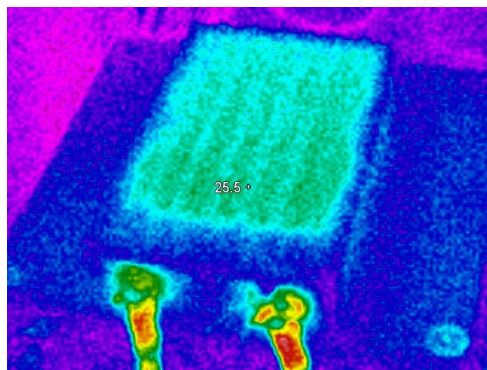


Figure 5.21. Thermal image of a Li-Ion battery cell.

5.4.2 Thermal conductivity experiment

An experimental set-up has been developed to measure the thermal conductivity in the direction of the thickness of the EiG Li-Ion battery cell analyzed in this thesis. The conductivity can be calculated by applying its definition:

$$k_{batt, x} \equiv -\frac{\dot{q}_x}{dT_{batt}/dx} \quad \left[\frac{W}{mK} \right] \quad (5.9)$$

To estimate this parameter, two quantities are needed:

- The heat flux in x direction, \dot{q}_x ;
- The temperature drop across the battery cell in the same direction, $\frac{dT_{batt}}{dx}$.

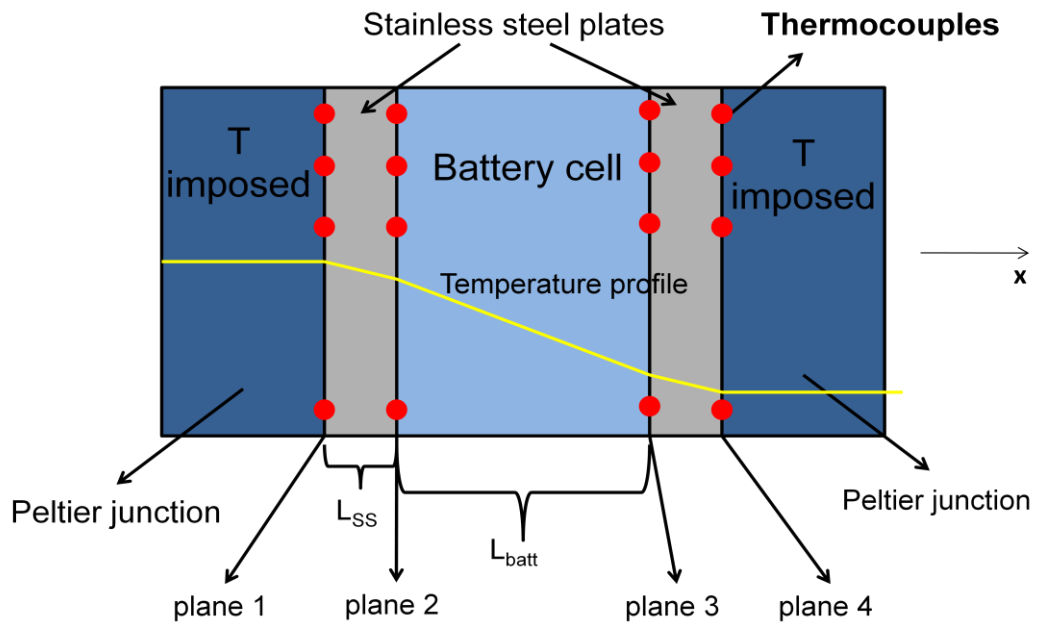


Figure 5.22. Experimental set-up for thermal conductivity measurement.

Figure 5.22 shows a schematic of the experimental set-up developed *ad hoc* to calculate the thermal conductivity of the battery cell.

The system built in the laboratory is composed, in the x direction, of a series of five elements:

1. Peltier junction;
2. Stainless steel plate;
3. Battery cell;
4. Stainless steel plate;
5. Peltier junction.

Figure 5.23, taken during the implementation of the experiment, shows half of the system described above.

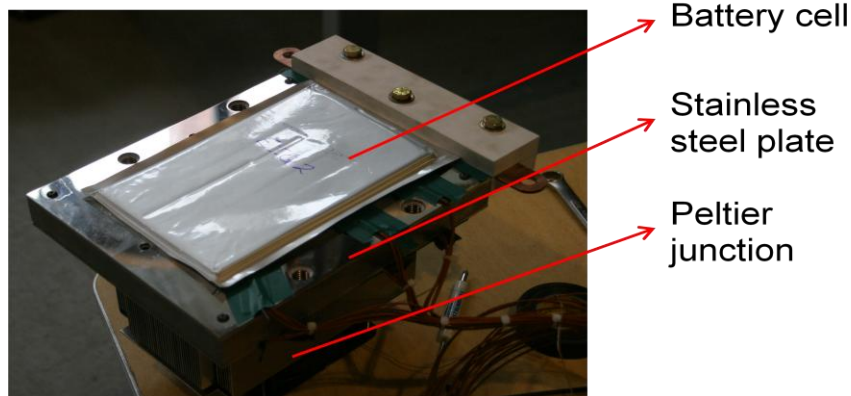


Figure 5.23. Peltier junction - stainless steel plate - battery cell sandwich for the thermal conductivity experiment.

Nine T-type thermocouples have been positioned in an equally spaced grid to completely cover the heat transfer surface of each of the four planes shown in Figure 5.22. This allows one to obtain a complete map of the temperature of the system.

The two Peltier junctions impose two different temperatures at the extremes of the system so that a heat flux is established in the x direction. The battery cell has been positioned in between of two plates of known material (stainless steel 304). The three components in series (plate-battery cell-plate) experience the same heat flux. Measuring the temperature drop across each stainless steel plate, of known thermal conductivity (k_{ss}), the heat flux can be computed as:

$$\dot{q}_x = - k_{ss} \frac{\Delta T_{ss}}{L_{ss}} \quad (5.10)$$

where ΔT_{ss} is an average of the temperature drops across the two plates.

As far as the temperature drop across the battery cell is concerned, ΔT_{batt} is directly measured. The temperature at each plane is an average of the nine measurements. In order to reach a steady-state condition, the experiment has run for a few hours. Figure 5.24 shows the temperatures at the four planes defined in Figure 5.22. The values shown result from an average of the last 200 s of the experiment.

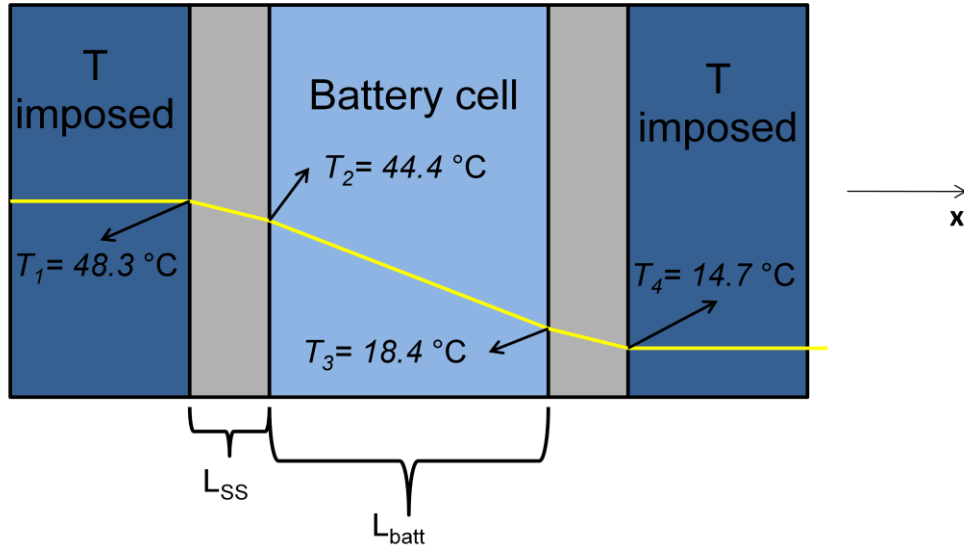


Figure 5.24. Temperature profile along the system considered in the thermal conductivity experiment.

Experimental results are shown Table 5.9.

Table 5.9. Thermal conductivity experiment result.

Dimension	Value
L_{ss} [mm]	25.4
k_{ss} [W/mK]	16.2
Average ΔT_{ss} [°C]	3.8
L_{batt} [mm]	7.2
Average ΔT_{batt} [°C]	26.0

Substituting Equation (5.10) into Equation (5.9), the battery cell conductivity is thus obtained as:

$$k_{batt} = - \frac{k_{ss} \frac{\Delta T_{ss}}{L_{ss}}}{\frac{\Delta T_{batt}}{L_{batt}}} \quad (5.11)$$

The thermal conductivity of the battery cell in the x direction turns out to be: $k_{batt,x} = 0.67$ W/mK, which is consistent with the range that can be found in the open literature (Table 4.3) and really close to the value calculated in Section 5.2.1 ($k = 0.696$ W/mK), confirming the reliability of the assumptions made in this thesis.

5.4.3 FEM comparison

In order to provide a validation framework for the 1D and the 1+1D model in the absence of experimental data, a FEM model was developed in COMSOL[®] (an advanced FEM simulator), with reference to the system geometry shown in Table 5.1 and Figure 5.3. Due to the nature of the system considered in this study, a 2D heat transfer problem is formulated in the x and y dimensions, assuming uniformity of the velocity and temperature fields along the z direction. This assumption allows for a partial simplification of the problem, without any relevant implication on the accuracy of the solution. The software solves simultaneously the coupled heat transfer equation and the incompressible Navier-Stokes equations in the air flow domains. In the battery cell domain, the 2D heat diffusion equation is solved, considering anisotropic thermal properties for the cell materials [10].

In order to solve the problem, boundary and initial conditions are needed. In this case, the air is assumed to enter the cooling channels at 3 m/s and at the initial instant the whole system presents a uniform temperature of 25 °C.

The FEM model uses as input the same heat generation rate adopted for the 1+1D model and shown in Figure 5.14.

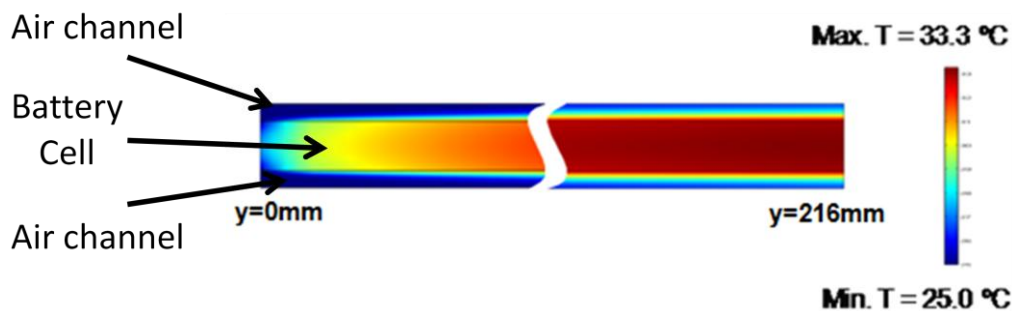


Figure 5.25. FEM prediction of the temperature distribution within a battery cell and two cooling channels.

Figure 5.25 shows the temperature field predicted by the FEM simulation at the time $t=327$ s, where temperatures of the battery cell reaches one of the peaks. Only the first 40 mm and the last 40 mm regions of the cell are shown in the figure, to give better temperature field resolutions. It is possible to observe that the thermal boundary layer in the air gradually develop along the flow direction.

A preliminary comparison of the 1+1D¹³ model prediction was done against the FEM simulation results. Figures 5.27-29 show the temperature dynamics at the center of the cell ($x=L$), as well as the cooling air temperature at three locations within the domain, namely the inlet of the cooling channel ($y=0$

¹³ The simulations were performed discretizing the battery cell into 200 lumps.

mm), at the outlet ($y=216$ mm) and at an intermediate location ($y=54$ mm), as shown in Figure 5.26.

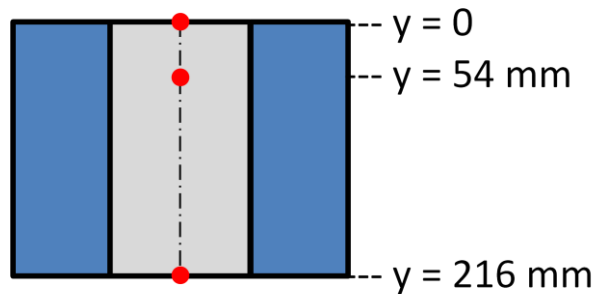


Figure 5.26. Locations at which the comparisons between 1+1D and FEM have been performed.

Due to the increasing of the air temperature along the flows, each lumps of the battery cell are subjected to slightly different boundary conditions which results in the temperature differences shown in figures :

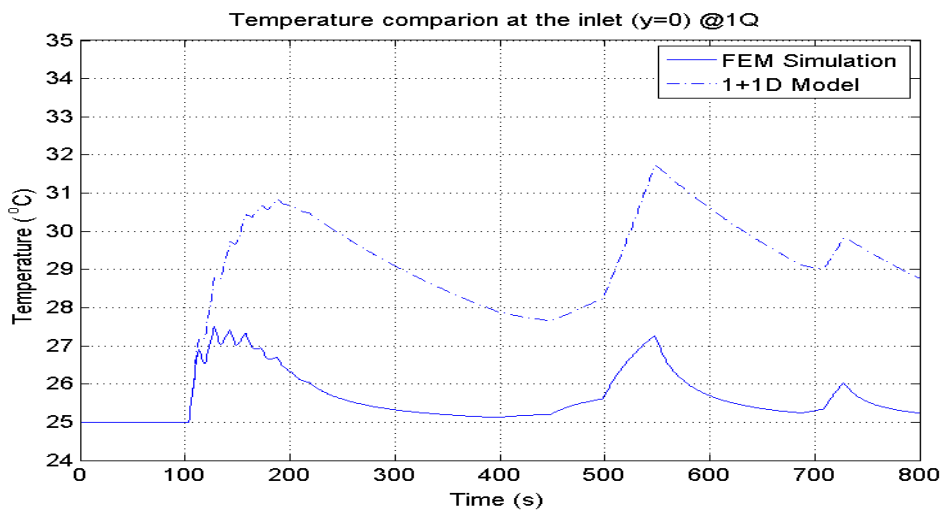


Figure 5.27. 1+1D and FEM temperature profiles at $y=0$ mm.

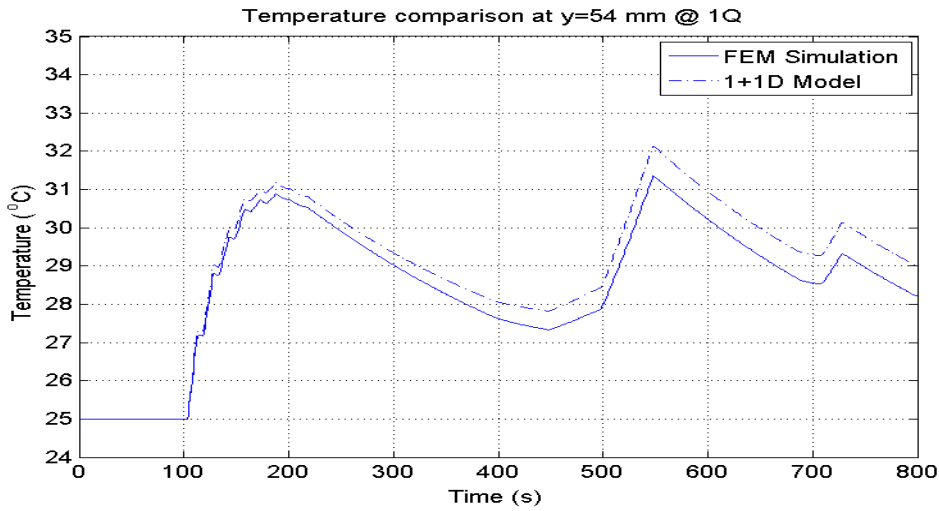


Figure 5.28. 1+1D and FEM temperature profiles at $y=54$ mm.

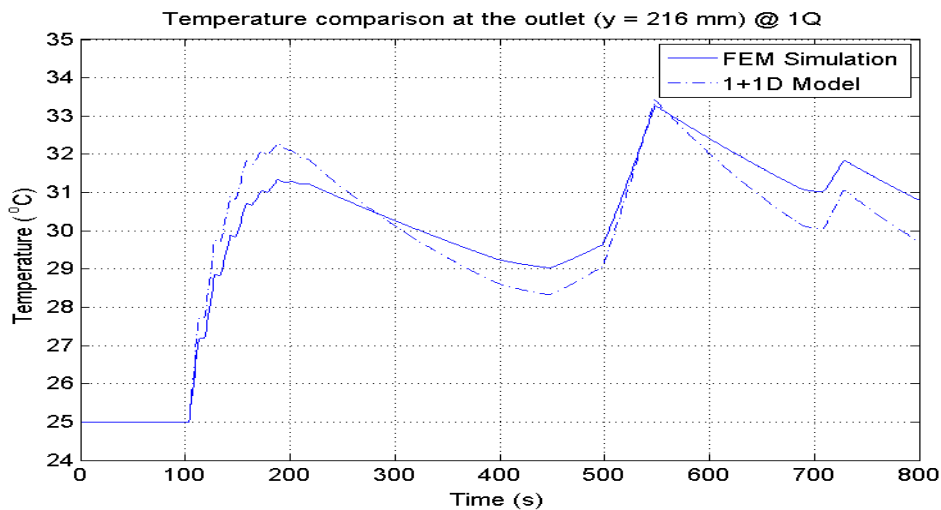


Figure 5.29. 1+1D and FEM temperature profiles at $y=216$ mm.

Analyzing the previous figures, it can be observed that the 1+1D model tends to overestimate the battery temperatures predicted by the FEM model, especially at the entrance of the cooling channel.

The reason for this behavior stems from the effects of the entry region, which have been neglected from the calculation of the convective heat transfer coefficient used in the 1+1D model. A fully developed laminar flow was assumed in the channel, hence leading to constant Nusselt number and constant heat transfer coefficient. In reality, the heat exchange between the battery surface and the coolant should be significantly higher at the entrance, and progressively decreasing along the flow direction.

Consequently, the heat transfer coefficient h is expected to present higher values in the entry region.

In order to calibrate the 1+1D model, the convective heat transfer coefficient was adjusted to characterize the effects of the entry region in the computation of the temperatures.

In order to calibrate h , the heat flux flowing from the cell to the cooling air calculated with COMSOL and the 1+1D model has been compared.

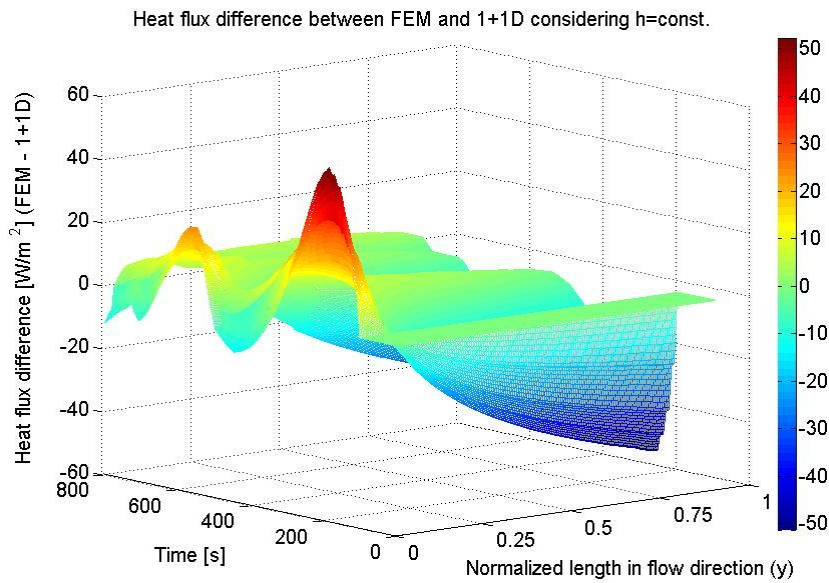


Figure 5.30. Comparison of the heat flux predicted by the FEM and 1+1D model.

From Figure 5.30, a noticeable heat flux difference between the FEM simulation and the 1+1D model prediction can be observed.

It is possible to directly calculate h using the numerical data available from the FEM simulation, considering the fact that the heat flux from the battery cell wall is: $\dot{Q} = Ah(T_w - T_\infty)$.

As a first-order approximation, h has been averaged along the time at each y position. This implies that the heat transfer coefficient is a function only with respect to space (y). Non-dimensionalizing the result with respect to the hydraulic diameter, the calibrated heat transfer coefficient results to be:

$$h = h(y^*) = \frac{70.223}{y^*} + 13.068 \quad (5.12)$$

where $y^* = \frac{y}{D_h}$

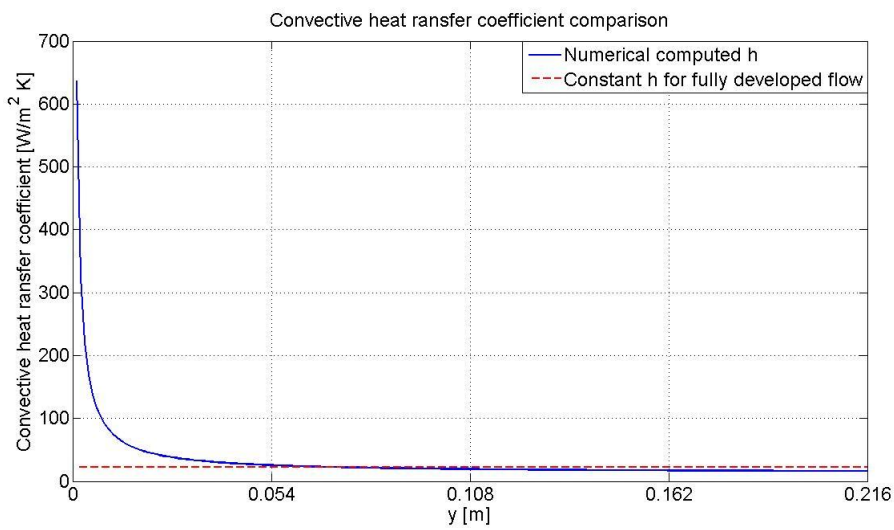


Figure 5.31. Trend of the calibrated heat transfer coefficient.

Comparing again the heat flux computed by the FEM simulator and the flux predicted by the calibrated 1+1D model, it can be noticed that the gap between the two simulations has been significantly reduced.

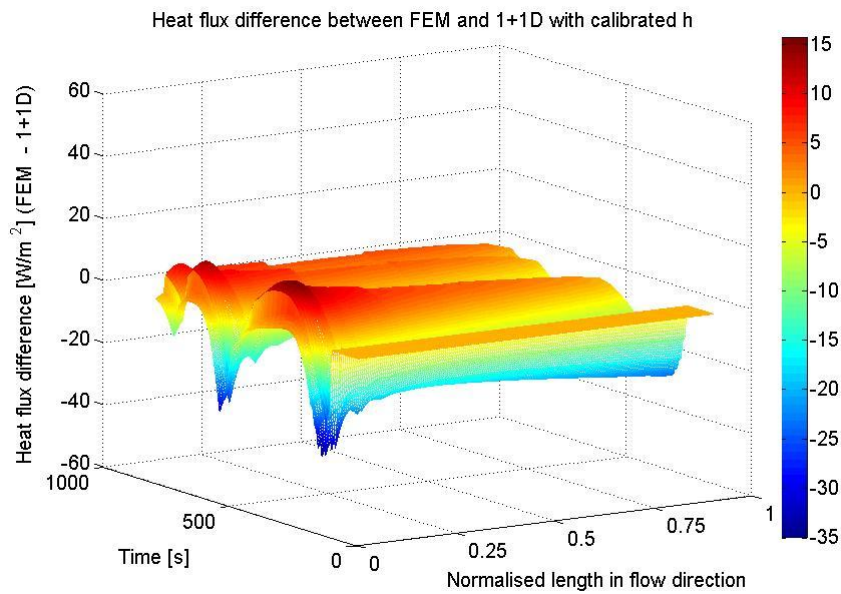


Figure 5.32. Comparison of the heat flux predicted by the FEM and calibrated 1+1D model.

The next three figures show the comparison between the FEM results and the calibrated 1+1D model predictions.

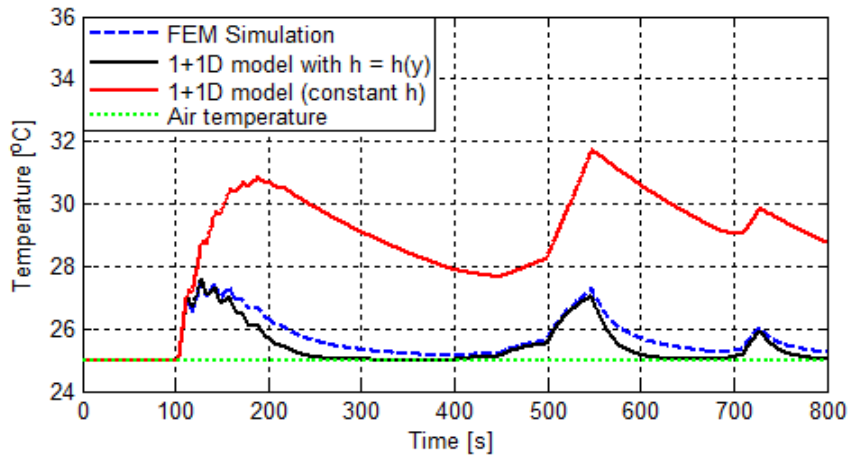


Figure 5.33, Calibrated 1+1D and FEM temperature profiles at $y=0$ mm.

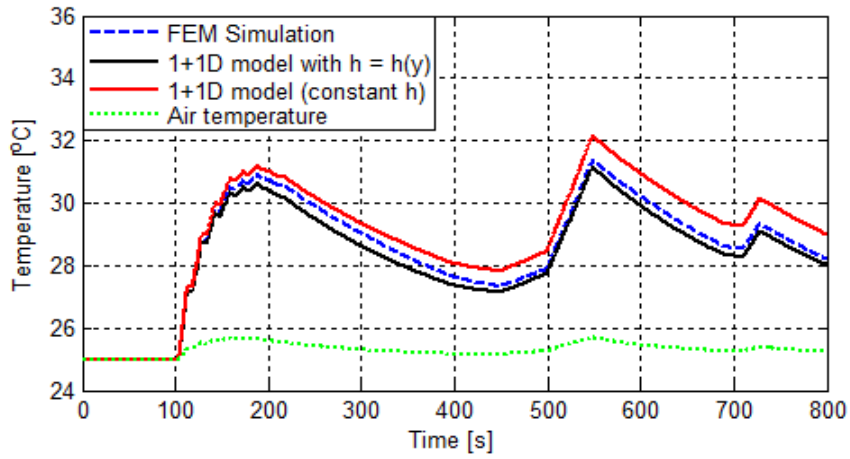


Figure 5.34, Calibrated 1+1D and FEM temperature profiles at $y=54$ mm.

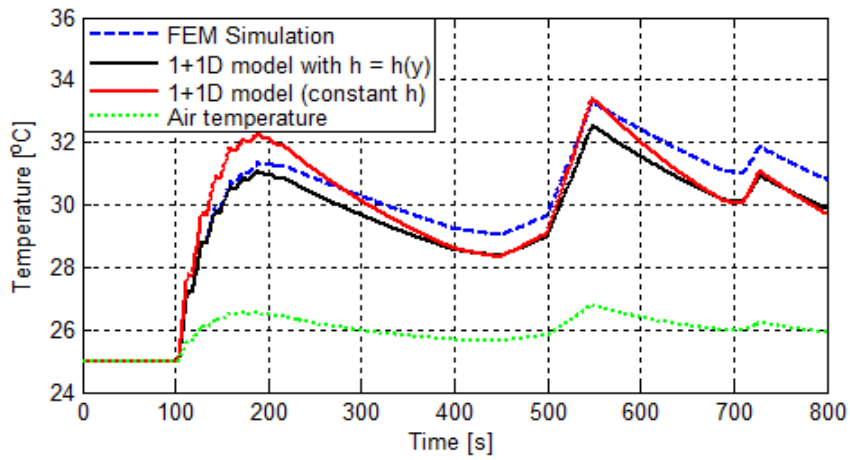


Figure 5.35, Calibrated 1+1D and FEM temperature profiles at $y=216$ mm.

5.5 Summary

In this chapter, the model methodology developed has been applied to a pouch-style Li-Ion battery module cooled by an air flow produced by EiG. First the thermal parameters of the battery cell have been calculated and the heat transfer coefficient has been computed. Then an experimental setup to calibrate and validate thermal models of Li-Ion battery cells has been developed. Starting from this setup, the thermal conductivity of the battery cell has been experimentally measured. The model results have then been compared with a 2D FEM simulation, in order to validate the model.

Although some minor errors between the 1+1D model results and the 2D FEM simulation are present, the developed model results reasonably accurate to predict the temperature distribution within a Li-Ion battery cell. The 1+1D model here developed is computationally more efficient than the FEM software. As a proof, Table 5.10 compares the computation time and memory requirements of the 1+1D model developed in 4.2.3, with reference to the simulation results shown in the above figures.

Table 5.10, Comparison of computational efficiency of different models.

Model	Computation Time [s]	Memory Usage [Mb]
1D	1.5	290
1+1D	58	300
FEM	2100	341

The 1+1D model present a simple structure and the approach used has a general applicability. Its accuracy and computational efficiency make the 1+1D model an ideal candidate to serve application in the area of simulation of battery packs, design of cooling systems and optimization of thermal management systems

CHAPTER 6

6. Conclusions

Li-Ion batteries are today considered the prime solution as energy storage system for EV/PHEV/HEV, due to their high specific energy and power. Since their performance, life and reliability are quite dependent on the operating temperature, great interest has been devoted to study solutions for cooling and control algorithms for battery thermal management.

This thesis has presented a computationally efficient, low-order modeling methodology to predict the dynamic temperature distribution in a prismatic Li-Ion battery cell. The modeling approach developed is general, in a sense that it can predict the temperature distribution within a cell under different conditions. Unlike most control-oriented models based on system identification techniques, the proposed approach relies only on physical principles. These models can find applications in the area of simulation and optimization of battery cooling systems.

In Chapter 4, a general one-dimensional thermal model has been developed to predict the temperature distribution inside a prismatic Li-Ion battery cell under different boundary and initial conditions. A one-dimensional boundary-value problem for heat diffusion in unsteady conditions has been defined and analytically solved, applying the integral transformation method.

To characterize the effects of the cooling system on the temperature distribution within the cell, the one-dimensional solution has been then extended to a 1+1D approach that accounts for the variability of the boundary conditions.

The modeling approach developed is characterized by a general structure, which allows one to easily select cooling parameters, such as cooling air velocity, air temperature, air duct geometry, etc., and compare the effects of different cooling systems. The approach adopted ensures consistency with the physical behavior of the system and relies on a limited set of physical parameters that can be obtained from the open literature, or calibrated if experiments or FEM simulation results are available.

In particular, a 1+1D model, with convective boundary conditions, was developed. An *ad hoc* experimental set-up has been developed to calibrate the thermal parameters of the model and a comparison with a FEM simulator was used to validate the results, as discussed in Chapter 5.

The consistency with the FEM solution, the simple structure, and the computational efficiency make the model an ideal candidate for simulation of battery packs, design of cooling systems or thermal management systems.

The models developed can serve application in the area simulation of battery packs performance, design of cooling systems and optimization of thermal management systems or as a tool to support the calibration of reduced-order electro-thermal battery dynamic models for on-board implementation.

6.1 Future work

In order to further validate the modeling approach proposed in this work, an experimental setup is being planned to measure the surface temperature distribution on a prismatic Li-Ion cell. The experimental setup has already been developed and the experiments are currently planned.

This would allow comparing the models predictions with experimental data and thus verifying the accuracy of the modeling approach and the consistency of the assumptions made.

The same methodology, moreover, can be applied to cylindrical cell, in order to compare the effect of the geometry on the thermal issues.

The models developed can be used for a comparative analysis of different cooling technologies or to develop a thermal management system, interfacing the simulator with a control algorithm.

Bibliography

- [1] D. Linden and T. Reddy, *Handbook of batteries*, third edition ed.: McGraw - Hill, 2001.
- [2] M. Wakihara, "Recent developments in lithium ion batteries," *Material Science and Engineering*, vol. R33, pp. 109-134, 2001.
- [3] T.Q. Duong, "Challenges in Developing Batteries for PHEV Applications," *First International Conference on Advanced Lithium Batteries for Automobile Applications*, Argonne National Laboratory, 2008.
- [4] S. Onori, L. Serrao, Y. Guezennec, and G. Rizzoni, "A Novel Model-Based Algorithm for Battery Prognosis," *7th IFAC Safeprocess Conference, 2009*.
- [5] Steve James, "ANALYSIS - The Lithium Boom Is Coming: The New Bubble?," *Reuters*, May 2009.
- [6] G. Bruscatello, G. Pedè, E. Vitale, and et al., *Sistemi di propulsione elettrica e ibrida.*: ENEA, 2009.
- [7] A. Pesaran, "Battery thermal models for hybrid vehicle simulations," *Journal of Power Sources*, no. 110 (2002) 377-382, 2001.
- [8] J. Newman and C. Pals, "Thermal Modeling of the Lithium/Polymer Battery - I Discharge behavior of a single cell," *Journal Electrochemical Society*, vol. 142, no. 10, 1995.
- [9] J. Newman and C. R. Pals, "Thermal Modeling of the Lithium/Polymer Battery - II Temperature profile in a cell stack," *Journal Electrochemical Society*, vol. 142, no. 10, 1995.
- [10] C.C. Wan, Y.Y. Wang S.C. Chen, "Thermal analysis of lithium-ion batteries," *Journal of Power Sources*, no. 140 (2005) 111-124, 2004.
- [11] M. Necati Ozisik, *Boundary value problems of heat conduction*. Scranton, Pennsylvania: International textbook company, 1969.
- [12] Ahmad A. Pesaran, "Battery Thermal Management in EVs and HEVs: Issues and Solutions," , Advanced Automotive Battery Conference, Las Vegas, Nevada, February 6-8, 2001.
- [13] J., Kalaitakis, K., Voulgaris, N. C Chatzakis, "Designing a New Generalized Battery Management," *IEEE Transactions on Industrial Electronics*, vol. 50(5), 2003.
- [14] L., Chehab, Z., Guezennec, Y., and Rizzoni, G. Serrao, "An aging Model of NiMH batteries for Hybrid Electric Vehicles," *Proceedings of the 2005 IEEE Vehicle Power*, 2005.
- [15] S., Perrin., M., and Jossen, A Piller, "Methods for State-of-Charge Determination and Their Applications," *Journal of Power Sources*, vol. 96,

pp. 113-120, 2001.


- [16] S. Yurkovich, B.J. Yurkovich, Y. Guezennec Hu Y., "Electro-thermal battery modeling and identification for automotive applications," , 2009.
- [17] C., Du, D., Liu, Z., and Ge, J. Cai, "State-of-Charge (SoC) estimation of high power NI-MH rechargeable battery with artificial neural network," *In Proceedings of the 7th World Congress on Intelligent Control and Automation*, 2010.
- [18] P., Fennie, C., and Reisner, D Singh, "Fuzzy Logic Modelling of State-of-Charge and Available Capacity of Nickel/Metal Hydride Batteries," *journal of power sources*, vol. 136, pp. 322-333, 2004.
- [19] Plett G., "Extended Kalman Filtering for Battery Management Systems of LiPB-Based HEV Battery Packs, part 3," *Journal of power sources*, vol. 134, pp. 277-292, 2004.
- [20] I. Kim, "The Novel State of Charge Estimation Method for Lithium Battery using Sliding Mode Observer," *Lournal of Power Sources*, vol. 163, pp. 584-590, 2006.
- [21] B.J. Yurkovich, S. Yurkovich, Y. Guezennec Y. Hu, "Electro-thermal battery modeling and identification for automotive applications," *Proceedings of the 2010 DSCC Conference*, 2010.
- [22] et al, *Advances in Lithium-Ion Batteries.*: Walter van Schalkwijk , B. Scrosati.
- [23] M. Muratori, N. Ma, M. Canova, and Y. Guezennec, "A 1+1D Thermal Dynamic Model of a LI-Ion Battery Cell," *ASME Dynamic Systems and Control Conference*, 2010.
- [24] Vlahinos A., Burch S.D. Pesaran A., "Thermal Performance of EV and HEV Battery Modules and Packs," , 1997.
- [25] T.F. Fuller, M. Doyle, and J. Newman, "Simulation and Optimization of the Dual Lithium Ion Insertion Cell," *Journal of electrochemical society*, vol. 141, January 1994.
- [26] Q. Guo, P. Ramadass, R.E. White S. Santhanagopalan, "Review of models for predicting the cycling performance of lithium ion batteries," *Journal of power sources*, vol. 156, pp. 620-628, 2006.
- [27] M. Doyle, T.F. Fuller, and J. Newman, "Modeling of Galvanostatic Charge and Discharge of the Lithium/Polymer/Insertion Cell," *Journal of electrochemical society*, vol. 140, June 1993.
- [28] J. Larminie and A. Dicks, *Fuell Cell Systems Explained.*: Wiley, 2003.
- [29] B. Haran, P.M. Gomadam, R.E. White, B.N. Popov P. Ramadass, "Development of First Principles Capacity Fade Model for Li-Ion Cells," *Journal of electrochemical society*, vol. 151, pp. A196-A203, 2004.

- [30] B.N. Popov, R.E. White G. Sikha, "Effect of Porosity on the Capacity Fade of a Lithium-Ion Battery," *Journal of electrochemical society*, vol. 151 (7), pp. A1104–A1114, 2004.
- [31] W.B. Gu, B.Y. Liaw C.Y. Wang, "Micro-Macroscopic Coupled Modeling of Batteries and Fuel Cell," *Journal of electrochemical society*, vol. 145, 1998.
- [32] D. Tapriyal, R.E. White V.R. Subramanian, *Electrochem. Sol. State Lett.* 7 (9), pp. A259–A263, 2004.
- [33] C. Suozzo, S. Onori, and G. Rizzoni, "Model-Based Fault Diagnosis For NiMH Battery," *1st Annual Dynamic Systems and Control Conference, October 20-22, 2008, Ann Arbor, Michigan, USA*.
- [34] Yann Guezennec B.J. Yurkovich, "Lithium-ion dynamic battery pack model and simulation for automotive applications," , 2009.
- [35] The Mathworks, Inc R.A. Jackey, University of Colorado G. L. Plett, and COMpact Power, Inc M. J. Klein, "Parametrization of a Battery Simulation Model Using Numerical Optimization Methods," 2009.
- [36] Thomas K.E., Hafezi H., Wheeler D.R. Newman J., "Modeling of lithium-ion batteries," *Journal of Power Sources*, no. 119–121 (2003) 838–843, 2003.
- [37] D. Bernardi, E. Pawlikowski, and J. Newman, "A General Energy Balance for Battery Systems," *Journal of Electrochemical Society*, vol. 132, no. 1, January 1985.
- [38] Gi-Heon Kim, Keyser M. Pesaran A., "Integration Issues of Cells into Battery Packs for Plug-in and Hybrid Electric Vehicles," , EVS24 International Battery, Hybrid and Fuel Cell Electric Vehicle Symposium, 2009.
- [39] K. W. Choi, N. P. Yao, and C. C. Christianson Johnsee Lee, "Three-Dimensional Thermal Modeling of Electric Vehicle Batteries,".
- [40] Y. Kobayashi, Y. Watanabe, Y. Watase, Y. Kitamura Y. Inui, "Simulation of temperature distribution in cylindrical and prismatic lithium ion secondary batteries," *Energy Conversion and Management*, no. 48 (2007) 2103-2109, 2006.
- [41] M. Hoh, G. Houchin-Miller, J. Fuhr Ch. Kuper, "Thermal Management of Hybrid Vehicle Battery Systems," , EVS24 International Battery, Hybrid and Fuel Cell Electric Vehicle Symposium, 2009.
- [42] S. Yurkovich, B.J. Yurkovich, Y. Guezennec Yiran Hu, "Electro-thermal battery modeling and identification for automotive applications," , 2009.
- [43] Yunus A. Çengel, *Heat Transfer: A Practical Approach, 2nd edition.*: McGraw-Hill, 2003.

- [44] Frank P. Incropera and David P. De Witt, *Fundamentals of heat and mass transfer - 5th edition.*: WILEY.
- [45] W.M. Kays A.L. London, *Compact heat exchangers.*: Krieger, 1994.
- [46] I. G. Currie, *Fundamental mechanics of fluids.*: Marcel Dekker, 2003.
- [47] J. H. Lienhard, *A heat transfer textbook*, Third edition ed.: Phlogiston press, 2008.
- [48] Vedat S. Arpaci, *Conduction heat transfer.*: Addison-Wesley.
- [49] Ralph Dinwiddie, S.S. Babu, Giorgio Rizzoni, Bharat Bhushan, Tim Frech Shrikant C. Nagpure, "Thermal diffusivity study of aged Li-ion batteries using flash method," *Journal of power sources*, no. 195 (2010) 872-876, 2009.
- [50] M. Muratori, M. Canova, Y. Guezennec, and G. Rizzoni, "A Reduced-Order Model for the Thermal Dynamics of Li-Ion Battery Cells".
- [51] R. Haberman, *Applied Partial Differential Equations*, 4th ed.: Pearson, 2004.
- [52] Masanori Monde, "Analytical method in inverse heat transfer problem using," *International Journal of Heat and Mass Transfer*, vol. 43, p. 3965±3975, 2000.
- [53] J. I. Frankel and M. Keyhani, "A Global Time Treatment for Inverse Heat Conduction Problems," *Journal of Heat Transfer*, vol. 119, November 1997.
- [54] R.K. Shah and A.L. London, *Advanced in heat transfer: Laminar flow forced convection in ducts.*: Academic Press, 1978.
- [55] J. Schiff, *The Laplace Transform.*: Springer, 1999.
- [56] E. A. Foumeny and P. J. Heggs, *Heat exchange engineering - compact heat exchangers: techniques of size reduction.*: Ellis Horwood Ltd, 1993.
- [57] Electropaedia. [Online]. <http://www.mpoweruk.com/>
- [58] A.A: Samarskii and P.N. Vabishchevich, *Computational heat transfer - Mathematical modelling.*: Wiley, 1995.
- [59] P. Ramadass, Bala Haran, Ralph White, and N. Popov, "Capacity fade of Sony 18650 cells cycled at elevated temperatures. Part II. Capacity fade analysis," *Journal of power sources*, vol. 112, 2002.
- [60] P. Ramadass, Bala Haran, Ralph White, and N. Popov, "Capacity fade of sony 18650 cells cycled at elevated temperatures Part I. Cycling performance," *Journal of power sources*, vol. 112, 2002.
- [61] W.J. Minkowycs and E.M. Sparrow, *Advances in numerical heat transfer - vol. II.*: Taylor and Francis, 2000.
- [62] P.C. Butler, R.G. Jungst, E. P. Roth D. H. Doughty, "Lithium battery thermal models," *Journal of Power Sources*, no. 110 (2002) 357 363, 2002.

- [63] Jackey R.A. - The Mathworks, Inc., "A simple, Effective Lead-Acid Battery Modeling Process for Electrical System Component Selection," 2007.
- [64] Johnsee Lee, "Battery thermal modeling - The methodology and applications,".
- [65] S. Onori, G. Rizzoni, Y. Guezennec L. Serrao, "A Novel Model-Based Algorithm for Battery Prognosis," *7th IFAC Safeprocess Conference*, 2009.
- [66] K. Smith, T. Markel A. Pesaran, "Impact of the 3Cs of Batteries on PHEV Value Proposition: Cost, Calendar Life and Cycle Life," *9th Advanced Automotive Battery Conference*, 2009.
- [67] Y. Hu, S. Yurkovich, Y. Guezennec, and R. Bornatico, "Model-Based Calibration for Battery Characterization in HEV Applications," *Proceedings of American Control Conference*, 2008.
- [68] J. Marcicki, S. Onori, and G. Rizzoni, "Nonlinear fault detection and isolation for a lithium-ion battery management system".
- ELSEVIER Journal of Power Sources
<http://www.sciencedirect.com/science/journal/03787753>
 - ECS The electrochemical society
<http://www.ecsdl.org/>
 - Electropaedia
<http://www.mpoweruk.com>
 - SAE Digital Library
<http://www.sae.org/servlets/index>
 - The SAO / NASA Astrophysics data system
<http://adsabs.harvard.edu/>
 - National Renewable Energy Laboratory
<http://www.nrel.gov/>

Appendix A: Product specification ePLBc020B

	PRODUCT SPECIFICATION	Rev. 03	Page 1/10
	ePLB C020B (Lithium Ion Polymer Battery)	Date	2009.04.02

PRODUCT SPECIFICATION
 for
Rechargeable Lithium Ion Polymer Battery

Model : ePLB C020B


Revision History

Revision	Date	Originator	Reason for change
0	2007-06-30	M.H.CHO, C.S.KIM	Original Release
1	2008-02-05	H.Y.LEE, C.S.KIM	Change in thickness
2	2008-09-01	H.Y.LEE	Change in weight
3	2009-04-02	H.Y.LEE	Change in Charge Cut-Off Voltage

Approval	Prepared	Reviewed	Approved
	/	/	/
Agreement	Production	Sales	Quality
	/	/	/

EIG, Ltd.

16 Block 1 Lot, the 4th provincial industrial complex, Mosi-ri
 Jiksan-eup, Cheonan-city, Chungcheongnam-do, Korea, 330-814
 TEL : + 82-41-589-5134 FAX : + 82-41-589-5147


	PRODUCT SPECIFICATION	Rev.	Page
		03	2/10
ePLB C020B (Lithium Ion Polymer Battery)		Date	2009.04.02

CONTENTS

1. Scope
2. Description and Model Name
3. Nominal Specifications
4. Dimension
5. Appearance
6. Standard Test Conditions
7. General Characteristics
8. Environmental Characteristics
9. Safety Characteristics
10. Warranty
11. Others

[Attachment]

1. Drawing of ePLB C020B

 PRODUCT SPECIFICATION	Rev.	Page
	03	3/10
ePLB C020B (Lithium Ion Polymer Battery)		Date
		2009.04.02

1. Scope

This Product Specification has been prepared to specify the rechargeable LIPB (Lithium Ion Polymer Battery) to be supplied to the customer by **EiG, Ltd.**


2. Description and Model Name

2-1 Description : Rechargeable LIPB (Lithium Ion Polymer Battery).

2-2 Model : ePLB C020B.

3. Nominal Specifications

Item	Specification
3-1 Nominal Capacity	20 Ah
3-2 Nominal Voltage	3.65 V
3-3 Standard Charge Method	CC(constant current) : 10 A and CV(constant voltage) : 4.15 V to 1 A
3-4 Rapid Charge Method	CC(constant current) : 20 A and CV(constant voltage) : 4.15V to 1 A
3-5 Standard Discharge Method	CC(constant current) : 10 A to 3.0 V
3-6 Max. Discharge Current (continuous)	100 A
3-7 Peak Discharge Current (peak < 10sec)	200 A
3-8 Cell Dimension	Thickness : 7.2±0.2 mm (Fully charged state)
	Width : 129±0.5 mm
	Length : 216±1.0 mm
3-9 Operation Temperature	Charge : 0 to 40℃
	Discharge : -30 to 55℃
3-10 Storage Temperature	1 year : -30~25℃
	3 month : -30~45℃
	1 month : -30~55℃
3-11 Weight	426±3 g

	PRODUCT SPECIFICATION	Rev.	Page
		03	4/10
ePLB C020B (Lithium Ion Polymer Battery)		Date	2009.04.02

4. Dimension

See the attachment (Appendix 1).

5. Appearance

There shall be no such defect as scratch, rush, discoloration and leakage which may adversely affect commercial value of the cell.

6. Standard Test Conditions

6-1 Environmental Condition

Unless otherwise specified, all tests stated in this specification are conducted at temperature of 25°C.

6-2 Measuring Equipment

(1) Ammeter and Voltmeter

The ammeter and voltmeter should have an accuracy of the grade 0.5 or higher.

(2) Slide caliper

The slide caliper should have 0.05 mm scale.

(3) Impedance meter

The impedance meter with AC 1 kHz should be used.

7. General Characteristics


7-1 Standard Charge

Charging with condition of CC(10 A)/CV(4.15 V to 1 A) at 25°C.

7-2 Standard Minimum Discharge Capacity

Capacity measured with CC(10 A) discharge to 3.0 V at 25°C within 2.5 hours after the standard charge.

Standard Minimum Discharge Capacity \geq 19.8 Ah

	PRODUCT SPECIFICATION	Rev.	Page
		03	5/10
ePLB C020B (Lithium Ion Polymer Battery)		Date	2009.04.02

7-3 Initial Internal Impedance

Internal impedance measured with fresh cell at AC 1 kHz after standard charge.

Initial internal impedance < 3 mΩ.

7-4 Charge Rate Capabilities

Capacity measured with condition of CC(various current below)/CV(4.15 V to 1 A) at 25°C after the cell is discharged with standard discharge method.

Current	0.2C (4 A)	0.5C (10 A)	1.0C (20 A)
Cut-off	0.05C (1 A)	0.05C (1 A)	0.05C (1 A)
Relative Capacity	>100%	100%	>95%

7-5 Discharge Rate Capabilities

Capacity measured with CC(various current below) discharge to 3.0 V at 25°C after the cell is charged with standard charge method.

Current	0.3 C (6 A)	0.5C (10 A)	1C (20 A)	5C (100 A)
Relative Capacity	>100%	100%	>95%	>80%

7-6 Temperature Dependence of Discharge Capacity

Capacity measured with CC(10 A) discharge to 3.0 V at various temperature below after the cell is charged with standard charge method.

Discharge Temperature	-20°C	-10°C	0°C	25°C	40°C	55°C
Relative Capacity	>45%	>65%	>85%	100%	>100%	>100%


7-7 Cycle Life

Capacity retention after 100, 500, 800 and 1000 cycles with the charge/discharge condition below.

- charge : CC(20 A)/CV(4.15 V to 1 A or 2.5 hr) at 25°C

- discharge : CC(20 A) to 3.0 V at 25°C

Cycle No.	1 st	100 th	500 th	800 th	1000 th
Relative Capacity	100%	>95%	>90%	>85%	>80%

	PRODUCT SPECIFICATION	Rev.	Page
		03	6/10
ePLB C020B (Lithium Ion Polymer Battery)		Date	2009.04.02

8. Environmental Characteristics

8.1 Vibration Test

(1) Test method

- Frequency: 10 Hz → 55 Hz → 10 Hz
- Amplitude: 0.8 mm
- Sweep speed: 1 ± 0.055 Hz/min

(2) Criteria

- No loss of functionality without apparent damage such as leakage, bulging, smoke and flame.


8.2 Thermal Shock

(1) Test method

- (i) Charge the cell with standard charge method.
- (ii) Store the cell at -40°C for 2 hours and then.
- (iii) Store the cell at 80°C for 2 hours.
- (iv) Repeat the step (ii) to (iii) 20 times.

(2) Criteria

- No loss of functionality without apparent damage such as leakage, bulging, smoke and flame.
- Change of cell thickness < 5%.
- Recovered capacity (standard discharge capacity) > 80%.

	PRODUCT SPECIFICATION	Rev.	Page
		03	7/10
ePLB C020B (Lithium Ion Polymer Battery)		Date	2009.04.02

8.3 Humidity

(1) Test method

- (i) Charge the cell with standard charge method.
- (ii) Store the cell at 50°C and 95%RH condition for 10 days.

(2) Criteria

- No loss of functionality without apparent damage such as leakage, bulging, smoke and flame.
- Change of cell thickness < 5%.
- Recovered capacity (standard discharge capacity) > 80%.

8.4 High Temperature Swelling

(1) Test method:

- (i) Charge the cell with standard charge method.
- (ii) Store the cell at 60°C for 24 hours.

(2) Criteria

- No loss of functionality without apparent damage such as leakage, bulging, smoke and flame.
- Change of cell thickness < 5%.
- Recovered capacity (standard discharge capacity) > 80%.

9. Safety Characteristics


9.1 Overcharge Test

(1) Test method

- (i) Charge the cell with standard charge method.
- (ii) Charge the cell with condition of CC(20 A)/CV(5 V for 2.5hr).

(2) Criteria

- No fire and no explosion.

	PRODUCT SPECIFICATION	Rev.	Page
		03	8/10
ePLB C020B (Lithium Ion Polymer Battery)		Date	2009.04.02

9.2 External Short Circuit Test

(1) Test method

- (i) Charge the cell with standard charge method.
- (ii) Connect the positive and negative terminal with a wire less than 100 mΩ for 2.5 hrs.

(2) Criteria

- No fire and no explosion.

9.3 Overdischarge Test

(1) Test method

- (i) Charge the cell with standard charge method.
- (ii) Discharge the cell with condition of CC(20 A) for 1.5hrs or achieved voltage reversal for 15 minutes.

(2) Criteria

- No fire and no explosion

9.4 Nail Penetration Test

(1) Test method

- (i) Charge the cell with standard charge method.
- (ii) Penetrate the center of the cell vertically with a metallic nail of 5 mm diameter at a rate of 40mm/sec.

(2) Criteria

- No fire and no explosion.


9.5 Hot Box Test

(1) Test method

- (i) Charge the cell with standard charge method.
- (ii) Heat the cell up to 160°C at a rate of 5°C/minute.
- (iii) Keep the cell at 160°C for 10 minutes.

(2) Criteria

- No fire and no explosion.

	PRODUCT SPECIFICATION	Rev.	Page
		03	9/10
ePLB C020B (Lithium Ion Polymer Battery)		Date	2009.04.02

9.6 Crush Test

(1) Test method

- (i) Charge the cell with standard charge method.
- (ii) Crush the cell with 13 kN force against the longitudinal and lateral axis of the cell.

(2) Criteria

- No fire and no explosion.

9.7 Impact Test

(1) Test method

- (i) Charge the cell with standard charge method.
- (ii) Place a bar of 8 mm diameter across the longitudinal and lateral axis of the sample cell.
- (iii) Drop 9.1 kg weight onto the bar from 61 cm height.

(2) Criteria

- No fire and no explosion.

10. Warranty

EIG, Ltd. will be responsible for any defect for 6 months from the date of manufacturing, as long as the cell is treated in accordance with the Product Specification and Handling Caution. Any other problem caused by malfunction of the equipment or unsuitable use of the cell is not under this warranty.


11. Others

11.1 Storage for a long time

When the cell is kept for a long time (3 months or more), it is recommended to be preserved at dry and low temperature condition.

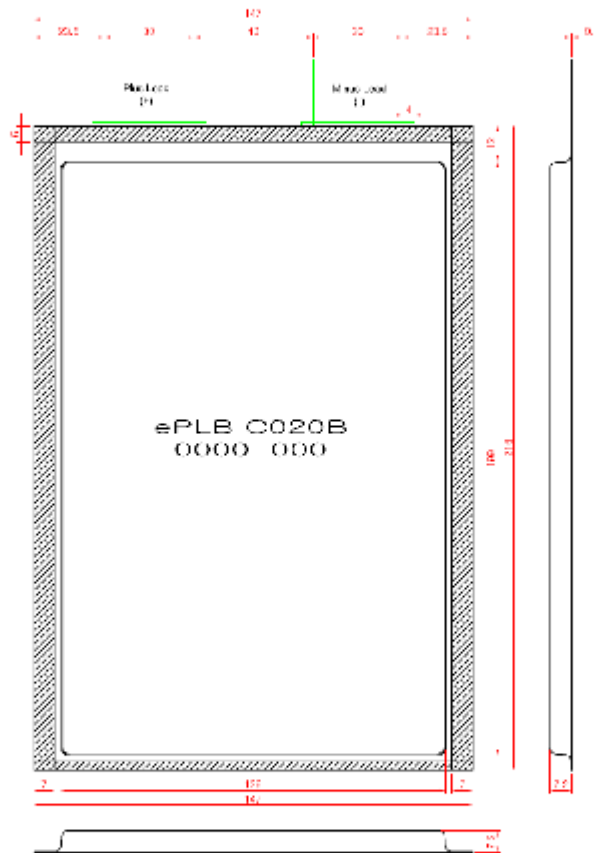
11.2 Other

Any matter that was not described in this Specification should be conferred with EIG, Ltd.

	PRODUCT SPECIFICATION	Rev.	Page
		03	10/10
ePLB C020B (Lithium Ion Polymer Battery)		Date	2009.04.02

[Appendix 1]

■ Drawing of ePLB C020B



Nominal Capacity		20 Ah
Nominal Voltage		3.86 V
Weight		426 g
Energy	Volume	880 Wh/L
Density	Weight	176 Wh/kg
AC Impedance (1 kHz)		< 8 mΩ

Appendix B: A reduced order model for the thermal dynamics of Li-Ion battery cells

CONFIDENTIAL. Limited circulation. For review only.

A Reduced-Order Model for the Thermal Dynamics of Li-Ion Battery Cells

Matteo Muratori*
Marcello Canova, Yann Guezennec, Giorgio Rizzoni**,¹

* Dipartimento di Energia - Politecnico di Milano,
Via Lambruschini 4, 20156 Milano - Italy.

** Center for Automotive Research - The Ohio State University,
930 Kinnear Rd, Columbus OH, 43212, USA.

Abstract: The electro-thermal dynamics of Li-Ion batteries for EVs and PHEVs applications is a topic of critical importance today. For applications related to control and diagnostics, the behavior of a battery pack is typically modeled using an equivalent circuit analogy approach. The model parameters, such as the open-circuit voltage and the battery internal resistance, are generally scheduled with respect to the temperature, which is often regarded as static input to the model. However, due to the internal heat generation and the conductivity of the materials, battery cells are characterized by a time-varying internal temperature that may be considerably different from the measured surface temperature. The phenomenon, often overlooked in these simplified models, must be properly accounted for in control-oriented applications, such as battery pack performance analysis, cell balancing, diagnostics and residual life estimation. This work proposes a control -or energy management- oriented model of the thermal dynamics of a prismatic Li-Ion cell, which predicts the internal temperature. Unlike most control-oriented models based on system identification techniques, the proposed approach defines a one-dimensional boundary-value problem for heat diffusion in unsteady conditions, which is solved by applying the Laplace transform and further reduced to a low-order linear model using the singular perturbation method. The model prediction is validated by comparison with the analytical solution of the boundary-value problem, for different charging/discharging profiles, and uses data acquired from experimental studies for additional validation.

Keywords: Control Oriented Models, Model Order Reduction, Thermal Systems, Lithium-Ion Batteries, Automotive

1. INTRODUCTION

The advancements in battery technology has been the driving force behind the recent developments in Plug-in Hybrid Electric Vehicles (PHEVs) and Battery Electric Vehicles (BEV). In particular, Lithium ion (Li-Ion) batteries provide high energy and power density energy storage to allow for extended all-electric driving.

For efficient and reliable utilization on the vehicle, the battery management systems (BMS) must continuously monitor the battery pack performance in order to protect the battery from premature aging and performance degradation (Chatzakis et al. (2003)). Model based battery monitoring algorithms, of particular importance in high power applications, use current and voltage measurements to estimate state of charge (SoC), available power, state of health (SoH) and temperature with interacting control systems based upon these estimates (Verbrugge and Koch (2006)).

The characterization and modeling of the electro-thermal dynamics of Li-Ion batteries is a topic of critical importance. In particular, control-oriented models that are capable of predicting the thermal dynamics of the system can

be a powerful tool to evaluate the impact of temperature on the battery life, as well as to improve the performance of a BMS and guarantee reliable operations of such energy storage systems.

However, the design of low-order electro-thermal models of battery cells is challenging. Models based on first principles (referred to as electrochemical models) are generally not suitable for control and estimation applications due to their inherent complexity in describing the chemical behavior of the cell (for example, as in Newman et al. (2003)). For this reason, phenomenological models based on the equivalent circuit analogy are often used as a compromise between accuracy and complexity (for example, see Hu et al. (2009)).

Equivalent circuit models contain several parameters, such as the open-circuit voltage, battery internal resistance and the dominant time constants, which are generally scheduled with respect to the battery SoC and temperature. In particular, the latter is often regarded as a static input to the model. The parameters identification is typically done with experimental data, using a set-up consisting of a programmable load that imposes a determined current profile to reproduce various battery usage conditions. A Peltier junction maintains the surface temperature of the

¹ Corresponding Author (M. Canova). Email: canova.1@osu.edu.

battery cell at a prescribed value. Thus, for model calibration, it is commonly assumed that the battery temperature is uniform and constant during the test.

However, experimental and CFD studies have demonstrated that, due to the internal heat generation and the conductivity of the materials, battery cells are characterized by a specific internal temperature distribution that may significantly differ from the measured surface temperature (for instance, see Chen et al. (2005) or Pesarin (2002)). Furthermore, the battery temperature is a dynamic state that may vary significantly during a test, with respect to the current input.

Such phenomena, which are often overlooked in these simplified models, should be accounted for to ensure safe operations, for diagnostics and residual life estimation. For instance, large temperature variations within the cell may lead to premature aging of the battery, hence the importance of including the prediction of the internal battery thermal behavior in system integration and control.

In this scenario, this paper proposes a control-or energy management-oriented model of the thermal dynamics of a prismatic Li-Ion cell, which predicts the internal temperature. Unlike phenomenological models, based on system identification methods, the proposed model relies on a physically-based approach based on the fundamentals of conduction heat transfer. Starting from the one-dimensional boundary-value problem of heat diffusion in unsteady conditions, a control-oriented model is found by applying a model order reduction method in the frequency domain.

2. STATEMENT OF THE PROBLEM

The objective is to design a low-order dynamic model that predicts the core temperature of a Li-Ion battery cell given the current demand and the output voltage. The system considered in the study, shown in figure 1, represents an experimental set-up typically utilized to generate calibration data for electro-thermal battery model identification. The set-up consists of a prismatic $LiFePO_4$ cell inserted in an aluminum casing. The temperature of the casing is controlled to a constant value by a Peltier junction. Due

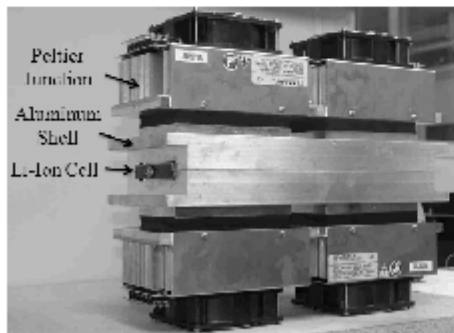


Fig. 1. A Peltier junction for prismatic cell testing.

to the high thermal conductivity of the aluminum and the

higher mass of the casing compared to the battery, it is reasonable to assume negligible temperature gradients within the casing. Hence, the external surface of the battery can be considered an input to the model. Further, due to the Joule effect and irreversibilities, heat is generated inside the battery at a rate depending on the current profile. It is also reasonable to assume that the generation term is uniformly distributed within the cell and only time dependent.

From a system dynamics standpoint, the battery cell can be considered as a MISO system, where the inputs are the heat generation rate and the external temperature, and the output is the internal temperature. In particular, the model will be solved for the temperature at the center of the cell, which is the peak value of the distribution since all the heat generated internally is removed only at the external surface.

3. MODEL DEVELOPMENT

In order to define the heat transfer problem and design the model, the battery cell is represented as a homogeneous slab of thickness $2L$. Note that, although the mathematical formulation of the problem is developed for a prismatic geometry, the proposed approach could be easily generalized to cylindrical cells.

Let x be the coordinate across the wall, T_w the wall temperature (set by the Peltier junction), and \dot{q} the rate of heat generated inside the battery. The heat generation rate, as well as the material properties, are considered homogeneous and isotropic. Figure 2 shows the scheme adopted by the model.

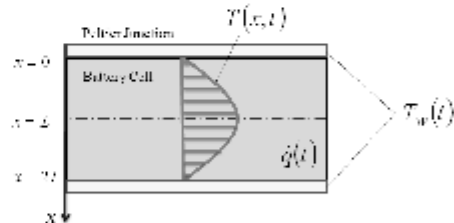


Fig. 2. Schematic of the cell geometry for the thermal model.

Assuming $T = T(x, t)$ the temperature at position x and time t , the heat transfer problem can be cast in the form of a Boundary-Value Problem (BVP) for a case of one-dimensional, unsteady heat conduction (Incropera et al. (1996); Arpaci (1966)):

$$\frac{\partial^2 T(x, t)}{\partial x^2} + \frac{1}{k} \dot{q}(t) = \frac{1}{\alpha} \frac{\partial T(x, t)}{\partial t} \quad (1)$$

where $\alpha = k(\rho c_p)^{-1}$, being k the spatially-averaged thermal conductivity of the cell, ρ the average density and c_p the specific heat. The above parameters were calculated from experimental data and numerical studies published in the open literature (Nagpure et al. (2009); Pals and Newman (1995)), and are summarized in table 1.

Table 1. List of model parameters

Parameter	Value	Units
$2L$	0.0072	m
k	0.666	$W(mK)^{-1}$
ρ	2,118	$kg(m^{-3})$
c_p	795	$J(kgK)^{-1}$
α	$3.95e^{-7}$	m^2s^{-1}

The rate of heat per unit volume $\dot{q}(t)$ generated inside the cell is computed as in Bernardi et al. (1985):

$$\dot{q}(t) = \frac{I}{V_{cell}} \left(E_0 - E - T \frac{dE_0}{dT} \right) \quad (2)$$

where I is the current, V_{cell} the cell volume, E_0 the open circuit voltage and E the voltage of the cell. For the $LiFePO_4$ cell considered in this study, the last term in equation (2) can be neglected (Hu et al. (2009)), allowing for a partial simplification of problem.

The BVP described by equation (1) is subject to boundary conditions of the first kind (imposed surface temperature). Since both walls are assumed at the same temperature, the cell temperature distribution is symmetric, hence the boundary conditions can be written as:

$$T(x=0, t) = T(x=2L, t) = T_w(t) \quad (3)$$

$$\left. \frac{\partial T(x, t)}{\partial x} \right|_{x=L} = 0$$

The BVP above could be solved numerically, for instance using the finite difference method. Instead, noting that the problem is described by a linear PDE, an analytical solution is found by applying the Laplace transform to the differential equation and boundary conditions. This way, a PDE problem in time domain is cast into an equivalent ODE problem in the complex domain (Doebelin (1980)).

Assuming zero initial condition for equation (1), the transformed BVP is obtained:

$$\frac{d^2 T(x, s)}{dx^2} - a^2 T(x, s) = -\frac{1}{k} Q(s) \quad (4a)$$

$$T(x=0, s) = T_w(s) \quad (4b)$$

$$\left. \frac{dT(x, s)}{dx} \right|_{x=L} = 0 \quad (4c)$$

where $a^2 = s\alpha^{-1}$ and $Q(s)$ is the transform of $\dot{q}(t)$.

Regarding s as a fixed parameter, (4a) is a linear ordinary differential equation, whose general solution can be written in the form:

$$T(x, s) = \frac{1}{ka^2} Q(s) + A(s) \cosh(ax) + B(s) \sinh(ax) \quad (5)$$

where the values of $A(s)$ and $B(s)$ are found by evaluating the boundary conditions (4b)-(4c).

This allows one to determine the general solution of the problem, hence the temperature dynamics at any spatial coordinate x . In particular, the temperature at the cell core is found by evaluating the solution at $x=L$:

$$T_L(s) = T(L, s) = \frac{\alpha \cosh(L\sqrt{\frac{s}{\alpha}}) - 1}{ks \cosh(L\sqrt{\frac{s}{\alpha}})} Q(s) + \frac{1}{\cosh(L\sqrt{\frac{s}{\alpha}})} T_w(s) \quad (6)$$

Equation (6) can be interpreted as the output of a continuous time dynamic system with $u(t) = [\dot{q}(t), T_w(t)]^T$ and $y(t) = T_L(t)$. In this sense, the solution of the BVP is equivalent to the impulse response of the system:

$$T_L(s) = G_1(s) Q(s) + G_2(s) T_w(s) \quad (7)$$

where the transfer functions G_1 and G_2 are transcendental:

$$G_1(s) = \frac{\alpha}{ks} \frac{\cosh\left(L\sqrt{\frac{s}{\alpha}}\right) - 1}{\cosh\left(L\sqrt{\frac{s}{\alpha}}\right)} \quad (8a)$$

$$G_2(s) = \frac{1}{\cosh\left(L\sqrt{\frac{s}{\alpha}}\right)} \quad (8b)$$

Analytical expressions for the inverse transforms for $G_1(s)$ and $G_2(s)$ do not exist. However, it is possible to study the behavior of the above transfer functions in the frequency domain. Figure (3) represents the frequency response of the two transfer functions, where the magnitude is shown in the frequency range of interest.

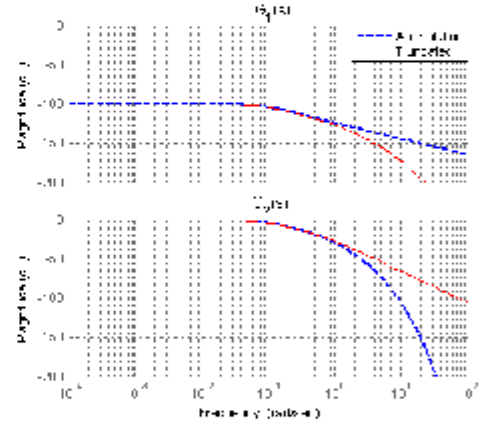


Fig. 3. Frequency response (magnitude) of the transcendental transfer functions G_1 and G_2 . The truncated transfer functions G_1^i and G_2^i ($i=8$), calculated with (12)-(14), are also plotted for comparison.

Since $G_1(s)$ and $G_2(s)$ are transcendental, they are characterized by an infinite number of poles and zeros that, for this case, can be determined analytically. In particular, the two transfer functions have a common set of poles:

$$p_n = -\frac{\pi^2}{L^2} \alpha \left(n - \frac{1}{2} \right)^2, \quad n = 1, 2, \dots \quad (9)$$

while $G_1(s)$ has zeros at:

$$z_n = -\frac{\pi^2}{L^2} \alpha \left(\frac{n-1}{2} \right)^2, \quad n = 1, 2, \dots \quad (10)$$

and the static gains are:

$$\begin{aligned} G_1(0) &= \frac{L^2}{2k} \\ G_2(0) &= 1 \end{aligned} \quad (11)$$

Since all the poles of $G_1(s)$ and $G_2(s)$ are real and negative, the system is stable and the transfer functions are bounded. Moreover, the frequency response plots shown in figure (3) denote that the system behaves as low pass filter.

In particular, $|G_2(j\omega)| \rightarrow 0$ at a faster rate than $|G_1(j\omega)|$, due to the absence of zeros in $G_2(s)$. Due to its faster convergence, $|G_2(j\omega)|$ is almost zero in the high frequency region, hence the transient response of the system is largely dominated by $G_1(s)$.

Based on the above considerations, the frequency behavior of G_1 can be approximated by a truncated transfer function of the form:

$$G_1^i(s) = K_1 \frac{(s-z_1)(s-z_2)\dots(s-z_{i-1})}{(s-p_1)(s-p_2)\dots(s-p_i)} \quad (12)$$

where i is a finite number and the gain K_1 is chosen to equalize the static gains of G_1^i and G_1 :

$$K_1 = G_1(0) \frac{p_1 p_2 \dots p_i}{z_1 z_2 \dots z_{i-1}} \quad (13)$$

Similarly, for the transfer function G_2 ,

$$G_2^i(s) = K_2 \frac{1}{(s-p_1)(s-p_2)\dots(s-p_i)} \quad (14)$$

where

$$K_2 = G_2(0) p_1 p_2 \dots p_i \quad (15)$$

The truncated transfer functions G_1^i and G_2^i ($i = 8$) are compared with G_1 and G_2 in figure (3). It is possible to observe that the transcendental transfer functions, which represent the exact analytical solution of the BVP, are well approximated by the truncated models in the low frequency regions. As expected, the accuracy deteriorates as the frequency increases.

The order of truncation can be chosen in relation with the frequency content of the input signals and the desired bandwidth. In a typical experimental setup for battery characterization, the signals are typically acquired up to a frequency of 10Hz. For applications related to the electro-thermal characterization of EV and PHEV batteries, this can be also considered the maximum frequency of interest.

In principle, the above consideration would allow one to simply truncate the models up to the desired frequency content. However, since the contribution of the higher order poles and zeros is neglected in the truncated system, the resulting model will have limited accuracy.

Figure 3 shows that, for the case considered, a truncation to the 8th order ensures accurate response up to only 1rad/s. In other words, it would be necessary to further increase the order of the model by adding high frequency terms until acceptable accuracy is obtained in the frequency range considered.

For this reason, a model order reduction method could be adopted to generate a model that achieves the accuracy required by the application with minimal complexity. The literature presents many model reduction algorithms for a variety of problems (see Ersal et al. (2008) for a review of proper modeling techniques).

The choice of a reduction algorithm is based on the specific system. In this case, it can be observed that the poles and zeros of G_1 and G_2 increase nearly proportionally to n^2 . Consequently, the difference between the large and small time constants in the system increases, or, in other words, the system tends to become numerically stiff.

For stiff systems where the poles and zeros are known, the singular perturbation method can be adopted to approximate the effects of the higher frequency components on a low order model (Khalil (1996)). In particular, a solution developed by Bhikkaji and Soderstrom (2001) for similar heat transfer problems is here adopted.

The reduction algorithm is based on a partial fractions decomposition of the functions G_1^i and G_2^i , truncated at a sufficiently high number of terms:

$$\begin{aligned} G_1^i(s) &= K_1 \left[\frac{A_1}{s-p_1} + \frac{A_2}{s-p_2} + \dots + \frac{A_i}{s-p_i} \right] \\ G_2^i(s) &= K_2 \left[\frac{B_1}{s-p_1} + \frac{B_2}{s-p_2} + \dots + \frac{B_i}{s-p_i} \right] \end{aligned} \quad (16)$$

where the coefficients A_i and B_i can be analytically calculated (Oppenheim and Schaffer (1975)).

Focusing on $G_1^i(s)$, it is now possible to operate a separation of the transfer function into its low and high frequency modes:

$$G_1^i(s) = G_1^k(s) + H_1(s) \quad (17)$$

where $k < i$ and

$$\begin{aligned} G_1^k(s) &= K_1 \left[\frac{A_1}{s-p_1} + \frac{A_2}{s-p_2} + \dots + \frac{A_k}{s-p_k} \right] \\ H_1(s) &= K_2 \left[\frac{A_{k+1}}{s-p_{k+1}} + \dots + \frac{A_i}{s-p_i} \right] \end{aligned} \quad (18)$$

In accordance to the singular perturbation method, the reduced order model is obtained by truncating $G_1^i(s)$ to $G_1^k(s)$, and then approximating the high frequency modes (here represented by $H_1(s)$) by introducing a correction factor.

The simplest correction is to assume that the effect of the high frequency component $H_1(s)$ is equal to its static gain $H_1(0)$, hence:

$$G_{r,1}(s) = G_1^k(s) + H_1(0) \quad (19)$$

The same holds for the other transfer function:

$$G_{r,2}(s) = G_2^k(s) + H_2(0) \quad (20)$$

The described algorithm was applied to generate the reduced models $G_{r,1}$ and $G_{r,2}$, starting from $G_1^i(s)$ and $G_2^i(s)$ truncated to the 15th order. This order of truncation ensures that accuracy is achieved up to the target frequency of 10rad/s. The resulting reduced model results into a 3rd order system.

The frequency response of the reduced order model is shown in figure 4 in terms of magnitude. The response is compared to the analytical solution of the BVP (equation (8)) and to the truncated models $G_1^i(s)$ and $G_2^i(s)$, where $i = 8$.

As expected, the reduced order models approximate the exact solution for a larger frequency range than the approximate solutions. On the other hand, $G_{r,1}$ and $G_{r,2}$ do not converge to zero as $s \rightarrow \infty$. This stems from

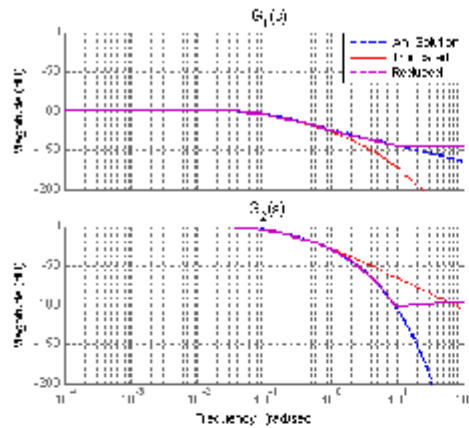


Fig. 4. Frequency response (magnitude) of the transcendental transfer functions G_1 and G_2 , compared to the truncated model (G_1^t , G_2^t) and the reduced order model (G_{r1} , G_{r2}).

the assumption earlier introduced of approximating the high frequency components by their static gains. This simplification procedure is commonly adopted when solving dynamic systems based on fluid dynamics and heat transfer problems. The impact of this approximation on the model is explained by inverse-transforming the reduced order model to time domain and noting that the high-frequency modes have been approximated by impulse function (Bhikkaji and Soderstrom (2001)).

4. RESULTS

The reduced order model was applied to the simulation of the thermal response of a Li-Ion cell during charging-discharging cycles. The experimental data were collected by instrumenting a prismatic $LiFePO_4$ cell (20Ah, 4.1V nominal) with the Peltier junction described in section 2.

The tests were performed by imposing a pulse current profile and measuring the output voltage. The cycle shown in figure 5 is extracted from a 24-hour test performed for the identification of low-order electro-thermal battery models. During the test, the cell surface temperature was controlled to a constant value of $25^\circ C$. The rate of heat generation was computed using equation (2).

In order to provide a meaningful comparison in the absence of direct measurements of the cell internal temperature, the response of the reduced order model was compared to the prediction of a one-dimensional heat transfer model. The 1D model was developed by solving the BVP problem described by equation (1) with the boundary conditions (3), for a uniform grid along the direction x (Ozisik (2002)).

The temperature distribution predicted by the 1D model is shown in figure 6 as a function of the direction x and time. It is worth observing that, although the temperature at the external surface of the battery is set to $25^\circ C$ by the Peltier

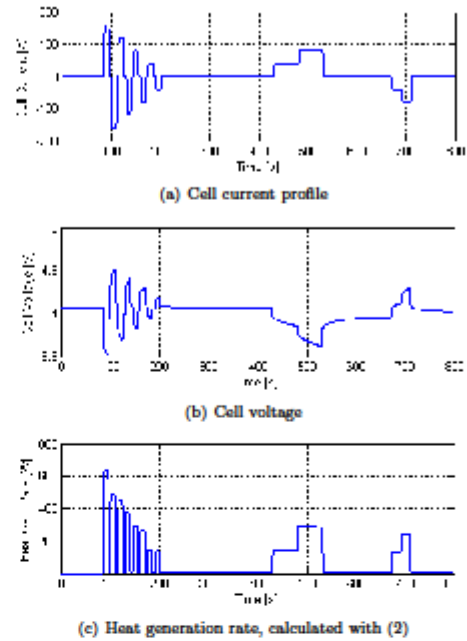


Fig. 5. Results from experimental testing of a $LiFePO_4$ cell for electro-thermal model identification.

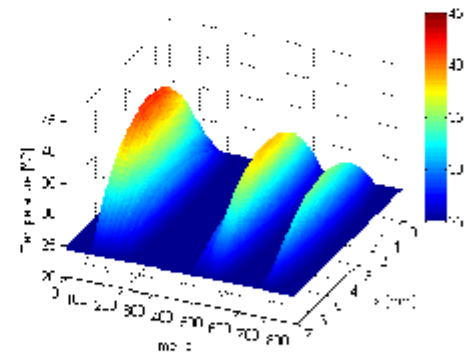


Fig. 6. Temperature distribution calculated by the 1D model along the direction x and time during the test shown in figure 5.

junction during the entire test, the internal temperature may reach considerably higher values due to the internal heat generation and the low thermal conductivity.

Figure 7 compares the temperature at the center of the cell ($x = 3.6mm$) predicted by the truncated model and by the reduced order model, with the corresponding solution of the 1D model. As mentioned above, the truncated model $G_1^t(s)$ is an 8th order transfer function, while the reduced model is a 3rd order system.

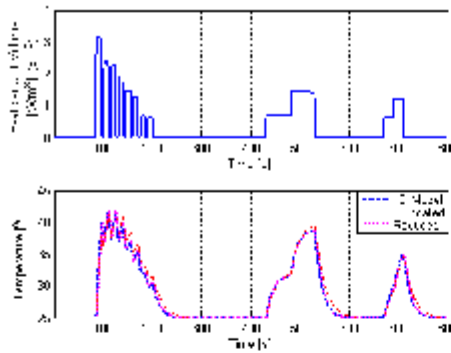


Fig. 7. Comparison of the temperature predictions.

Both model follow the temperature dynamics during the test quite closely. Focusing on a portion of the test, shown in figure 8, it is possible to visualize the improved accuracy of the reduced order model compared to the truncated model. In particular, the latter tends to filter out and delay the output. This behavior can be explained by the lower bandwidth where the frequency response of the model well matches the exact solution, as shown in the upper plot of figure 4.

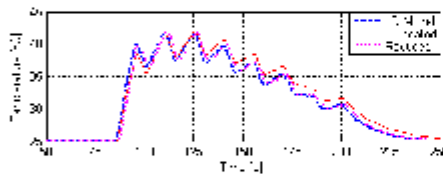


Fig. 8. Comparison of the temperature prediction of different models during a portion of the battery test.

Note that the reduced order model achieves accurate response without the need of performing any calibration, as a result of the fundamental analytical procedure adopted. However, due to the simplifications made to the heat diffusion equation and the thermal properties of the materials, it is likely that errors will be present when comparing the models to experimental data or results from electro-thermal CFD simulations. In such case, the thermal properties (such as the conductivity and the specific heat) can be considered as parameters to calibrate for improving the model accuracy.

5. CONCLUSION

This work describes a reduced order model of the thermal dynamics of a Li-ion cell, which predicts the internal temperature. Unlike control-oriented models, based on phenomenological approaches and system identification methods, the proposed model was developed adopting a fully analytical procedure.

A one-dimensional boundary-value problem for unsteady heat diffusion in a prismatic geometry was defined and solved analytically by applying the Laplace transform

method. The transcendental transfer function obtained was then approximated to a truncated linear transfer function. Finally, the singular perturbation method was applied for model order reduction. The approach adopted ensures consistency with the physical behavior of the system and relies on a limited set of physical parameters that can be obtained from the open literature, or calibrated if experiments or CFD simulation results are available.

The resulting model was validated by comparison with a one-dimensional thermal model, for different charging/discharging current profiles obtained from experimental tests. The consistency with the 1D solution and the simple structure make the model an ideal candidate for model-based control and diagnostic algorithms, for the integration into battery management systems, or as a tool to support the calibration of electro-thermal battery dynamic models.

REFERENCES

- Arpaci, V. (1966). *Conduction heat transfer*. Addison Wesley.
- Bernardi, D., Pawlikowski, E., and Newman, J. (1985). A General Energy Balance for Battery Systems. *Journal of the Electrochemical Society*, 132, 5.
- Bhikkaji, B. and Soderstrom, T. (2001). Reduced Order Models for Diffusion Systems Using Singular Perturbations. *Energy & Buildings*, 33(8), 769-781.
- Chatzakis, J., Kalaitzakis, K., Voulgaris, N., and Manias, S. (2003). Designing a New Generalized Battery Management System. *IEEE transactions on Industrial Electronics*, 50(5), 990-999.
- Chen, S., Wan, C., and Wang, Y. (2005). Thermal Analysis of Lithium-Ion Batteries. *Journal of Power Sources*, 140(1), 111-124.
- Doebelin, E. (1980). *System Modeling and Response: Theoretical and Experimental Approaches*. John Wiley & Sons.
- Ersal, T., Fathy, H., Rideout, D., Louca, L., and Stein, J. (2008). A Review of Proper Modeling Techniques. *Journal of Dynamic Systems, Measurement, and Control*, 130, 061008.
- Hu, Y., Yurkovich, B.J., Yurkovich, S., and Guzzennac, Y. (2009). Electro-Thermal Battery Modeling and Identification for Automotive Applications. In *Proceedings of 2009 ASME Dynamic Systems and Control Conference, October 12-14, 2009, Hollywood, CA, USA*.
- Incropera, F., DeWitt, D., Bergman, T., and Lavine, A. (1996). *Fundamentals of Heat and Mass Transfer*. John Wiley & Sons New York.
- Khalil, H. (1996). *Nonlinear systems*. Prentice hall Englewood Cliffs, NJ.
- Nagure, S., Dinwiddle, R., Babu, S., Rizzone, G., Bhushan, B., and Frech, T. (2009). Thermal Diffusivity Study of Aged Li-Ion Batteries Using Flash Method. *Journal of Power Sources*, 195(3), 872-876.
- Newman, J., Thomas, K., Hafzi, H., and Wheeler, D. (2003). Modeling of Lithium-Ion Batteries. *Journal of Power Sources*, 119, 838-843.
- Oppenheim, A. and Schaffer, R. (1975). *Digital Signal Processing*. Prentice-Hall.
- Ozisik, M. (2002). *Boundary Value Problems of Heat Conduction*. Dover Pubes.
- Pals, C. and Newman, J. (1995). Thermal Modeling of the Lithium/Polymer Battery. *Journal of the Electrochemical Society*, 142, 3274.
- Pesaran, A. (2002). Battery Thermal Models for Hybrid Vehicle Simulations. *Journal of Power Sources*, 110(2), 377-382.
- Verbrugge, M. and Koch, B. (2006). Generalized Recursive Algorithm for Adaptive Multiparameter Regression. *Journal of the Electrochemical Society*, 153, A187.

Appendix C: A model order reduction method for the temperature estimation in a cylindrical Li-Ion battery cell

CONFIDENTIAL. Limited circulation. For review only.

A MODEL ORDER REDUCTION METHOD FOR THE TEMPERATURE ESTIMATION IN A CYLINDRICAL LI-ION BATTERY CELL

Matteo Muratori
Dipartimento di Energia
Politecnico di Milano
Milan, Italy

Ning Ma, Marcello Canova, Yann Guezennec
Center for Automotive Research
The Ohio State University
Columbus, Ohio, 43212
Email: canova.1@osu.edu

ABSTRACT

The thermal characterization of Li-Ion batteries for EVs, HEVs and PHEVs is a topic of great relevance, especially for the evaluation of the battery pack state of health (SoH) during vehicle operations and for battery life estimation.

This work proposes a reduced-order model that estimates the thermal dynamics of a cylindrical Li-Ion battery cell respect to the variations in current demands. Unlike most "black-box" dynamic models, based on system identification techniques, the proposed approach relies on the definition of a boundary-value problem for unsteady heat diffusion, in the form of a linear partial differential equation. The problem is then converted into a linear ODE problem by applying the Laplace transform method. Further, a model-order reduction method is applied to approximate the solution of the problem into a low-order linear model that estimates the temperature dynamics at the center and at the external surface.

In this paper, the model is applied to the temperature estimation during a battery discharging transient. The model uses electrical data acquired from experimental tests and is validated by comparison with a 3D FEM thermal simulation.

INTRODUCTION

The advancements in Lithium ion (Li-Ion) battery technology has been the driving force behind the recent developments in Plug-in Hybrid Electric Vehicles (PHEVs) and Battery Electric Vehicles (BEV). For efficient and reliable utilization of the battery pack, it is critical monitoring its conditions in order to protect the cells from premature aging and avoid performance degradation (1). Model based battery monitoring algorithms, of particular importance in high power applications, use current,

voltage measurements and some cell surface temperatures to estimate state of charge (SoC), available power, state of health (SoH) and temperature with interacting control systems based upon these estimates (2).

In this scenario, the electro-thermal characterization of Li-Ion batteries is a topic of critical importance (3). In particular, control-oriented models that are capable of predicting the response of the system in real-time can be a powerful tool to monitor the battery during vehicle operations and, ultimately, to improve the performance of a Battery Management System and guarantee reliable operations of such energy storage systems (4; 3).

The design of low-order electro-thermal models of battery cells is challenging. Models based on first principles (referred to as electrochemical models) are generally not suitable for control and estimation applications due to their inherent complexity in describing the chemical behavior of the cell (for example, as in (5)). For this reason, phenomenological models based on the equivalent circuit analogy are often used as a compromise between accuracy and complexity (for example, see (6; 3)).

Equivalent circuit models contain several parameters, such as the open-circuit voltage, battery internal resistance and the dominant electrical time constants, which are generally scheduled with respect to the battery SoC and temperature. In particular, the latter is often regarded as a static input to the model, hence assuming that the battery temperature has no space distribution during the test and that a single, lumped temperature is either constant or externally prescribed in time. However, due to the heat generated by the electrochemical reactions and the conductivity of the materials, battery cells are characterized by a well defined internal temperature profile that may significantly differ from the temperature at the external surface (among oth-

Preprint submitted to 3rd Annual Dynamic Systems and Control Conference.
Received March 15, 2010.

ers, see (7) or (8)). Furthermore, the battery temperature is a dynamic variable, which strongly depends on the battery inputs (current and voltage), and on the cooling system adopted (such as convective cooling, or in presence of insulation or conductive materials).

The characterization of battery thermal dynamics, often overlooked in simplified electro-thermal models, becomes particularly relevant at low temperature conditions (cold-start) or at high discharge rates. In any case, it is necessary to properly account for battery temperature for in control-oriented applications, such as battery pack performance analysis, cell balancing, diagnostics and residual life estimation. For instance, large temperature variations within the cell may lead to premature aging of the battery, hence the importance of including the prediction of the internal battery thermal behavior in system integration and control.

This work proposes a reduced-order model that estimates the dynamics of the core temperature and surface temperature of a cylindrical Li-Ion battery cell in presence of natural convective cooling. Unlike most phenomenological models, based on system identification ("black-box") techniques, the proposed model relies on a physically-based approach based on the fundamentals of heat transfer theory. First, a one-dimensional boundary-value problem for unsteady heat diffusion is defined, assuming uniform internal heat generation and convective boundary conditions. From this formulation, a real-time model in the form of a linear system is obtained by converting the PDE problem into a linear ODE problem and applying a model order reduction method in the frequency domain. The paper describes the development of the model and a comparison of its results with a detailed 3D FEM thermal simulation is presented.

PROBLEM DESCRIPTION AND MODELING ASSUMPTIONS

The objective of this study is to design a low-order model that predicts the temperature dynamics of a Li-Ion battery cell, given the current and voltage profiles. The system considered in the study is a A123 ANR26650 cylindrical $LiFePO_4$ cell, with nominal capacity of 2.3Ah and nominal voltage of 3.3V. The cell, whose main geometric data are summarized in Figure 1, is commonly used for high-power applications, ranging from power tools to automotive.

For specific applications, such as racing electric motorcycles, the cylindrical cells are assembled into a compact pack that is located under the seat and is generally cooled by air convection. With this in mind, a simple experimental setup was arranged considering one cylindrical cell connected to a programmable load. The cell is positioned in ambient air at constant temperature, to represent a critical operating condition where the battery is cooled only by natural convection. This represents a worst-case scenario, representative of a case where the battery is left in absence of forced cooling.

The current input and the battery voltage output were



Figure 1. Geometric data of ANR26650 cell.

recorded from a test, as shown in Figure 2. The tests reproduces a hard acceleration for an electric motorcycle and is rather aggressive on the battery. In detail, the battery is subject very high current values in about 90s, with peak current that corresponds to discharge rate of about 15C.

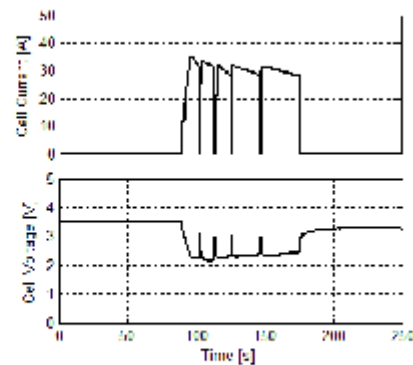


Figure 2. Experimental results for rapid discharging transient.

Due to the high current values and the very short duration of the test, significant heat generation takes place inside the battery, due to internal resistances and irreversible heat generation. At the same time, convection heat transfer takes place at the external surface, partially removing the heat generated. The two phenomena lead to the creation of an internal temperature distribution that varies dynamically in relation with the current, voltage and the thermal parameters. For this reason, a model that estimates the internal temperature of the battery cell in real-time could be a useful tool for providing feedback during testing, or in the definition of a management system.

For modeling purposes, the battery cell can be considered as a MIMO system, where the inputs are the heat generation rate, the thermal parameters and the environment temperature, and the outputs are the internal temperature and the surface temperature. The model will be solved, in particular, for the temperature at

the center of the cell, which is assumed as the peak value of the distribution since all the heat generated internally is removed only at the external surface. It is also reasonable to assume that the generation term is uniformly distributed within the cell and only time dependent.

DESCRIPTION OF BATTERY THERMAL MODEL

In the model, the battery cell is assumed as a homogeneous cylinder of radius R . Note that, although the mathematical formulation of the problem is developed for a specific shape, the proposed approach could be easily generalized to other geometries and different boundary conditions. Let r be the radial coordinate of the system, T_{ar} the temperature of the ambient, and \dot{q} the rate of heat generated inside the battery. Figure 3 shows the scheme adopted by the model.

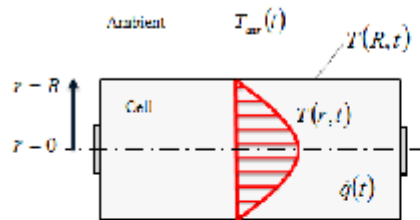


Figure 3. Schematic of the cell geometry for the thermal model.

As a first approximation of the real system, it is here assumed that the heat generation rate is uniformly distributed and the material properties are homogeneous and isotropic. Further, no heat is removed by conduction through the terminals. Such assumptions allow for reducing the characterization of the battery temperature distribution to a one-dimensional problem. This represents a reasonable approximation of the real behavior of the system, with the exception of the regions near the current collectors. Here, due to the anisotropy of the materials and the high current densities, high temperatures and temperature gradients are usually present, forcing one to rely only on 3D FEM analysis tools to obtain a reliable prediction of the local temperature distribution.

The heat transfer problem can be cast in the form of a Boundary-Value Problem (BVP) for a case of one-dimensional, unsteady heat conduction for a cylindrical system ((9); (10)):

$$\frac{\partial^2 T(r,t)}{\partial r^2} + \frac{1}{r} \frac{\partial T(r,t)}{\partial r} + \frac{1}{k} \dot{q}(t) = \frac{1}{\alpha} \frac{\partial T(r,t)}{\partial t} \quad (1)$$

where $\alpha = k(\rho c_p)^{-1}$, being k the average thermal conductivity of the cell, ρ the average density and c_p the average specific heat.

The above parameters were determined starting from published data ((11); (12)), and are summarized in table 1.

Table 1. List of model parameters

Parameter	Value	Units
k	0.488	$W(mK)^{-1}$
ρ	1,824	$kg(m)^{-3}$
c_p	825	$J(kgK)^{-1}$
α	$3.24e^{-7}$	m^2s^{-1}

The rate of heat per unit volume $\dot{q}(t)$ (Wm^{-3}) generated inside the cell is computed as in (13):

$$\dot{q}(t) = \frac{I}{V_{cell}} \left(E_0 - E - T \frac{dE_0}{dT} \right) \quad (2)$$

where I is the current, V_{cell} the cell volume, E_0 the open circuit voltage and E the voltage of the cell.

Note that, substituting Equation (2) into (1), a nonlinear heat conduction problem is obtained, leading to a considerably complex problem that might not be solved with analytical methods. However, for the $LiFePO_4$ cells, it is often possible to neglect the last term in equation (2) in a temperature range above $25^\circ C$, allowing for a partial simplification of problem (3).

To solve the BVP described by equation (1) two boundary conditions and one initial conditions are needed. Due to the presence of convective cooling at the external surface, a boundary condition of the third kind can be formulated there. Another condition is given by the circular symmetry of the system, hence:

$$\left. \frac{\partial T(r,t)}{\partial r} \right|_{r=R} = -\frac{h}{k} (T(R,t) - T_{ar}(t)) \quad (3)$$

$$\left. \frac{\partial T(r,t)}{\partial r} \right|_{r=0} = 0$$

where the convection coefficient h is a model parameter that can be initially estimated from the empirical correlations for natural convection heat transfer (9).

The above BVP could be solved numerically, for instance using the finite difference method on a defined grid (10). Noting that the system is described by a linear PDE, it is also possible to solve the problem applying the Laplace transform (14; 15). With this approach, the boundary-value problem in time domain is transformed into an equivalent ODE problem in the complex domain, which can be solved analytically.

Assuming zero initial condition for equation (1), the transformed BVP is obtained:

$$\frac{d^2 T(r,s)}{dr^2} + \frac{1}{r} \frac{dT(r,s)}{dr} - a^2 T(r,s) = -\frac{1}{k} Q(s) \quad (4a)$$

$$\left. \frac{dT(r,s)}{dr} \right|_{r=R} = -\frac{h}{k} (T(R,s) - T_{air}(s)) \quad (4b)$$

$$\left. \frac{dT(r,s)}{dr} \right|_{r=0} = 0 \quad (4c)$$

where $a^2 = s\alpha^{-1}$ and $Q(s)$ is the transform of $\dot{q}(t)$.

Regarding s as a fixed parameter, equation (4) has the following solution:

$$T(r,s) = \frac{1}{ka^2} Q(s) + C_1(s) J_0(ar) + C_2(s) Y_0(ar) \quad (5)$$

where J_l and Y_l denote the l^{th} order Bessel function of the first kind and second kind, respectively (14).

The integration constants $C_1(s)$ and $C_2(s)$ can be found by evaluating the boundary conditions (4b)-(4c). This allows one to determine the general solution of the problem, hence the temperature dynamics at any coordinate r . In particular, the temperature at the center of the cell is found by evaluating the solution at $r = 0$:

$$T(0,s) = \frac{1}{ka^2} Q(s) + \frac{h}{k} \frac{\left(T_{air}(s) - \frac{1}{ka^2} Q(s) \right)}{\frac{h}{k} J_0(aR) - aJ_1(aR)} \quad (6)$$

while the surface temperature is obtained by imposing $r = R$:

$$T(R,s) = \frac{1}{ka^2} Q(s) + \frac{h}{k} \frac{\left(T_{air}(s) - \frac{1}{ka^2} Q(s) \right)}{\frac{h}{k} J_0(aR) - aJ_1(aR)} J_0(aR) \quad (7)$$

Equations (6) and (7) can be interpreted as the outputs of a continuous time dynamic system where $u(t) = [\dot{q}(t), T_{air}(t)]^T$ and $y(t) = [T(0,t) T(R,t)]^T$. In this sense, the solution of the BVP is equivalent to the impulse response of the system:

$$\begin{bmatrix} T(0,s) \\ T(R,s) \end{bmatrix} = \begin{bmatrix} G_{11}(s) & G_{12}(s) \\ G_{21}(s) & G_{22}(s) \end{bmatrix} \begin{bmatrix} \dot{q}(t) \\ T_{air}(t) \end{bmatrix} \quad (8)$$

where the matrix $G(s)$ is formed by the transcendental transfer

functions:

$$G_{11}(s) = \frac{\frac{h}{k} J_0\left(R\sqrt{\frac{s}{\alpha}}\right) - \sqrt{\frac{s}{\alpha}} J_1\left(R\sqrt{\frac{s}{\alpha}}\right) - \frac{h}{k}}{ks \frac{h}{k} J_0\left(R\sqrt{\frac{s}{\alpha}}\right) - \sqrt{\frac{s}{\alpha}} J_1\left(R\sqrt{\frac{s}{\alpha}}\right)} \quad (9a)$$

$$G_{12}(s) = \frac{\frac{h}{k}}{\frac{h}{k} J_0\left(R\sqrt{\frac{s}{\alpha}}\right) - \sqrt{\frac{s}{\alpha}} J_1\left(R\sqrt{\frac{s}{\alpha}}\right)} \quad (9b)$$

$$G_{21}(s) = \frac{\alpha}{ks \frac{h}{k} J_0\left(R\sqrt{\frac{s}{\alpha}}\right) - \sqrt{\frac{s}{\alpha}} J_1\left(R\sqrt{\frac{s}{\alpha}}\right)} \quad (9c)$$

$$G_{22}(s) = \frac{\frac{h}{k} J_0\left(R\sqrt{\frac{s}{\alpha}}\right)}{\frac{h}{k} J_0\left(R\sqrt{\frac{s}{\alpha}}\right) - \sqrt{\frac{s}{\alpha}} J_1\left(R\sqrt{\frac{s}{\alpha}}\right)} \quad (9d)$$

In principle, one could inverse transform the above transfer functions and obtain an analytical solution in time domain. However, a more convenient approach to obtain a system model that is amenable to control applications can be found by studying the frequency behavior of the system and defining a set of rational transfer functions that reasonably approximate its response in the desired frequency range.

To this end, Figure (4) represents the frequency response of the four transfer functions. From these diagrams, it is possible to formulate the following considerations:

1. In general, the four transfer functions have a response similar to a low-pass filter;
2. The frequency response of the transfer functions $G_{11}(s)$ and $G_{21}(s)$, characterizing the system response to the internal heat generation rate, suggests that their behavior could be reasonably approximated by a low-order system with real poles;
3. The transfer function $G_{12}(s)$, describing the influence of the air temperature on the temperature at the center of the cell has a very rapid rate of decay. This implies that the external temperature has a limited influence on the cell internal temperature, and its effects are visible only after a considerable time;
4. On the other hand, the behavior of the transfer function $G_{22}(s)$ suggests that the surface temperature $T(R,s)$ responds faster to a change in the air temperature, as expected.

Further information on the system response can be obtained by studying the poles and zeroes. Since the four transfer functions of equation (9) are transcendental, they are characterized by

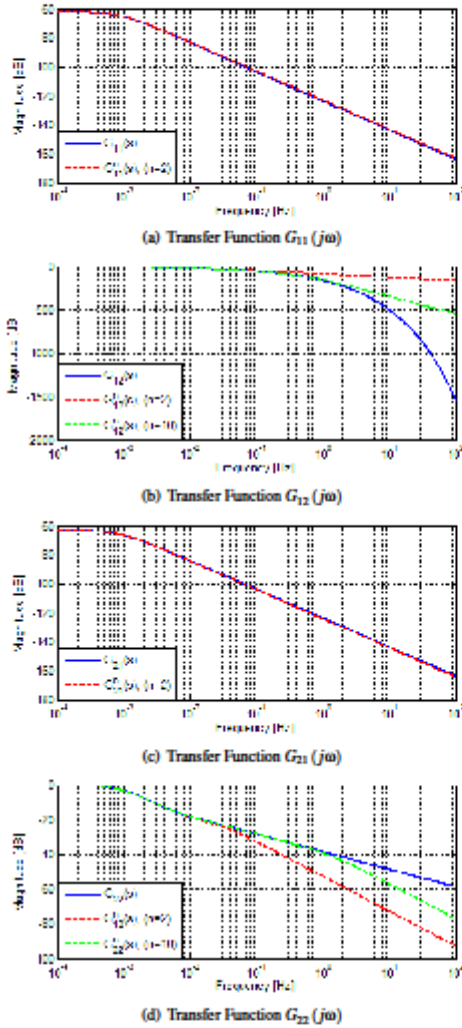


Figure 4. Frequency response (magnitude) of the four transcendental transfer functions, compared to the approximated response of the corresponding truncated models.

an infinite number of poles p and zeros z that can be determined numerically by setting each numerator and denominator to zero. Due to the properties of the Bessel functions, it is possible to observe that all the poles and zeroes are real and negative. Thus the system can be considered stable and all the transfer functions bounded.

In particular, $|G_{12}(j\omega)| \rightarrow 0$ at a faster rate than the other functions, due to the absence of zeroes in $G_{12}(s)$. Due to its faster convergence, $|G_{12}(j\omega)|$ is almost zero in the high frequency region, hence the transient response of the system is largely dominated by $G_{11}(s)$, $G_{21}(s)$ and $G_{22}(s)$.

Based on the above considerations, the behavior of each transfer function $G_{ij}(s)$ can be approximated by a truncated rational transfer function of the form:

$$G_{ij}^n(s) = K_{ij} \frac{(s-z_1)(s-z_2)\dots(s-z_{n-1})}{(s-p_1)(s-p_2)\dots(s-p_n)} \quad (10)$$

where n is a finite number and the gain K_{ij} is chosen to equalize the static gains of G_{ij}^n and G_{ij} :

$$K_{ij} = G_{ij}(s \rightarrow 0) \frac{p_1 p_2 \dots p_n}{z_1 z_2 \dots z_{n-1}} \quad (11)$$

Figure (4) compares the truncated transfer functions G_{11}^n , G_{12}^n , G_{21}^n and G_{22}^n ($n = 2$) are compared with the corresponding transcendental transfer function, which represent the exact analytical solution of the BVP described by Equation (1). It is evident that G_{11} and G_{21} are well approximated by low-order models in their entire frequency range. On the other hand, the functions G_{12} and G_{22} , are reasonably approximated by the truncated models only in the low frequency regions, while, as expected, the accuracy deteriorates as the frequency increases.

The order of truncation can be chosen in relation with the frequency content of the input signals and the desired bandwidth. In a typical experimental setup for battery electro-thermal characterization, the signals are typically acquired up to a frequency of 10Hz, which is commensurate with the frequency content of the current and power demand experienced in vehicles. Therefore, this effective bandwidth can be confidently considered as the maximum frequency of interest.

In principle, the above consideration would allow one to simply truncate the models up to the desired frequency content. However, since the contribution of the higher order poles and zeros is neglected in the truncated system, the resulting model will have limited accuracy.

Figure 4 shows that, for the functions G_{12} and G_{22} , a truncation to the 10^k order ensures accurate response up to only 1Hz. In other words, it would be necessary to dramatically increase the order of the model by adding high frequency terms until acceptable accuracy is obtained in the frequency interval considered.

For this reason, a model order reduction method could be adopted to generate a model that achieves the accuracy required by the application with minimal complexity. Several model reduction algorithms have been presented for a variety of systems (see (16) for a review of proper modeling techniques). In this case, it can be shown that the poles of G_{12} and G_{22} increase nearly proportionally to n^2 . Consequently, the difference between the large and small time constants in the system increases, or, in other words, the system tends to become numerically stiff.

For stiff systems with known poles and zeroes, the singular perturbation method can be adopted to approximate the effects of the higher frequency components on a low order model (17). This model reduction procedure is commonly adopted when solving dynamic systems that are based on fluid dynamics and heat transfer problems. In particular, the method shown in (18) is here adapted to this more complex case. The reduction algorithm is based on defining the functions G_{12}^n and G_{22}^n up to a sufficiently high order of truncation and decomposing them into partial fractions. For simplicity, only G_{12}^n is considered to describe the following model reduction methodology:

$$G_{12}^n(s) = K_{12} \left[\frac{A_1}{s-p_1} + \frac{A_2}{s-p_2} + \dots + \frac{A_n}{s-p_n} \right] \quad (12)$$

where the coefficients A_i and B_i can be analytically calculated ((19)). With the above form, it is possible to operate a separation of the transfer function into its low and high frequency modes:

$$G_{12}^n(s) = G_{12}^k(s) + H_{12}(s) \quad (13)$$

where $k < n$ and

$$G_{12}^k(s) = K_1 \left[\frac{A_1}{s-p_1} + \frac{A_2}{s-p_2} + \dots + \frac{A_k}{s-p_k} \right] \quad (14)$$

$$H_{12}(s) = K_2 \left[\frac{A_{k+1}}{s-p_{k+1}} + \dots + \frac{A_n}{s-p_n} \right]$$

In accordance to the singular perturbation method, a reduced order model can be obtained by truncating $G_{12}^n(s)$ to $G_{12}^k(s)$ and then approximating the high frequency modes (here represented by $H_{12}(s)$) by introducing a correction factor. The simplest correction is to assume that the effect of the high frequency component $H_{12}(s)$ is equal to its static gain $H_{12}(0)$, hence:

$$G_{r12}(s) = G_{12}^k(s) + H_{12}(0) \quad (15)$$

The described algorithm is applied to generate the reduced models G_{r12} and G_{r22} , starting from the transfer function $G_{12}^n(s)$ and $G_{22}^n(s)$ truncated to the 20^{th} order. This order of truncation ensures that accuracy is achieved up to the target frequency of 10Hz. The resulting reduced model results into a 3rd order system.

The frequency response of the reduced order model is shown in figure 5 in terms of magnitude. The response is compared to the analytical solution of the BVP (equation (9)) and to the truncated models $G_1^i(s)$ and $G_2^i(s)$, where $i = 8$.

As expected, the reduced order models can well approximate the exact solution in a relatively larger frequency range than the truncated solutions. On the other hand, it is possible to observe that G_{r12} and G_{r22} do not converge to zero as $s \rightarrow \infty$. This

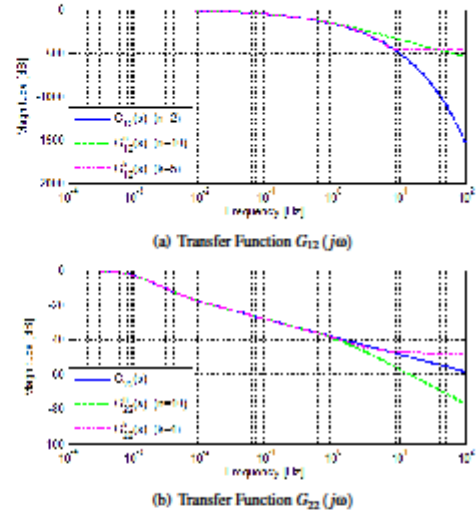


Figure 5. Frequency response (magnitude) of the transcendental transfer functions G_{12} and G_{22} , compared to the truncated model G_{12}^n , G_{22}^n ($n = 10$) and the reduced order model G_{r12} ($k = 5$), G_{r22} ($k = 4$).

stems from the assumption earlier introduced of approximating the high frequency components by their static gains. In (18) it is shown that the impact of this approximation on the model can be explained by inverse-transforming the reduced order model to time domain and noting that the high-frequency modes have been approximated by impulse function.

1 ANALYSIS OF MODEL RESULTS

The reduced order model was applied to simulate the thermal response of the cylindrical Li-Ion cell during the aggressive discharge transient shown in Figure 2. The rate of internal heat generation (input to the model) was computed from the current and voltage profiles using equation (2), while the ambient temperature was considered constant and equal to 23°C. The battery, initially at ambient conditions, is heated by applying current for about 90s. Then, current is removed and the battery is cooled down by natural convection in the ambient.

In order to provide a meaningful validation in the absence of direct temperature measurements, the response of the model was compared to the prediction of a detailed 3D FEM thermal simulator that uses the geometry of the A123 ANR26650 cylindrical $LiFePO_4$ cell shown in Figure 1. The model solves the 3D unsteady heat diffusion equation within the cell domain, considering uniform internal heat generation (imposed as an input) and assuming anisotropic thermal properties for the cell materials (7). The FEM model created consists of 13,900 meshing elements, and calculates the solution using an integration time

step of one second. The thermal behavior of the cell during the rapid discharge and cooling-down phases is simulated by assuming convective boundary condition with a heat transfer coefficient $h = 10W/m^2K$.

Figure 6 shows the dynamically varying temperature fields in the central cross-section of the cell from the 3D FEM simulation. Temperature fields at four time points, $t = 0$ (initial condition), $t = 178s$ (peak temperature), and $t = 360, 990s$ (cooling-down phase) are shown.

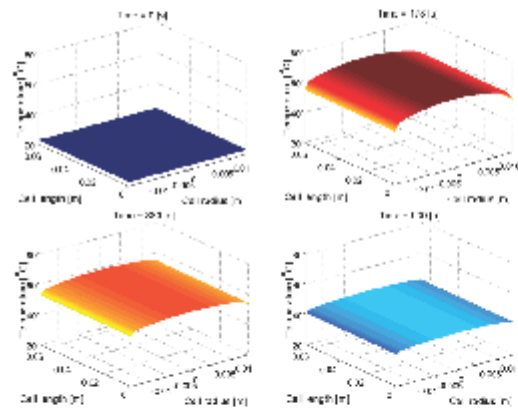


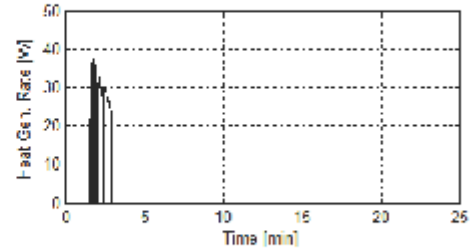
Figure 6. Simulated temperature field in the central cross section of the cell at four time points: $t = 0$, $t = 178s$, $t = 360s$, and $t = 990s$.

The reduced order model was calibrated by varying the convection coefficient h to match the temperature predicted by the FEM simulator at the external surface of the battery. Validation was performed by comparing the temperature at the center of the cell.

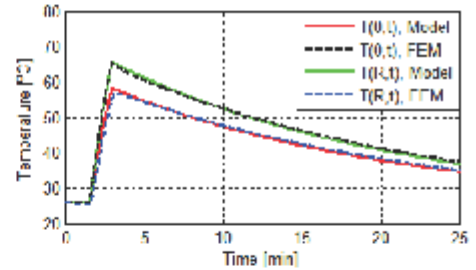
Figure 7 compares the two temperatures predicted by the model to the results of the the FEM simulator. It can be noticed that the model follows the temperature dynamics during the test quite closely. It is worth observing that the model achieves a reasonably accurate response with very limited calibration, as a result of the fundamental analytical procedure adopted. However, due to the simplifications made to the heat diffusion equation and the thermal properties of the materials, it is likely that errors will be present when comparing the reduced order battery model to experimental data. In such case, the thermal properties (such as the conductivity and the specific heat) can be considered as parameters to calibrate for improving the model accuracy.

2 CONCLUSION

This work presents the development of a control-oriented model to characterize the thermal dynamics of cylindrical a Li-



(a) Battery heat generation rate



(b) Battery internal temperature and surface temperature

Figure 7. Comparison of the thermal model predictions with FEM results.

ion battery cell, predicting the internal temperature and surface temperature in relation with the battery current and voltage inputs, and assuming convective cooling conditions. Instead of applying phenomenological approaches and system identification methods, the proposed model was developed adopting a fully analytical procedure.

A one-dimensional boundary-value problem for unsteady heat diffusion in a cylindrical geometry was defined and solved analytically by applying the Laplace transform method. The transcendental transfer function obtained was then approximated to a truncated linear transfer function. Finally, a model order reduction method was applied to increase the model in the frequency range of interest, while limiting the model complexity. The proposed approach ensures consistency with the physical behavior of the system and relies on a limited set of physical parameters that can be obtained from the open literature, or calibrated if experiments or simulation results are available.

The model described in the paper was validated by comparison with a detailed 3D FEM thermal simulation model, considering a rapid discharging transient that is representative of an acceleration test for a high performance electric vehicle. The validation shows that the model is consistent with the FEM solution found for this problem, with very limited calibration effort.

A set of laboratory tests is currently being performed to provide experimental data for improving the validity of the model.

The data, including temperature measurements at various locations on the external surface of the battery as well as thermal imaging through an infrared camera, will allow for characterizing the temperature distribution at the external surface. This will allow for evaluating the accuracy of the assumptions made, and to improve the model calibration. As a future work, the model developed will be integrated into an electro-thermal battery dynamic model to improve the accuracy of the voltage and SoC predictions under various cooling conditions.

REFERENCES

- [1] Chatzakis, I., Kalitzaakis, K., Voulgaris, N., and Manias, S., 2003. "Designing a New Generalized Battery Management System". *IEEE transactions on Industrial Electronics*, 50(5), pp. 990-999.
- [2] Verbrugge, M., and Koch, B., 2006. "Generalized Recursive Algorithm for Adaptive Multiparameter Regression". *Journal of the Electrochemical Society*, 153, p. A187.
- [3] Hu, Y., Yurkovich, B. J., Yurkovich, S., and Guezennec, Y., 2009. "Electro-Thermal Battery Modeling and Identification for Automotive Applications". In Proceedings of 2009 ASME Dynamic Systems and Control Conference, October 12-14, 2009, Hollywood, CA, USA.
- [4] Yurkovich, B. J., and Guezennec, Y., 2009. "Lithium Ion Dynamic Battery Pack Model and Simulation for Automotive Applications". In Proceedings of 2009 ASME Dynamic Systems and Control Conference, October 12-14, 2009, Hollywood, CA, USA.
- [5] Newman, J., Thomas, K., Hafezi, H., and Wheeler, D., 2003. "Modeling of Lithium-Ion Batteries". *Journal of Power Sources*, 119, pp. 838-843.
- [6] Hu, Y., Yurkovich, S., Guezennec, Y., and Bormatic, R., 2008. "Model-Based Calibration for Battery Characterization in HEV Applications". In Proceedings of 2008 American Control Conference, June 11-13, 2008, Seattle, WA, USA.
- [7] Chen, S., Wan, C., and Wang, Y., 2005. "Thermal Analysis of Lithium-Ion Batteries". *Journal of Power Sources*, 140(1), pp. 111-124.
- [8] Pesaran, A., 2002. "Battery Thermal Models for Hybrid Vehicle Simulations". *Journal of Power Sources*, 110(2), pp. 377-382.
- [9] Incropera, F., DeWitt, D., Bergman, T., and Lavine, A., 1996. *Fundamentals of Heat and Mass Transfer*. John Wiley & Sons New York.
- [10] Arpaci, V., 1966. *Conduction heat transfer*. Addison Wesley.
- [11] Naggure, S., Dinwiddle, R., Babu, S., Rizzoni, G., Bhushan, B., and Frech, T., 2009. "Thermal Diffusivity Study of Aged Li-Ion Batteries Using Flash Method". *Journal of Power Sources*, 195(3), pp. 872-876.
- [12] Pals, C., and Newman, J., 1995. "Thermal Modeling of the Lithium/Polymer Battery". *Journal of the Electrochemical Society*, 142, p. 3274.
- [13] Bernardi, D., Pawlikowski, E., and Newman, J., 1985. "A General Energy Balance for Battery Systems". *Journal of the Electrochemical Society*, 132, p. 5.
- [14] Myers, G., 1998. *Analytical methods in conduction heat transfer*. Amcmt Publications.
- [15] Van Der Tempel, I., 2002. "Transient Heat Conduction in a Heat Generating Layer Between Two Semi-Infinite Media". *Journal of Heat Transfer*, 124, p. 299.
- [16] Emsal, T., Fathy, H., Rideout, D., Louca, L., and Stein, J., 2008. "A Review of Proper Modeling Techniques". *Journal of Dynamic Systems, Measurement, and Control*, 130, p. 061008.
- [17] Khalil, H., 1996. *Nonlinear systems*. Prentice hall Englewood Cliffs, NJ.
- [18] Bhikkaji, B., and Soderstrom, T., 2001. "Reduced Order Models for Diffusion Systems Using Singular Perturbations". *Energy & Buildings*, 33(8), pp. 769-781.
- [19] Oppenheim, A., and Schaffer, R., 1975. *Digital Signal Processing*. Prentice-Hall.

Appendix D: A 1+1D thermal dynamic model of a Li-Ion battery cell

CONFIDENTIAL. Limited circulation. For review only.

A 1+1D THERMAL DYNAMIC MODEL OF A LI-ION BATTERY CELL

Matteo Muratori
Dipartimento di Energia
Politecnico di Milano
Italy
Muratori.2@osu.edu

Ning Ma, Marcello Canova, Yann Guezennec
Center for Automotive Research
The Ohio State University
Columbus, OH, 43212

ABSTRACT

Li-Ion batteries are today considered the prime solution as energy storage system for EV/PHEV/HEV, due to their high specific energy and power. Since their performance, life and reliability are quite dependent on the operating temperature, great interest has been devoted to study solutions for cooling and control algorithms for thermal management.

In this context, this paper presents a computationally efficient model that characterizes the internal temperature distribution of a battery cell, conceived to serve as a tool for the development of thermal management systems for automotive battery packs. The model is based on the unsteady heat diffusion equation, for which an analytical solution is obtained through the integral transform method. First, a general one-dimensional thermal model is developed to predict the temperature distribution inside a prismatic Li-Ion battery cell under different boundary conditions. Then, a specific case with convective boundary conditions is studied with the objective of characterizing a cell cooled by a forced air flow. To characterize the effects of the cooling system on the temperature distribution within the cell, the one-dimensional solution is then extended to a 1+1D model that accounts for the variability of the boundary conditions in the flow direction.

The calibration and validation of the model will be presented, adopting a detailed 2D FEM simulator as a benchmark.

NOMENCLATURE

A	Area [m^2]
c_p	Specific heat at constant pressure [$J/kg K$]
c_v	Specific heat at constant volume [$J/kg K$]
h	Convective heat transfer coefficient [$W/m^2 K$]
k	Thermal conductivity [$W/m K$]
I	Current [A]
L_c	Characteristic length [m]
m	Mass [kg]
\dot{m}	Mass flow rate [kg/s]

\dot{q}	Heat generation rate [W/m^3]
T	Temperature [$^{\circ}C$]
T_{∞}	Free stream temperature [$^{\circ}C$]
v	Velocity [m/s]
V	Voltage [V]
V_{oc}	Open circuit Voltage [V]
α	Thermal diffusivity [m^2/s]
ρ	Density [kg/m^3]

INTRODUCTION

Due to their high specific energy and power, Li-Ion batteries have recently generated considerable research interest for their application to the automotive field, such as energy storage system for BEV/HEV/PHEV. To this end, great effort is being devoted to address the safety, performance and aging issues of Li-Ion batteries [1], [2]. In particular, several studies have demonstrated strong correlations between performance and aging with the temperature distribution within the battery [3] [4] [5].

For this reason, detailed studies of the temperature field within Li-Ion battery cells during charging and discharging conditions have been proposed by several authors (see [6], [7], [8] or [9]). Most of these studies are conducted utilizing FEM thermal simulators, often coupled with detailed models that characterize the electrochemical reactions and transport phenomena. Such simulators are extremely useful to gain understanding on how the temperature distribution affects the performance of the cell and to provide important information for cell design, for instance the identification of hot spots. On the other hands, such tools are too complex to be applied to studies oriented to the characterization of the electro-thermal performance of modules and packs, or for the designs of battery cooling systems and control algorithms. Here, computationally efficient models that can provide a reasonable estimate of the cell thermal field with limited calibration effort can be useful tools for battery pack designers and integrators, allowing them

to study design and control solutions in a simulation environment.

To this extent, this paper proposes a general methodology to design models characterizing the thermal behavior of Li-Ion battery cells, with the intent to serve applications in the areas of performance and thermal management studies for battery pack cooling systems. To meet this objective, the model must be sufficiently simple to be executed near to real-time, yet accurate enough to provide a reasonably accurate estimate of thermal dynamics inside the cell.

The methodology is here applied to design a simplified thermal model of a prismatic (pouch-style) Li-Ion battery cell that approximates the dynamic temperature distribution in presence of internal heat generation and convective boundary conditions. The paper describes in detail the model assumptions and the mathematical framework. A comparative study is then conducted to benchmark the model predictions with results from a detailed FEM simulator.

PROBLEM OVERVIEW AND MODELING APPROACH

Although the modeling methodology presented in this study is generally applicable to any battery cell, a 20Ah prismatic (pouch-style) cell for automotive applications is considered as the reference geometry.



FIGURE 1. PRISMATIC LI-ION BATTERY CELL

Figure 1 shows the system considered, while Table 1 reports the essential battery cell data.

TABLE 1. DATA OF THE LI-ION CELL.

Parameters	Values
Length	216mm
Width	129mm
Thickness	7.2mm
Capacity	20 Ah
Nominal Voltage	3.65 V

Mathematical Formulation of the Thermal Model

The starting point for the model development is the unsteady non-homogeneous heat diffusion equation, which describes the temperature distribution in a given region over time [10] [11]:

$$\frac{\partial}{\partial x} \left(k_x \frac{\partial T}{\partial x} \right) + \frac{\partial}{\partial y} \left(k_y \frac{\partial T}{\partial y} \right) + \frac{\partial}{\partial z} \left(k_z \frac{\partial T}{\partial z} \right) + \dot{q} = \rho c_p \frac{\partial T}{\partial t} \quad (1)$$

However, due to the specific geometry of the cell, the thickness results one order of magnitude smaller than the other two dimensions. Assuming isotropic properties for the cell materials and neglecting edge effects and the tabs, it is possible to simplify the problem to a one-dimensional unsteady heat conduction along the thickness direction x :

$$\frac{\partial^2 T}{\partial x^2} + \frac{\dot{q}(x,t)}{k} = \frac{1}{\alpha} \frac{\partial T}{\partial t} \quad (2)$$

where $\alpha = k/(\rho c_p)$ represents the thermal diffusivity of the material [m^2/s]. The above assumptions can also be explained by performing a simple order of magnitude analysis ([12] or [13]). Figure 2 shows a cross-section of the battery cell, identifying the domain where Equation 2 is applied.

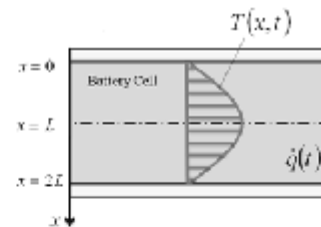


FIGURE 2. CROSS-SECTION OF THE BATTERY CELL

To solve Equation 2, one initial condition and two boundary conditions are needed. In particular, the boundary conditions can be of three different kinds:

- Specified temperature of an exposed surface;
- Specified heat flux from or to an exposed surface (insulation and symmetry are particular cases of this kind of boundary condition);
- Convection or radiation heat transfer on an exposed surface.

The combination of Equation (2) with any two of the above boundary conditions results into a non-homogeneous, transient, boundary-value problem (BVP), for which several solution methods have been developed [14]. In particular, analytical methods have the advantage of not requiring a discretization of the domain or an iterative solution algorithm, hence allowing for a more computationally efficient model. However, such solution is possible only if the BVP allows for a closed-form solution. If the partial differential equation is non-homogeneous (which is the case in presence of internal heat generation), the integral transformation method can be applied to obtain an analytical solution [15].

The integral transformation method is a projection method where a boundary value problem is solved using a functional space to remove the dependence of the partial differential equation from the spatial variables. The transformation method adopted depends on the integration domain of the partial

differential equation and on the boundary conditions of the problem:

$$\text{Integral Transform: } \bar{F}(\beta_m) = \int_{x=0}^{2L} K(\beta_m, x) \cdot F(x) dx \quad (3)$$

$$\text{Inversion Formula: } F(x) = \sum_{m=1}^{\infty} K(\beta_m, x) \cdot \bar{F}(\beta_m) \quad (4)$$

The Kernel, K , is the transformation operator that transitions the BVP from a dimensional space into a functional space, where it is possible to determine a solution that describes the time evolution of the system. Then, by applying the inverse transform operator, the complete solution (including the spatial characterization) is obtained.

The eigenvalues β_m and the inversion formula are obtained from the expansion of an infinite series of eigenfunctions that solve the following eigenvalue problem:

$$\begin{cases} \frac{d^2X}{dx^2} + \beta X = 0 & \text{in } 0 \leq x \leq 2L \\ \frac{dX}{dx} = 0 & \text{at } x = 0 \\ X = 0 & \text{at } x = 2L \end{cases} \quad (5)$$

The eigenvalues β_m and the Kernel functions are tabulated in relation on the range of the space variables (finite, semi-infinite or infinite extend) and on the type of the boundary conditions [15].

By applying the integral transform method to Equation 2, the following solution is obtained:

$$T(x, t) = \sum_{m=1}^{\infty} e^{-\beta_m^2 t} K(\beta_m, x) \cdot \left[F(\beta_m) + \int_{t=0}^t e^{\beta_m^2 \tau} A(\beta_m, \tau) d\tau \right] \quad (6)$$

where:

$$A(\beta_m, t) = \frac{\alpha}{k} q(\beta_m, x) + \alpha \left(\frac{K(\beta_m, x=0)}{k} f_1 + \frac{K(\beta_m, x=L)}{k} f_2 \right)$$

and the terms f_1 and f_2 are functions that represent general boundary conditions:

$$f_1(t) = -k_1 \frac{\partial T}{\partial x} + h_1 T = h_1 T_{\infty} \quad (7)$$

$$f_2(t) = -k_2 \frac{\partial T}{\partial x} + h_2 T = h_2 T_{\infty} \quad (8)$$

Note that, by properly simplifying Equation 7 and 8, it is possible to obtain various boundary conditions (imposed temperature, imposed heat flux, convection).

Following the procedure outlined above, it is possible to obtain the analytical solution of a 1D temperature distribution with respect to time and the x -direction, with uniform internal heat generation and subject to various boundary conditions. In the following sections, the solution will be applied to a case of convective boundary condition, which is representative of automotive battery cooled by a forced air flow.

1D Thermal Model with Convection

With reference to the diagram shown in Figure 3, a prismatic battery cell subject to forced convective cooling is

here considered. The cooling is realized by forcing a steady-state air flow through channels located on both sides of the cell.

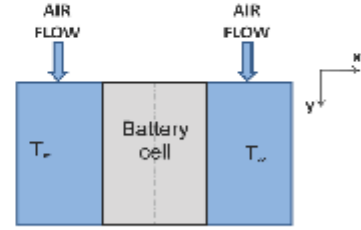


FIGURE 3. SCHEMATIC OF THE MODEL WITH CONVECTIVE COOLING CONDITIONS.

The air approaches the cooling channels at a prescribed temperature and removes heat from the cell. A heat transfer coefficient h can be computed from empirical correlations available in the open literature, i.e. [12] or [16]. As a first approximation, fully developed laminar flow is assumed in the channel, hence allowing for imposing a constant heat transfer coefficient.

With this assumption, the boundary value problem for the 1D model can be cast in the following form:

$$\begin{cases} \frac{\partial^2 T}{\partial x^2} + \frac{\dot{q}(x,t)}{k} = \frac{1}{\alpha} \frac{\partial T}{\partial t} \\ -k \frac{\partial T}{\partial x} = h(T - T_{\infty}) & \text{for } x = 0, t > 0 \\ -k \frac{\partial T}{\partial x} = h(T - T_{\infty}) & \text{for } x = 2L, t > 0 \\ T = T_0 & \text{for } 0 \leq x \leq 2L, t = 0 \end{cases} \quad (9)$$

Assuming that the battery cells are arranged in a parallel cooling case system (for example, as shown in [6]), the two air flows are considered to be equivalent, namely at the same bulk velocity and temperature. Based on [15], the eigenvalues β_m associated to the BVP described in Equation 9 are the solution of the following transcendental equation:

$$\tan(2\beta_m L) = \frac{\beta_m(H_1 + H_2)}{\beta_m^2 - H_1 H_2} \quad (10)$$

where $H = \frac{k_{conv}}{h_{conv}}$. The associated Kernel function is:

$$K = \sqrt{2} \frac{\beta_m \cos(\beta_m x) + H_1 \sin(\beta_m x)}{\left[(\beta_m^2 + H_1^2) \left(2L + \frac{H_2}{\beta_m + H_1} \right) \right]^{1/2}} \quad (11)$$

Figure 4 shows the Kernel function calculated using the thermal parameters summarized in Table 2.

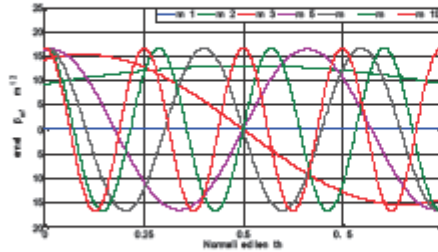


FIGURE 4. KERNEL FUNCTION FOR CONNECTION CONDITIONS.

There are an infinite numbers of kernel terms and therefore the accuracy of the solution increases if more terms are considered. However we noticed that the terms after the fifth do not improve the accuracy for this specific problem, and thus they are negligible.

TABLE 2. PARAMETERS OF THE THERMAL MODEL FOR

Parameters	Values
k [W/mK]	0.696
ρ [kg/m ³]	2118
c_p [J/kg K]	795
h [W/m ² K]	22

The 1D model is defined by applying Equation 6 with the Kernel function defined in Equation 11. The heat generation rate is determined according to [17]:

$$\dot{Q} = I \left(V_{oc} - V - \frac{\partial V_{oc}}{\partial T} T \right) \quad [W] \quad (12)$$

and it is assumed to be spatially uniform within the cell (hence neglecting the effects of tabs, hot spots, etc...). Furthermore, the dependence of the open circuit voltage from the temperature has been neglected, as a first approximation ([18] - [19]).

Extension to 1+1D Thermal Model

The 1D model developed above is able to characterize the temperature distribution and heat flux along the direction x , assuming uniform air temperature. However, as the air flows in the channel, it is gradually heated due to the convection, ultimately decreasing its ability to extract heat from the cell.

In order to characterize the air temperature variation along the air flow direction (here denoted with y), the 1D model described above has been extended to 1+1D model, where the system (battery cell with cooling channels) is discretized into a finite number N of lumps along the y -direction. Assuming a constant air flow rate in the y direction, the forward Euler discretization method is adopted to determine the air temperature in each lump, in the direction of the flow.

Considering the i^{th} lump, the energy equation can be applied to determine the air temperature, assuming uniform distribution in the control volume (well-mixed assumption):

$$m c_p \frac{dT_{air,i}}{dt} = m c_p T_{air,i-1} - m c_p T_{air,i} + A h (T_{w,i} - T_{air,i}) \quad (13)$$

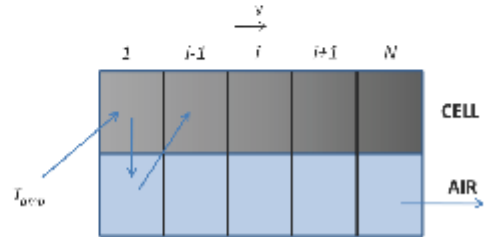


FIGURE 5. SOLUTION SCHEME FOR THE 1+1D MODEL.

Figure 5 shows a conceptual scheme of the model. The methodology adopted to solve the 1+1D model is summarized as follows:

- The 1D model is applied to compute the battery temperature distribution in the i^{th} lump, along the x -direction. To this end, the temperature $T_{air,i-1}$, relative to the lump $(i-1)$, is used to determine the boundary conditions for the BVP.
- Once the cell temperature profile is calculated, the value at the wall ($x=2L$) is applied to Equation (13) to solve the energy balance for the air flow in the i^{th} lump.

By applying this scheme, it is possible to approximate the variation of the boundary conditions that are used to model the temperature variation in the direction of the air flow.

It is possible to obtain a grid-independent solution by choosing a number of discretization elements greater than 100 in the y -direction.

RESULTS

This section summarizes the results obtained with the proposed modeling approach. A brief description of results obtained with the 1D model on a single lump will be presented and then the results of the 1+1D model will be shown. At this stage, the calibration and validation of the models have been conducted utilizing the results of a detailed FEM thermal simulation, performed with COMSOL®.

Temperature Distribution with 1D Model

In order to calculate the temperature distribution within the battery cell, a heat transfer coefficient $h=22.3$ [W/m²K] was chosen. Such value is appropriate for forced laminar flow [12], [16].

The heat generation profile, calculated with Equation 12, is based on voltage and current data obtained from an experimental test for the characterization of electro-thermal

battery models [18], [20]. The current, voltage and heat generation rate profile are shown in Figure 6.

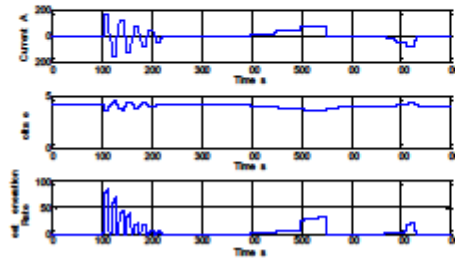


FIGURE 6. CURRENT, VOLTAGE AND HEAT GENERATION RATE PROFILES.

Figure 7 shows the evolution of the battery cell temperature as the internal heat generation rate varies in time. In particular, the temperature at the center of the cell ($x=L$) and at the wall ($x=2L$) are represented in the same plot.

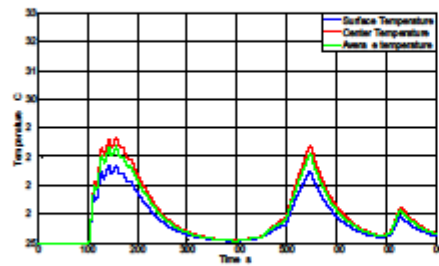


FIGURE 7. CHARACTERIZATION OF BATTERY CELL TEMPERATURES IN 1D MODEL.

It is possible to observe that the system responds with a relatively slow dynamics, particularly when the heat generation rate is zero (e.g., when no current is applied). This is a consequence of the very low convection coefficient, which limits the ability of the air to extract heat from the system. As a result, the battery internal temperature increases with the internal heat generation with a nearly uniform profile along the x direction.

This behavior is confirmed in Figure 8, where the time evolution of the complete temperature profile along the cell thickness is shown. As expected the temperature distribution is almost flat, due to the cell conductivity and slow heat removal from the boundaries.

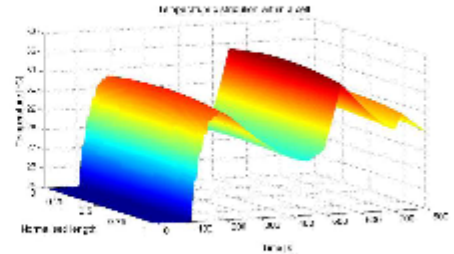


FIGURE 8. CHARACTERIZATION OF BATTERY CELL TEMPERATURE DISTRIBUTION IN 1D MODEL.

Temperature Distribution with 1+1D Model and Validation

In order to provide a validation framework for the 1D and the 1+1D model in the absence of experimental data, a FEM model was developed in COMSOL[®], with reference to the system geometry shown in Table 1. Due to the nature of the system considered in this study, a 2D heat transfer problem is formulated in the x and y dimensions, assuming uniformity of the velocity and temperature fields along the z direction. This assumption allows for a partial simplification of the problem, without any relevant penalty on the accuracy of the solution. The model solves simultaneously the coupled heat transfer equation and the incompressible Navier-Stokes equation in the air flow domains. In the battery cell domain, the 2D heat diffusion equation is solved, considering anisotropic thermal properties for the cell materials [9]. In particular, a simulation consisting of 448 meshing elements has been performed for a total time of 800 s at 1 s time step.

In order to solve the problem, boundary and initial conditions are needed: in this case, it is assumed that the air enters the channels at 3 m/s and that the initial temperature is uniform for the whole system and equal to 25 °C.

Figure 9 shows the temperature field predicted by the FEM simulation at the time $t=748$ s, where temperatures of the battery cell reaches one of the peaks. Only the first 40mm and the last 40mm regions of the cell are shown, to give better temperature field resolutions. It is possible to observe the thermal boundary layer in the air gradually developing along the flow.

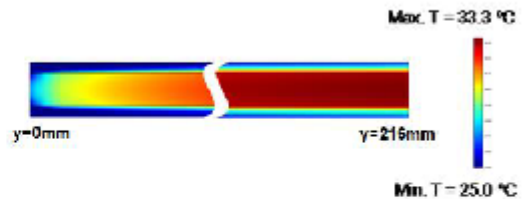


FIGURE 9. TEMPERATURE DISTRIBUTION IN THE COOLING CHANNEL PREDICTED BY THE FEM MODEL AT $t=748$ s.

A preliminary comparison of the 1+1D model prediction was done against the FEM simulation results. Figures 10-12 show the temperature dynamics at the center of the cell ($x=L$), as well as the cooling air temperature at three locations within the domain, namely at the entrance ($y=0mm$), at the outlet ($y=216mm$) and at an intermediate location ($y=54mm$). Due to the increasing air temperature along the flows, each lumps of the battery cell are subjected to slightly different boundary conditions which results in the temperature differences shown in the figures.

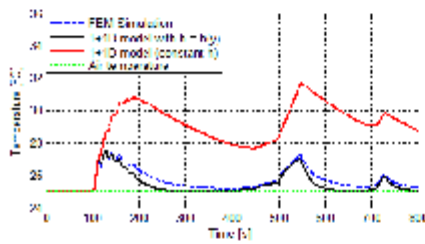


FIGURE 10. COMPARISON OF CELL AND AIR TEMPERATURE DYNAMICS AT THE INLET $y=0mm$.

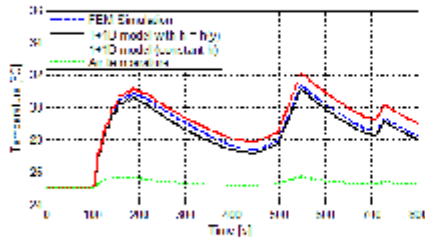


FIGURE 11. COMPARISON OF CELL AND AIR TEMPERATURE DYNAMICS IN THE CHANNEL $y=54mm$.

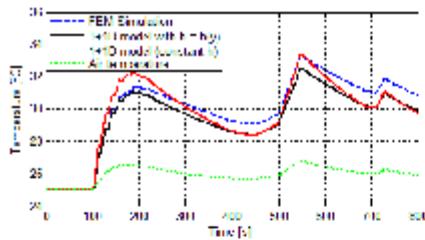


FIGURE 12. COMPARISON OF CELL AND AIR TEMPERATURE DYNAMICS AT THE OUTLET $y=216mm$.

It is immediately observed that, with the parameters listed in Table 2, the 1+1D model tends to overestimate the battery temperatures predicted by the FEM model, especially at the entrance of the cooling channel.

The reason for this behavior stems from the fact that the effects of the entry region have been neglected from the calculation of the convective heat transfer rate. In fact, a fully developed laminar flow was assumed in the channel, hence leading to constant Nusselt number and thus constant heat transfer coefficient. In reality, the heat exchange between the battery surface and the coolant should be significantly higher at the entrance, and progressively decreasing along the flow direction as the fluid reaches the outlet section. Consequently, the heat transfer coefficient h is expected to present higher values in the entry region. This behavior is confirmed by the fundamental heat transfer theory for laminar flows, where empirical correlations have been specifically developed to estimate the average convection coefficient for a developing flow in the entry region of a channel [16].

As a result, the convective heat transfer coefficient was calibrated to characterize the effects of the entry region in the computation of the temperatures. In particular, the parameter h was non-dimensionalized: $y^* = \frac{y}{D_h}$, where D_h is the hydraulic diameter of the duct. The calibrated convective heat transfer coefficient h is expressed as:

$$h = h(y) = \frac{a}{y^*} + b \quad (14)$$

where the parameters a and b have been calibrated through a comparison with the FEM simulator.

The results of the calibrated 1+1D model are represented on the same figures (9-11), showing how the variable convection coefficient allows for improving the model results.

Although some minor errors between the 1+1D model results and the 2D FEM simulation are present, the developed model results reasonably accurate and computationally efficient. As a proof, Table 3 compares the computation time and memory requirements of the models discussed in the paper, with reference to the simulation results shown in the above figures.

TABLE 3. COMPARISON OF COMPUTATIONAL REQUIREMENTS OF THE MODELS.

Model	Computation Time [s]	Memory Usage [Mfb]
1D	1.5	290
1+1D	58	300
FEM	2100	341

CONCLUSION AND FUTURE WORK

This paper presents a computationally efficient, low-order model that predicts the dynamic temperature distribution in a prismatic Li-Ion battery cell. The model is general, in a sense that it can predict the temperature distribution within a cell under different boundary conditions. In particular, a 1+1D model was developed to evaluate the thermal dynamics of a battery cell in presence of convective cooling.

The consistency with the 2D FEM solution, the simple structure, and the computational efficiency make the model an ideal candidate for real-time model-based control and diagnostic algorithms.

The model developed is characterized by a general structure, which allows one to easily select cooling parameters, such as cooling air velocity, air temperature, air duct geometry, etc., and compare the effects of different cooling systems. As part of the future developments of the current work, a comparative analysis of the performance of cooling bar system and conventional forced cooling air flow will be performed.

Further, to provide additional validation results for the 1D and the 1+1D model, an experimental setup is currently being planned to measure the surface temperature distribution on a prismatic Li-Ion cell.

REFERENCES

- [1] S. Onori, G. Rizzoni, Y. Guezennec L. Serrao, "A Novel Model-Based Algorithm for Battery Prognosis," *7th IFAC SafeProcess Conference*, 2009.
- [2] S. Onori, N. Madella, Y. Guezennec, G. Rizzoni V. Marano, "Lithium-Ion Battery Life Estimation for Plug-In Hybrid Electric Vehicles," *Proceedings of IEEE Vehicle Power and Propulsion Conference*, 2009.
- [3] K. Smith, T. Markel A. Pesaran, "Impact of the 3Cs of Batteries on PHEV Value Proposition: Cost, Calendar Life and Cycle Life," *9th Advanced Automotive Battery Conference*, 2009.
- [4] P. Ramadass, Bala Haran, Ralph White, and N. Popov, "Capacity fade of sony 18650 cells cycled at elevated temperatures Part I. Cycling performance," *Journal of power sources*, vol. 112, 2002.
- [5] P. Ramadass, Bala Haran, Ralph White, and N. Popov, "Capacity fade of Sony 18650 cells cycled at elevated temperatures. Part II. Capacity fade analysis," *Journal of power sources*, vol. 112, 2002.
- [6] A. Pesaran, "Battery thermal models for hybrid vehicle simulations," *Journal of Power Sources*, no. 110 (2002) 377-382, 2001.
- [7] J. Newman and C. Pals, "Thermal Modeling of the Lithium/Polymer Battery - I Discharge behavior of a single cell," *Journal electrochemical Society*, vol. 142, no. 10, 1995.
- [8] J. Newman and C. R. Pals, "Thermal Modeling of the Lithium/Polymer Battery - II Temperature profile in a cell stack," *Journal Electrochemical Society*, vol. 142, no. 10, 1995.
- [9] C.C. Wan, Y.Y. Wang S.C. Chen, "Thermal analysis of lithium-ion batteries," *Journal of Power Sources*, no. 140 (2005) 111-124, 2004.
- [10] Yunus A. Çengel, *Heat Transfer: A Practical Approach*, 2nd edition.: McGraw-Hill, 2003.
- [11] Vedat S. Arpacı, *Conduction heat transfer*: Addison-Wesley.
- [12] Frank P. Incropera and David P. De Witt, *Fundamentals of heat and mass transfer - 5th edition*: WILEY.
- [13] I. G. Currie, *Fundamental mechanics of fluids*: Marcel Dekker, 2003.
- [14] R. Haberman, *Applied Partial Differential Equations*, 4th ed.: Pearson, 2004.
- [15] M. Necati Ozisik, *Boundary value problems of heat conduction*. Scranton, Pennsylvania: International textbook company, 1969.
- [16] R.K. Shah and A.L. London, *Advanced in heat transfer: Laminar flow forced convection in ducts*: Academic Press, 1978.
- [17] D. Bernardi, E. Pawlikowski, and J. Newman, "A General Energy Balance for Battery Systems," *Journal of Electrochemical Society*, vol. 132, no. 1, January 1985.
- [18] Y. Hu, S. Yurkovich, Y. Guezennec, and R. Bortnico, "Model-Based Calibration for Battery Characterization in HEV Applications," *Proceedings of American Control Conference*, 2008.
- [19] M. Muratori, M. Canova, Y. Guezennec, and G. Rizzoni, "A Reduced-Order Model for the Thermal Dynamics of Li-Ion Battery Cells".
- [20] Y. Hu, B. J. Yurkovich, S. Yurkovich, and Y. Guezennec, "Electro-Thermal Battery Modeling and Identification for Automotive Applications," *Proceedings of the ASME Dynamic Systems and Control Conference*, 2009.